# Novel Reinforcement for Flexibly-Formed Concrete Structures

Yang, Yuanzhang

*Award date:*
2018

*Awarding institution:*
University of Bath

# Novel Reinforcement for Flexibly-Formed Concrete Structures

submitted by

Yuanzhang Yang

for the degree of Doctor of Philosophy

of the

University of Bath

Department of Architecture and Civil Engineering

September 2018

# Abstract

Concrete is the most widely used artificial material around the world, the production of which is associated with over 5% of total carbon emissions. Conventional concrete structures have prismatic geometries partly due to rigid formworks, resulting in inefficient use of materials. Fabric formwork has been used to enable structural optimisation, capitalising on the flexibility of woven fabrics and unique fluidity of wet concrete. However, a significant drawback is the complexity of fabricating steel reinforcement cages for flexibly formed concrete elements, which normally have variable-depth geometries. Both curving flexural reinforcement into the designed profiles and producing shear links of variable dimensions requires additional costs of time and labour.

In this dissertation, a new reinforcing system, Wound-Fibre-Reinforced Polymer (W-FRP), is proposed as a durable alternative for the reinforcement of flexibly formed concrete beams, thereby unlocking the potential to minimise carbon emissions associated with concrete construction. An automated method has been developed to produce W-FRP cages, which are light-weight, easily transported and adaptable to many beam geometries created using fabric formwork. Based on the design and optimisation process developed in this research, three series of structural testing were undertaken to investigate the structural behaviour of W-FRP reinforced concrete beams with both prismatic and variable-depth geometries. Modelling and parametric analysis are undertaken to achieve the optimum design of fabric formed T beams reinforced with W-FRP. Through testing and analysis, further practical guidance is provided for designers.

The experimental and theoretical research in this thesis has shown the great effectiveness and constructability of the W-FRP reinforcing system, with which up to 23% concrete saving can be achieved without compromising structural performance. The geometry, W-FRP shear reinforcement, and anchorage design have been shown as the key factors influencing the structural behaviour of W-FRP reinforced beams. It is possible to optimise the W-FRP patterns to achieve up to 50% increase in shear performance without additional reinforcement use. Capitalising on flexible fabric formwork and W-FRP shear reinforcement, this thesis demonstrates that constructing more durable and sustainable concrete structures can be achieved in a feasible and practical manner.

## Declaration

The author declares that, except for where specific reference is made to work done by others, or for commonly accepted and commonly understood ideas, and unless otherwise stated in the text, the contents of the thesis are his own work. This thesis has not been previously submitted, in part or whole, to any institution or university for any diploma, degree or other qualification.

# Acknowledgement

The research in this dissertation was carried out in the Department of Architecture and Civil Engineering at the University of Bath between 2014 and 2018.

I would like to express my sincere gratitude to my supervisors Dr. John Orr, Prof. Tim Ibell, Dr. Antony Darby and Dr. Mark Evernden. Their encouragement, patience and knowledge attributed to excellent supervision, helping me throughout my PhD study, research and writing of this dissertation.

The financial support from EPSRC and Chinese Scholarship Council also has my gratitude. Without their support, I cannot come to the UK for my doctoral study.

I also want to thank everyone who supported me throughout this project, especially Dr. Spadea for his help in both research and life and all the staff in the laboratory in this department for their support in my experimental research.

Finally, I am thankful to my parents. It has been tough for them to only see me three times in four years. Your understanding helped to go through the hard time in my study.

# Contents

# List of Figures

# List of Tables

# Chapter 1

# Introduction

## 1.1 Research background

Concrete is the worlds most widely used artificial material and accounts for a large proportion of global raw material expenditure (Flower and Sanjayan, 2007). Due to the magnitude of concrete consumption, annual Portland cement production reached 4.1 gigatonnes in 2017 (USGS, 2018). The production of cement results in a significant number of carbon emissions from the decomposition of carbonates and the combustion of fossil fuels to generate the significant energy required to heat the raw ingredients (Boden et al., 2013), which account for more than 5% of global CO2 emissions (Boden et al., 2013).

The environmental impact of producing cement and constructing concrete structures has been recognised (Mehta, 2001; Chen et al., 2010; Huntzinger and Eatmon, 2009). New design philosophies and research interests have been moving towards sustainable concrete structures, the construction of which results in fewer carbon emissions and embodied energy (Mehta, 2002; Naik, 2008).

In Structural Engineering, one route to reducing carbon emissions from concrete structures is structural optimisation, putting materials where they are required (Ibell et al., 2013). Creating optimised geometries for concrete structures can result in structural, environmental and economical benefits: lighter weight, hence lower dead load and lower usage of material, thus less cost and lower carbon emission and embodied energy. In addition, optimised structures usually have non-prismatic geometries which can be architecturally interesting.

Although reinforced concrete has been used in construction for over 100 years, the main obstacle to building optimised concrete structures in practice is the formwork (Nervi, 1956). Traditional timber and steel formwork are rigid to form prismatic concrete structural elements, which often have constant flexural and shear capacity along their length, whereas the bending moment and shear force normally vary in practice. Consequently, for a typical concrete structure, only 60% of the concrete works to resist applied load (Thirion, 2013). Although traditional formworks can be used to cast non-prismatic concrete elements, this requires special design and fabrications, which create additional costs of time and labour.

In addition to traditional formwork, many solutions have been developed to construct optimised concrete structures, such as wax moulds (Naik, 2008), 3D printed formwork (Peters, 2014), Expanded Polystyrene foam (EPS) formwork (Janssen, 2011) and Vacuumatic formwork (Huijben, 2016). However, compared to traditional formwork, these techniques involve much higher costs, associated with complex fabrications, specialised production equipment and re-usability issues.

Fabric formwork is a novel flexible forming system that uses permeable woven fabric as the container of wet concrete (West, 2016; Veenendaal et al., 2011b). Capitalising on the flexibility of woven fabric, complex and architecturally interesting geometries of concrete structures can be created (Figure 1-1), without additional costs and limitation, associated with the production of non-prismatic timber or steel moulds.

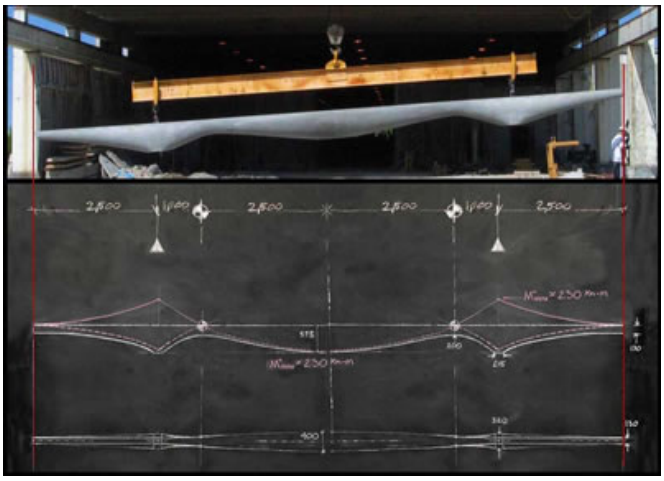

Figure 1-1: Fabric formed beam (Image courtesy: Mark West)

By providing everywhere the strength and stiffness required by an envelope of design actions, the optimisation of reinforced concrete elements using fabric formworks have been undertaken by many researchers (West, 2016; Veenendaal et al., 2011b; Orr, 2012;

Kostova, 2016; Lee, 2011) (Figure 1-1). It has been shown that the fabric formed beams can reduce concrete use by over 40%, compared to equivalent strength prismatic beams (Garbett et al., 2010; Orr, 2012). In addition to saving concrete by forming optimised geometries, there are many advantages of fabric formworks over traditional forming systems (Orr, 2012; Kostova, 2016).

Woven fabrics are much lighter than traditional formworks. Capitalising on the tensile strength of fabrics, fabric formworks do not require additional supports and bracing systems to resist the lateral pressure created in the forming process. The permeable fabrics also allow water to leak from the mould during casting, which significantly improves the surface quality (Orr et al., 2012). The water leak brings higher strength of surface concrete and lower porosity and hence reduces the rate of carbonation and chloride penetration. The better surface quality of concrete provides further possibilities to be architectural elegant using fabrics, as shown in Figure 1-2.

Figure 1-2: Architectural possibilities using fabric formwork (Image courtesy: Michel Fisac)

## 1.2 Challenges

Fabric formed concrete structures require reinforcement that is adaptable to complex geometries. As the most widely used reinforcement in structural engineering, steel rebars can still be used in optimised beams, as shown in Figure 1-3. However, complex steel reinforcing cages require additional efforts (Orr, 2012): (i) the flexural reinforcement needs to be curved precisely into the correct profile to provide the designed bar force in tension zone and (ii) due to the variable-depth geometry, all the stirrups along the beam axis have different geometries.

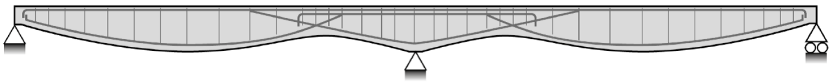

Figure 1-3: Complex steel reinforcement of optimised beam (Image courtesy: John Orr)

Fibre reinforced polymer reinforcement (FRP) has been applied in structural engineering since the 1980s (ACI-440.1R, 2015). Prior to resin coating, the raw fibres used to produce FRP are flexible. Besides, FRP reinforcement can be curved more easily than steel due to the relatively lower elastic modulus. Therefore, there is a great potential for developing flexible FRP reinforcement cages for specific concrete structural elements with non-prismatic geometries.

The research presented this thesis aims to develop a simple and effective solution to reinforce the fabric formed beams. The reinforcing system composed of novel Wound Fibre Reinforced Polymer (W-FRP, shown in Figure 1-4) shear reinforcement and commercial FRP bars is proposed, that capitalises on the flexibility of carbon fibre tows and ease of curving FRP bars compared with steel reinforcement (Kostova, 2016). The proposed W-FRP shear reinforcement is expected to be feasible, economical and practical to be applied in fabric formed concrete beams.

Figure 1-4: Wound FRP cage for concrete beam (Image courtesy: John Orr)

However, research challenges still prevent the use of the W-FRP reinforcing cage in fabric formed concrete beams. First, the feasibility of the proposed reinforcing system has not been well understood, as limited research has been undertaken on the performance of W-FRP shear reinforcement and W-FRP reinforced concrete.

Previous research has focussed on steel reinforced fabric formed concrete structures.

With the proposed W-FRP reinforcing system, fabric formed structures incorporate the variable-depth geometry and linear-elastic reinforcement, which may lead to more complicated structural behaviour.

Finally, since W-FRP provides the potential of efficiently constructing concrete structures with complex geometries, a new design method needs to be developed to minimise the material use of concrete and W-FRP reinforcement.

## 1.3 Objectives and approach

The main objectives of the research undertaken in this thesis are:

1. To demonstrate the constructability of the W-FRP reinforced concrete beams formed by fabric formwork, with a new automated winding method to produce the W-FRP cages.
2. To determine the material properties of W-FRP shear reinforcement and its effectiveness of enhancing the shear performance of concrete beams.
3. To determine the static mechanical performance and stiffness properties of W-FRP reinforced beams with prismatic and variable depth geometry.
4. To establish a new process by which a W-FRP reinforced concrete beam can be designed to minimise its concrete and reinforcement use and the structural behaviour of the can be accurately predicted, based on the experimental and theoretical work.
5. To compare the W-FRP reinforced concrete beams to conventional concrete beams and show the advantage of W-FRP reinforced concrete beams in concrete use.

This thesis addresses these objectives through a combination of experimental, theoretical and analytical work in seven chapters. Chapter 2 presents a full review of the literature, related to the research undertaken on fabric formwork, fabric-formed concrete beams and existing design approaches. Chapter 3 details the methodology in this research, including proposed design and optimisation methods, experimental research philosophy and parametric analysis of modelling. Chapter 4, Chapter 5 and Chapter 6 detail the experimental work undertaken and corresponding analysis of each series of testing. Chapter 7 presents the modelling and parametric analysis. Finally, conclusions and future work are summarised in Chapter 8.

## 1.4 Funding and supervisory board

This research has been funded as part of an Engineering and Physical Science Research Council (EPSRC) and China Scholarship Council (CSC). Dr John Orr is the lead academic supervisor, supported by Professor Tim Ibell, Dr Antony Darby and Dr Mark Evernden.

## 1.5 Publications

Journal papers:

- **Yang, Y.**, Orr, J., Spadea, S. (2018). Shear behaviour of variable-depth concrete beams with Wound Fibre Reinforced Polymer shear reinforcement, Journal of Composites for Construction (accepted).
- Spadea, S., Orr, J., Nanni, A., & **Yang, Y.** (2017). Wound FRP shear reinforcement for concrete structures. Journal of Composites for Construction, 21(5), 04017026.

Conference papers:

- **Yang, Y.** and Orr, J and Ibell, T and Spadea, S (2017). Structural performance of flexibly formed concrete T beams with wound FRP reinforcement.ACIC 2017 - Proceedings of the 8th Biennial Conference on Advanced Composites in Construction.pp. 283-288.
- **Yang, Y.**, Orr, J., & Spadea, S. (2018). Wound FRP for Concrete Beams with Optimised Geometries. High Tech Concrete: Where Technology and Engineering Meet.
- **Yang, Y.**, Orr, J., Ibell, T. and Darby, A., 2015. Shear strength theories for beams of variable depth. In: IASS2015 Annual International Symposium on Future Visions IASS/ISOFF, 2015-08-16 - 2015-08-20.
- Spadea, S., Orr, J. and **Yang, Y.**, 2015. Bespoke Reinforcement for Optimised Concrete Structures. In: IASS Annual Symposium: Future Visions - IASS/ISOFF 2015, 2015-08-16 - 2015-08-20.

# Chapter 2

# Literature review

## 2.1 Introduction

Chapter 2 provides a detailed literature review of the research background of this thesis. The development of fabric formwork and the construction techniques of fabric formed beam elements are discussed. The constitutive relations of materials including concrete and FRP are reviewed as a fundamental design basis for new design methods. The design methodologies adopted in previous research are discussed with the experimental research and reinforcing techniques of fabric formed beams in four aspects: flexure, shear, anchorage and stiffness. Finally, the research gaps between existing literature and the research aims of this thesis are summarised.

## 2.2 Fabric formwork

This section presents a literature review of fabric formwork for concrete beams. The development of fabric formwork from its initial application to the present research is discussed. Three construction techniques for fabric formed beams are presented.

### 2.2.1 Development

One of the applications of fabric formwork in concrete construction was undertaken by Lilienthal (1899), who developed a casting system for concrete slab using fabrics (Figure 2-1) and obtained a patent in 1899. This forming technique was applied in the housing projects and buildings in Berlin, Germany, throughout the 1890s (West, 2016).

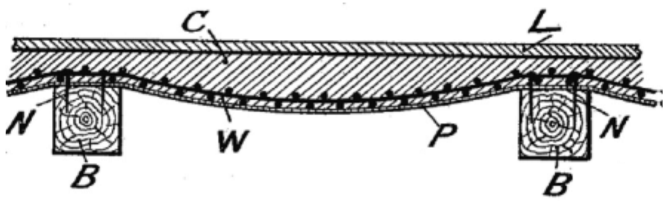


Figure 2-1: Fabric formed floor (Image courtesy: Lilienthal, 1899)

Similar concepts were developed and repeated (West, 2016), one of which is the 'Nofrango' system (Figure 2-2 (a)) by Waller (1934). Hessian fabrics were used to construct concrete elements such as floors and roofs. More possibilities using fabric formwork were explored by Waller (1955), as shown in the Ctesiphon system (Figure 2-2 (b)). Fabrics were used to cast these convenient shells elements across Europe during the 1940s and 1970s (Veenendaal et al., 2011b). The simplicity of this system was fully demonstrated by the ease of construction, not relying on skilled workers (Veenendaal et al., 2011b).

In addition to the initial purpose of reducing construction cost, explorations of fabric formwork to create aesthetic concrete facade were undertaken by Miguel Fisac (West, 2016; Veenendaal et al., 2011b; Hawkins et al., 2016). A construction method using fabric formwork was developed and patented for prefabricated wall panels in the 'MUPAG' centre, Madrid (Figure 2-3 (a)). More architectural possibilities of wet concrete formed by fabric formwork are demonstrated by the 'P-wall' in New York (Figure 2-3 (b)). Further possibilities were investigated by applying fabric forming techniques in constructing elements such as walls, stairs, roof canopies, solar shades and even furniture. 'Zero

waste fabric formwork' was developed by Kenzo Unno (Veenendaal et al., 2011b) to construct concrete walls, as shown in Figure 2-4.

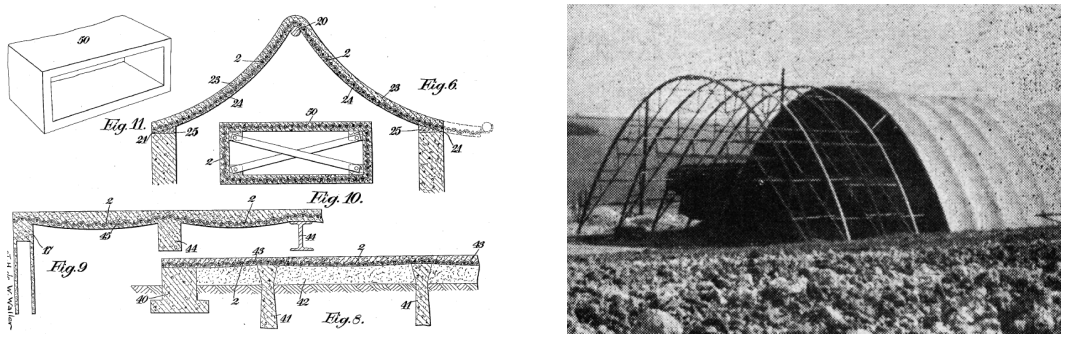


(a) (b)

Figure 2-2: Fabric formed concrete structures by Waller: (a) Patented fabric formed elements and (b) Ctesiphon system

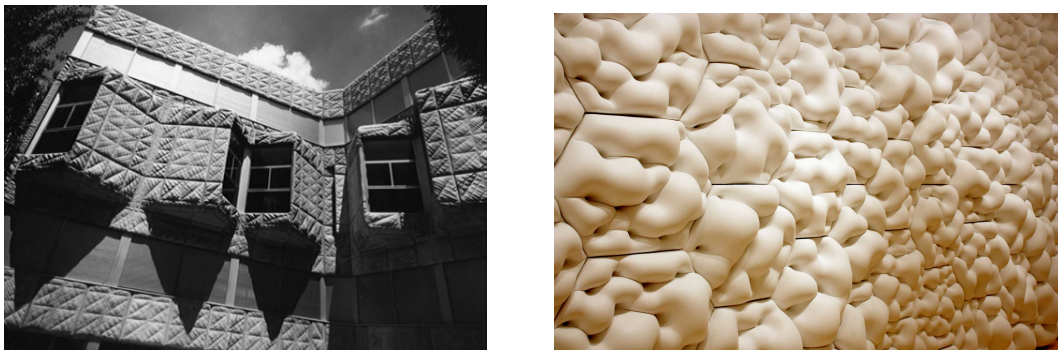

(a) (b)

Figure 2-3: (a) 'MUPAG' centre (Image courtesy: Michel Fisac) and (b) P-wall (Image courtesy: Andrew Kudless)

The most influential research in recent years was carried out at the 'Centre for Architectural Structures and Technology' (C.A.S.T), University of Manitoba. The research conducted by Professor West (2016) demonstrated the great potential of fabric formwork in Architecture and Structural Engineering. The construction methods and form-finding methods for beams, trusses, columns and shells were explored by physical modelling as shown in Figure 2-5. Structural performance of variable depth beams was also investigated by Hashemian (2012).

Further contributions to the development of fabric formwork and investigations into fabric formed beams, floors, columns and walls have been undertaken around the world (Hawkins et al., 2016). International conferences of flexible formwork were successfully held at the University of Manitoba in 2008, the University of Bath in 2012, and in

Amsterdam in 2015. The research around the world has contributed to the development of fabric formed concrete in form-finding, innovative forming techniques, durability, reinforcement and design methods.

Figure 2-4: Zero waste fabric formwork (left) and fabric formed wall (Image courtesy: Kostova (2016))

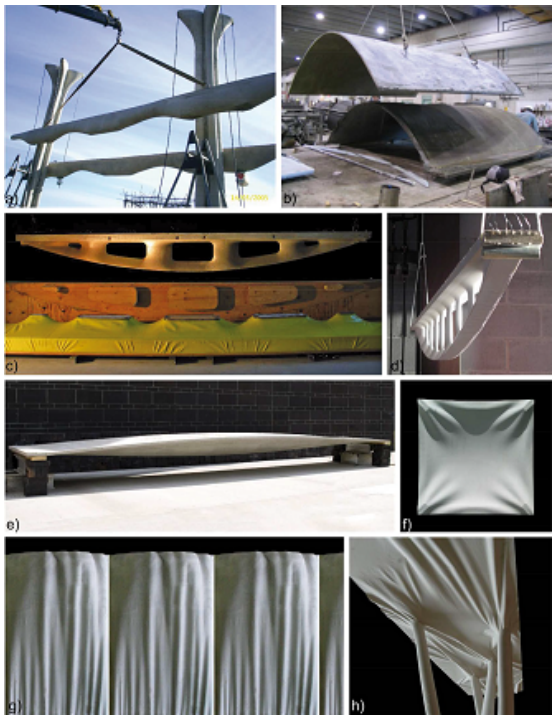

Figure 2-5: Fabric formed concrete elements by Mark West (Image courtesy: Hawkins et al. (2016))

Fabric formwork has shown advantages compared to traditional timber or steel formworks during its development (Orr, 2012; Kostova, 2016). The flexibility of woven fabrics

allows the designers to construct concrete elements of interesting and complex geometries without additional costs associated with the construction. This flexibility creates the opportunity of optimising structural concrete structures and reducing carbon emissions and embodied energy associated with concrete structures. Lightweight, inexpensive and widely available fabrics provide a considerable reduction in storage, handling and transportation costs (Tayfur, 2016). Better surface quality of concrete can be achieved using fabric formwork by allowing water leak from the concrete fluid (Orr et al., 2011b).

In recent research, the design and structural performance of fabric formed beam elements have been investigated mainly by through experimental research conducted at the University of Edinburgh (Lee, 2011) and the University of Bath (Bailiss, 2006; Garbett, 2008; Orr, 2012; Kostova, 2016). The design methods and detailed of experimental investigations are further reviewed in section 2.4.

### 2.2.2 Construction techniques of fabric formed beams

Compared with traditional formwork, the fabric formwork requires different techniques so that when the beam is cast, the concrete is formed into the desired geometry as it hardens. Special designs are also required to ensure constructibility, e.g. reinforcement positioning. To address the challenges, three types of techniques of fabric forming were developed for beams: (i) spline mould, (ii) keel mould and (iii) pinch mould (Orr, 2012).

The spline mould is composed of one flat sheet of fabric and one spline (a metal bar) as (Figure 2-6). The spline is needed for forming the bottom line of the beam with non-prismatic geometry and pulling down the fabric to create prestress and result in a more economical volume of concrete in tension area (Veenendaal, 2008).

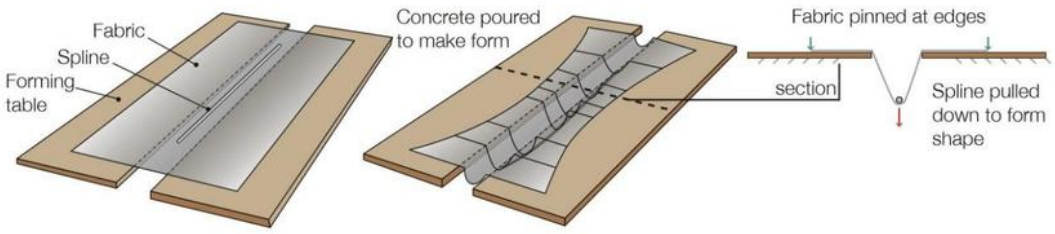


Figure 2-6: Spline mould construction (Image courtesy: Orr (2012))

The keel mould has a keel and two fabric sheets to contain the wet concrete. With the two fabric sheets stitched to the forming table, the keel mould uses the keel to secure

the bottom profile of variable depth geometry of the beam. An advantage of using the keel moulds is that the geometry of beams can be precisely controlled (Veenendaal, 2008). A construction diagram of the keel mould is shown in Figure 2-7.

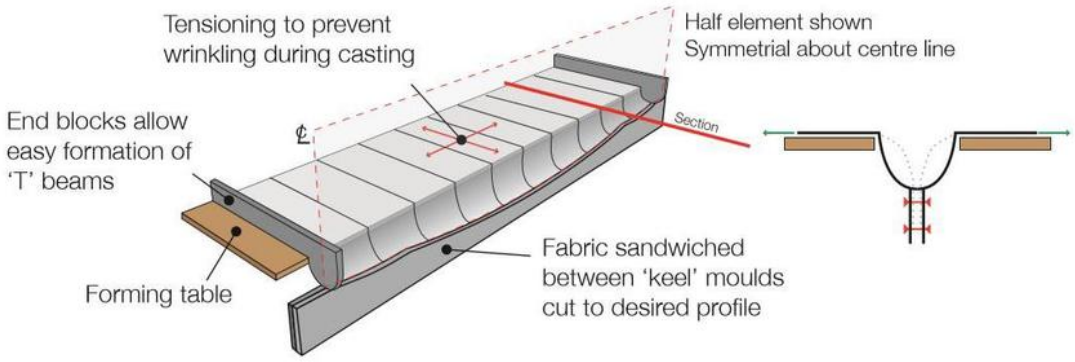


Figure 2-7: Construction method of keel mould (Image courtesy: Orr (2012))

The pinch mould is constructed based on the spline mould or the keel mould. The woven fabric on the two sides of the beam could be pinched together to create hollow spaces (Figure 2-8). Therefore trusses or optimised beams can be created by removing the concrete at the pinched locations.

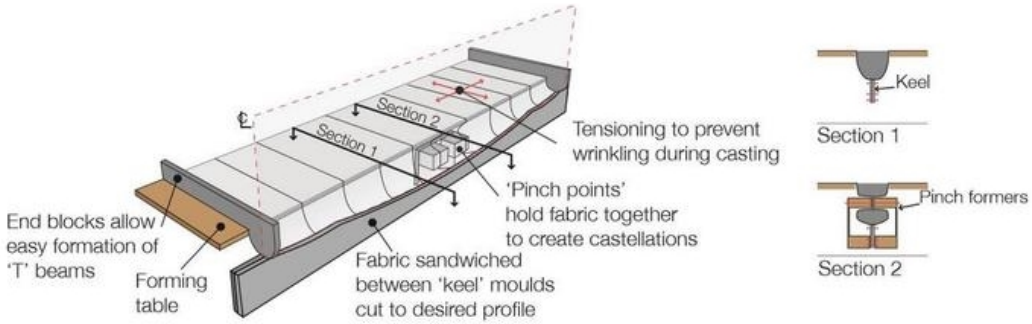


Figure 2-8: Pinch mould construction (Image courtesy: Orr (2012))

## 2.3 Material behaviour

The design of fabric formed concrete beams relies on the fundamental constitutive relations of the materials: concrete and reinforcement. Fibre Reinforced Polymer (FRP) reinforcement have been applied in fabric formed beams (Orr et al., 2011c; Kostova et al., 2017). This section presents the review of concrete and FRP reinforcement as the basis of the subsequent design of fabric formed concrete beams in section 2.4.

### 2.3.1 Concrete

Concrete, one of the most widely used construction material (Flower and Sanjayan, 2007; Barcelo et al., 2014), is composed of four basic components: sand, aggregate, cement and water. The widespread use of reinforced concrete (RC) structures relies on the understanding of the material behaviour of concrete. Under compression, failure of concrete is essentially the tension failure of the hardened cement paste, initiated by the gradual formations of bond cracks at the aggregate-paste interface, the cracks through mortar and the cracks through aggregate (Scrivener and Gartner, 1987; Richart et al., 1928).

Due to the randomly formed micro-cracks, the stress-strain behaviour of concrete under uniaxial compression is non-linear, and various stress-strain relation models have been formulated (Ottosen, 1979; Lubliner et al., 1989). For practical purposes, the design codes and guidelines of RC structures adopt simplified stress-strain relations for concrete.

ACI-318 (2008) does not specify a stress strain model. Designers are allowed to assume rectangular, trapezoidal, parabolic, or any other shaped stress-strain models that result in the prediction of strength in substantial agreement with results of comprehensive tests. The model developed by Hognestad et al. (1955) is widely accepted by engineers to describe stress-strain relations of concrete under short-term loading, as shown in Figure 2-9, where $\epsilon_0$ (taken as 0.002) is the strain at peak stress $f_c$ and $\epsilon_{cu}$ (taken as 0.003) is the ultimate strain.

CSA-A23.3-4 (2004) has a similar specification to ACI-318 (2008), allowing users to assume stress-strain relations, but the same Hognestad model is widely accepted with a different ultimate strain $\epsilon_{cu}$, taken as 0.0035.

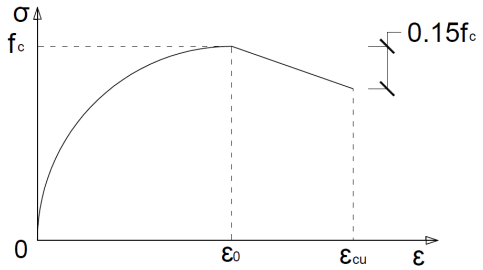


Figure 2-9: Stress-strain relation of concrete of Hognestad et al. (1955)

In Europe, the Model code (FIB, 2010) adopts a stress strain model defined by Equation

2.1. Different concrete strength classes have different values of $\epsilon_0$ varying from 0.0019 to 0.0030. The resulting stress strain curve is shown in Figure 2-10. BS-EN-1992-1-1 (2004) adopts the same equation (Equation 2.1) to define the stress-strain relation but a different value of $k$ is adopted, as defined in Equation 2.2.

$$\frac{\sigma_c}{f_c} = \frac{-k\eta + \eta^2}{1 + (k-2)\eta} \tag{2.1}$$

where $\sigma_c$ (MPa) is compression stress; $f_c$ (MPa) is strength of concrete, $\eta$ is ratio of compression strain to strain at the strength of concrete $\epsilon_0$ and $k$ is the ratio of tangent modulus at origin to secant modulus from the origin to the peak compressive stress.

$$k = 1.05 E_c \epsilon_0 / f_c \tag{2.2}$$

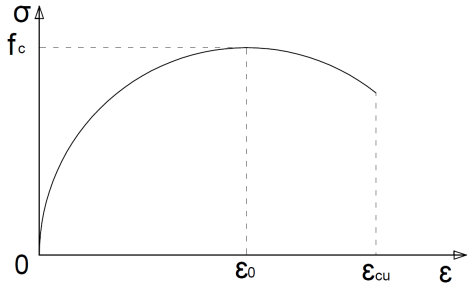


Figure 2-10: Stress strain relation of concrete in Model Code (FIB, 2010)

### 2.3.2 Confined concrete

Concrete performance is usually considered in terms of axial strain. However, the axial stress-strain relations may not reflect the actual behaviour of the concrete element, as the compression zone concrete in a flexural concrete element is often under a complex state of tri-axial stress (Kotsovos and Pavlovic, 1999). The concrete in the central compression zone is confined by the surrounding material with secondary stresses in transverse and radial directions (Kotsovos and Pavlovic, 1999).

In addition, concrete can be designed intentionally with confinement, such as spirals, to achieve better compressive performance (Whitehead, 2002; Rousakis et al., 2007; Yin et al., 2016). Under triaxial conditions, only applying confining stresses of around 10% of axial compression stress can improve the cylinder strength by 50% (Kotsovos and Pavlovic, 1999). Concrete under triaxial stress also has far greater strain capacity

for the same peak stress than is found under uniaxial compression. The stress-strain relations adopted in BS-EN-1992-1-1 (2004) are shown in Figure 2-11.

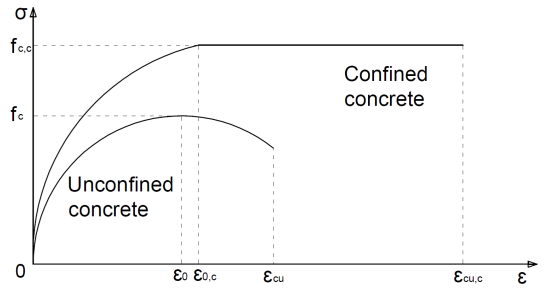


Figure 2-11: Stress strain relations of confined concrete from BS-EN-1992-1-1 (2004)

The design stress-strain relations of confined concrete has been explored by many researchers. Mander et al. (1988) built a theoretical model to describe the uni-axial compressive performance of confined concrete which has been extensively tested against experimental data. For concrete confined by transverse reinforcement, the ultimate compressive axial strain is calculated using an experimentally derived formula by Seible et al. (1995) based on Mander's model in Equation 2.3.

$$\epsilon_{cu} = 0.004 + 1.4\frac{\rho_y f_y \epsilon_y}{f'_{cc}} \tag{2.3}$$

where $\epsilon_{cu}$ is ultimate strain of confined concrete; $\rho_y$, $f_y$ and $\epsilon_y$ are steel reinforcement ratio, yield strength and yielding strain respectively; $f'_{cc}$ is confined concrete strength.

FRP confinement has also been utilised to improve concrete strength and deformability (Lillistone and Jolly, 2000; Lam and Teng, 2003b; Whitehead, 2002; Rousakis et al., 2007). Early studies of design-oriented modelling of FRP confined concrete directly adopted the parabolic shaped Mander model that is used for steel confinement concrete (Lam and Teng, 2003a). However, Spoelstra and Monti (1999) argued that due to the linear elastic property, the FRP-confined concrete shows an ever-increasing branch, as opposed to the plateau of the steel-confined model.

The existing design-oriented stress-strain models for FRP-confined concrete have adopted simplifications to formulate a typical bilinear stress-strain curve (Ozbakkaloglu et al., 2013). Modelling has evolved from the bilinear model with two straight lines (Karbhari and Gao, 1997) to the model composed of the modified Hognestad's parabola and a straight line (Lillistone and Jolly, 1997). A simple and accurate stress strain model for FRP-confined concrete was developed by Lam and Teng (2003a) for design use, as

shown in Figure 2-12.

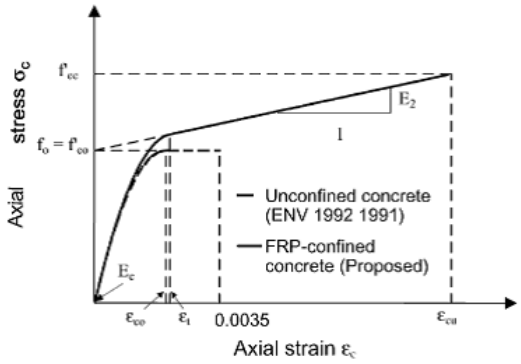


Figure 2-12: Design based model for FRP confined concrete (Lam and Teng, 2003a)

### 2.3.3 FRP reinforcement

#### 2.3.3.1 Material Characteristics

Fibre reinforced polymer (FRP) is a composite material, made of polymer matrix reinforced with fibres. As an emerging alternative to steel reinforcement, FRP reinforcement has been commercially available and applied in Civil Engineering since the 1980s (ACI-440.1R, 2015). Due to the light weight, high strength and corrosion resistance, FRP reinforcement has been successfully used in RC structures exposed to extreme environments, such as bridge decks and oil platforms (Razaqpur and Spadea, 2014).

Of the two components of FRP, the continuous fibres provide the strength and stiffness while the polymeric matrix provides the binding between fibres and protects the fibres from damage (Bakis et al., 2002). Commercially available FRP bars mainly include four types based on the fibres: glass, carbon, aramid and basalt, Table 2.1.

Table 2.1: Tensile properties for typical fibres for FRP reinforcement (FIB-bulletin-40, 2007)

| Fibre type | Density (kg/mˆ3) | Tensile strength (MPa) | Elastic Modulus (GPa) | Ultimate Strain (%) |
|---|---|---|---|---|
| Glass | 2300-2500 | 1800-3500 | 70-85 | 2.0-4.6 |
| Carbon | 1750-1950 | 2500-4000 | 240-650 | 0.5-1.1 |
| Aramid | 1440 | 2700-4200 | 60-175 | 1.4-4.4 |
| Basalt | 2800 | 4840 | 90 | 3.1 |

Glass fibres are the most widely used type of fibres due to their low cost and high tensile strength. However, the elastic modulus of glass fibres is the lowest among the common fibres of FRP. Carbon fibres have the highest stiffness and medium tensile strength. Carbon fibres also have very high resistance to aggressive environments. The disadvantage is that the cost of carbon fibres is also the highest. Aramid fibres are organic fibres having low gravity and high tensile strength to weight ratio. Basalt fibres are obtained from molten volcanic lava, and they have better mechanical performance than glass. The most important property of basalt fibres is their fire resistance which is an essential factor in the structural design. The tensile properties of the four typical fibres are shown in Table 2.1 (FIB-bulletin-40, 2007).

Thermosetting resins are the most common polymeric matrix used to impregnate continuous fibres. They are plastics irreversibly cured from a soft, solid or viscous liquid polymer or resin. Compared with the fibres, they have a much lower strength (less than 150 MPa) and stiffness (less than 10 GPa). The common thermosetting resins include epoxy, polyesters and vinyl ester (Bakis et al., 2002).

Impregnating the fibres with polymeric resins, the resulting FRP reinforcement exhibits mechanical performance (tensile strength and elastic modulus) between the fibres and polymeric resins. Agarwal et al. (2017) gave Equation 2.4 to determine the elastic modulus of FRP reinforcement. Accordingly, the tensile strength of FRP is also between the fibres and resins as shown in Equation 2.5.

$$E_L = E_{fL}V_f + E_m(1 - V_f) \tag{2.4}$$

where $E_{fL}$ is elastic modulus of the fibre; $E_m$ is elastic modulus of resin matrix; $E_L$ is elastic modulus of FRP and $V_f$ is volume ratio of fibres to FRP

$$f_{Lt} = f_{ft}[V_f + \frac{E_m}{E_{fL}}(1 - V_f)] \tag{2.5}$$

where $f_{Lt}$ is tensile strength of FRP reinforcement and $f_{ft}$ is tensile strength of the fibres.

Unlike steel, all FRP reinforcement exhibit a linear elastic behaviour under tension up to failure. The stress-strain relation diagrams of typical FRP reinforcement and steel bars are shown in Figure 2-13. For commercial FRP reinforcement bars, the ultimate tensile stress also varies along with the cross-section area. Increasing diameter results in higher ultimate tensile force but reduced ultimate tensile stress according to previous

testing (FIB-bulletin-40, 2007). Therefore the producers normally provide the different mechanical properties of FRP bars based on the different diameters.

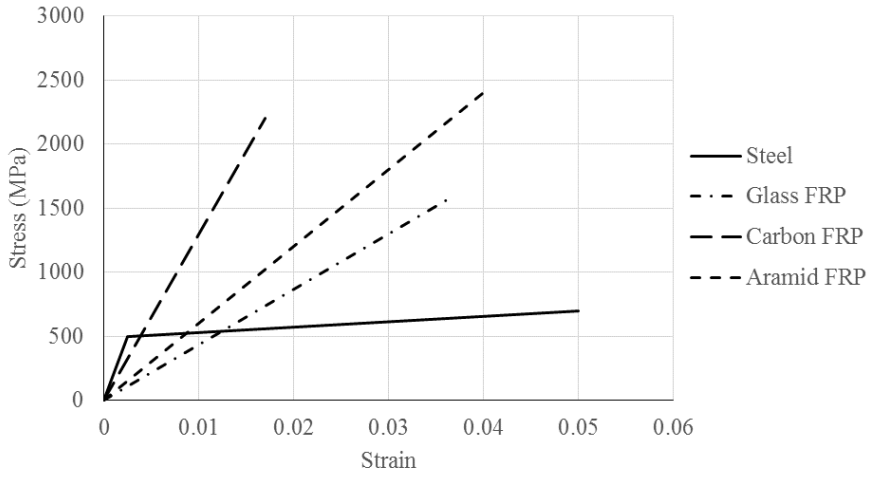


Figure 2-13: Stress strain relation diagram of steel and FRP reinforcement (FIB-bulletin-40, 2007)

#### 2.3.3.2 FRP shear reinforcement

FRP is also used as shear reinforcement. FRP links are usually produced as a closed rectangular hoop to develop sufficient anchorage (El-Sayed et al., 2007). The resulting bends of FRP shear links exhibit significantly reduced strengths due to the curvature, localised stress concentrations and intrinsic weakness of fibres perpendicular to their longitudinal axis (El-Sayed et al., 2007; Ahmed et al., 2009b; El-Sayed and Soudki, 2010). The bent corner strength of FRP shear links is influenced by many factors (El-Sayed et al., 2007) including: (i) the radius of the bend, $r_b$, (ii) diameter of links with round cross section, $d_b$ and (iii) the tensile strength of straight FRP bars, $f_{fu}$ .

Codified shear design methods for FRP RC structures specify the strength of shear links with round cross-section using empirical equations considering these three factors. ACI-440.1R (2015) limits the design strength of FRP shear links, $f_{fv}$, to the lesser value of strength at an ultimate strain of 0.4% and strength at the bent portion of shear links given by Equation 2.6.

$$f_{fb} = (0.05\frac{r_b}{d_b} + 0.3)f_{fu} \tag{2.6}$$

where $f_{fb}$ is strength at the bent corner; $r_b$ is radius of bent corner; $d_b$ is diameter at the bend and $f_{fu}$ is the ultimate tensile strength of FRP.

CSA-S806 (2012) limits the ultimate strain in any FRP shear reinforcement to 0.5% to limit crack widths (Razaqpur and Spadea, 2014). A shear strength reduction factor, taken as 0.40, is also incorporated to consider the weak corner of bent shear links as shown in Equation 2.7 where $f_{fu}$ is limited by ultimate strain of 0.005.

$$f_{fb} = 0.4 f_{fu} \tag{2.7}$$

Other design codes, such as CSA-S6 (2006), also define the corner strength with similar expressions to Equation 2.6. The strength of straight portions of FRP shear links, $f_{fu}$, is considered with additional reduction factors to limit the corner strength. This thesis mainly considers FRP shear design following the ACI-440.1R (2015) and CSA-S806 (2012). Therefore these more complicated design equations are not reviewed in detail.

In contrast to FRP shear links of circular cross-section, FRP shear links of rectangular cross-section are found to have higher corner strength (Lee et al., 2013). The beneficial effect of the rectangular cross-section is attributed to the smaller distance between outer and inner radius at the corner compared with circular shear links with same cross section area. Equation 2.8 was formulated empirically based on test data by Lee et al. (2013) to calculate the corner strength of FRP shear links having a rectangular cross-section.

$$f_{fb} = (0.02\frac{r_b}{d_{fi}} + 0.47) f_{fu} \tag{2.8}$$

where $d_{fi}$ is equivalent diameter of rectangular shear link cross section, calculated as Equation 2.9.

$$d_{fi} = \frac{2}{\sqrt{\pi}} t_f \tag{2.9}$$

where $t_f$ is thickness of the FRP links.

### 2.3.4 Summary

This section presents the material behaviours of concrete, steel reinforcement and shear reinforcement, which have been used in fabric formed concrete beams. Understanding

the fundamental stress-strain relations of the materials is crucial to the design of fabric formed beams.

The corner of FRP shear reinforcement has been shown to be weaker than straight FRP reinforcement. Design codes, guidelines and researchers have adopted different methods to address the weaker corners of FRP. For the new W-FRP shear reinforcement, the corner strength should be appropriately considered in the research of this thesis.

## 2.4 Design and tests of fabric formed concrete beams

Fabric formwork has been used to cast optimised concrete beam elements. With variable depth geometries, fabric formed beams exhibit different structural behaviours when compared to prismatic beams. In this section, design methods and reinforcing techniques used in existing experimental research of fabric formed beams reinforced with FRP are reviewed with respect to four aspects: flexure, shear, anchorage and deflection.

### 2.4.1 Flexural design

#### 2.4.1.1 Sectional design

Geometry design based on flexure loading profile is the starting point for minimising the concrete use in fabric formed beams. The most widely accepted method of geometry design in the research of fabric formed beams is a sectional analysis method (Hashemian, 2012; Orr, 2012; Kostova, 2016). The assumptions used for prismatic steel reinforced concrete design, such as plane section remaining plane, can be incorporated.

The sectional analysis method requires a beam to be divided into numerous equidistant segments by taking vertical cuts, as shown in Figure 2-14. Flexural design is conducted separately on each segment based on design codes, such as BS-EN-1992-1-1 (2004) and ACI-318 (2008), to provide sufficient bending strength. For each cross-section of the segments, the effective depth is optimised to be the minimum value to resist the applied bending moment envelope.

For each segment, the applied bending moment is resisted by the concrete and reinforcement, as shown in Figure 2-15. Three equations of the stress equilibrium, force equilibrium and strain compatibility can be formulated to calculate the minimum effective depth

requirement. By calculating the minimum effective depth of all segments, the final geometry of the fabric formed beam is determined by assembling all segments with rationalised depth (Kostova, 2016).

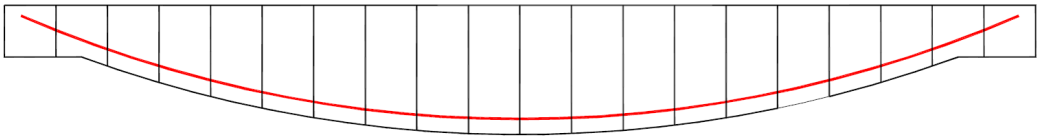

Figure 2-14: Segments sequence of flexural design

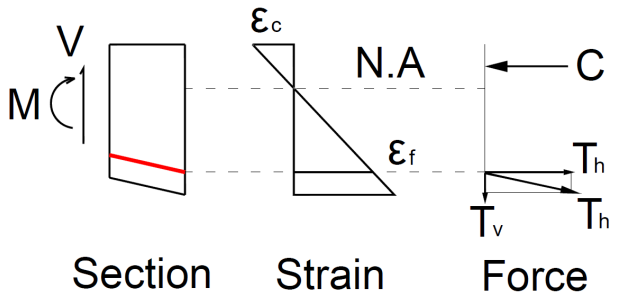


Figure 2-15: Equilibrium of a segment

For FRP reinforced concrete structures, ACI-440.1R (2015) specifies the flexural strength of a cross section as $M_n$, Equation 2.10, to be used when the FRP reinforcement ratio $\rho_f$ exceeds the balanced reinforcement ratio $\rho_{fb}$, Equation 2.11. When the reinforcement ratio $\rho_f$ is less than $\rho_{fb}$, the concrete in compression zone is not the governing factor to determine the flexural strength. Equation 2.13 is used to calculate the flexural strength of the cross-section, where $c$ is the compression zone depth, calculated by the strain compatibility of the cross-section.

$$M_n = \rho_f f_f (1 - 0.59 \frac{\rho_f f_f}{f_c'}) b d^2 \tag{2.10}$$

where $f_f$ is tensile stress of FRP reinforcement, as shown in Equation 2.12; $f_c^{'}$ is concrete strength; $b$ is width of the cross section and $d$ is effective depth of the cross section.

$$\rho_{fb} = 0.85\beta_1 \frac{f_c^{'}}{f_{fu}} \frac{E_f \epsilon_{cu}}{E_f \epsilon_{cu} + f_{fu}} \tag{2.11}$$

$$f_f = (\sqrt{\frac{(E_f \epsilon_{cu})^2}{4} + \frac{0.85\beta_1 f_c'}{\rho_f} E_f \epsilon_{cu}} - 0.5 E_f \epsilon_{cu}) \leq f_{fu} \tag{2.12}$$

where $\epsilon_{cu}$ is ultimate compressive strain of concrete, taken as 0.003 (ACI-440.1R, 2015); $E_f$ is elastic modulus of FRP reinforcement; $f_{fu}$ is ultimate tensile strength of FRP reinforcement and $\beta_1$ is factor taken as 0.85 for concrete strength, which is reduced continuously at a rate of 0.05 per each 7 MPa of strength in excess of 28 MPa but is not taken less than 0.65.

$$M_n = A_f f_{fu}(d - \frac{\beta_1 c}{2}) \tag{2.13}$$

CSA-S806 (2012) adopts the same philosophy to conduct the flexural design. However, there are different specifications on the stress distribution in compression zone of concrete. The factor 0.85 in Equation 2.11 is replaced with $\alpha_1$ (Equation 2.14) to specify the average compressive stress and $\beta_1$ is defined with different value as shown in Equation 2.15.

$$\alpha_1 = 0.85 - 0.0015 f_c^{'} \geq 0.67 \tag{2.14}$$

$$\beta_1 = 0.97 - 0.0025 f_c^{'} \geq 0.67 \tag{2.15}$$

Although other sophisticated design methods based on finite element analysis and topology optimisation were also used to design the geometry of the fabric formed concrete beams (Veenendaal et al., 2011a; Hawkins et al., 2016), this thesis tries to investigate the design methods that could be easily adopted by engineers. Therefore no further detailed review of these methods is given.

#### 2.4.1.2 Fabric formed beams reinforced with FRP reinforcement

Investigations into fabric formed concrete beams reinforced with FRP reinforcement are limited. A test of a fabric formed beam reinforced with a single CFRP bar was designed for the 'splayed anchorage' system (Darby et al., 2007) and demonstrated the problematic positioning of longitudinal curves of the reinforcement, which inspired the research of Kostova (2016).

Kostova (2016) subsequently investigated the possibility of applying FRP materials as an alternative to steel reinforcement in flexible formed concrete beams. Twelve fabric formed beams reinforced with FRP flexural reinforcement (Figure 2-16) were designed and tested. The research of Kostova (2016) demonstrating that without compromising structural performance, the constructibility of fabric formed beams can be improved

by using the flexibility of FRP bars. The FRP longitudinal bars were easily positioned by attaching them to the fabric formwork.

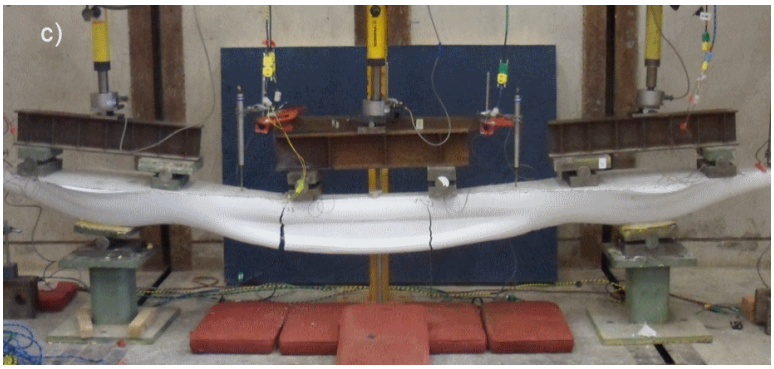


Figure 2-16: Failure of fabric formed beam reinforced with FRP reinforcement (Image courtesy: Kostova (2016))

Using FRP reinforcement does not change the basic philosophy of sectional analysis but due to the fundamental difference between FRP and steel in constitutive relations, the stress equilibrium, force equilibrium and strain compatibility of each segment are different. Following the sectional analysis method, Kostova (2016) developed a Matlab based model to calculate the effective depth of each segment. Each cross section was horizontally divided into layers to determine the stress and strain state of concrete in different relative distance to the neutral axis.

The linear elastic nature of FRP reinforcement results in a possible lack of ductility. Helical FRP reinforcement has been applied in concrete beam elements to improve their deformability (Ibell et al., 2009; Mohamed et al., 2014). An example is shown in Figure 2-17 (Whitehead, 2002).

Kostova (2016) adopted similar circular AFRP helices in fabric formed beams, confirming that the confined concrete could improve the deformability of fabric formed beams reinforced with FRP reinforcement and showing good agreement with the sectional analysis model (Kostova, 2016).

The flexural design of FRP reinforced concrete is addressed in many existing design codes and guidelines, such as ACI-440.1R (2015) and CSA-S806 (2012). Equations modified from the steel reinforced concrete design have been tested against various test data and show good correlations (Razaqpur and Spadea, 2014). Building on the work by Kostova (2016), the feasibility of using existing flexural design methods for fabric formed beams reinforced with FRP reinforcement has been confirmed.

Figure 2-17: An AFRP helix cage for prismatic beams (Image courtesy: Whitehead (2002))

### 2.4.2 Shear design

Previous research has shown that the fabric formed beams reinforced with steel have lower shear strength than the prismatic beams with equivalent flexural strength. Limited research has investigated the shear performance and the shear design methods of FRP reinforced beams of non-prismatic geometries. This section presents the shear design methods that can be potentially applied in this research, FRP shear reinforcement and the applications of FRP shear reinforcement in fabric formed beams.

#### 2.4.2.1 Truss analogy

The truss analogy was proposed by Ritter (1899) and Morsch (1908) and it has been adopted by many present design codes and guidelines of reinforced concrete, such as ACI-318 (2008) and BS-EN-1992-1-1 (2004). The truss analogy assumes reinforced concrete as the compression chords and stirrups as tension chords of a truss. The shear reinforcement provides the tensile force resisting the applied shear force.

In the original assumption of Morsch (1908), the angle of compression strut in concrete is 45 degrees to the horizontal axis. Early researchers calibrated the truss analogy and found the consistent difference between the predictions of shear strength and test results (Orr, 2012). An additional concrete contribution then was considered by the codes and guidelines to address this problem. The total shear resistance is taken as the summation of shear contributions from concrete and shear reinforcement as shown in

Equation 2.16.

$$V_n = V_c + V_s \tag{2.16}$$

where $V_n$ is total shear resistance; $V_c$ is contribution of concrete and $V_s$ is contribution of shear reinforcement.

The truss analogy has been successfully applied in steel reinforced concrete design and adopted by most of the existing design codes and guidelines (BS-EN-1992-1-1, 2004; ACI-318, 2008; CSA-A23.3-4, 2004). In the codified shear design methods based on truss analogy, the lower bound theory is assumed that 'If any stress distribution throughout the structure can be found which is everywhere in equilibrium internally and balances certain external loads and at the same time does not violate the yield condition, those loads will be carried safely by the structure' (Calladine, 2013). Relying on the yielding of steel, designers do not need to understand the actual stress distribution but only need to find out the internal equilibrium of the truss.

Although the lower bound theory behind truss analogy is not necessarily appropriate to be applied in structures reinforced with linear elastic reinforcement as it relies on the yielding of reinforcement, shear design equations used for steel reinforced elements are modified to predict the shear performance of FRP reinforced concrete after being calibrated with experimental data of prismatic beams (Razaqpur and Spadea, 2014; El-Sayed and Soudki, 2010). The modifications of shear design equations are made by incorporating the influence of different properties of FRP shear reinforcement.

The shear design based on ACI-440.1R (2015) also adopts the expression of concrete contribution and reinforcement contribution as specified in Equation 2.16. The value of concrete contribution ($V_c$) and reinforcement contribution (replaced to $V_{fv}$) to shear are shown in Equation 2.17 and Equation 2.18 respectively, where $c$ is cracked transformed section neutral axis depth and it equals to $kd$. The value of $k$ is shown in Equation 2.19.

$$V_c = 0.4\sqrt{f'_c}b_w c \tag{2.17}$$

$$V_{fv} = \frac{A_{fv} f_{fv} d}{s} \tag{2.18}$$

$$k = \sqrt{2\rho_f n_f + (\rho_f n_f)^2} - \rho_f n_f \tag{2.19}$$

where $A_{fv}$ is cross section area of FRP shear reinforcement; $f_{fv}$ is design strength of FRP shear reinforcement which is limited by the corner strength of FRP shear reinforcement (section 2.3.3); $s$ is the spacing of shear reinforcement; $\rho_f$ is longitudinal reinforcement ratio and $n_f$ is the modulus of elasticity ratio between FRP and concrete.

CSA-S806 (2012) adopts the modified shear design equations from CSA-A23.3-4 (2004). The contribution of concrete is modified to Equation 2.20 and the contribution of FRP reinforcement to shear is modified to Equation 2.21. As presented in section 2.3.3, the design strength of FRP shear links is limited by the factor 0.4 to consider the lower strength at bends of shear links (Razaqpur and Spadea, 2014).

$$V_c = 0.05\lambda\phi_c k_m k_r (f_v^{'})^{\frac{1}{3}} b_w d_v \tag{2.20}$$

$$V_{fv} = \frac{0.4\phi_f A_{fv} f_{fu} d_v \cot\theta}{s} \tag{2.21}$$

where $\lambda$ is factor to account concrete density; $\phi_c$ is resistance factor for concrete; $k_m$ is coefficient taking into account the effect of moment at section on shear strength; $k_r$ is coefficient taking into account the effect of reinforcement rigidity on its shear strength; $f_v^{'}$ is concrete strength; $f_{fu}$ is the tensile strength of FRP shear reinforcement limited by $0.005E_{fv}$ and $\phi_f$ is resistance factor for FRP reinforcement.

#### 2.4.2.2 MCFT

The Modified Compression Field Theory (MCFT) was developed for RC members subjected to shear and torsion (Vecchio and Collins, 1986; Vecchio and Collins, 1988). In the MCFT, cracked concrete is defined with its own stress-strain relations. Equilibriums thus can be formulated for concrete, stirrups and longitudinal bars (Figure 2-18 and Figure 2-19). Using the actual stress distribution in reinforced concrete, MCFT does not rely on the lower bound theory, which makes it potentially viable in FRP reinforced beams.

The stress and strain states of RC element can be described by Equation set 2.22 and 2.23. Having constitutive relations of different materials defined by Equation set 2.24 and behaviour cracked concrete interfaces defined by Equation set 2.25, the behaviour of reinforced concrete subjected to shear can be calculated by solving the 15 non-linear equations.

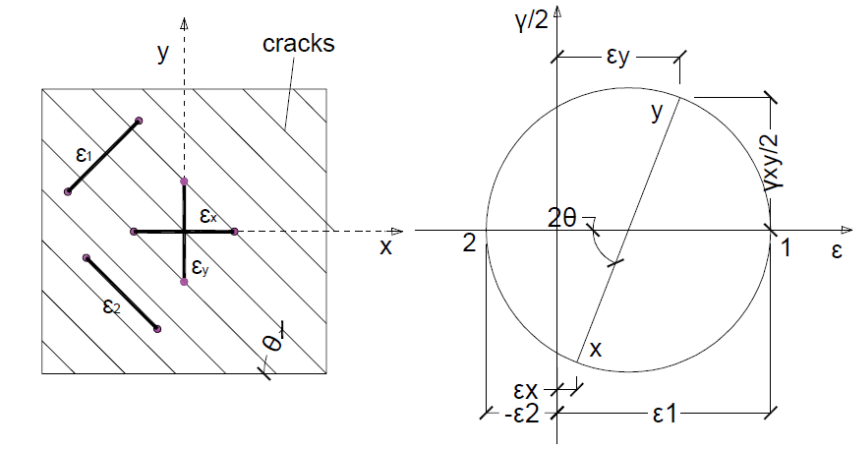


Figure 2-18: Strain compatibility of cracked concrete element in MCFT

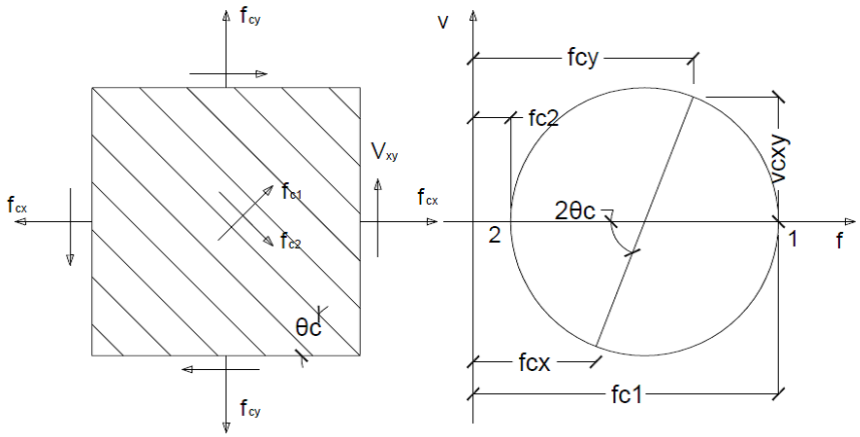


Figure 2-19: Stress equilibrium of cracked concrete element in MCFT

Stress equilibriums:

$$f_x = \rho_{sx} f_{sx} + f_1 - v_{cxy}/\tan\theta \tag{2.22a}$$

$$f_y = \rho_{sy} f_{sy} + f_1 - v_{cxy}\tan\theta \tag{2.22b}$$

$$v_{cxy} = (f_1 + f_1)/(\tan\theta + \cot\theta) \tag{2.22c}$$

Strain compatibility:

$$\epsilon_x + \epsilon_y = \epsilon_1 + \epsilon_2 \tag{2.23a}$$

$$\tan^2 = \frac{\epsilon_x - \epsilon_2}{\epsilon_y - \epsilon_2} \tag{2.23b}$$

$$\gamma_{xy} = 2(\epsilon_x - \epsilon_2)\cot\theta \tag{2.23c}$$

Constitutive relations:

$$f_{sx} = E_s\epsilon_x \leq f_{yx} \tag{2.24a}$$

$$f_{sy} = E_s\epsilon_y \leq f_{yy} \tag{2.24b}$$

$$f_2 = \frac{f_c^{'}}{0.8 + 170\epsilon_1}[2\frac{\epsilon_2}{\epsilon_c^{'}} - (\frac{\epsilon_2}{\epsilon_c^{'}})^2] \tag{2.24c}$$

$$f_1 = 0.33\sqrt{f_c^{'}}/(1 + \sqrt{500\epsilon_1}) \tag{2.24d}$$

Cracking behaviour:

$$w = s_\theta \tag{2.25a}$$

$$s_\theta = 1/(\sin\theta/s_x + \cos\theta/s_y) \tag{2.25b}$$

$$v_{ci} = \frac{0.18\sqrt{f_c^{'}}}{0.31 + 24w/(a_g + 16)} \tag{2.25c}$$

$$f_{sxcr} = (f_x + v_{xy}\cot\theta + v_{ci}\cot\theta)/\rho_x \tag{2.25d}$$

$$f_{sycr} = (f_y + v_{xy}\tan\theta - v_{ci}\tan\theta)/\rho_y \tag{2.25e}$$

Solving the 15 non-linear equations is not easy for engineers to conduct the design of concrete structures. Bentz et al. (2006) simplified the equations of MCFT and made the design using this method more practical by making empirical assumptions. Hoult et al. (2008) also simplified the MCFT based on experimental research on prismatic beams. The simplified version of MCFT is also the basis of shear design in CSA-A23.3-4 (2004) despite the truss analogy expression of the shear contribution of shear reinforcement (section 2.4.2).

For concrete beams reinforced with FRP stirrups, El-Sayed and Soudki (2010) calibrated the simplified MCFT design approach. The test results of 37 prismatic specimens reinforced with FRP longitudinal bars and shear links were compared with the simplified MCFT equations and empirical equations adopted in the design codes and guidelines for FRP reinforced concrete. The comparisons showed that MCFT provides more

reasonable and reliable predictions.

As a sectional analysis method, MCFT modelling relies on the shear stress distribution. The shear stress distribution calculation normally adopts Jourawksi's method (Paglietti and Carta, 2009) which assumes the plane cross sections remain plane and materials of each cross section are linear-elastic. The resulting shear stress distribution of each cross-section has a parabolic geometry as shown in Figure 2-20.

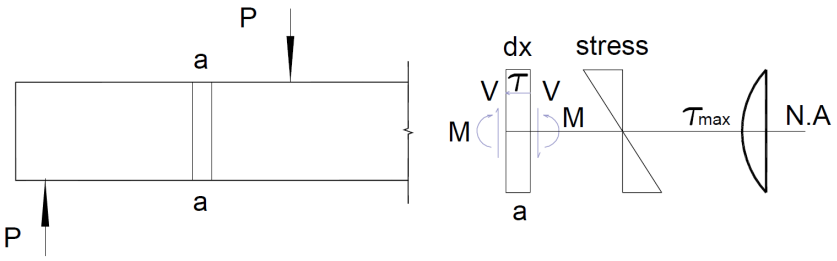


Figure 2-20: Parabolic shear stress distribution (Jourawski, 1856)

However, when it comes to non-linear material, a 'longitudinal stiffness method' is adopted by Bentz (2000) to calculate the shear stress distribution. It is argued that the variations of bending stresses over the depth of the sections result in different shear stress distribution as shown in Figure 2-21.

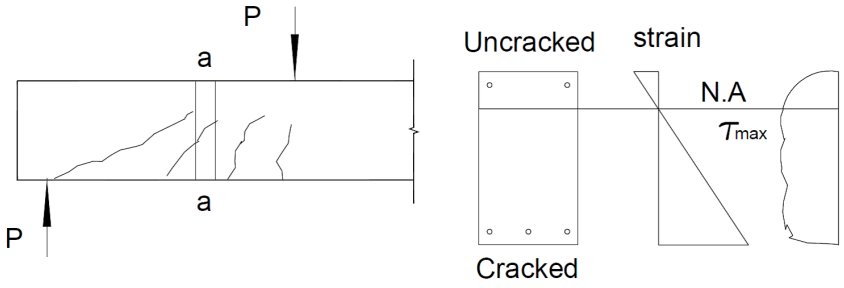


Figure 2-21: Shear stress distribution of cracked RC concrete beam

Although simplifications to MCFT have been made for prismatic beams by researcher (Bentz et al., 2006; Hoult et al., 2008) and design codes (CSA-A23.3-4, 2004), it is proposed to use the classical MCFT equations in this research as the MCFT relates the behaviour of cracked concrete to the average shear stress, which is influenced significantly by the geometry of the beam. Little work has been done to instruct the shear design of fabric formed concrete beams with MCFT using the actual shear stress distribution.

When considering elastic behaviour in a statically determinate beam, the maximum shear stress at a specific cross section in variable depth beams no longer occurs at the mid-depth of the cross section. Following the work of Timoshenko (1956) and Oden and Ripperger (1981), Paglietti and Carta (2009) shows that comparing the two elastic beams in Figure 2-22 (a), the maximum shear stress $\tau_{max}$ in the variable depth beam occurs at the bottom and its value is much larger than the $\tau_{max}$ in the prismatic beam under the same load, which occurs at the mid-depth of the section.

Comparing the two cracked RC beams in Figure 2-22 (b), Paglietti and Carta (2009) and Yang et al. (2015) show that $\tau_{max}$ appears at the neutral axis for both beams (Yang et al., 2015). The value of $\tau_{max}$ in the tapered beam could be higher if the prismatic beam and tapered beam have the same effective depth of a cross-section under the same loading profile. Using the shear design equations of design codes and guidelines for RC structures, which assume parabolic shear stress distribution of elastic prismatic beams, the design shear strength could be unconservative due to the misunderstanding of shear stress distribution (Yang et al., 2015).

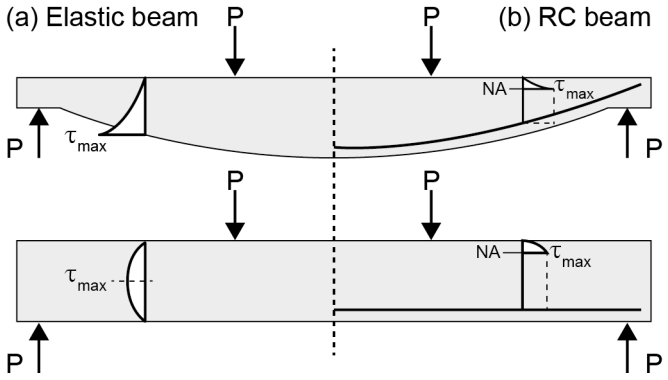


Figure 2-22: Shear stress distribution of beams with different geometries

#### 2.4.2.3 Inclined flexural reinforcement

Non-prismatic beams often have inclined flexural reinforcement. This inclined reinforcement provides inclined tensile force to resist bending moment, while the vertical component of the bar force resists shear, Figure 2-15. With appropriate design of flexural reinforcement, the horizontal component and vertical component of the tensile force of the longitudinal bars can theoretically resist flexure and shear as shown in Equation 2.26 (Orr et al., 2014). The shear resistance, $V_{td}$, provided by inclined flexural reinforcement with an inclination angle of $\alpha$ should be equal to the applied shear force $V_a$. $M_f$ is applied bending moment and $z$ is lever arm of the cross-section.

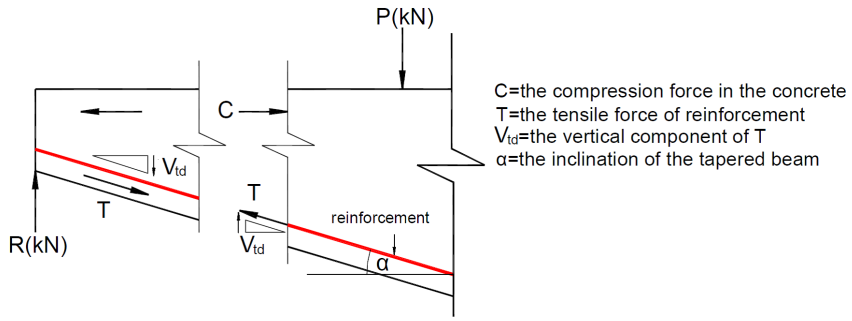


Figure 2-23: Shear contribution of inclined chord

$$V_{td} = \frac{M_f}{z} \tan \alpha \geq V_a \tag{2.26}$$

Except for the shear contributions of concrete and steel shear reinforcement, the inclined longitudinal bars should be taken into account to resist shear. In addition to the flexural tensile force, Orr et al. (2014) suggested that for fabric formed concrete beams, the positive effect of the additional tensile force should also be considered in the shear design. The additional tensile force arises from the equilibrium of truss analogy (BS-EN-1992-1-1, 2004).

BS-EN-1992-1-1 (2004) specified the additional tensile force as $\Delta F_{td}$ as shown in Equation 2.27. CSA-A23.3-4 (2004) specifies that the longitudinal reinforcement shall be designed to resist the additional tension forces caused by shear. On the flexural tension side, the value of additional tensile force is calculated as shown in Equation 2.28.

$$\Delta F_{td} = 0.5 V_{Ed} (\cot \theta - \cot \alpha) \tag{2.27}$$

Where $V_{Ed}$ is the design shear force; $\theta$ is angle of concrete strut and $\alpha$ is angle of shear reinforcement.

$$\Delta F_{td} = (V_a - 0.5 V_s - V_p) \cot \theta \tag{2.28}$$

Where $V_a$ is applied shear force; $V_s$ is shear contribution of steel shear links; $V_p$ is factored vertical component of the effective prestressing force or the flexural compression and tension for variable depth elements and $\theta$ is angle of concrete strut.

CSA-S806 (2012) adopts the similar expression of Equation 2.28 but in order to consider the different property of FRP reinforcement, $V_s$ is replaced as $V_{fv}$ in Equation 2.21. The value of $\cot\theta$ is replaced with a constant value of 1.3.

Experimental research of steel reinforced non-prismatic beams have been conducted (Hashemian, 2012; Bailiss, 2006; Garbett, 2008; Orr, 2012), showing that it is not sufficient to only rely on the flexural reinforcement to resist shear. Limited research has been conducted, focusing on the shear contribution of inclined FRP reinforcement in fabric formed beams.

Although the codes and guidelines for FRP reinforced concrete specified the positive effect of longitudinal bars, the design equations of contributions of concrete and FRP shear reinforcement were calibrated with prismatic beams. This makes the validity of the empirical equations questionable when they are applied in fabric formed beams.

The effect of inclined longitudinal bars in the codified shear design in section 2.4.2 has not been considered in MCFT (section 2.4.2.2). Therefore, challenges of considering complex shear stress distribution and shear contribution of inclined longitudinal bars should be addressed to apply the MCFT in the shear design of fabric formed beams.

The tensile force of longitudinal bars has been explicitly specified as discussed, but the shear contribution of longitudinal bars cannot be directly calculated since it is associated with the applied load. Therefore, further research is required to investigate a new design approach and the validity of codified design of fabric formed beams reinforced with FRP reinforcement.

#### 2.4.2.4 FRP shear reinforcement and applications

Capitalising on the flexibility of FRP reinforcement, solutions have been proposed to address one major drawback of fabric formed beam constructions, the complicated production of steel shear reinforcement. Flexible CFRP grids impregnated with resin (Figure 2-24) were proposed and used as shear reinforcement in prismatic beams (Orr et al., 2011a), demonstrating the potential of FRP grids as flexible shear reinforcement of fabric formed beams.

CFRP rectangular spirals, produced by Grant (2013), Figure 2-25, offer another potential solution by winding shear spiral reinforcement directly around the longitudinal bars of a fabric formed beam. Kostova (2016) applied the spiral CFRP shear reinforcement to beam elements and examined two types of winding methods as shown in Figure 2-26.

The second type, which had vertical central legs, exhibited considerable improvement to the shear strength of the beam elements, shown as the bottom two images in Figure 2-26. The shear design of the specimens was based on truss analogy from the ACI-440.1R (2015) (see section 2.4.2.1).

Figure 2-24: CFRP grid shear reinforcement (Image courtesy: Orr et al. (2011a))

Figure 2-25: CFRP spiral shear reinforcement (Image courtesy: Grant (2013))

Figure 2-26: CFRP spiral shear reinforcement of fabric formed beams (Image courtesy: Kostova (2016))

As discussed in section 2.3.3, the bent corner is a key factor limiting the design strength of FRP shear reinforcement. However, there is very limited research on the design strength of the proposed FRP shear reinforcement and the shear capacity of the FRP reinforced non-prismatic beams.

The concept of winding impregnated fibres to fabricate FRP shear reinforcement is developed, named as Wound FRP (W-FRP). Further investigations into the material properties and feasibility in concrete beams have been conducted collaboratively by the author and Spadea et al. (2017b), which will be presented fully in Chapter 4. The design strength of single W-FRP shear link has been characterised by Spadea et al. (2017a) to instruct the shear design. The test design is shown in Figure 2-27.

It has been confirmed that the corner strength limits the performance of the single W-FRP shear link, as discussed in section 2.3.3.2. Equation 2.29 was formulated empirically to define the corner strength of W-FRP, which has a 5mm radius at bends (Spadea et al., 2017a). Similar to the circular cross-section FRP reinforcement, W-FRP having a larger cross section shows lower tensile strength and stiffness. The influence of cross-section area is considered by the equivalent diameter $d_{fi}$, as shown in Equation 2.29.

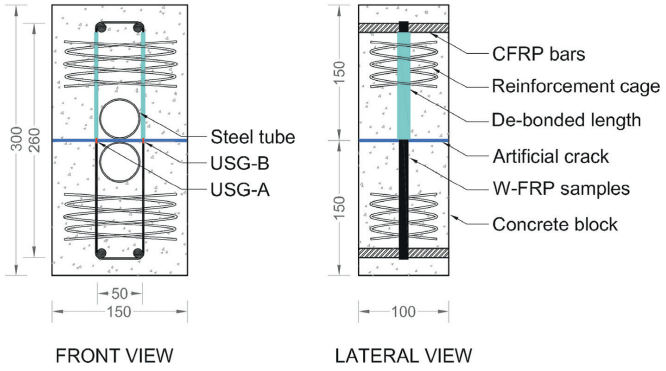


Figure 2-27: Strength test design of W-FRP shear link (Image courtesy: Spadea et al. (2017a))

$$f_{fb,WFRP} = (0.03\frac{r_b}{d_{fi}} + 0.35) \cdot f_{fu,WFRP} \leq f_{fu,WFRP} \tag{2.29}$$

W-FRP shear reinforcement provides numerous possibilities for shear design (Spadea et al., 2017b). The shear links can be arranged vertically or diagonally to the beam axis, which indicates great potential of optimising the shear design by reinforcing locations where it is required. However, the W-FRP in current research was produced by hand-winding, which makes achieving constant quality difficult. Further investigations into the manufacturing method, shear link behaviour and shear design of W-FRP reinforced beams are required.

### 2.4.3 Anchorage for FRP reinforcement

Early work used welded steel end plate (Hashemian, 2012; Garbett, 2008) and 'T bars' (Lee, 2011) in the optimised concrete beams to provide sufficient strength to resist the potential high stress in steel flexural reinforcement at ends, as shown in Figure 2-28 and Figure 2-29. Unlike the easy welding shown in Figure 2-28, welding multiple bars of larger diameters to a single plate could be potentially difficult in practice and welding techniques cannot be applied in FRP reinforcement.

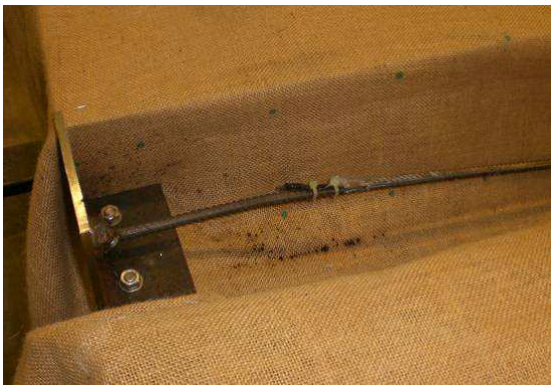

Figure 2-28: Welded steel plate to steel longitudinal bar (Image courtesy: Garbett (2008))

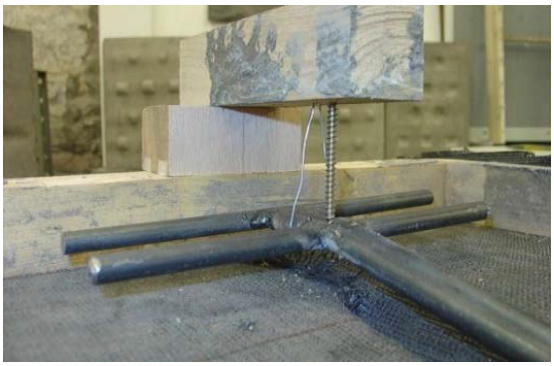

Figure 2-29: 'T bar' anchorage (Image courtesy: Lee (2011))

Only relying on chemical and mechanical bond between concrete and sand coating, FRP bars have lower bonding strength than steel rebars. Based on the Bertero, Eligehausen and Popov relationship (BEP model) (Eligehausen et al., 1982) (Figure 2-30 a), which was developed to simulate bond between steel reinforcement and concrete, research has investigated the bond model for FRP reinforcement (Malvar, 1994; Focacci et al., 2000). The modified BEP model, developed by Cosenza et al. (2002) (Figure 2-30 b), considers that FRP bars cannot carry constant maximum bond stress created by the

steel reinforcement ribs. The modified BEP model can be described by Equation 2.30.

$$\frac{\tau_R}{\tau_1} = (\frac{s}{s_1})^{\alpha} .....for(s < s_1) \tag{2.30a}$$

$$\frac{\tau_R}{\tau_1} = 1 - p(\frac{s}{s_1} - 1) .....for(s_1 < s < s_3) \tag{2.30b}$$

$$\tau_R = \tau_3 .....for(s > s_3) \tag{2.30c}$$

where $\tau_R$ is bond stress; $s$ is bar slip; $\alpha$ is a curve fitting parameter which is empirically determined and $s_1$ to $s_3$ are shown in Figure 2-30.

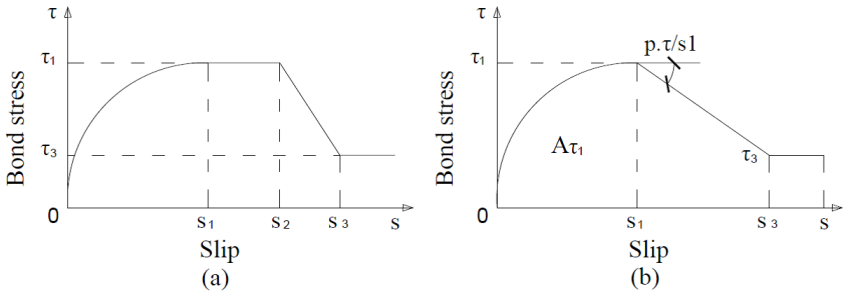


Figure 2-30: Bond slip models for FRP bars: (a) BEP model and (b) modified BEP model

In order the improve the anchorage strength of FRP bars, bends and hooks (Figure 2-31) has been designed. However, the production of FRP bars with hooks can only be done during the manufacturing process in the factory. Besides, due to the low stiffness and low strength on lateral direction, the bends and hooks of FRP bars are not as efficient as in steel (Ahmed et al., 2009b).

Headed GFRP bars were adopted as an alternative anchorage to improve the pull-out strength by Ahmed et al. (2009a). Pull-out tests showed that the resistance of headed GFRP bars is greater than 50% of the tensile strength of the bars. However, the strength of this anchorage is limited by the slip between the attached head and bar or the failure of the head.

A new mechanical anchorage 'splayed bar' has been developed as an alternative (Darby et al., 2007). By splaying the end of FRP bars, the anchorage strength can be improved by the wedging action and larger contact area between the splay and concrete.

Tallis (2005) carried out nine pull-out tests of GFRP bars with 'splayed anchorage'


Figure 2-31: Traditional bends and hooks at anchorage zone

embedded in concrete cubes. The tests investigated the influence of wedge length and splay angles on the anchorage strength.

Winkle (2005) used the same test method to investigate the influence of confinement provided by helical AFRP reinforcement (Whitehead, 2002) on the anchorage strength of various types of bars with straight or splayed end. The coupon tests demonstrated that splayed smooth bars provide an order of magnitude increase in anchorage strength compared with the same type straight bar; the combination of wedge/helix anchorage method helps to prevent brittle failure of the surrounding concrete.

Orr et al. (2011c) improved the 'splayed anchorage' with a 'fin splay, comprised a triangular plate glued along the full length of the wedge, as shown in Figure 2-32. Beam pull-out tests were conducted to investigate the performance of the fin 'splayed anchorage' in fabric formed beams. However, no bond slip relation was established for this type of anchorage.

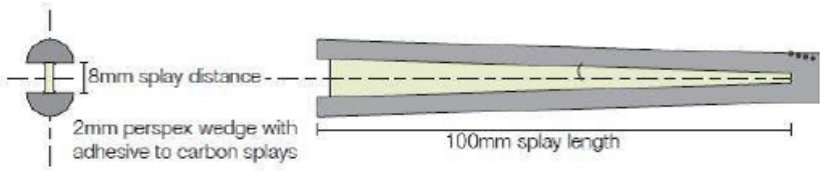


Figure 2-32: Fin splay (Image courtesy: Orr et al. (2011c))

Kostova (2016) conducted a series of pull-out tests of 'splayed anchorage' in prismatic and tapered beams, as shown in Figure 2-33, to investigate the bond-stress relations. The tests demonstrated the influence of wedge length, wedge angle, surface coating, FRP confinement and the type of FRP bars. The 'splayed anchorage' was also installed on the fabric formed beams and provided sufficient anchorage.

The bond-slip relation model of the splayed bars was formulated empirically by Kostova (2016). For a 'splayed anchorage' with length $L_w$ and angle $\alpha_w$, the force equilibriums are shown in Figure 2-34, where $F_b$ is anchorage strength of the FRP bar; $N$ is normal

reaction force from concrete; $\mu$ is coefficient of friction between bar and concrete; $\tau$ is bond stress over the triangle wedge surface area $A_{tot}$.

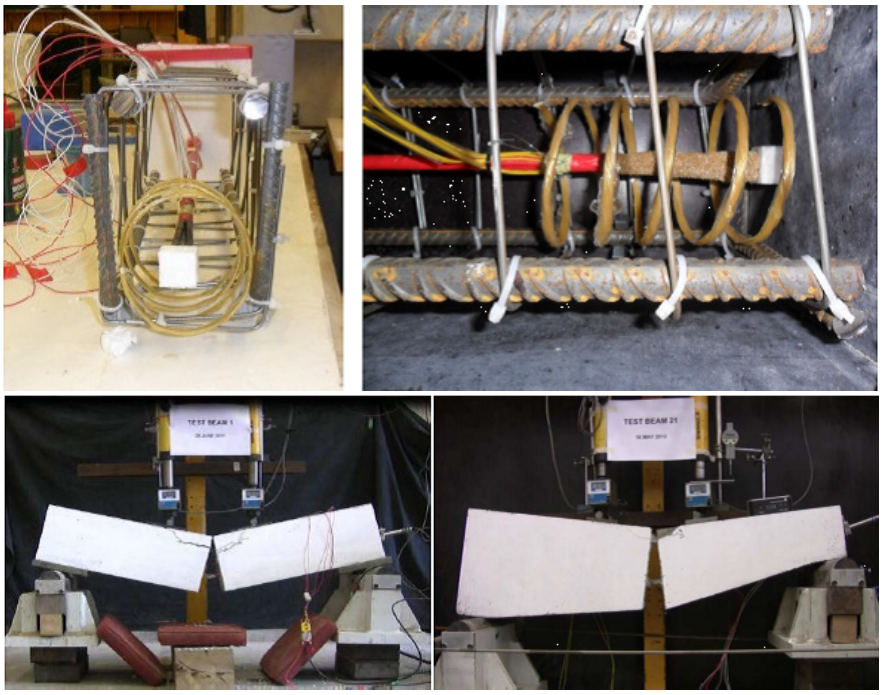

Figure 2-33: Pull-out tests of 'splayed anchorage's (Image courtesy: Kostova (2016))

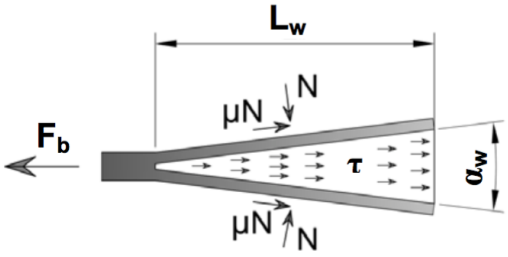


Figure 2-34: Equilibrium of 'splayed anchorage' (Image courtesy: Kostova (2016))

The strength of the splayed bar $F_b$ can be predicted by Equation 2.31, which has been calibrated with the test data of Kostova (2016). The model is valid until the bar slip reaches 0.3mm.

$$F_b = 1200 L_w \sin^2(\frac{\alpha_w}{2}) + 1500 m L_w \sin(\alpha_w) + \tau_w A_w + \tau_b(\pi d_b - 2t_w)L_w \qquad (2.31)$$

where $\tau_w$ and $\tau_b$ are bond stresses in the wedge plate and bar; $d_b$ is diameter of bar and $t_w$ is thickness of the wedge with other variables defined in Figure 2-34.

Limited research has been undertaken to address the safety of the anchorage zone by investigating the development of tensile force of longitudinal bars. The existing research of fabric formed beams only explored the possibility of the reinforcing anchorage strength. Without understanding the mechanism of the force development in longitudinal bars at the anchorage zone, there will be only anchorage designs with overly redundant strength. Therefore, more investigations should be conducted into the tensile force of longitudinal bars.

### 2.4.4 Deflection prediction

When FRP flexural reinforcement is used in the prismatic beams, service limit state design could control the design. Service limit state design mainly refers to deflection control, because the cracking width control is to prevent corrosion, whilst FRP reinforcement is corrosion resistant (ACI-440.1R, 2015).

The experimental research by Hashemian (2012) demonstrated that the stiffness of specimens that had bending-moment geometry is lower than prismatic specimens (Hashemian, 2012). Applying FRP reinforcement in fabric formed beams could further reduce the stiffness. Therefore, deflection prediction of fabric formed beams reinforced with FRP should be considered carefully. This section reviews and assesses the deflection prediction methods adopted in previous research.

#### 2.4.4.1 Empirical method

The empirical method for calculating deflection is widely accepted in design codes and guidelines (e.g. ACI 440.1R). Equations are formulated empirically to simulate the effective moment of inertia ($I_e$). The deflection is calculated using basic structural mechanics using the effective moment of inertia. ACI-440.1R (2015) suggests a modified expression of the effective moment of inertia based on the work of Bischoff and Gross (2010b) as shown in Equation 2.32.

$$I_e = \frac{I_{cr}}{1 - \gamma(1 - I_{cr}/I_g)(M_{cr}/M_a)^2} \leq I_g \tag{2.32}$$

where $M_{cr}$ is the cracking moment of the cross section; $M_a$ is applied moment; $I_{cr}$ is moment of inertia of cracked section; $I_g$ is gross moment of inertia, e.g. for a rectangular section, $I_g$=$bh^3/12$ and factor $\gamma$ is dependent on load and boundary conditions and

accounts for the length of the uncracked regions of the member and for the change in stiffness in the cracked regions.

The problem of the empirical method is that the equations from the design codes and guidelines (ACI-440.1R, 2015; ACI-318, 2008) are calibrated for prismatic beams. For fabric formed concrete beams, the optimised geometries reduce the stiffness, shown by the tests results (Hashemian, 2012; Lee, 2011) and thereby the empirical methods requires further validation.

#### 2.4.4.2 Sectional analysis method

There has been limited work focusing on the serviceability of non-prismatic RC beams. Most of the existing research has been conducted to simulate the performance of elastic or non-elastic beams of variable cross-section with highly sophisticated but not practical models. The theoretical models are normally based on suitable modifications of Euler Bernoulli or Timoshenko beam model coefficients (Shooshtari and Khajavi, 2010) and an accurate description of stress (Balduzzi et al., 2016).

For practical solutions for RC beams of variable depth geometry, Lee (2011) used 'moment - curvature' method to analyse the T beams (section 2.4.2). The beam is divided into many sections. For each section, the second moment of area and curvature ($M/EI$) are calculated respectively based on the beam geometry and applied load. The area 'curvature diagram' of each segment is calculated and then multiplied by the distance from the centroid of the segment to the support. Then the deflection is calculated as the integration of each segment. However, the deflection predictions of Lee (2011) showed 24% to 63% difference from the test results and Lee (2011) suggested it could be the shear cracks development that caused the unconservative predictions.

For FRP reinforced concrete beam elements, CSA-S806 (2012) specifies the computation of deflections should be based on the integrated curvatures of sections. A moment-curvature relation is assumed to be trilinear as shown in Figure 2-35, where $M$ is the moment and $\kappa$ is curvature. For beams and one-way slabs with typical boundary conditions, CSA-S806 (2012) proposes equations to simplify the calculation. For simply supported beams carrying one point load at mid-span in Figure 2-36, the deflection is calculated by Equation 2.33.

$$\delta_{max} = \frac{PL^3}{48E_cI_{cr}}[1 - 8\eta(\frac{L_g}{L})^3] \tag{2.33}$$

Where, $L_g$ is the distance from the support to the point where $M = M_{cr}$ in a simply supported beam, or distance from the free end to the point where $M = M_{cr}$ in a cantilever beam; $\eta$=(1-$I_{cr}/I_g$) and the other variables are shown in Figure 2-35 and Figure 2-36.

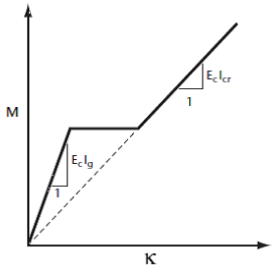


Figure 2-35: Moment curvature relation of FRP reinforced concrete of CSA-S806 (2012)

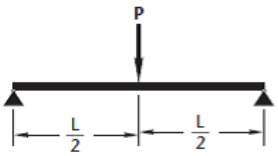


Figure 2-36: Deflection calculation of simply supported beams of CSA-S806 (2012)

Kostova (2016) adopted a similar sectional analysis method which requires the double integration of curvatures of each segment as shown in Equation 2.34. The curvature of each cross section is obtained from known bending moment profiles and the equilibrium of cross-section as shown in Equation 2.35. The sectional analysis method was correlated well with the test data of fabric formed beams reinforced with FRP (Kostova, 2016).

$$\Delta = \int \int \kappa dx dx \tag{2.34}$$

where $\kappa$ is curvature of each cross section and $x$ is the coordinate of horizontal axis.

$$\kappa = \frac{\epsilon_c}{\chi} \tag{2.35}$$

where $\epsilon_c$ is concrete strain at the extreme compression fibre and $\chi$ is the depth to the neutral axis.

In addition, the effective moment inertia method proposed by Bischoff and Gross (2010b) has been used to analyse the load-displacement relations of fabric formed beams (Orr, 2012). A fabric formed beam can be divided into numerous sections and the effective moment of inertia $I_e$ at a specific section of a variable stiffness beam can

be calculated based on the approach proposed by Bischoff and Gross (2010b), as shown in Equation 2.36. Thereby the curvature of each section can be calculated as $M/(EI_e)$ and the deflection of the beam can be calculated as double integrations of curvature of sections based on the boundary conditions. This proposed sectional analysis methods had good correlations with the test data of fabric formed T beams by Orr (2012).

$$I_e = \frac{I_{cr}}{1 - \gamma\eta(M_{cr}/M_a)^2} \leq I_g \tag{2.36}$$

Where $\gamma$ is a factor to account for integration as shown in Equation 2.37 and $\eta$ is a factor to account for tension stiffening as shown in Equation 2.39. The factors used in this equation are derived from virtual work considerations (Bischoff and Gross, 2010b).

$$\gamma = \frac{1.6\xi^3 - 0.6\xi^4}{(M_{cr}/M_a)^2} + 2.4\ln(2 - \xi) \tag{2.37}$$

$$\xi = 1 - \sqrt{1 - M_{cr}/M_a} \tag{2.38}$$

$$\eta = 1 - I_{cr}/I_g \tag{2.39}$$

This method was developed for beams with variable stiffness and it has been adopted by ACI-440.1R (2015), as shown in section 2.4.4.1. This method has been shown effective validated against steel reinforced concrete beams with variable depth geometry (Orr, 2012). Further investigations are required to explore its validity in fabric formed beams reinforced with FRP bars.

## 2.5 Research challenges

This Chapter presents an overview of research into fabric formed beams. The research background of fabric formwork, material behaviour and design methodologies and structural performance are reviewed. With the understanding of existing literature, major challenges are listed as follows:

1. The constructability of concrete beams with variable depth geometries is to be demonstrated using fabric formwork and automated winding techniques to produce the W-FRP cages.
2. The material properties of W-FRP shear reinforcement are required to be investigated.
3. The flexural, shear and stiffness performance of W-FRP reinforced beams with

prismatic and variable depth geometries are required to be investigated and the influence of W-FRP on shear performance needs to be quantified.

4. Based on the experimental and theoretical work, a well established procedure should be developed to guide engineers to design W-FRP reinforced concrete beams with minimised concrete use and to accurately predict the structural behaviour.

5. The advantage of W-FRP reinforced concrete beams in concrete use should be demonstrated by comparing the W-FRP reinforced concrete beams to conventional concrete beams.

In next Chapter, the methodology of the research to address the above challenges is presented.

# Chapter 3

# Methodology

## 3.1 Introduction

This chapter presents the research methodology for this thesis. A new design philosophy is presented to instruct the subsequent experimental research. The schedule of experimental research, which will investigate the novel reinforcement for flexibly formed beams, is presented. The modifications of the design philosophy are made based on the experimental research and formulated as parametric analysis to instruct the design.

## 3.2 Design philosophy

This section presents the design philosophy that has been developed iteratively during the progression of the experimental research. The methods of flexural design, shear design and load-displacement prediction for variable depth concrete beams, which are simply supported and all FRP reinforced, are shown in Figure 3-1 and further details of design procedure are introduced in the following subsections.

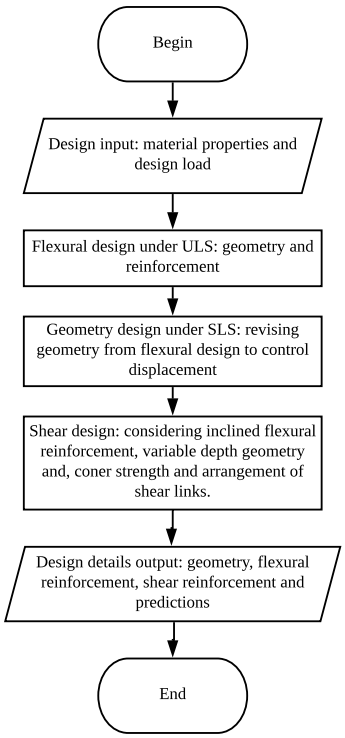


Figure 3-1: Design method of fabric formed beams reinforced with W-FRP

### 3.2.1 Flexural design under ULS

The sectional design method for fabric formed beams has shown good validity for fabric formed concrete beams reinforced with glass fibre bars (Kostova, 2016). The flexural design of FRP reinforced concrete beams has been well addressed by the design codes and guidelines (ACI-440.1R, 2015; CSA-S806, 2012). The flexural design procedure in this section is investigated using these two code and guideline.

For a given bending strength demand, the dimensions and reinforcement details can be calculated following the code and guideline. For prismatic beams, the flexural design

only needs to consider the critical cross-section, which carries the maximum bending moment. The prismatic geometry determined in flexural design can be optimised by minimising the effective depth of each cross-section to provide the demanded nominal bending strength. With a given load, clear span and the material properties of concrete and FRP reinforcement, the flexural design and optimisation procedures are formulated with the following steps:

1. Calculate the bending moment diagram; select the critical cross-section as the one carrying maximum bending moment and choose an appropriate beam width given clear span.

2. Based on design bending moment and beam width, calculate the minimum effective depth and flexural reinforcement ratio at the critical cross-section to achieve a balanced failure mode, where concrete crushing and FRP reinforcement rupture occur at the same time.

3. Divide the beam into various cross-sections by vertical cuts and calculate the minimum effective depth at each cross-section following ACI-440.1R (2015) and CSA-S806 (2012) to meet the flexural strength demand.

4. Add appropriate concrete cover to each cross-section, assemble the cross-sections and rationalise the geometry of the beam by connecting all cross-sections with a smooth curve (expressed as a quadratic equation).

Following the above procedures, the geometry of a beam is optimised in flexure at the Ultimate Limit State. It is normal to conduct the shear design based on this geometry. However, the geometry of an FRP-reinforced beam is usually controlled by the Service Limit State (SLS) design, due to the lower elastic modulus of FRP reinforcement. The geometry obtained in this section is only the initial step of the whole design procedure, which could be very different from the final design. Therefore, the shear design will be conducted after the beam geometry is modified to account for deflection criteria.

In addition, the design procedure in this thesis focuses on simply supported beams. For more complex cases, such as continuous beams under multiple loading cases, although the flexural design procedure in this section can be directly used by considering the combined loading profile, the joint design of columns and beams needs to be carefully considered as the variable depth geometry may result in complex reinforcement arrangement, which is different from the conventional joint design.

### 3.2.2 Geometry design under SLS

The equivalent moment of inertia method (Bischoff and Gross, 2010a), as reviewed in section 2.4.4, is proposed as a prediction method for the load deflection relations of fabric formed beams reinforced with FRP reinforcement. The effective moment of inertia ($I_e$) of each cross-section is calculated with the Equation 2.36. Using this effective moment of inertia approach, the load-displacement relations of the optimised beam geometry from section 3.2.1 can be calculated as follows.

1. Calculate the properties of each cross-section along the beam axis. The section properties include the moment of inertia before cracking $I_g$, compression zone depth before cracking $x_u$, moment of inertia after cracking $I_{cr}$, compression zone depth after cracking $x_c$ and cracking moment $M_{cr}$.

2. Divide the ultimate flexural capacity acquired from section 3.2.1 into various loading steps and calculate the equivalent moment of inertia $I_e$ at each loading step. Where the applied moment $M_a$ on each cross-section is lower than $M_{cr}$, $I_e$ equals to $I_g$; otherwise $I_e$ is calculated following Equation 2.36.

3. Calculate the curvature of each cross-section $M_a/EI_e$ and integrate $M_a/EI_e$ along the beam length to calculate the rotation of the sections at each loading step. Add a constant to set the rotation of the mid-span as zero since all the specimens are simply supported.

4. Integrate again along the beam length to calculate the deflection, adding a constant to set the deflection of the supports to zero.

5. Plot the load-displacement curves of all the cross-sections along the beam length.

It is very likely that the calculated displacement exceeds the limits specified by the code and guideline (ACI-440.1R, 2015; CSA-S806, 2012) under Service Limit State. ACI-440.1R (2015) specifies the maximum displacement as $l/240$ ($l$ is the clear span length) for beams and one-way slabs under SLS. The stiffness of the beam with optimised geometry could be potentially addressed by prestressing the reinforcement. However, it also can be addressed by revising the geometry design from flexural design under Ultimate Limit State (ULS).

By increasing the effective depth at each section proportionally, the displacement at mid-span of a beam could be controlled to the required level. With the revised geometry from Service Limit State (SLS), the flexural design needs to be rechecked and adjusted following the design procedures from section 3.2.1. It is possible that geometry revision

changes the flexural failure mode from concrete crushing to bar rupture. Adjustment of flexural reinforcement needs to be undertaken and then the geometry design under SLS needs to be conducted again until the displacement is under control and the failure mode is desirable. Finally, the beam geometry is determined by satisfying the flexural and load-displacement requirement with minimum concrete usage.

This geometry design procedure may be applicable to continuous beams with variable depth geometries. However, research has shown the displacement of variable depth beam (steel reinforced) can be predicted using Partial-interaction method (Tayfur, 2016). Further investigations need to be undertaken to develop new methods or use the existing methods to design the geometry of continuous beams under SLS.

### 3.2.3 Shear design

As codified shear design methods are designed for prismatic beams, this section presents the proposed revisions to the codified equations and the MCFT model to formulate a systematic shear design procedure. Four potential contributing factors to shear are considered and presented in the following sections.

#### 3.2.3.1 Inclined longitudinal bars

Under applied load, the longitudinal bars of a variable-depth beam carry tensile force as shown in Figure 3-2. Taking a cut along the assumed concrete strut (Figure 3-2), the tensile force of longitudinal bars at the support is composed of the flexural tensile force created by bending moment ($T_f$) and the additional tensile force created by shear ($T_v$). The flexural tensile force can be calculated directly by the equilibrium of the cross-section. Although the additional tensile force of longitudinal bars is explicitly specified as shown in Equation 2.27 and Equation 2.28, it cannot be determined directly due to its relation to the applied load. As the W-FRP shear reinforcement will be applied in the experimental research of this thesis, the modified expression of Equation 2.28 for FRP reinforcement from CSA-S806 (2012) is adopted, as shown in Equation 3.2.

$$V_u = V_c + V_f + V_t \tag{3.1}$$

$$T_v = 1.3(V_a - 0.5V_f - V_p) \tag{3.2}$$

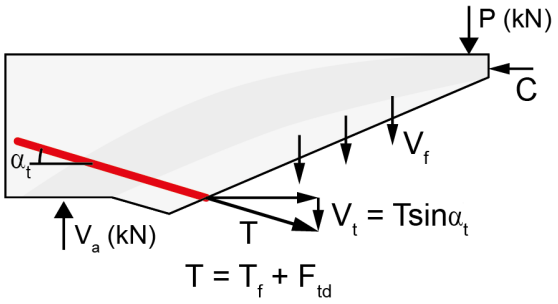


Figure 3-2: Shear resistance of inclined longitudinal reinforcement

Where $V_a$ is applied shear force; $V_f$ is shear contribution of W-FRP shear links and $V_p$ is the factored vertical component of the effective prestressing force or the flexural compression and tension for variable depth elements.

As $V_t$ is related to the shear capacity $V_u$, the calculation of shear capacity should be iterated until the shear demand is equal to shear capacity.

For a given beam geometry and shear design, the iteration procedures at a certain cross-section are proposed as follows:

1. Assume an applied load $P_a$ (point load or uniformly distributed load) and calculate the applied shear force $V_a$ and bending moment $M_a$;

2. Calculate the shear contribution of shear links $V_f$, contribution of concrete $V_c$, the flexural tensile force of longitudinal bars $T_f$ and the additional tensile force $T_v$ (Equation 3.2) based on the applied load;

3. Calculate the shear capacity $V_u$ following Equation 2.4.2 with $V_c$, $V_f$ and the vertical component of $T_f$+$T_v$;

4. Calculated the corresponding applied load $P_u$ and compare it with $P_a$;

5. Where the load $P_u$ is different from the assumed load $P_a$, assume a different load $P_a$ and repeat from step one to step four;

For the MCFT model (Vecchio and Collins, 1986), the same procedures are proposed to calculate the shear contribution of inclined flexural reinforcement. However, the shear contributions of concrete and shear reinforcement are not considered separately. The value of $V_c$+$V_f$ is replaced as the integral of maximum shear stress distribution, which can be carried by the cracked reinforced cross-section. This shear stress distribution is presented in section 3.2.3.2.

#### 3.2.3.2 Variable depth geometry

The design codes and guidelines (ACI-440.1R, 2015; CSA-S806, 2012) for FRP reinforced concrete adopt sectional shear design method based on a truss analogy. For prismatic beams, the critical cross-section is selected as the one carrying maximum shear force. However, due to the variable depth geometry, the critical cross-section cannot be determined immediately. The effective depth of the cross-section influences the concrete contribution to shear and the inclined flexural reinforcement also influences the total shear resistance as discussed in section 3.2.3.1. Therefore, the shear strength of all cross-sections should be checked using the codified shear design equations and Equation 3.1 to determine the critical cross-section and the ultimate shear capacity.

The MCFT model (Vecchio and Collins, 1986) is also a sectional design method. However, the shear strength is determined by the integral of maximum shear stress distribution, which is influenced by the geometry of beams, as presented in the literature (section 2.4.2.2). The actual shear stress distribution in the cracked variable-depth concrete beams is considered in the proposed revisions in the MCFT model. This maximum stress can be calculated using the fifteen classical non-linear equations used to consider the stress equilibriums, strain compatibility, constitutive relations and cracking behaviours in the MCFT model (Vecchio and Collins, 1986; Bentz et al., 2006) when the shear link rupture in the tension zone occurs.

The equations have been solved with a 'Matlab' code, developed by the author (see Appendix A). For simplification, the concaved shear stress distribution in the compression zone (Figure 2-22) is assumed as a parabola and the integral is simplified as 1/3 of the depth of compression zone multiplied by the maximum shear stress. Finally, the shear strength of a specific cross-section is calculated using Equation 3.1 by taking the concrete contribution and shear reinforcement contribution as the integral of the maximum shear stress distribution.

#### 3.2.3.3 Corner strength of W-FRP

As reviewed in section 2.3.3.2, in codified design methods (ACI-440.1R, 2015; CSA-S806, 2012), the design strength of FRP shear reinforcement with circular cross-sections is limited using the corner strength of shear links, reduction factors and ultimate strains. The rectangular cross-section of W-FRP shear links, which arises from their manufacturing process, is beneficial and leads to higher corner strengths than conventional circular cross-section shear links of the same area (Spadea et al., 2017a).

Therefore, the shear strength of W-FRP reinforced beam can be improved due to the higher corner strength of W-FRP reinforcement by improving the arrangement of shear links to maximise the ratio of corner radius to effective diameter. This positive effect of higher corner strength of W-FRP shear links should be considered.

In the proposed revisions of the codified design methods, the actual corner strength of W-FRP shear links is considered together with the existing limits of the design strain. For the ACI-440.1R (2015), the design strength of W-FRP shear links is limited to the minimum value of (i) strength at an ultimate strain of 0.4%; (ii) strength at the bent portion of shear links given by Equation 2.6 and (iii) actual bent corner strength of W-FRP shear links (Equation 2.29).

For the revisions of CSA-S806 (2012), the design strength of W-FRP shear links is limited to the minimum value of the (i) strength at the ultimate strain of 0.5%; (ii) 0.4 of the ultimate tensile strength of straight W-FRP and (iii) the actual corner strength from testing. Note that the strength reduction factor of 0.40 present in Equation 2.21 is removed and included instead in condition (ii) above as a limit on $f_{fu}$ to align this proposal with Razaqpur and Spadea (2014). The shear contribution of shear links following CSA-S806 (2012) is calculated in Equation 3.3 instead of Equation 2.21.

$$V_{fv} = \frac{\phi_f A_{fv} f_{fv} d_v \cot\theta}{s} \tag{3.3}$$

where, $f_{fv}$ is design strength of FRP shear reinforcement limited by proposed three conditions in revised CSA S806 with other variables defined in Equation 2.21.

In the revised MCFT model (Vecchio and Collins, 1986), constitutive relations of steel reinforcement is replaced with the linear elastic property of W-FRP shear reinforcement with a design strength limited by the actual corner strength (Spadea et al., 2017a) since the MCFT model allows designers to define material properties. With different layers of carbon fibres, the corner strength of W-FRP varies (Spadea et al., 2017a). Therefore, even with the same shear reinforcement ratio, the different arrangement of W-FRP in different cross-section areas could influence the predictions of the revised MCFT model (Vecchio and Collins, 1986) and the codified designs (ACI-440.1R, 2015; CSA-S806, 2012).

#### 3.2.3.4 Inclined shear reinforcement

Due to the flexibility of W-FRP shear reinforcement, the links can be arranged at a variable angle to the horizontal axis, Figure 3-3. As inclined transverse reinforcement can provide a more effective mechanism for resisting shear (BS-EN-1992-1-1, 2004), the W-FRP arrangement can be improved to provide the maximum shear resistance. This beneficial effect of diagonal W-FRP shall be considered.

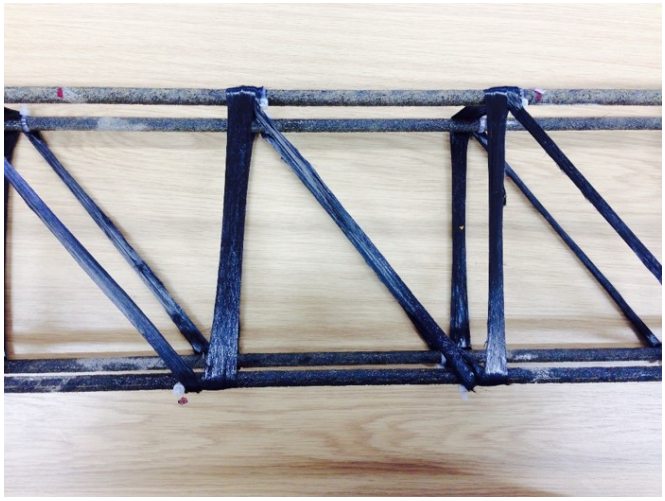

Figure 3-3: Variable angle arrangement of W-FRP

ACI-440.1R (2015) specifies the positive effect of diagonal shear links with Equation 3.4. This equation can be directly used to consider the diagonal W-FRP shear links. However, W-FRP shear reinforcement could be potentially arranged vertically and diagonally. To include the effect of shear links with two orientations in the proposed revisions of codified shear design, the shear contributions of W-FRP shear reinforcement ($V_f$) following ACI-440.1R (2015) and CSA-S806 (2012) are rewritten as Equation 3.5 and Equation 3.6 respectively.

$$V_f = \frac{A_{fv} f_{fv} d}{s} (\sin\alpha + \cos\alpha) \tag{3.4}$$

where, $\alpha$ is angle between diagonal shear links and horizontal axis.

$$V_f = \frac{A_{fv} f_{fv} d}{s} (1 + \sin\alpha + \cos\alpha) \tag{3.5}$$

$$V_f = \frac{\phi_f A_{fv} f_{fv} d}{s} \cot\theta (1 + \sin\alpha + \cos\alpha) \tag{3.6}$$

The MCFT model (Vecchio and Collins, 1986) ultilises shear reinforcement ratio $\rho_{fv}$ to calculate shear strength, Equation 3.7 is proposed to consider the diagonal and vertical shear links in the revisions for the MCFT model.

$$\rho_{fv} = \frac{A_{fv}}{b_w s}(1 + \sin\alpha + \cos\alpha) \tag{3.7}$$

Where, $b_w$ is the width of the beam.

#### 3.2.3.5 Shear design procedures

For a beam geometry designed in flexure under both Ultimate Limit State and Service Limit State, the shear design procedures based on the codified design methods include the following steps:

1. Calculate shear and bending demand along the beam axis based on the ultimate bending capacity;
2. Initially estimate the area of transverse FRP reinforcement required at each section that has been used in the flexural design and optimisation;
3. Calculate the value of $V_c$ following the codified equations (Equation 2.17 and Equation 2.20) and the value of $V_f$ following Equation 3.5 or Equation 3.6 depending on the code or guideline being used, with the design strength of W-FRP shear reinforcement specified in section 3.2.3.3;
4. At each section, following the iteration procedures in section 3.2.3.1, calculate the value of $V_u$ using Equation 3.1;
5. Where $V_u$ is less than the shear demand from step 1, iterate area of transverse reinforcement and transverse reinforcement arrangement, through steps 4-6 until the member resistance is greater than or equal to the required shear and bending demand;
6. Output member shear reinforcement arrangement.

The shear design procedures based on the MCFT model (Vecchio and Collins, 1986) include the following steps:

1. Calculate shear and bending demand along element based on the ultimate bending capacity;

2. Initially estimate the area of transverse FRP reinforcement required at each section that was divided in the flexural design and optimisation;

3. At each section, assuming an applied shear force $V_a$, calculate the strain of longitudinal bars and the shear contribution of longitudinal bars $V_t$ with the flexural tensile force and additional tensile force (Equation 3.2);

4. At each section, using the tensile strain of longitudinal bars, the shear resistance of concrete and shear links ($V_v$=$V_c$+$V_f$) is calculated as the integral of the shear stress distribution (Figure 2-22(b)) when the stress of the shear links across the shear crack reach their capacity at the corners (Equation 2.29). The shear reinforcement ratio is given by Equation 3.7, accounting for any inclination of the reinforcement to the longitudinal axis;

5. At each section calculate the value of $V_u$ using Equation 3.1 and the iteration procedures in section 3.2.3.1;

6. Where $V_u$ is less than the shear demand from step 1, iterate the area of transverse reinforcement and transverse reinforcement arrangement, through steps 4-7 until the member resistance is greater than or equal to the required shear and bending demand;

7. Output the shear reinforcement design.

The geometry optimisation results in smaller effective depth at the support area and hence lower shear contribution $V_c$. Consequently, more shear reinforcement may be needed. However, the smaller support depth also increases the shear contribution from inclined flexural reinforcement ($V_t$) as the angle of the flexural bar to horizontal axis becomes higher. This change could compensate the reduced $V_c$. Therefore, when the optimisation of geometry (concrete use) and shear reinforcement arrangement conflict with each other, the geometry optimisation is considered first.

After the flexural design under ULS, geometry design under SLS and shear design, the design details of a simply supported and W-FRP reinforced beam with variable depth geometry are obtained. The validity of proposed design methodology still requires verification through experimental research. The schedule of tests is presented in the following section.

## 3.3 Experimental research

The design philosophy presented in section 3.2 has been developed in parallel with the experimental research. The experimental research has been proposed in order to understand the behaviour of W-FRP shear reinforcement and the structural behaviour of W-FRP reinforced beams to fill the research gaps as presented in section 2.5. This section presents the progressive testing schedule: (i) material characterisation of W-FRP and (ii) structural tests of W-FRP reinforced beams. The test road map is shown in Figure 3-4.

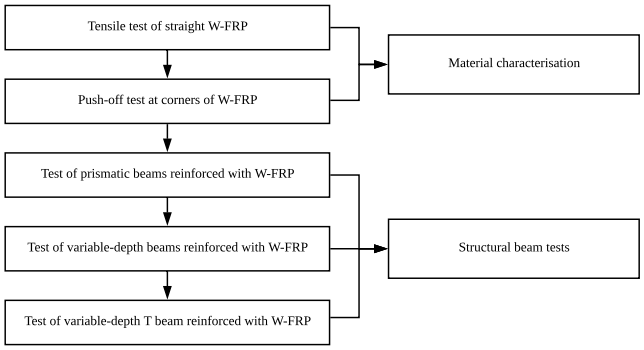


Figure 3-4: Test roadmap

The material characterisation tests were conducted collaboratively with Spadea et al. (2017b) and details of the research are fully presented in Chapter 4. Six tensile test specimens were designed to understand the material properties of W-FRP reinforcement at the straight portions following BS-EN-ISO-527-4 (1997) and BS-EN-ISO-527-5 (1997). Push-off tests were designed and conducted to investigate the corner strength of W-FRP shear links following CSA-S806 (2012) to instruct the shear design of W-FRP reinforced concrete.

The structural testing of W-FRP reinforced concrete started from prismatic beams, Figure 3-5, to investigate the effectiveness of W-FRP shear reinforcement. Six prismatic beam specimens (P series) were designed and tested to failure under four-point bending. The existing design methods of FRP reinforced concrete, which are also the basis of the proposed revisions in section 3.2, were examined. The details the testing and analysis are presented in Chapter 4.

In order to understand the influences of variable depth geometry and W-FRP shear reinforcement on shear strength, eight variable depth beam specimens (TP series) were designed and tested to failure under three-point bending, Figure 3-5. Comparisons of the prismatic specimens and the tapered specimens were made, showing the differences in material usage and structural performance. The details the testing and analysis are presented in Chapter 5.

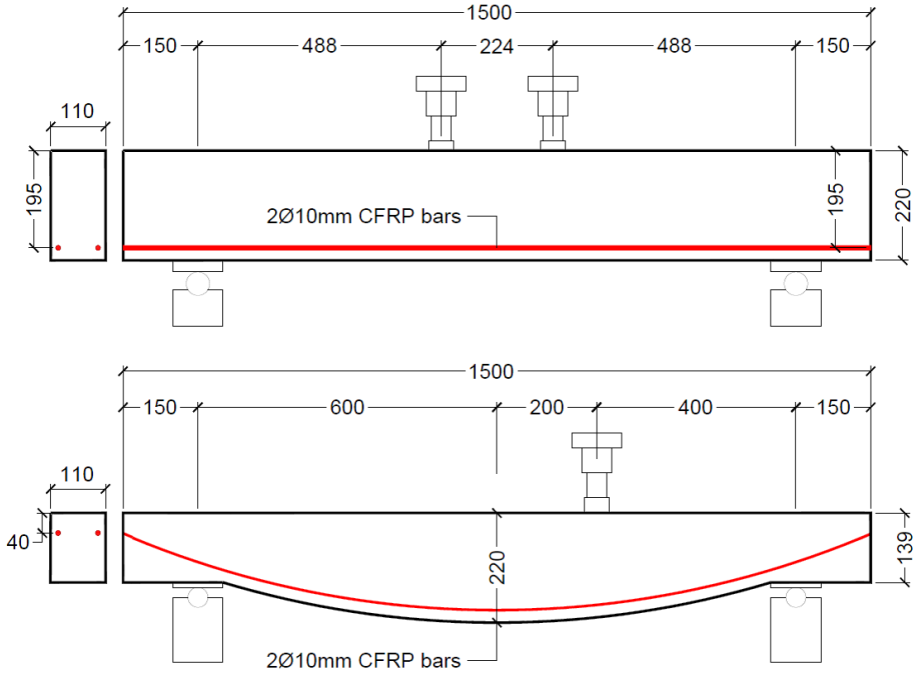


Figure 3-5: Geometry of the prismatic and variable depth specimens

Based on the knowledge acquired from the above two series of tests, full-scale flexibly formed T beam specimens (T series) were tested, Chapter 6. To investigate the flexural strength, shear strength and stiffness, eleven T beam specimens are designed and tested until failure under seven-point bending, as shown in Figure 3-6. An automated winding technique and fabric formwork were used in the specimen fabrications.

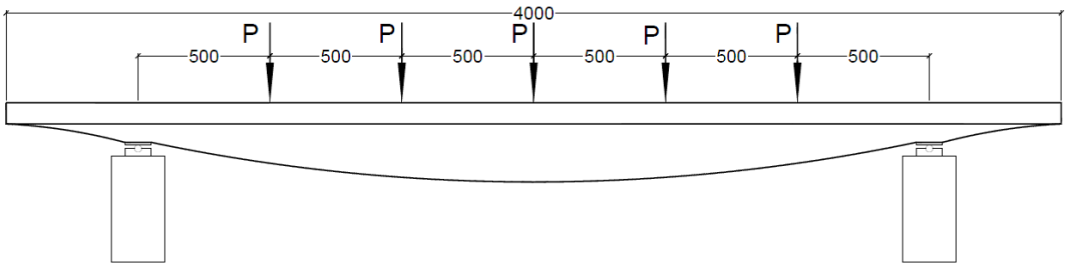


Figure 3-6: Geometry of T beam specimens

## 3.4 Modelling and parametric analysis

Analysis is undertaken to examine the shear contributions of flexural and shear reinforcement, the influence of shear reinforcement, geometry, and anchorage. With the analysis, the design methodology in section 3.2 is developed.

Revisions have been undertaken in the proposed MCFT method (section 3.2) so that the revised model can precisely simulate the structural behaviour of the T beam specimens in the full loading process. The validity of the model has been examined and further parametric analysis has been undertaken to explore the optimum design of the T beam specimens. The details of the modelling and parametric analysis have been fully presented in Chapter 7.

Based on the modelling and design methodology discussed in this Chapter, design guidance has been formulated to instruct designers to design an optimised beam reinforced with W-FRP which uses the minimum concrete and reinforcement and to predict the structural performance.

## 3.5 Summary

This chapter presents the research methodology of this thesis. The design methodology has been proposed. Experimental research methodology is presented in brief. The introduction of Modelling and parametric analysis is presented. The main work in this Chapter is summarised as follows:

- The design methodology based on codified equations and the MCFT model is proposed to address the flexure, shear and load-displacement relation design of

beams with optimised geometries.

- Three series of progressive experimental research are proposed to investigate the material properties of W-FRP shear reinforcement and the structural behaviour of W-FRP reinforced beams. During the testing, the specimen fabrication will help to demonstrate the constructability of W-FRP beams. Comparisons of the beam specimens to equivalent prismatic beams will show the advantage of W-FRP reinforced beams with variable geometries in concrete saving.
- The modelling and parametric analysis based on the experimental research is introduced to revise the proposed design methodology to provide accurate predictions and design guidance.

In next Chapter, the experimental research of W-FRP shear reinforcement and testing of W-FRP in prismatic beams are presented following the proposed research methodology.

# Chapter 4

# W-FRP reinforcement

**Material characterisation and W-FRP reinforced prismatic beams**

## 4.1 Introduction

This chapter presents fundamental investigations into the material properties and effectiveness of W-FRP shear reinforcement presented in section 2.4.2.4. Tensile tests and push-off tests of laboratory-produced W-FRP are presented to show the tensile properties at the straight portion and the weaker strength at the corner portion. Four-point bending tests of six prismatic beam specimens are presented to show the effectiveness of W-FRP in reinforced concrete beams. The main findings of the research in this chapter are discussed and summarised. The work of this chapter has been published in journal paper 'Spadea, S., Orr, J., Nanni, A., Yang, Y. (2017). Wound FRP shear reinforcement for concrete structures. Journal of Composites for Construction, 21(5).'.

## 4.2 W-FRP material property tests

In this section, W-FRP shear reinforcement is defined and presented along with an illustration of the manufacturing process. To instruct the design of W-FRP reinforced concrete, the fundamental material properties of W-FRP are required to be understood. Therefore, the tensile strength of W-FRP at the straight portion and the strength of W-FRP shear links at the corner were tested.

### 4.2.1 Wound Fibre Reinforced Polymer

As discussed in section 2.4.2.4, many solutions have been proposed to address the complicated fabrication of shear reinforcement in fabric formed beams with variable-depth geometry. Among these solutions, W-FRP is proposed as an alternative to steel shear reinforcement, produced by winding continuous fibre tows impregnated with resin epoxy (before setting) around longitudinal reinforcing bars. Capitalising on the flexibility of carbon fibre tows, the cages composed of W-FRP shear reinforcement and FRP flexural bars are expected to be lightweight, easily transported, easy to precisely locate in casting mould and adaptable to complex geometries.

Consequently, the difficulties of manufacturing the steel reinforcement cages for fabric formed beams could be potentially addressed using W-FRP shear reinforcement. In addition, the corrosion resistance of W-FRP could potentially increase the durability of reinforced concrete structures and thereby reduce the life-cycle cost.

A wet-layup method has been developed to manufacture W-FRP in this thesis. In the wet-layup winding, carbon fibres are first impregnated by passing them through a resin bath. Then the wet carbon fibres are wound around a mandrel consisting of longitudinal reinforcement used for a beam with prismatic or variable-depth geometry. The wet-layup winding results in closed-shape FRP stirrups (two-legged) after curing.

C T50-4.0/240- E100 50k carbon fibre tows (50K filaments) from Sigrafil and a two-component epoxy resin Tyfo S were used to manufacture the W-FRP reinforcement in this thesis. The material properties of the carbon fibres and epoxy from manufacturer are shown in Table 4.1 and Table 4.2.

Table 4.1: Properties of 50k carbon fibre filament

| Description | C T50-4.0/240-e100 |
|---|---|
| Filament diameter | 7$\mu$m |
| Number of filament | 50k |
| Tensile strength | 4000MPa |
| Elastic Modulus | 240GPa |
| Elongation at break | 1.7% |

Table 4.2: Properties of Tyfo S two component epoxy

| Description | Tyfo S |
|---|---|
| Curing time | 72 hours |
| Tensile strength | 72.4MPa |
| Elastic Modulus | 3.2GPa |
| Elongation at break | 5.0% |

### 4.2.2 Tensile properties of straight W-FRP

#### 4.2.2.1 Specimen design and manufacture

To characterise the strength of W-FRP, shear link samples were manufactured (Spadea et al., 2017b) by winding the eight layers of impregnated fibres around rectangular wooden moulds (850x280mm) with rounded corners (15cm radius), as shown in Figure 4-1. Three different cross sections were produced by changing the width and thickness of the shear links as shown in Table 4.3. The ratio between fibres and epoxy were maintained at 0.55/0.45, comparable to a pultrusion process. Given the shear links were manufactured by hand, there were inevitable variations of dimension parameters at different locations of the shear links. Therefore the parameters of shear link dimensions are taken as average values.

Table 4.3: Geometry of W-FRP shear link sample

| Specimens | $N$ | $A_{cf}$ $(mm^2)$ | $A_r$ $(mm^2)$ | $A_f$ $(mm^2)$ | $R$ $(cm)$ | $w_f$ $(mm)$ | $t_{fe}$ $(mm)$ |
|---|---|---|---|---|---|---|---|
| WB_1 | 8 | 15.4 | 18.8 | 34.2 | 15 | 6 | 5.7 |
| WB_2 | 8 | 15.4 | 18.8 | 34.2 | 15 | 15 | 2.3 |
| WB_3 | 8 | 15.4 | 18.8 | 34.2 | 15 | 25 | 1.4 |

Where, $N$ is the number of layers of 50k carbon fibre tows; $A_{cf}$ is area of carbon fibres;

$A_r$ is area of resin; $A_f$ is cross-section area of the shear link samples; $R$ is radius of the corners; $w_f$ is width of the shear links and $t_{fe}$ is the average equivalent thickness of shear links.

Figure 4-1: W-FRP shear link samples

In order to understand the tensile properties of the W-FRP shear links at the straight portions, six specimens were designed and tested following BS-EN-ISO-527-4 (1997) and BS-EN-ISO-527-5 (1997). As shown in Figure 4-2, all the specimens were 400mm long with a test length of 150mm and an anchor length of 120mm at the two ends. The tested straight portions were taken from the W-FRP shear link sample 3 (Table 4.3) with a cross-section of 25mmx1.4mm as shown in Figure 4-3.

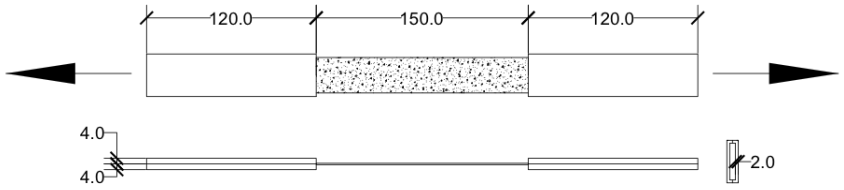


Figure 4-2: Diagram of tensile test specimens

Following the design, the specimens were fabricated as follows: (i) anchor preparation; (ii) assembling and (iii) curing. Aluminium tabs were manufactured to act as the anchors of the specimens. The tabs were designed with a channel in the middle rather than flat cross-section to accommodate the cross-section of W-FRP reinforcement and 1mm adhesive on the reinforcement surface. Then the tabs were transversely notched (0.5mm) on the inner sides to create mechanical interlock with the adhesive (Figure 4-4). The adhesive surface of the tabs was then cleaned with ethanol for later specimen assembling.

The anchor area of the W-FRP strips was gently sanded and then degreased. Araldite

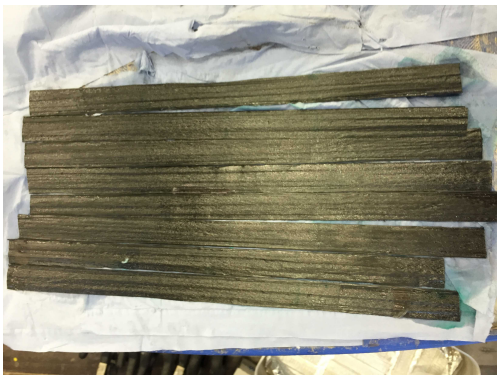

Figure 4-3: Straight portions of W-FRP shear links used for tensile tests

Figure 4-4: Notched aluminum anchor tabs

standard two-component structural epoxy was applied on the surface of the prepared W-FRP strips. The strips were then fastened to the aluminium tabs with clamps and cured at room temperature for an hour.

Finally, the specimens were cured in a 105 °C oven for 24 hours, following the manufacturers recommended curing method. The resulting specimens are shown in Figure 4-5. The black dots and white background of the testing part of the specimens are speckle patterns used for Digital Image Correlation (DIC). One strain gauge was installed in the middle of each specimen to record strains during testing.

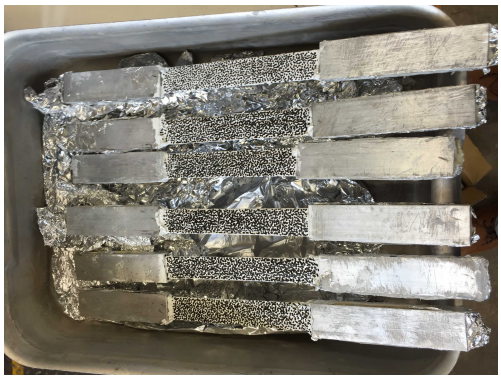

Figure 4-5: Tensile test specimens

#### 4.2.2.2 Testing method

The specimens were tested in tension until failure with a universal testing machine (Figure 4-6) under an elongation rate of 1mm/min. To improve the performance of adhesive joint, metallic clamps were installed on the first 75mm portion of the aluminium tabs to apply a passive pressure of 10 MPa by controlling the torque of the screws. The 50mm end portion of the tabs was gripped in the testing machine with a 20MPa pressure.

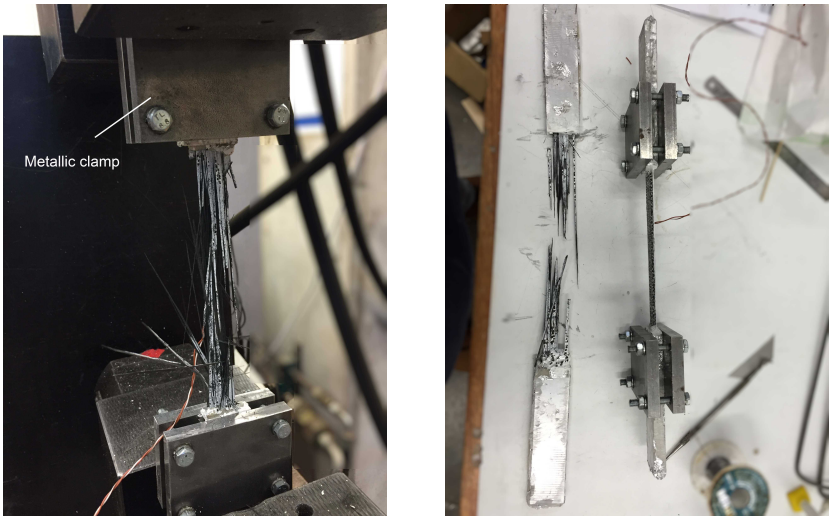


(a) (b)

Figure 4-6: Failure of the tensile test specimen

#### 4.2.2.3 Testing results

The maximum load and strain recorded in tests are shown in Table 4.4 and Figure 4-7. Using the test data, the tensile strength and elastic modulus of W-FRP reinforcement are calculated, Table 4.4.

Table 4.4: Test results of straight portions of W-FRP

| Specimens | Failure load $F_u$ (kN) | Failure strain $\epsilon_u$ (%) | Strength $f_{fu}$ (MPa) | Elastic modulus $E_f$ (GPa) |
|---|---|---|---|---|
| WL1 | 45.1 | 1.46 | 1805 | 124 |
| WL2 | 46.8 | 1.28 | 1872 | 146 |
| WL3 | 45.7 | 1.29 | 1827 | 142 |
| WL4 | 48.6 | 1.28 | 1942 | 152 |
| WL5 | 49.5 | 1.34 | 1981 | 148 |
| WL6 | 51.6 | 1.37 | 2062 | 150 |
| Average | 47.9 | 1.34 | 1915 | 143 |
| SD | 2.2 | 0.06 | 90 | 9 |
| COV | 4.7% | 4.7% | 4.7% | 6.6% |

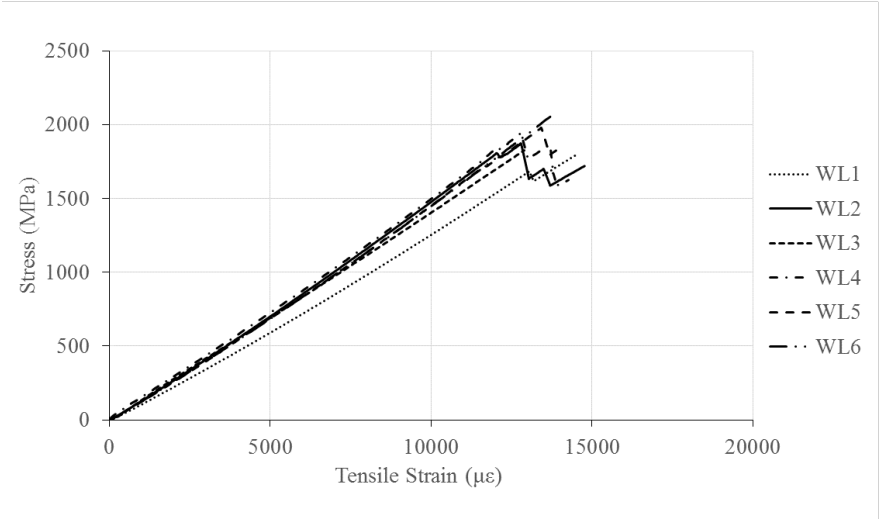


Figure 4-7: Stress - strain relations of the specimens

All the specimens exhibited linear elastic stress-strain relations. The straight portions of the laboratory-produced W-FRP shear links exhibited high tensile strength and modulus with small variations as shown in Table 4.4.

### 4.2.3 Corner strength of W-FRP shear links

#### 4.2.3.1 Test design

Push-off tests were designed and conducted following CSA-S806 (2012) Annex F to investigate the strength of W-FRP shear links at the corners (Spadea et al., 2017b). The corner strength of FRP shear links are influenced by the ultimate tensile strength, $f_{fu}$, the radius of the bend, $R$, and the diameter of links with round cross-section, $d_b$ (El-Sayed et al., 2007). The initial design of specimens considered the latter two factors, given that the ultimate tensile strength of straight portions had been tested as presented in section 4.2.2. The radius of shear link corners was chosen as 15mm and 30mm. The three cross section designs in Table 4.3 were used to have different equivalent diameters calculated by Equation 2.9 proposed by Lee et al. (2013).

The same W-FRP shear links used in tensile tests in section 4.2.2 were designed to be cast into two concrete blocks as shown in Figure 4-8. In Block B, the straight part of the shear links was debonded using a layer of polytetrafluorethylene tape treated with the debonding agent so that the strength of the corners could be obtained with the failure load occurring in Block B.

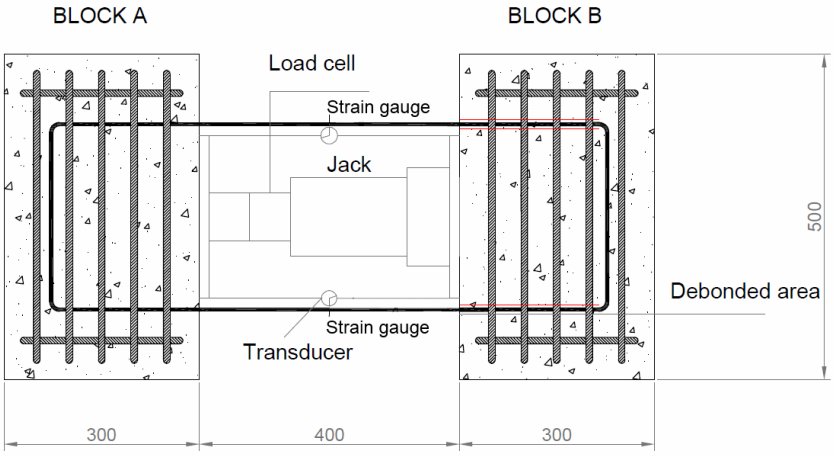


Figure 4-8: Test design of push off tests

A hydraulic jack was used to apply even load to the two concrete blocks with steel and rubber plates. Block A of the specimens was mounted on two pin supports and Block B was mounted on two rollers to minimise the friction between Block B and the testing bed. The rollers and pins were placed under the concrete blocks. With increasing load

applied to the two concrete blocks, the corner of W-FRP shear links will rupture so that the corner strength of W-FRP can be obtained.

#### 4.2.3.2 Test program

The actual test setup is shown in Figure 4-9. Two specimens were tested under displacement control. The shear links in specimens had a cross-section of 25mmx1.4mm with corner radius of 15mm and 30mm respectively. A 200kN load cell was installed to measure the load and transducers were installed between the two concrete blocks to record the relative displacement. Two strain gauges were installed on the straight part of the two legs of the shear link to monitor the strains and hence stress in the shear links ($\epsilon_1$ and $\epsilon_2$).

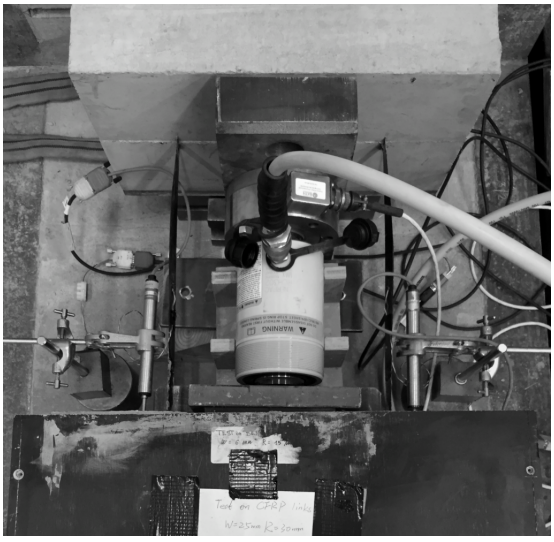

Figure 4-9: Test setup of push off tests

The specimen WB_I which had the corner radius of 15mm failed prematurely at 6.3kN because the round corner of the shear link at the debonding side (Block B) was not fully surrounded by concrete. The W-FRP shear link fractured in the middle of the corner as shown in Figure 4-10. Specimen WB_II which had the corner radius of 30mm was tested successfully with failure occurring at the end of the debonded straight portion of the shear link.

Figure 4-10: Failure of W-FRP shear links: WB_I (top) and WB_II (bottom)

#### 4.2.3.3 Test results

The test results are shown in Table 4.5. The corner strength $f_b$ is calculated based on the strain of the failed leg ($\epsilon_2$) and the elastic modulus in Table 4.4. Specimen WB_II failed with an average strain of 0.73% of the two legs, which is 54% of the ultimate tensile strain of the straight portion as shown in Table 4.4. The test results of the specimen WB_II are in accordance with the previous research that the corners are the critical factor in determining the design strength of FRP shear reinforcement (El-Sayed et al., 2007).

Table 4.5: Test results summary of the specimen WB_I and WB_II

| Specimens | Equivalent thickness $t_{fe}$ (mm) | $R$ (mm) | Failure load $F_b$ (kN) | $\epsilon_1$(%) | $\epsilon_2$(%) | Corner strength $f_b$ (MPa) | $f_b/f_{fu}$ |
|---|---|---|---|---|---|---|---|
| WB_I | 1.4 | 15 | 6.3 | 0.13 | 0.08 | - | - |
| WB_II | 1.4 | 30 | 46.5 | 0.70 | 0.75 | 1072 | 0.54 |

Further tests were conducted by Spadea et al. (2017b) to investigate the influence of the equivalent diameter, corner radius and production methods of W-FRP shear links (wet-layup and dry-winding). The test results of six specimens that have the same corner radius of 15mm and different cross-section dimensions were published (Spadea

et al., 2017b) and the test results of the specimens consisting of wet-layup W-FRP shear links are shown in Table 4.6.

Table 4.6: Test results from the push off tests of Spadea et al. (2017b)

| Specimens | Equivalent thickness $t_{fe}$ (mm) | $R$ (mm) | Failure load $F_b$ (kN) | $\epsilon_1(\%)$ | $\epsilon_2(\%)$ | $f_b/f_{fu}$ |
|---|---|---|---|---|---|---|
| WB.06 | 5.7 | 15 | 50.2 | 0.71 | 0.82 | 0.61 |
| WB.25 | 2.3 | 15 | 76.5 | 1.17 | 1.01 | 0.87 |
| WB.25 | 1.4 | 15 | 75.3 | 1.05 | 1.13 | 0.87 |

The limited valid experimental data of the push-off tests is insufficient to determine the design strength of W-FRP shear links but it confirms that the corner is the governing factor that limits the design strength of W-FRP links. During the course of this thesis, further experimental investigations have been conducted by Spadea et al. (2017a) into the performance of W-FRP shear links with different layers of 50k carbon fibres and the same bend radius of 10mm. An empirical equation (Equation 2.29) was proposed based on the test data of corner strength of W-FRP shear links. The work of Spadea et al. (2017a) are used in later beam testing to determine the design corner strength of W-FRP.

## 4.3 Prismatic beam test design

Following the material property testing, this section presents investigations into the Shear behaviour of W-FRP reinforced prismatic beams. Testing details and analysis are presented in the following sections.

### 4.3.1 Specimen design

#### 4.3.1.1 Geometry and material property

Six prismatic beams were designed to be tested under four-point bending to understand the influence of W-FRP on the shear behaviour of prismatic specimens, as shown in Figure 4-11. All the beams were designed with the same geometry of 1500mm x220mm x110mm to fit 2 specimens in one standard steel mould (3000mm in length) available in the laboratory of the Department of Architecture & Civil Engineering, University

of Bath. The clear span was set as 1200mm. The loading points were designed to be 488mm away from the support to set the shear span/depth ratio as 2.5 to maximise the probability of shear failure (Kani, 1964).

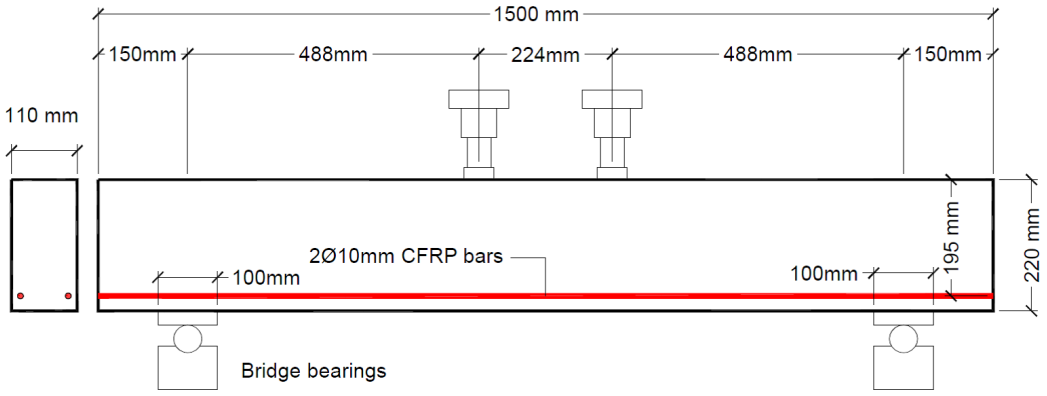


Figure 4-11: Test setup

All the specimens were designed with the same flexural reinforcement of two ⌀10mm Aslan CFRP bars (200 Series) to ensure the same flexural capacity. The tensile properties of the flexural bars taken from manufacturer data are shown in Table 4.7. The concrete was designed as C35/45 and mixed in the laboratory. With the existing material in the lab, the concrete mix is designed according to BRE 'Design of normal concrete mixes' (Teychenne et al., 1975) as shown in Table 4.8. The concrete cover was set as 20mm with the resulting distance between the outer-surface of concrete and the centre of longitudinal bars as 25mm.

Table 4.7: Tensile properties of flexural bars

| Reinforcement | Cross section area per unit ($mm^2$) | Ultimate capacity (kN) | Tensile strength (MPa) | Ultimate strain (%) | Elastic modulus (GPa) |
|---|---|---|---|---|---|
| Aslan bars | 71.3 | 154.1 | 2172 | 1.75 | 125 |

Table 4.8: Concrete mix design per $m^3$

| Quantities ($m^3$) | Cement (kg) | Water (kg) | Aggregate (kg) | Sand (kg) |
|---|---|---|---|---|
| 1 | 526 | 205 | 1008 | 671 |

#### 4.3.1.2 Flexural Design

Following ACI-440.1R (2015) and CSA-S806 (2012), the flexural capacity of the beams was determined by establishing the equilibrium of the critical cross sections, determined by the four-point bending setup (Figure 4-11). By setting the safety and material factors as 1.0, the flexural capacity predictions are calculated as shown in Table 4.9. For both predictions, the flexural failure is controlled by concrete crushing.

Table 4.9: Flexural predictions

| Code and guideline | $f_f$ (MPa) | $c$ (mm) | $M_u$ (kNm) | $P_u$ (kN) |
|---|---|---|---|---|
| ACI 440.1R | 986 | 53.7 | 24.4 | 100 |
| CSA S806 | 1074 | 52.9 | 26.0 | 106 |

Where, $f_f$ is the tensile stress of longitudinal bars at ultimate capacity; $c$ is the depth of compression zone at ultimate capacity; $M_u$ is the bending strength prediction of the cross sections and $P_u$ is the prediction of ultimate capacity in total load following the test setup in Figure 4-11.

Premature debonding failure needs to be avoided by providing reinforcement bonding length beyond the support. According to ACI-440.1R (2015), the requirement of development length should be satisfied following Equation 4.1, where $l_d$ is the development length; $M_n$ is bending strength; $V_u$ is applied shear force and $l_a$ is the bonding length beyond support.

$$l_d \leq \frac{M_n}{V_u} + l_a \tag{4.1}$$

Following the flexural design, the required $l_d$ was calculated as 600mm and $\frac{M_n}{V_u}$ was calculated as 488mm. The minimum value of $l_a$ was calculated as 112mm. A 150mm bonding length beyond the centre of the supports was designed to ensure sufficient anchorage strength.

#### 4.3.1.3 Shear Design

In order to investigate the influence of W-FRP on shear behaviour of the prismatic beam specimens, the six specimens were divided into three groups (P1, P2 and P3) with different shear designs. Two P1 specimens were designed with no shear reinforcement

as the reference, expected to fail in shear. Two P2 specimens were transversely under-reinforced with W-FRP shear links, expected to fail in shear. Two P3 specimens were transversely over-reinforced with W-FRP shear links, expected to fail in flexure.

Whilst the shear links can be arranged in different patterns with the geometrical flexibility of W-FRP, the experimental research of the prismatic beams in this chapter focuses on the influence of W-FRP on shear capacity. A constant spacing of 180mm was set for all the transversely reinforced specimens, which resulted in both vertical and inclined shear links at 45° so that the diagonal links could be perpendicular to shear cracks following the 45-degree truss analogy (ACI-440.1R, 2015).

The shear reinforcement of groups P2 and P3 was made of three and eight layers of 50k carbon fibre tows (section 4.2.1) respectively. The shear designs of the three groups of specimens are shown in Figure 4-12 and Table 4.10, where all the shear links were two-legged with a closed rectangular geometry. The red dots labelled as 1, 2 and 3 are strain gauge locations (see section 4.3.2.2). The top flexural bars were removed because the FRP bars are considered as zero strength and stiffness in compression zone of concrete (ACI-440.1R, 2015; CSA-S806, 2012).

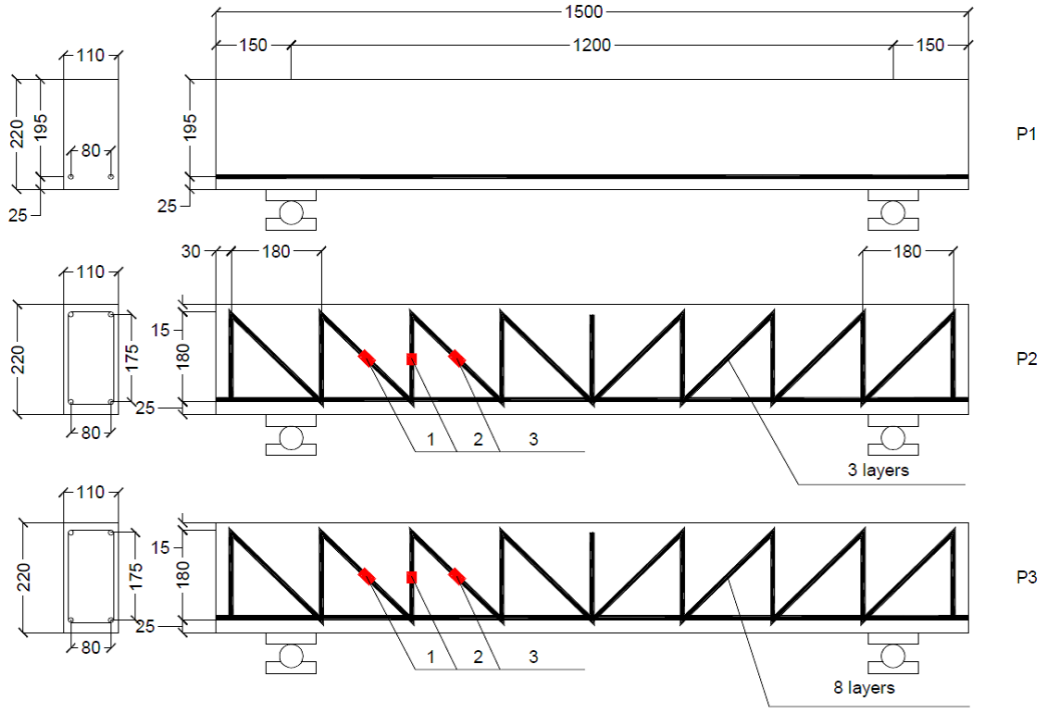


Figure 4-12: Shear design and strain gauges in group P1 to P3

Table 4.10: Shear design details of P2 and P3

| Specimen | Spacing of vertical links (mm) | Angle of diagonal links (degrees) | Cross section area of W-FRP links ($mm^2$) |
|---|---|---|---|
| P2 | 180 | 45 | 12.8 |
| P3 | 180 | 45 | 34.2 |

As proposed in Chapter 3, ACI-440.1R (2015) and CSA-S806 (2012) were adopted to predict the shear capacities of the specimens. The corner strength of W-FRP shear links in the shear design (Figure 4-12) is shown in Table 4.11. Although the W-FRP has shown higher corner strength, the strain limits from the codes and guidelines governed the design strength of W-FRP following the proposed revisions specified in section 3.2.3.3. The design strength of W-FRP shear links was limited to the tensile strength at the strain of 0.4% for ACI-440.1R (2015) design and 0.5% for the CSA-S806 (2012) design.

Table 4.11: Corner strength of W-FRP shear reinforcement

| Reinforcement | $A_f$ ($mm^2$) | $f_{fu}$ (MPa) | $f_{fb}$ (MPa) | $\epsilon_b$ (%) | $E_f$ (GPa) |
|---|---|---|---|---|---|
| W-FRP links | 12.8 | 1484 | 715 | 0.67 | 107 |
| | 34.2 | 1312 | 583 | 0.44 | 105 |

The vertical and diagonal W-FRP shear links were considered by using Equation 3.5 in ACI-440.1R (2015) and Equation 3.6 in CSA-S806 (2012) to calculate the shear contribution of shear links $V_f$, as proposed (see section 3.2.3.4).

Finally based on the shear designs (Figure 4-12), the shear capacities of the specimens were calculated following the shear design equations of ACI-440.1R (2015) and CSA-S806 (2012) by removing the material and safety factors. The codified predictions of the total applied load at shear failure based on the test setup in Figure 4-11 are shown in Table 4.12.

MCFT (Vecchio and Collins, 1986) was also adopted to predict the shear capacities. In contrast to the codified predictions, MCFT adopts the actual corner strength of W-FRP shear links (Table 4.11) as the design strength (Equation 2.29). The influence of diagonal links is considered using Equation 3.7 to calculate the shear reinforcement ratio $\rho_{fv}$. With the reinforcement ratio and strength of shear links, the shear capacities of the specimens were calculated using MCFT through the following steps:

1. Assume the shear capacity of the beams as $V_u$ and calculate the shear stress and the strain at the mid-depth of critical cross-section (Bentz et al., 2006) based on the assumed $V_u$;

2. Using equilibrium of stress and compatibility of strain of the cross-section, calculate the stress and strain;

3. Calculate the shear reinforcement response under the assumed shear capacity;

4. Compare the shear reinforcement response to the calculated corner strength following Equation 2.29;

5. Where the stress of W-FRP reinforcement is not equal to the corner strength, iterate the assumed shear capacity through steps (i)-(iv);

6. Output the shear capacity $V_u$ when the stress of W-FRP shear links matches the corner strength.

The MCFT predictions of the total applied load at shear failure based on the test setup in Figure 4-11 are shown in Table 4.12, where the predicted failure modes of the specimens are determined by comparing the shear predictions and the flexural predictions in Table 4.9.

Table 4.12: Predictions of shear failure load and expected failure mode

| Specimen | Shear predictions (kN) | | | Predicted failure mode |
|---|---|---|---|---|
| | $P_{ACI}$ | $P_{CSA}$ | $P_{MCFT}$ | |
| P1 | 20.3 | 40.6 | - | Shear failure |
| P2 | 77.8 | 78.9 | 98.2 | Shear failure |
| P3 | 173.6 | 140.1 | 211.9 | Flexure failure |

### 4.3.2 Test Program

#### 4.3.2.1 Specimen fabrication and concrete strength testing

The cages of the prismatic beams were hand-wound. As shown in Figure 4-13, for each specimen reinforced with W-FRP, four longitudinal bars were placed around four spacers to form a winding mandrel. The winding of carbon fibres was conducted as follows:

1. Tie cable ties on the longitudinal bars to mark the winding position and to stop the carbon fibres from sliding at the corners.
2. Wind the carbon fibre tows (Table 4.1) around the mandrel to fit the designs, as shown in Figure 4-12.
3. Coat each fibre link with epoxy matrix (Table 4.2).
4. Ensure that all carbon fibre tows are coated with epoxy and remove excess epoxy.
5. Cure the cage in laboratory condition for 72 hours and remove the top bars as discussed in 4.3.1.3.

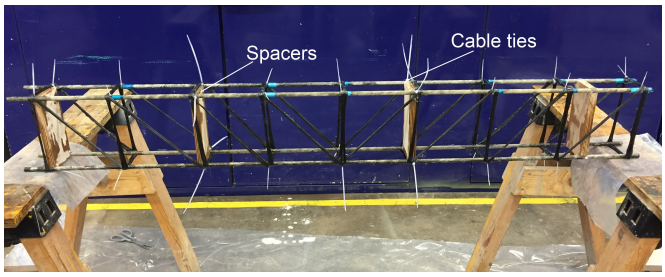


Figure 4-13: Cage fabrication

The casting was conducted in the concrete laboratory of the University of Bath, following BS-1881-125:2013 (2013) with the concrete mix design shown in Table 4.8. The specimens were tested at 28 days. Eighteen cubes and nine cylinders were cast and tested to show the concrete strength at testing day, as shown in Table 4.13. Actual material properties of concrete, flexural bars and W-FRP shear reinforcement are used in the following analysis.

Table 4.13: Concrete strength at 28 days

| | Cylinder strength (MPa) | Cube strength (MPa) |
|---|---|---|
| Average | 34.7 | 43.5 |
| SD | 3.81 | 3.63 |
| COV | 11.0% | 8.3% |

#### 4.3.2.2 Test setup and instrumentation

The specimens were tested until failure under four-point bending. The specimens were supported by two bridge bearings, which are pin supports allowing the top plate to

slide as shown in Figure 4-14. Two hand-operated hydraulic jacks were used to apply even loads at the designed loading point.

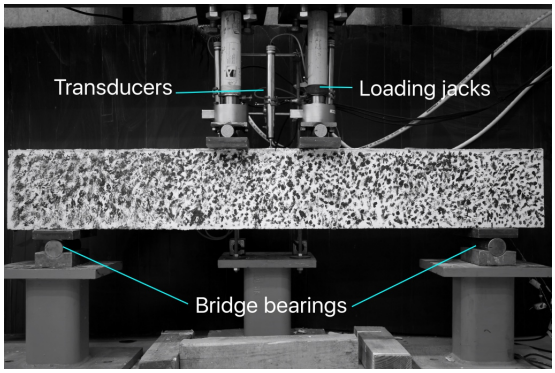


Figure 4-14: Test setup

To investigate the performance of the shear links of P2 and P3 specimens, the three shear links in the shear span were strain-gauged as shown in Figure 4-12. Displacement transducers were installed at the loading points and mid-span to measure the displacement of the beams (Figure 4-14).

A Digital Image Correlation (DIC) speckle pattern was painted on one side of all specimens, Figure 4-14. A camera was set up two metres away to record the images of the specimens as deformed. By taking photos of the specimens at each loading step, the progression of the cracks and strain development of the beams can be analysed. Similar DIC recoding was undertaken for the subsequent testing of tapered beams (Chapter 5) and T beams (Chapter 6). However, as not all the DIC patterns had the best quality, only qualitative DIC analysis was undertaken. Compared to the strain gauge and transducer data, the DIC analysis results cannot provide stronger support to understand the structural behaviour of the specimens being tested. Therefore, all the DIC analysis results are not included in this thesis.

### 4.3.3 Test Results

#### 4.3.3.1 Results Summary

All specimens failed in the expected failure modes. The test summary of failure mode, peak load and corresponding deflection at mid-span is shown in Table 4.14. The flexural failure of P3 was caused by concrete crushing at mid-span. The load-displacement curves are shown in Figure 4-15.

Table 4.14: Test summary of prismatic beam test

| Specimens | Failure mode | Peak applied load $P_u$ (kN) | Deflection at peak load (mm) |
|---|---|---|---|
| P1-1 | Shear failure | 37.8 | 3.2 |
| P1-2 | Shear failure | 39.2 | 4.5 |
| P2-1 | Shear failure | 115.1 | 12.1 |
| P2-2 | Shear failure | 123.9 | 14.3 |
| P3-1 | Flexural failure | 148.5 | 15.1 |
| P3-2 | Flexural failure | 150.0 | 16.0 |

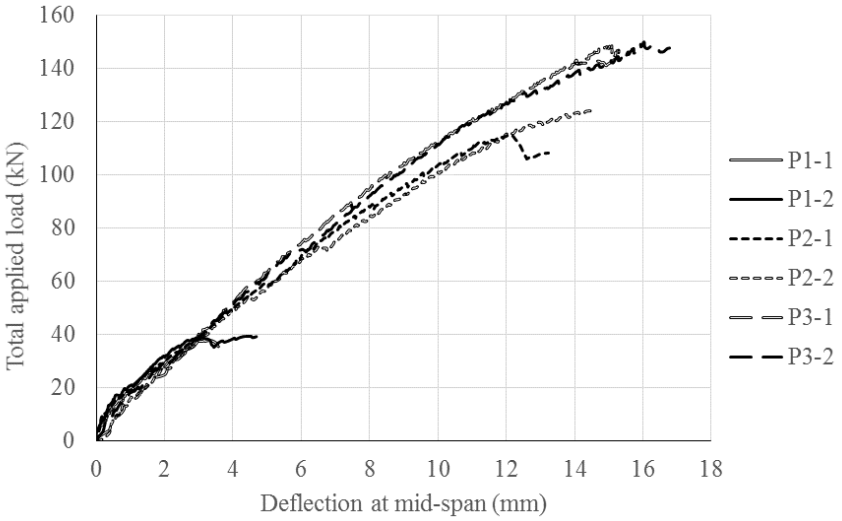


Figure 4-15: Load - deflection curves of W-FRP reinforced beams

#### 4.3.3.2 Test observations

Both specimens in group P1 failed in shear. When the applied load was close to their ultimate capacity, a major shear crack propagated near the support along the reinforcement level and then diagonally up to the loading point as shown in Figure 4-16 and Figure 4-17. Both specimens failed in shear at approximately 38kN.

Both specimens in group P2 failed in shear with rupture of shear links. The shear crack development of P2 specimens was very similar to the group P1. Due to the W-FRP shear reinforcement, the shear crack propagation started at a higher load of 70kN to 80kN and there were several shear cracks developing in the shear span of P2-1 and P2-2. The shear link rupture occurred at about 120kN and there was only one major shear crack widened in each specimen of group P2, as shown in Figure 4-18 and Figure 4-19. Then the P2 specimens failed in shear.

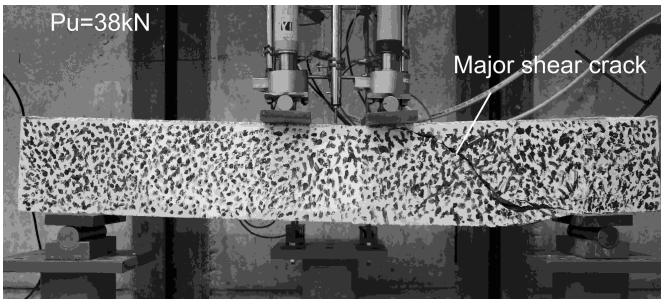


Figure 4-16: Failure of specimen P1-1

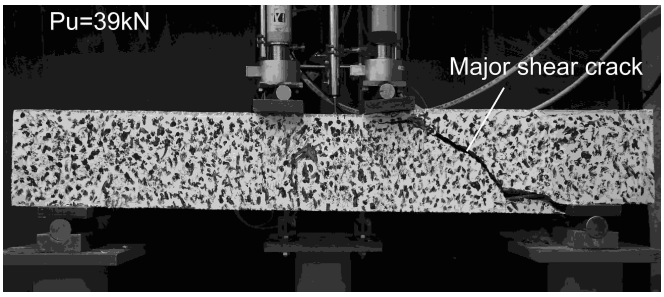


Figure 4-17: Failure of specimen P1-2

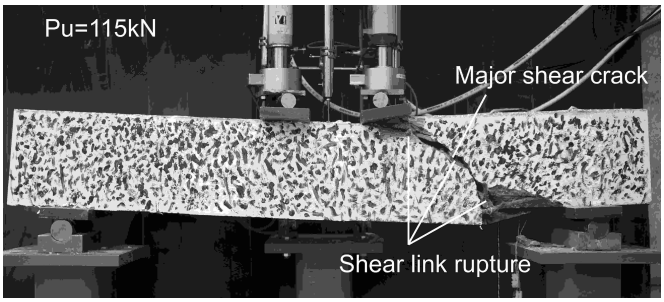


Figure 4-18: Failure of specimen P2-1

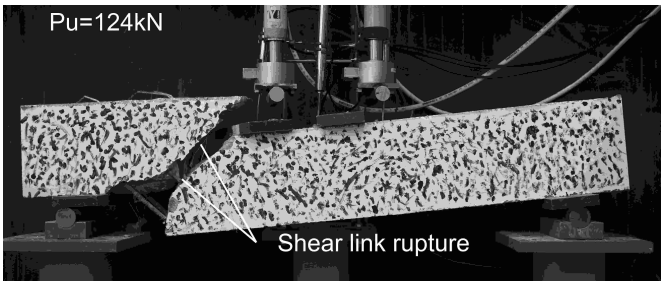


Figure 4-19: Failure of specimen P2-2

Both specimens in group P3 failed in flexure. With load increasing from zero, bending cracks developed from the mid-span to the supports. Shear cracks developed within

shear spans at about 44kN. At about 140kN, the concrete between the two hydraulic jacks of specimen P3-1 started to crush as shown in Figure 4-20. The same phenomenon was found in P3-2 with additional concrete crushing found to the left side of the load as shown in Figure 4-21. Specimen P3-1 failed at 148kN due to the concrete crushing and specimen P3-2 failed at 150kN with debonding of longitudinal bars due to the loss of concrete cover.

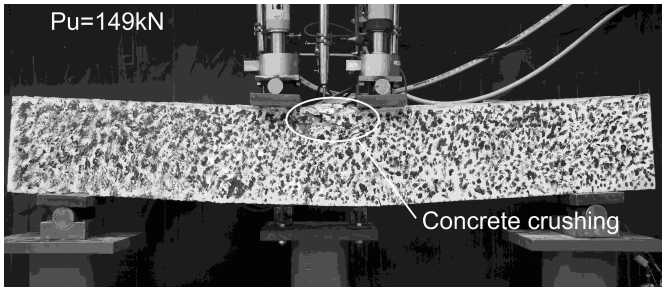


Figure 4-20: Failure of specimen P3-1

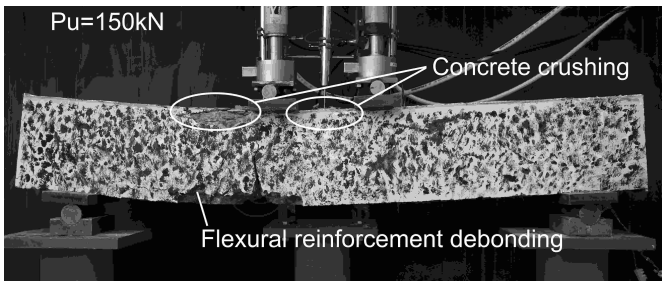


Figure 4-21: Failure of specimen P3-2

#### 4.3.3.3 Strain Gauge Data

The strains of shear links in different specimens are plotted against the total applied load in Figure 4-22, where 'D' indicates diagonal links and 'V' indicates vertical links. The strain gauges of P2-1 in link 1 and 2 (Figure 4-12) showed abnormal load-strain relations, which could be caused by the detaching of the gauges. Therefore, the strain data of P2-1 is not taken into account in the further analysis in section 4.3.4.2. Table 4.15 shows the strains of the shear links at the failure loads of the specimens, where, '-' means the loss of strain gauges.

Table 4.15: Strains of W-FRP shear links at failure load

| Specimen | Peak applied load $P_u$ (kN) | Gauge 1 ($\mu\epsilon$) | Gauge 2 ($\mu\epsilon$) | Gauge 3 ($\mu\epsilon$) |
|---|---|---|---|---|
| P2-1 | 115.1 | 151 | 1068 | - |
| P2-2 | 123.9 | 6606 | 4691 | 7221 |
| P3-1 | 148.5 | 3135 | - | 4881 |
| P3-2 | 150.0 | 4157 | 1162 | 4892 |

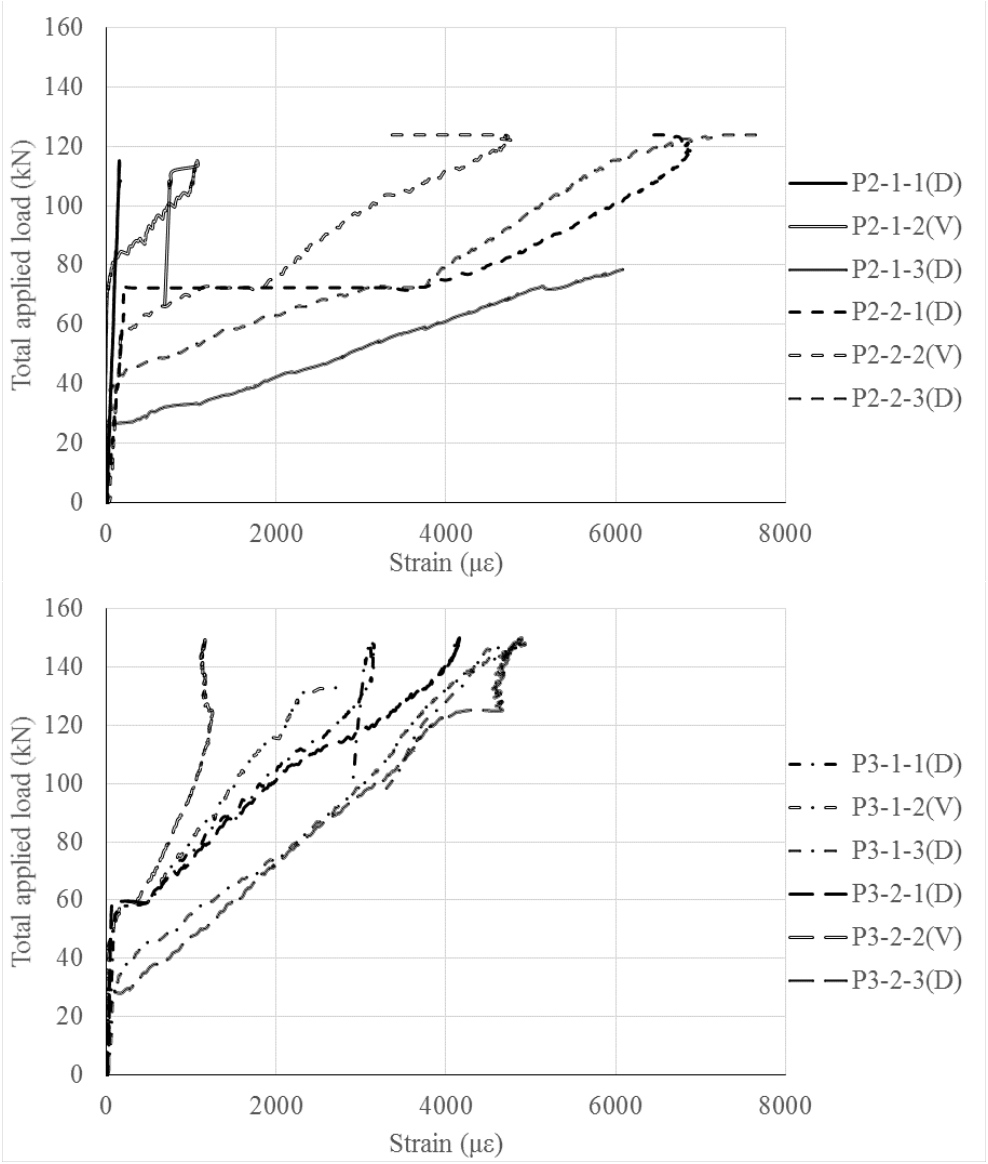


Figure 4-22: Load - strain curves of shear links in P2 and P3

### 4.3.4 Analysis and Discussion

#### 4.3.4.1 Failure mode and ultimate capacity

Two failure modes were observed from the testing as expected (Table 4.12). As the shear reinforcement ratio increased, so did the ultimate capacity of the specimens. On average, the shear capacity of group P2 was 210% higher than group P1 (Table 4.14). With shear links of larger cross-section, the shear capacity of P3 exceeded its flexural capacity and specimens of P3 failed in flexure. The ultimate capacity of P3 was 288% higher than group P1. The flexural failure of P3 specimens demonstrates that an appropriate amount of W-FRP shear reinforcement is capable of ensuring sufficient shear capacity to prevent shear failure.

Although 150mm bonding length was designed for specimen P3-2, end slip occurred in the longitudinal bars, which indicates that the anchorage of the specimens should be considered more carefully. However, this Chapter did not focus on the anchorage. Further research is conducted to investigate the influence of anchorage, which will be presented in Chapter 6.

Minor differences in stiffness were found in the three groups of specimens as shown in Figure 4-15. Before the failure of group P1, the stiffness of the specimens was consistent and the load-displacement relation was linear-elastic. The stiffness of group P2 and P3 remained the same until 60kN, at which point P2 started to reduce in stiffness compared to P3. When the deflection of groups P2 and P3 reached 14mm, the load carried by P3 was about 20kN higher than P2 (Figure 4-15).

The higher stiffness of group P3 could only be caused by the larger amount of W-FRP shear reinforcement as the major difference between P2 and P3 is the amount of shear reinforcement if the small variations in concrete strength are neglected. Compared to P2, the larger cross-section area of each shear link of P3 resulted in lower strains at the same load as shown in Figure 4-22, which indicates that the shear crack width of P3 could be controlled better. The smaller shear crack width results in lower displacement and hence higher stiffness.

In addition, the inclined shear links provide a horizontal component of tensile force that reduces the curvature caused by bending moment. At the same load, the lower strains of gauges 1 and 3 in P3 show the cross-section at the gauge locations could have lower curvature than that of P2. As the deflection of an elastic beam can be calculated as the double integration of the curvatures of the cross-section along the beam axis

(see section 3.2.2), the smaller curvature caused by the larger amount of W-FRP shear reinforcement could make a difference to stiffness.

#### 4.3.4.2 Performance of W-FRP shear links

Two types of rupture failure of W-FRP links were observed in the failed shear links: i) corner rupture (Type I) and ii) straight part rupture (Type II). The Type I rupture occurred at the joint of shear links and the longitudinal bars. When the joint was located at the shear cracks, the diagonal link and vertical link both ruptured at the corners. The diagonal links which crossed the diagonal part of the shear cracks had Type II rupture and, normally, the rupture occurred at the intersection of the shear link and shear crack.

Failing in Type I rupture, the diagonal link P2-2-1 (Figure 4-12) had a maximum strain of 0.66%, which correlates well with the corner strain, calculated using Equation 2.29 (Spadea et al., 2017a). However, the strain of vertical link P2-2-2 only reached 0.47%, which is 30% lower than the strain of P2-2-1. The failure of P2-2-2 could be caused by the failure of the reinforcement joint, initiated by the rupture of P2-2-1.

As shown in Figure 4-19, the diagonal link P2-2-3 (Figure 4-12) had the Type II rupture. However, the strain of P2-2-3 at failure only reached 0.72% (Figure 4-22) which is much lower than the ultimate tensile strain of W-FRP at straight portions of 1.34% (Table 4.4). This indicates that the rupture of W-FRP shear links at the straight portions could be caused by other reasons than just uniaxial tension. The relative displacement of the two parts of P2 specimens divided by the major shear crack (Figure 4-18 and Figure 4-19) creates deformation of W-FRP shear links in the transverse direction. As the strength of FRP reinforcement in the transverse direction is much lower than the axial direction, the relatively low strain of P2-2-3 at failure could be caused by this relative displacement and the resulting failure strength of the W-FRP at the straight portion is similar to the corner strength of the first type of rupture.

The diagonal links normally encountered higher strain than the vertical links as shown in Figure 4-22, which could be caused by the shear reinforcement pattern of diagonal and vertical links. The elongation of the diagonal shear links caused by the direct opening of the shear cracks could be smaller than the vertical links as the diagonal links had the larger relative angle to the shear cracks. However, following the assumption that plane cross section remains plane after carrying load, the bending moment can result in additional tensile strain in the diagonal links but not in the vertical links.

Influenced by both flexure and shear, the diagonal links can thereby have larger strains than the vertical links. Given that the bending moment is smaller at the sections closer to the support, the strain difference between vertical links and diagonal links that are closer to the support is also smaller, as shown by the load-strain curves in Figure 4-22.

The corner strength of W-FRP shear links was not fully utilised, shown by the relatively low strains of the vertical links failed in Type I rupture type and the diagonal links failing in Type II rupture. The higher strains of diagonal links show that the diagonal links worked more efficiently to resist flexure and shear, which indicates that the ways of arranging W-FRP shear links could result in different performances of the beam specimens. More shear reinforcement patterns need to be explored to investigate this influence. It may be possible to increase the efficiency of shear links by exploring the optimum pattern of W-FRP shear reinforcement.

#### 4.3.4.3 Vertical resistance of W-FRP links

In order to understand the shear contribution provided by W-FRP shear links, the tensile force carried by the gauged shear links is calculated, using the tensile properties of the W-FRP shear links at the straight portions (Table 4.4) and the strain data, as shown in Table 4.16. Based on the angle of diagonal links, the shear contribution of each link is calculated as the vertical component of the link force. The ratio of the shear contribution between diagonal links (1 and 3) and vertical link (2) are calculated. The shear contribution of vertical link (2) is taken as 1.00.

Table 4.16: Tensile force carried by W-FRP shear links

| Shear link | Applied shear force (kN) | Tensile force in shear links (kN) | Vertical component of link force (kN) | Ratio |
|---|---|---|---|---|
| P2-2 shear link 1 | 61.9 | 17.8 | 12.6 | 1.00 |
| P2-2 shear link 2 | 61.9 | 12.6 | 12.6 | 1.00 |
| P2-2 shear link 3 | 61.9 | 19.5 | 13.7 | 1.08 |
| P3-1 shear link 1 | 67.6 | 22.3 | 15.7 | 0.65 |
| P3-1 shear link 2 | 67.6 | 24.1 | 24.1 | 1.00 |
| P3-1 shear link 3 | 67.6 | 29.5 | 20.9 | 0.87 |
| P3-2 shear link 1 | 75.0 | 29.9 | 21.1 | 2.51 |
| P3-2 shear link 2 | 75.0 | 8.4 | 8.4 | 1.00 |
| P3-2 shear link 3 | 75.0 | 35.2 | 24.9 | 2.96 |

As shown in Table 4.16, there are large variations (from 8.4kN to 24.9kN) in the vertical

component of link force. These variations could be caused by the random propagation of shear cracks. However, the respective average shear contribution of link 1, 2 and 3 in P3-1 and P3-2 is 18.4kN, 16.3kN and 22.9kN. The average ratio is 1.13:1.00:1.40, which is closer to 1.00:1.00:1.08 than the ratios in two individual specimens in group P3. It shows the diagonal links exhibited slightly higher contributions to shear and again confirms the higher efficiency of diagonal links in shear carrying, compared to the vertical links. The links which crossed the cross sections under larger bending moment may have larger shear contribution due to the larger horizontal component, as discussed in section 4.3.4.2.

In addition to the performance of particular shear links, the total shear contribution of the W-FRP is analysed. The total shear contributions provided by shear links ($V_f$) in P2-2 and P3 specimens are calculated as the summation of the shear contribution of each link, as shown in Table 4.16. The ratio of $V_f$ to the applied shear force $V_a$ (taken as half of the total applied load) in the shear span is plotted against $V_a$ as shown in Figure 4-23. Given that data noise can create considerable variations in the value of $V_f/V_a$ at the beginning of the testing, the curves are plotted from 5kN.

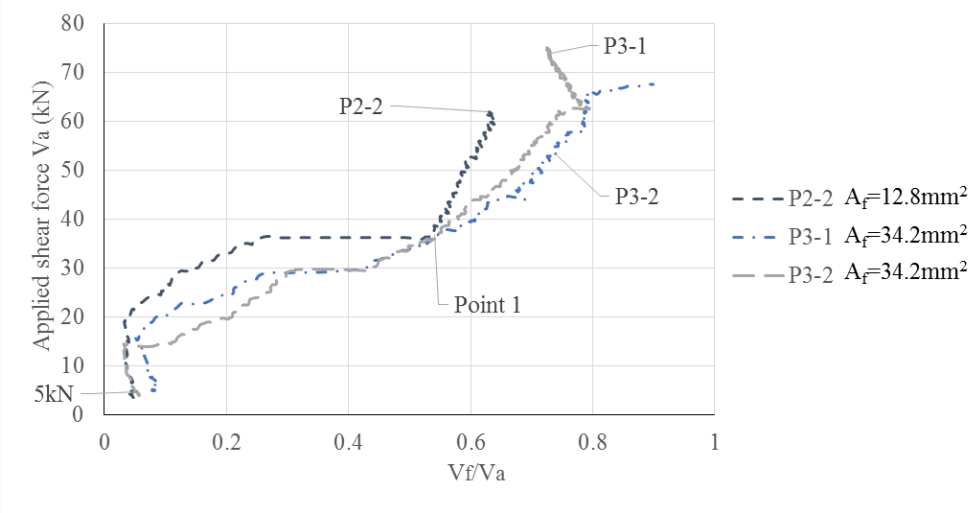


Figure 4-23: Shear resistance of W-FRP shear links

As shown in Figure 4-23, the amount of W-FRP reinforcement influences the ratio of $V_f/V_a$. Except for Point 1 at approximately 37kN of applied shear force, the shear contribution of W-FRP links in P3 specimens was higher than P2. The maximum value of $V_f$ in P3-1 and P3-2 reached 61kN and 54kN respectively, accounting for 90% and 72% of the applied shear force respectively. However, $V_f$ of specimen P2-2 only reached 39kN, which accounts for only 62% of the applied shear force. Therefore, increasing

the cross section area of W-FRP shear links results in higher shear contribution from shear reinforcement, accounting for higher percentage in total shear resistance.

#### 4.3.4.4 Prediction examination

The predictions of shear capacity (Table 4.12) are compared with the test results in Table 4.17, in which, $P_{exe.}$ is the average ultimate capacity of two specimens in the same group; $P_{ACI}$ is the ultimate capacity predicted by ACI-440.1R (2015); $P_{CSA}$ is the CSA-S806 (2012) prediction and $P_{MCFT}$ is the prediction of the MCFT (Vecchio and Collins, 1986).

For specimen P1, ACI-440.1R (2015) exhibits a conservative prediction when only the shear contribution of concrete is considered. CSA-S806 (2012) prediction is closest to the test results but it overestimated the concrete contribution. The MCFT is not able to predict the shear performance of beams without shear links.

Table 4.17: Prediction calibration

| Specimens | $P_{ACI}$ | $P_{exe.}/P_{ACI}$ | $P_{CSA}$ | $P_{exe.}/P_{CSA}$ | $P_{MCFT}$ | $P_{exe.}/P_{MCFT}$ |
|---|---|---|---|---|---|---|
| P1 | 20.3 | 1.89 | 40.6 | 0.94 | - | - |
| P2 | 77.8 | 1.53 | 78.9 | 1.51 | 98.2 | 1.21 |
| P3 | 173.6 | 0.86 | 140.1 | 1.06 | 211.9 | 0.71 |
| Average | - | 1.43 | - | 1.18 | - | 0.96 |

For the under-reinforced specimens P2, the MCFT exhibits the best predictions among all three methods, with the test results 21% higher than the prediction. Both ACI-440.1R (2015) and CSA-S806 (2012) are very conservative with average ultimate capacity of P2 53% and 51% higher than the ACI-440.1R (2015) and CSA-S806 (2012) predictions, respectively.

Since specimens P3 failed in flexure, their shear capacity predictions cannot be examined. When comparing the test results with the flexural predictions, all the predictions are similar, approximately 50% lower than the test results. Firstly, the material properties of longitudinal bars given by the manufacturer are conservative. The W-FRP shear links at the mid-span in P3 specimens (Figure 4-12) may provide confinement to the concrete in the compression zone, resulting in higher actual concrete strength than the test results acquired from the cube and cylinder testing (Table 4.13). The diagonal shear links at the mid-span could also contribute to higher flexural capacity by providing a horizontal tensile force. All the three factors resulted in the underestimation of the

flexural capacity.

The conservatism of the codified predictions of the shear capacity in specimen P2 could be caused by the underestimated strength of shear links since the design strength of shear links is governed by the specified strain limits (0.4% for ACI-440.1R (2015) and 0.5% for CSA-S806 (2012)). The actual corner strength of W-FRP shear links adopted in the MCFT model is larger than the values specified in the codes or guidelines and closer to the actual failure strain of the shear links in Table 4.13. Therefore, the MCFT exhibits the better predictions of shear failure in group P2.

While the conservative codified predictions are useful for structural safety, it is more favourable to have accurate predictions when the design aim is to minimise concrete and shear reinforcement use. For W-FRP reinforced beams with non-prismatic geometries, the shear contribution of W-FRP could not be the only factor influencing the shear performance. Further research is required to examine the proposed revisions of the design methods as discussed in the Chapter 3.

## 4.4 Conclusions

This chapter has presented the experimental research on W-FRP shear reinforcement. Tensile test of W-FRP straight strips and push off tests of the W-FRP shear links were conducted to explore the material properties and bent strength at the corners. Six prismatic concrete beams reinforced with different amounts of W-FRP shear reinforcement were tested to investigate the efficiency of W-FRP and the validity of the design methods. The experiments and analysis in this section support the following conclusions:

- The straight portion of the W-FRP shear links exhibited high tensile strength of 1915MPa and an elastic modulus of 143GPa. The corner is the governing factor determining the design strength of W-FRP links, shown by the lower corner strength from the push-off tests. Test data of W-FRP shear links (Spadea et al., 2017a) are adopted to instruct shear design of W-FRP reinforced concrete beams.
- All the beam specimens failed in the expected failure mode. The flexural failure of P3 has shown that W-FRP shear reinforcement is feasible for concrete structures and it is capable of ensuring sufficient shear capacity to prevent shear failure.
- W-FRP shear reinforcement rupture at the corners and straight portions was found in the prismatic beam tests. Both types of rupture have shown that the tensile strength of W-FRP straight portions cannot be fully utilised.

- The diagonal links exhibited higher strains than the vertical links, which could be due to the diagonal links being influenced by both flexure and shear whilst the vertical links only carried shear force. On average, the shear contributions of diagonal shear links were slightly higher than the vertical links. The higher efficiency of diagonal links in both flexure and shear indicates that there is a possibility of improving the shear performance of the beams by varying the patterns of W-FRP.
- MCFT shows conservative and more accurate predictions for P2 specimens, which were transversely under-reinforced, compared with ACI-440.1R (2015) and CSA-S806 (2012) method. The conservatism of the codified predictions is caused by the conservative strain limits used for specifying the design strength of W-FRP shear reinforcement.

Following material characterisation tests and prismatic beam tests, the next chapter presents variable depth beam tests to investigate the influence of non-prismatic geometry and W-FRP reinforcement on shear behaviour.

# Chapter 5

# Shear behaviour of variable-depth concrete beams reinforced with W-FRP

## 5.1 Introduction

This chapter presents the investigations into tapered concrete beams reinforced with W-FRP shear reinforcement. Eight tapered beams were designed and tested in five groups with variable-depth geometry, four shear reinforcement ratios, and six W-FRP shear reinforcement arrangements capitalising on the flexibility of carbon fibres. The various contributing factors to shear performance are examined and analysed. The predictions based on the proposed revisions to design methods based on codified equations (ACI-440.1R, 2015; CSA-S806, 2012) and the MCFT model (Vecchio and Collins, 1988) are examined against the test results.

## 5.2 Test design and manufacture of specimens

In this section, the design philosophy is presented, along with the manufacturing method for the specimens.

### 5.2.1 Geometry and test setup

To compare the shear behaviour of variable-depth beams to the prismatic beams in Chapter 4, the specimens were designed with the same mid-span depth (220mm), width (110mm), length (1500mm) and clear span (1200mm). The effective depths along the beam axis of all the variable-depth specimens were optimised based on the prismatic beam geometry. Theoretically, the optimised geometry of the specimens should provide the required flexural and shear capacity to resist the envelope of applied loads everywhere following the design procedures in Chapter 3.

The profile of the curved longitudinal bars was simplified as a parabola. At the two ends of the beams, the distance of the centre of longitudinal bars to the top surface of the beams was set as 50mm for ease of fabrication. With specified effective depth at mid-span and the ends, the effective depths along the beam axis were simulated with Equation 5.1 in which $d$ is that of the beam (mm); 195 is the effective depth of mid-span (mm) and $x$ is the distance from the mid-span (mm).

$$d = 195 - 2.71 \times 10^{-4} x^2 (mm) \tag{5.1}$$

With the calculated effective depth along the horizontal axis and the same 20mm concrete cover of the prismatic beams (Chapter 4), the geometry of the tapered beams is shown in Figure 5-1. Since in the tests of the prismatic beams (Chapter 4), the symmetrical four-point bending setup could not control the failure locations, the specimens were arranged to be tested under three-point bending to failure. The test setup in Figure 5-1 does ensure that the specimens fail at the side with the loading jack.

The cross-sections within the shear span (Figure 5-1) had variable effective depth. The loading jack was placed at 400mm away from the adjacent support to set the ratio of shear span ($a_v$) to effective depth ($d$) as 2.5, in line with the prismatic beam tests (Chapter 4), as the average effective depth of the cross sections in the shear span of the variable-depth specimens was 160mm.

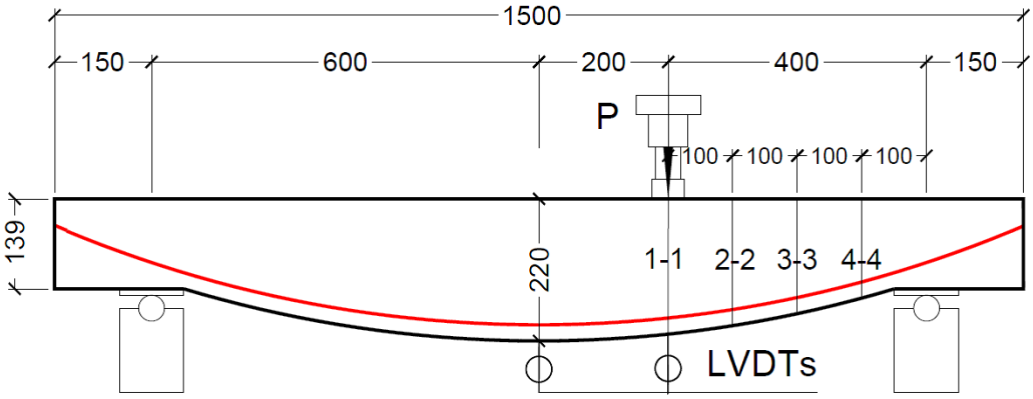


Figure 5-1: Geometry of the specimen and test setup

### 5.2.2 Concrete and reinforcement

All of the non-prismatic specimens were designed with the same reinforcement used in the prismatic beam tests (Chapter 4) including the longitudinal bars (⌀10mm, Aslan 200 series) and W-FRP shear reinforcement. The concrete strength was set as C35/45. The tensile properties of the longitudinal bars and corner strength of the W-FPR shear links were updated based on the work of Spadea et al. (2017a) as shown in Table 5.1.

Table 5.1: Material properties of flexural and shear reinforcement

| Reinforcement | $A_f$ (mm$^2$) | $f_{fu}$ (MPa) | $f_{fb}$ (MPa) | $\epsilon_b$ (%) | $E_f$ (GPa) |
|---|---|---|---|---|---|
| W-FRP shear links | 4.3 | 1537 | 957 | 0.88 | 109 |
| | 8.6 | 1503 | 745 | 0.68 | 108 |
| | 21.4 | 1426 | 654 | 0.62 | 106 |
| Longitudinal bars ⌀10mm | 71.3 | 2648 | - | 1.85 | 143 |

Where $A_f$ is the cross-section area of the reinforcement per unit; $f_{fu}$ is the tensile strength of the reinforcement; $f_{fb}$ is the corner strength of W-FRP shear reinforcement; $\epsilon_b$ is the strain at the corner strength and $E_f$ is the elastic modulus of the reinforcement.

### 5.2.3 Flexural design

The variable-depth geometry of the specimens (Figure 5-1) resulted in a variation in bending strength along the horizontal axis. The bending failure of the specimens could only occur at the loading point in the shear span due to the unsymmetrical test setup. Therefore, the shear span was evenly divided into four segments and the predictions of bending strength of the resulting four cross sections were calculated following ACI-440.1R (2015) and CSA-S806 (2012) as shown in Table 5.2. For each cross-section, the bending strength, $M_u$ decreased with their reduced effective depth.

Table 5.2: Bending strength along shear span

| Cross section | Distance from the support (mm) | $d$ (mm) | $M_{u,ACI}$ (kNm) | $P_{u,ACI}$ (kN) | $M_{u,CSA}$ (kNm) | $P_{u,CSA}$ (kN) |
|---|---|---|---|---|---|---|
| 1 | 400 | 184 | 23.3 | 87 | 24.8 | 93 |
| 2 | 300 | 170 | 19.5 | 98 | 20.8 | 104 |
| 3 | 200 | 151 | 16.1 | 120 | 17.1 | 128 |
| 4 | 100 | 127 | 12.1 | 181 | 12.8 | 192 |

In which, $d$ is the effective depth of the cross sections; $M_u$ is the bending strength of the cross sections and $P_u$ is the total applied load when the resulting bending moment on the cross sections is equal to $M_u$ based on the test setup (Figure 5-1).

### 5.2.4 Shear design

The work in Chapter 4 has confirmed that the diagonal shear links could have larger contribution to shear, as discussed in section 3.2.3.4. By optimising W-FRP patterns, less reinforcement use could be achieved to have the same shear capacity of W-FRP reinforced beam. In order to investigate the influence of W-FRP shear reinforcement ratio and pattern on the shear performance of variable depth beams, four different shear reinforcement ratios and six shear reinforcement patterns were designed. The specimens were divided into 5 groups (TP1 to TP5) according to the different shear reinforcement ratios and patterns as shown in Figure 5-2.

Specimen TP1 and TP4 were designed as the reference specimens. The former was designed with no shear reinforcement for shear failure and the latter for flexure failure with an over-reinforced shear reinforcement ratio of 0.75% which was calculated following

Equation 3.7 in Chapter 3. The shear links of TP4 had a cross-section of 25.6mm$^2$ composed of six layers of impregnated 50K carbon fibres (C T50-4.0/240-E100) with 150mm spacing of the vertical links following the similar patterns used for the prismatic beams in Chapter 4 so that the design shear capacity (see Table 5.3) is higher than the design flexural capacity (see Table 5.2).

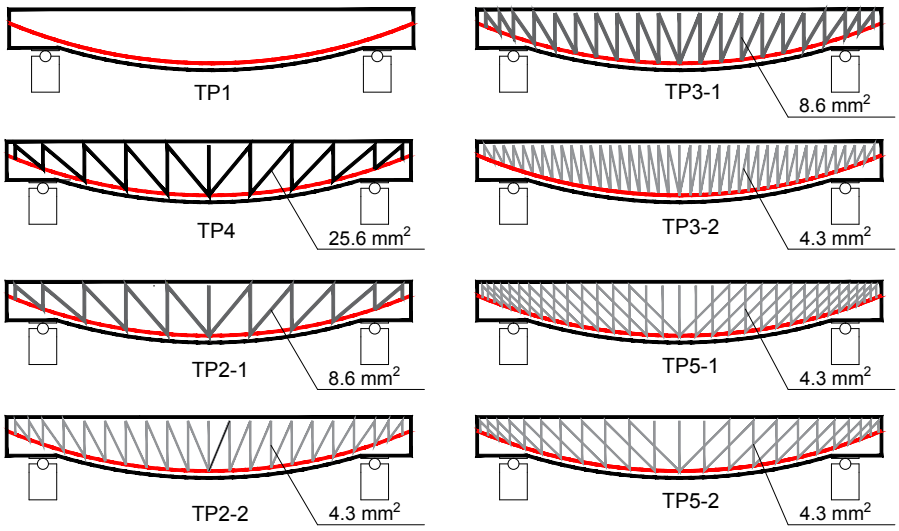


Figure 5-2: Shear reinforcement patterns

Having the same shear reinforcement pattern as TP4, TP2-1 was designed with shear links with a smaller cross-section area of 8.6mm$^2$, which was composed of two layers of 50K carbon fibres. The resulting shear reinforcement ratio was 0.25%. In order to investigate the influence of the shear reinforcement pattern, the shear links of TP2-2 were arranged to have a 75mm spacing of vertical links and a cross-section area of 4.3mm$^2$ (one layer of 50k carbon fibre tow), the resulting shear reinforcement ratio of which maintained 0.25%.

In order to investigate the influence of the shear reinforcement ratio, TP3-1 and TP3-2 were designed with a higher shear reinforcement ratio of 0.50%. TP3-1 was designed with the same shear reinforcement pattern as TP2-2 but the cross-section area of shear links was 8.6mm$^2$ (two layers of 50k carbon fibre tows). The shear reinforcement pattern of TP3-2 was optimised to have 35mm spacing between the vertical links and a cross-section area of 4.3mm$^2$ to investigate the influence of the patterns of W-FRP

shear reinforcement.

Group TP5 was designed to investigate the different methods of arranging the shear reinforcement patterns. Instead of the same spacing between the vertical links, diagonal links was designed to have a cross-section area of 4.3mm$^2$ with a constant 45° angle. The resulting spacing between vertical links became variable. By adjusting the spacing of the vertical links at the mid-span (see Figure 5-2), the shear reinforcement ratios of TP5-1 and TP5-2 were designed as 0.50% and 0.30%.

As presented in Chapter 3, the two codified methods (ACI-440.1R, 2015; CSA-S806, 2012) and the MCFT model (Vecchio and Collins, 1988) are revised in this thesis to address the variable-depth geometry and the design strength of W-FRP reinforcement. The proposed revisions in Chapter 3 are formulated based on the analysis of tests in both Chapter 5 and Chapter 6. Following the calculation procedures (Chapter 3), the shear strengths of cross sections in the shear span were calculated with 'Matlab' codes in the Appendix. Finally, the shear predictions of the revised codified methods and revised MCFT model (total applied load) following the designed test setup (Figure 5-1) were obtained, as shown in Table 5.3 in which $P_{v,ACI}$ are the total applied load predictions of the revised ACI440.1 ($v$ stands for shear capacity); $P_{v,CSA}$ are the total applied load predictions of the revised CSA S806 and $P_{v,MCFT}$ is the total applied load of the revised MCFT model. The design strains of W-FRP shear links were limited to 0.4% in the ACI-440.1R (2015) predictions and 0.5% in the CSA-S806 (2012) prediction but in the MCFT predictions, actual corner strength (Table 5.1) was adopted.

Table 5.3: Shear predictions

| Specimen | Shear reinforcement ratio $\rho_{vf}$ (%) | $P_{v,ACI}$ (kN) | $P_{v,CSA}$ (kN) | $P_{v,MCFT}$ (kN) |
|---|---|---|---|---|
| TP1 | 0 | 20.1 | 34.6 | - |
| TP2-1 | 0.25 | 50.4 | 84.8 | 40.9 |
| TP2-2 | 0.25 | 50.4 | 84.8 | 65.2 |
| TP3-1 | 0.50 | 80.2 | 123.7 | 93.7 |
| TP3-2 | 0.50 | 80.2 | 123.7 | 137.1 |
| TP4 | 0.75 | 110.4 | 156.3 | 126.4 |
| TP5-1 | 0.50 | 74.1 | 116.5 | 124.0 |
| TP5-2 | 0.30 | 56.6 | 93.2 | 80.7 |

## 5.3 Specimen fabrication

The specimens were fabricated in the Structural Laboratory of the Department Architecture and Civil Engineering, University of Bath. In this section, the cage fabrication, preparation of mould and concrete casting are presented.

### 5.3.1 Cage fabrication

In order to create the variable-depth geometry, the longitudinal bars need to be elastically curved following the designed profile. Due to their limited length, the longitudinal bars cannot maintain the curved geometry without additional supports. Accordingly, a tendon made of the same carbon fibres used for W-FRP shear links was installed at the two ends of the bars to ensure the curved profile (Figure 5-3). The two ends were notched to provide an anchorage zone for the tendon. Steel bolts were fixed on the end of the tendon to prevent it from sliding. By adjusting the length of the tendon, the longitudinal bars were curved and able to maintain the designed profile as shown in Figure 5-4.

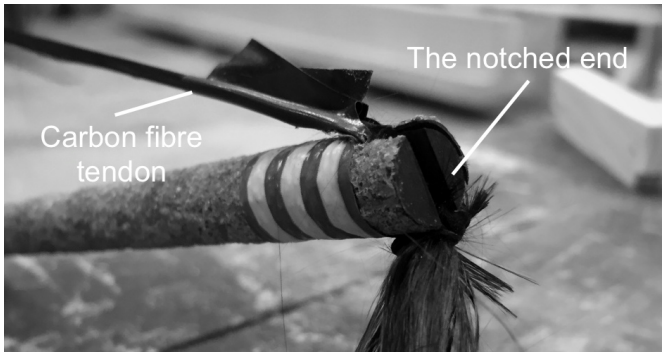


Figure 5-3: Notched end of longitudinal bars and carbon fibre tendon

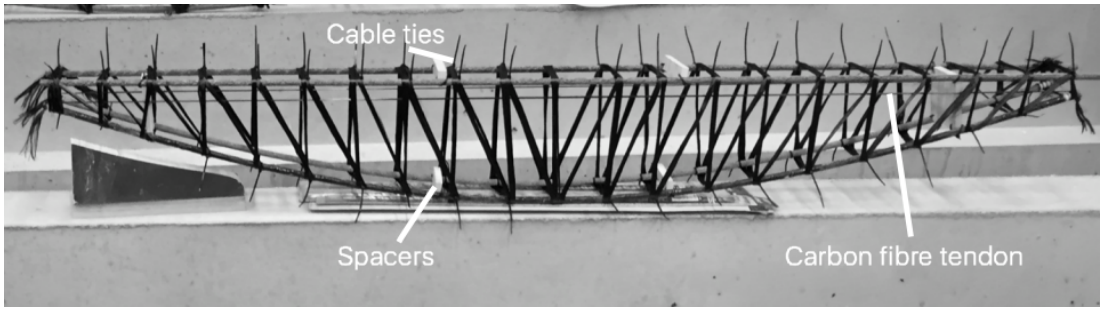


Figure 5-4: Wound carbon fibre tows on longitudinal bars

As shown in Figure 5-4, cable ties were used to mark the winding positions of the shear links and to prevent the wet carbon fibre tows from sliding. Timber spacers were used to assemble the longitudinal bars. After assembling the longitudinal bars and marking winding positions, the 50K carbon fibre tows were wound around the longitudinal bars. The carbon fibre tows were impregnated with the Tyfo S two component epoxy as shown in Figure 5-5. The wet carbon fibre tows were compressed by hand to ensure all the carbon fibres coated with epoxy and to remove any redundant resin. After being cured for 72 hours, the cages were ready for casting. In line with the prismatic beams (Chapter 4), the top bars were removed before casting because FRP bars are considered as having zero stiffness and strength under compression in the design codes (ACI-440.1R, 2015; CSA-S806, 2012).

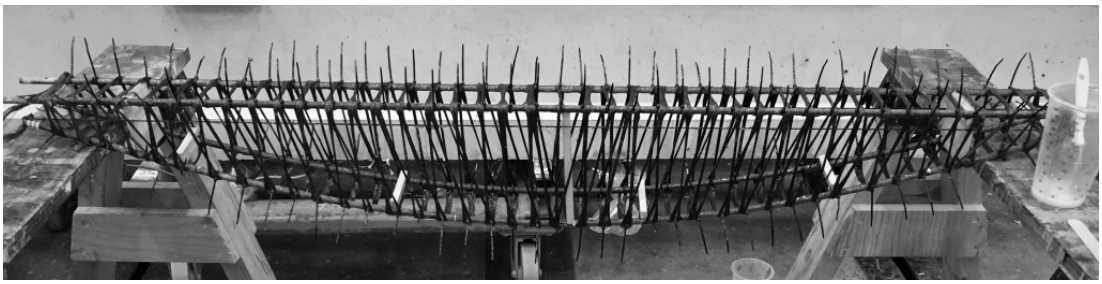

Figure 5-5: Impregnated cage

### 5.3.2 Mould preparation

The same standard steel moulds (3000mm x220mm x110mm) used to cast the prismatic beams were used for the non-prismatic specimens. In order to create the tapered geometry, two foam wedges were fabricated following the designed bottom profile of the specimens. The top surface of the wedges was covered with duct tape to create a smooth surface and then placed in the moulds. The prepared cages were placed in the moulds for casting.

### 5.3.3 Casting

C35/45 ready-mix concrete from Wright Minimix Ltd and Bristol and Bath Concrete Ltd was ordered for the casting. The actual materials in the mix from the batch data report include: (i) 929kg 20mm aggregate; (ii) 595kg dust; (iii) 552kg sand; (iv) 608kg 10mm aggregate; (v) 314.4kg OPC cement; (vi) 314kg GGBS cement and (vii) 263.8kg water.

Fourteen concrete cubes were cast following BS-EN-12390-1 (2012) and were tested at 28 days to determine the concrete strength. The recorded cube strengths are shown in Table 5.4 in which $f_{cu}$ is the cube strength and $f_c$ is the cylinder strength calculated as 80% of the cube strength. In the following analysis, the calculated cylinder strength is adopted as the concrete strength.

Table 5.4: Concrete strength

| | $f_{cu}$ (MPa) | $f_c$ (MPa) |
|---|---|---|
| Average | 35.6 | 28.5 |
| SD | 2.4 | - |
| CV | 6.8% | - |

## 5.4 Test program

### 5.4.1 Test setup

All specimens were set up following the design in section 5.2. As shown in Figure 5-6, all specimens were tested under three-point bending with a clear span of 1200mm and a shear span of 400mm. All specimens were supported with the same bridge bearings used for the prismatic beam tests, which were composed of pin supports and top support plates that were allowed to slide. All the specimens were loaded with 5kN increment before 60kN and a 2kN increment was adopted afterwards until failure so as to obtain clear observations of the failure modes.

### 5.4.2 Instrumentation

As shown in Figure 5-6, a 200kN loading cell was installed below the loading jack. Transducers were placed at the mid-span and the loading point (behind the loading jack) of the specimens to record displacement. A strain gauge was placed on one longitudinal bar at the loading point on each specimen. A concrete gauge was placed on the side surface of the specimens (10mm away from the top surface) next to the edge of the loading plate in the shear span. One of the two legs of the shear links within shear span was gauged to record the performance of W-FRP shear reinforcement. The strain gauge positions of the shear links are shown in Figure 5-7.

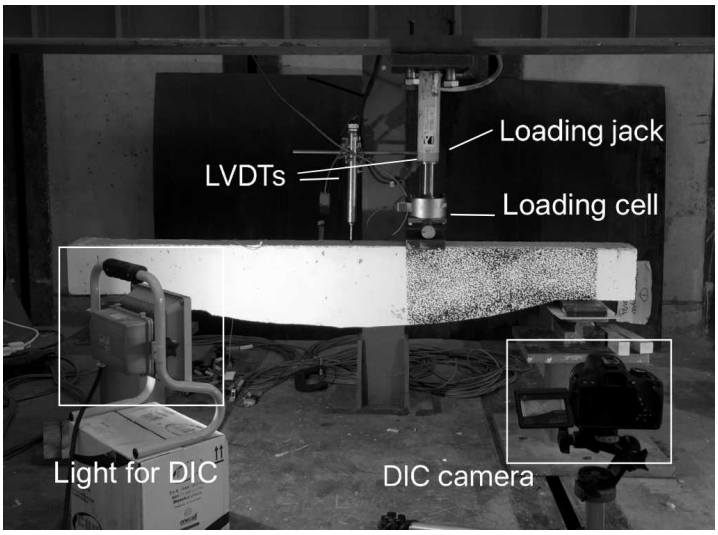


Figure 5-6: Test setup

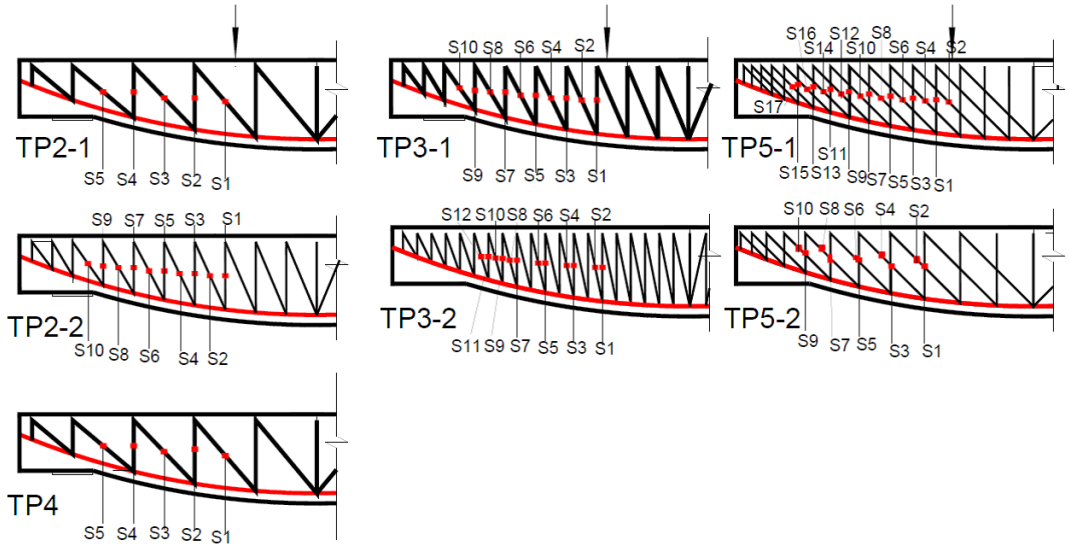


Figure 5-7: Shear links gauge convention

## 5.5 Test results

### 5.5.1 Test results summary

#### 5.5.1.1 Failure mode

Three failure modes were observed: (i) diagonal tension shear failure (DT); (ii) shear compression failure (SC) and (iii) flexural end slip failure (ES). Diagonal tension failure

(DT) was observed in specimens TP1 and TP2-1, which was initiated by the major shear crack penetrating the web. Shear compression failure (SC) was observed in specimens TP2-2, TP3-1, TP3-2, TP5-1 and TP5-2, which occurred with concrete crushing and the rupture of shear reinforcement. End slip failure (ES) was observed in TP4, which was initiated by concrete crushing and pull-out of the longitudinal bars. The test results are summarised in Table 5.5. TP5-2A was tested up to 94.9kN with a displacement of 11.6mm and the hydraulic jack reached its maximum capacity. The same specimen was reloaded and tested to failure as TP5-2B.

Table 5.5: Test results summary

| Specimen | Shear reinforcement ratio $\rho_{fv}$ (%) | Failure Mode | Ultimate capacity $P_u$ (kN) | $P_u$ compared with reference TP1 | Displacement at loading point $d_v$ (mm) |
|---|---|---|---|---|---|
| TP1 | - | DT | 31.6 | - | - |
| TP2-1 | 0.25 | DT | 61.9 | 196% | 8.3 |
| TP2-2 | 0.25 | SC | 92.6 | 293% | 14.8 |
| TP3-1 | 0.50 | SC | 94.9 | 300% | 14.1 |
| TP3-2 | 0.50 | SC | 110.8 | 350% | 18.7 |
| TP4 | 0.75 | ES | 100.3 | 317% | 13.2 |
| TP5-1 | 0.50 | SC | 94.0 | 297% | 12.8 |
| TP5-2A | 0.30 | - | 94.9 | 300% | 11.6 |
| TP5-2B | 0.30 | SC | 89.0 | 281% | 10.3 |

#### 5.5.1.2 Load-displacement curve

The load-displacement curves of the specimens at the loading point are shown in Figure 5-8 but TP1 is not shown due to the failure of the transducer. All the specimens had similar stiffness after flexural cracks initiated at about 5kN. Varying amounts of concrete crushing were observed at different loads in the specimens except for TP1 and TP2-1. Following the onset concrete crushing, the specimens exhibited decreasing stiffness. Specimen TP3-2 exhibited continuously increasing capacity (10%) and deformability (15%) compared to the point of concrete crushing, whereas TP2-2 and TP5-1 exhibited 9.5% higher deformability after concrete crushing, whilst maintaining their capacities.

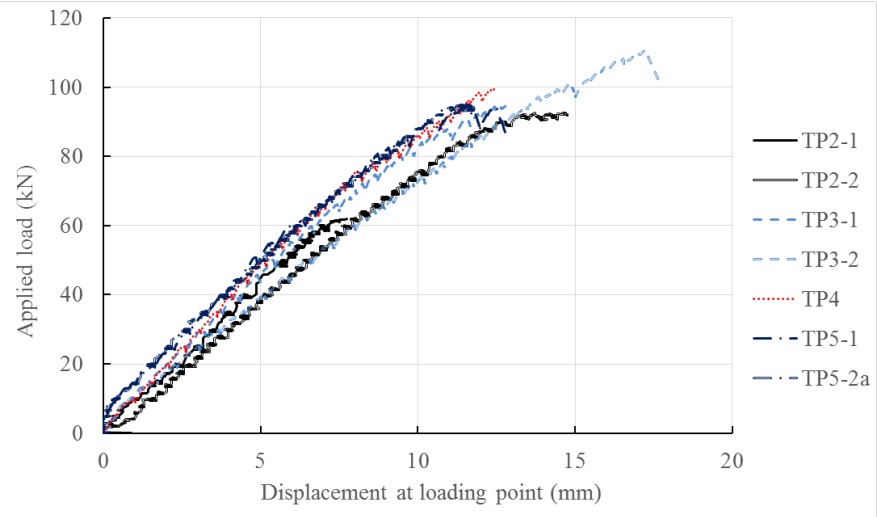


Figure 5-8: Load - displacement curves

#### 5.5.1.3 Strain data

Except for TP1, TP2-1 and TP2-2, the strain gauges on the longitudinal bars stopped giving valid data before the specimens failed. The highest recorded strains and their corresponding loads are shown in Table 5.6 with the load-strain curves of the longitudinal bars shown in Figure 5-9, where the curves stops at the gauge failure. Table 5.7 shows the minimum, maximum and average strain recorded from the gauged leg of the shear links crossing the main shear crack at the failure load.

Table 5.6: Recorded strain of longitudinal bars and corresponding loads

| Specimen | TP1 | TP2-1 | TP2-2 | TP3-1 | TP3-2 | TP4 | TP5-1 | TP5-2 |
|---|---|---|---|---|---|---|---|---|
| Load $P$ (kN) | 31.6 | 61.9 | 92.6 | 82.3 | 65.6 | 88.3 | 82.5 | 80.1 |
| Strain $\epsilon_f$ (%) | 0.07 | 0.55 | 0.77 | 0.53 | 0.55 | 0.99 | 1.25 | 1.73 |

### 5.5.2 Test observations

#### 5.5.2.1 Diagonal tension shear failure

Specimen TP1 and TP2-1 failed in diagonal tension shear failure. Under 5kN of applied load, the first flexural cracks were observed at the bottom face of the specimens below

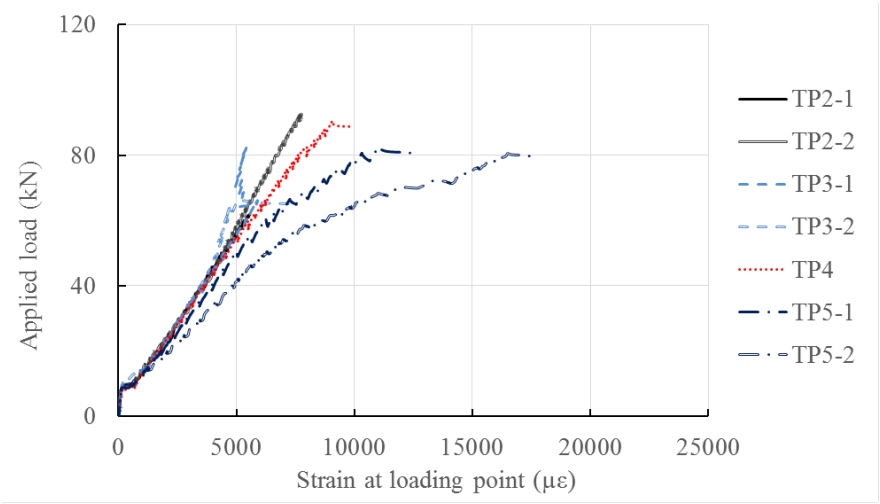


Figure 5-9: Load - strain curves of longitudinal bars

Table 5.7: Strain in shear links crossing the major shear cracks

| Specimen | Strain of shear links $\epsilon_{fv}$ (%) | | | | | |
|---|---|---|---|---|---|---|
| | Vertical links | | | Diagonal links | | |
| | *Min.* | *Ave.* | *Max.* | *Min.* | *Ave.* | *Max.* |
| TP2-1 | 0.44 | 0.44 | 0.44 | 0.27 | 0.40 | 0.52 |
| TP2-2 | 0.74 | 0.87 | 1.01 | 0.43 | 0.86 | 1.07 |
| TP3-1 | 0.28 | 0.35 | 0.42 | 0.39 | 0.48 | 0.57 |
| TP3-2 | 0.35 | 0.56 | 0.81 | 0.85 | 0.87 | 0.89 |
| TP4 | 0.14 | 0.14 | 0.14 | 0.25 | 0.40 | 0.54 |
| TP5-1 | 0.03 | 0.47 | 0.81 | 0.37 | 0.53 | 0.78 |
| TP5-2 | 0.27 | 0.45 | 0.73 | 0.45 | 0.63 | 0.73 |

the loading jack. After increasing the load, more cracks propagated from the loading point to the support. When the applied load reached 14kN, a shear crack formed in the shear span of TP1 and developed towards the loading point. A similar shear crack was observed on TP2-1 at 44kN. When the applied load reached 31.6kN, TP1 failed with the shear crack splitting the specimen into two parts as shown in Figure 5-10 whilst TP2-1 failed at 61.9kN with the shear crack penetrating the compression zone and the shear links rupturing, as shown in Figure 5-11. The load in all the observation figures in section 5.5.2 shows the failure load of the specimen.

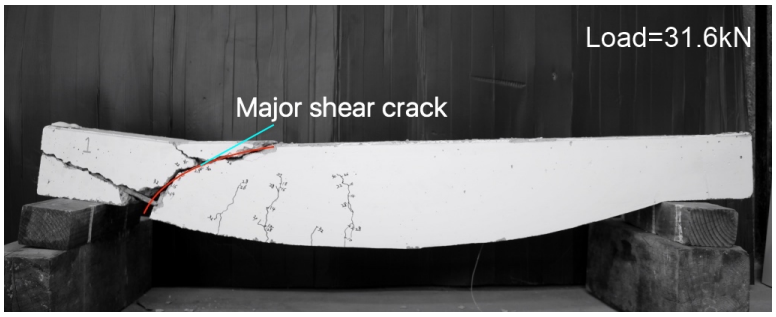


Figure 5-10: Diagonal tension failure of TP1

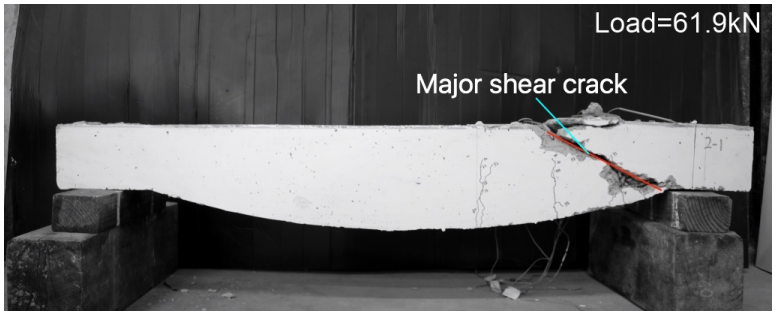


Figure 5-11: Diagonal tension failure of TP2-1

#### 5.5.2.2 Shear compression failure

Specimens TP2-2, TP3-1, TP3-2, TP5-1 and TP5-2 were designed to fail in shear and they failed in shear compression failure (SC). Similar to specimens TP1 and TP2-1 which failed through diagonal tension failure, flexural cracks of the SC specimens developed below the loading jack after 5kN. Except for T3-2 having its first shear crack formed close to the support at 25kN, the SC specimens had their first shear crack formed at between 40kN to 45kN from a bending crack. Under approximately 80kN of applied load, the shear cracks of the SC specimens (except T3-2) propagated horizontally in the compression zone resulting in the concrete crushing. For specimen T3-2, the shear crack propagated horizontally at about 100kN. After concrete crushing, the shear links across the major shear crack ruptured. The specimens after failure are shown in Figure 5-12, Figure 5-13, 5-14, Figure 5-15 and Figure 5-16.

#### 5.5.2.3 Flexural end slip failure

Specimen TP4 was designed for flexural failure of concrete crushing but failed in end slip unexpectedly. The first flexural crack propagated at 5kN of applied load and first

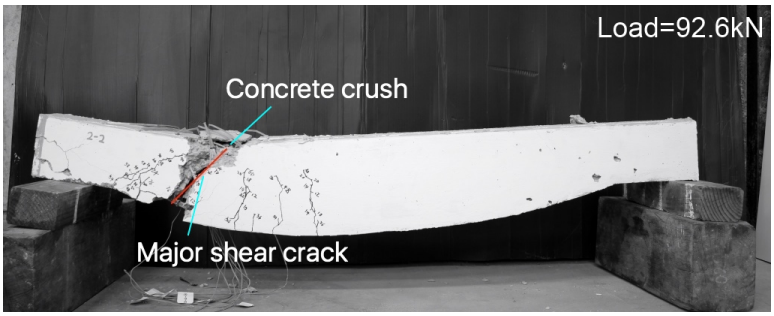


Figure 5-12: Shear compression failure of TP2-2

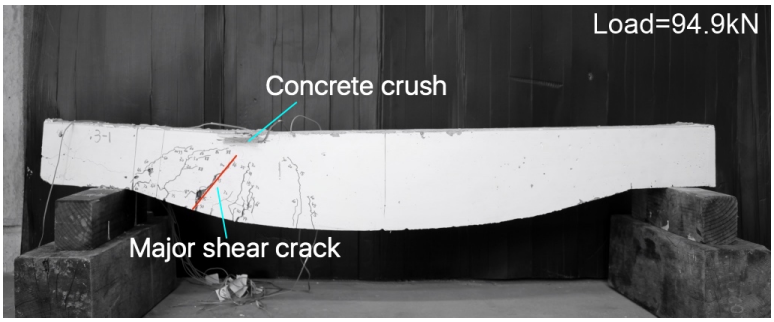


Figure 5-13: Diagonal tension failure of TP3-1

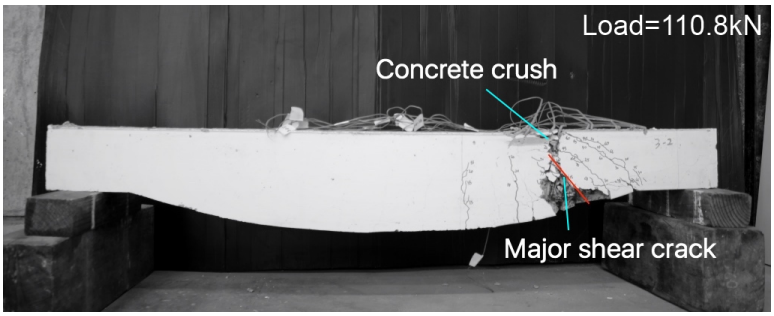


Figure 5-14: Shear compression failure of TP3-2

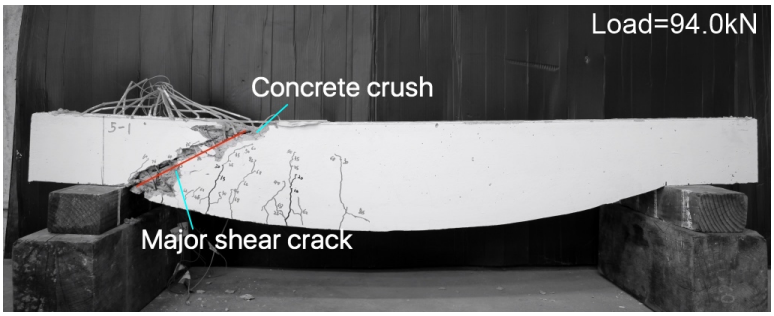


Figure 5-15: Shear compression failure of TP5-1

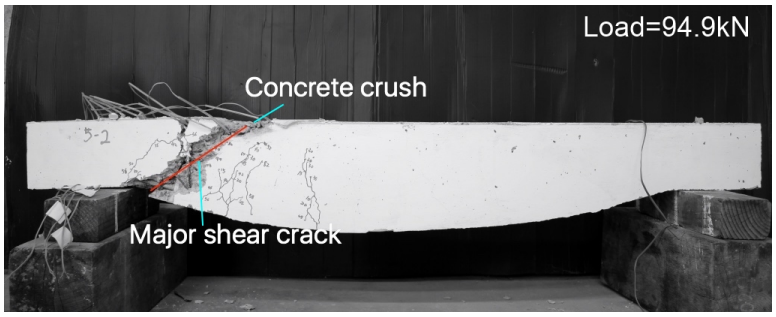


Figure 5-16: Shear compression failure of TP5-2

shear crack at 40kN. Under 84kN of applied load, a horizontal crack was found in the compression zone resulting in concrete crushing as shown in Figure 5-17. At the failure load, a major flexural crack opened and the longitudinal bars were pulled out from the support area but no shear link rupture was found.

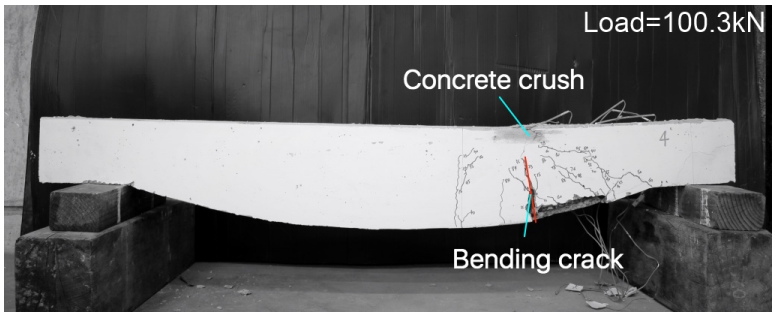


Figure 5-17: Flexural end slip failure of TP4

### 5.5.3 Cracking pattern and failed shear links

During the tests, the crack patterns were recorded. The crack development presented in section 5.5.2 are shown in Figure 5-18 and Figure 5-19. The cracked and crushed concrete of the failed specimens were removed carefully. The failed shear links were observed and recorded as shown in Figure 5-18 and Figure 5-19. The dots are rupture points of the W-FRP shear links from the observation after the tests and the red lines are the major cracks observed from the tests.

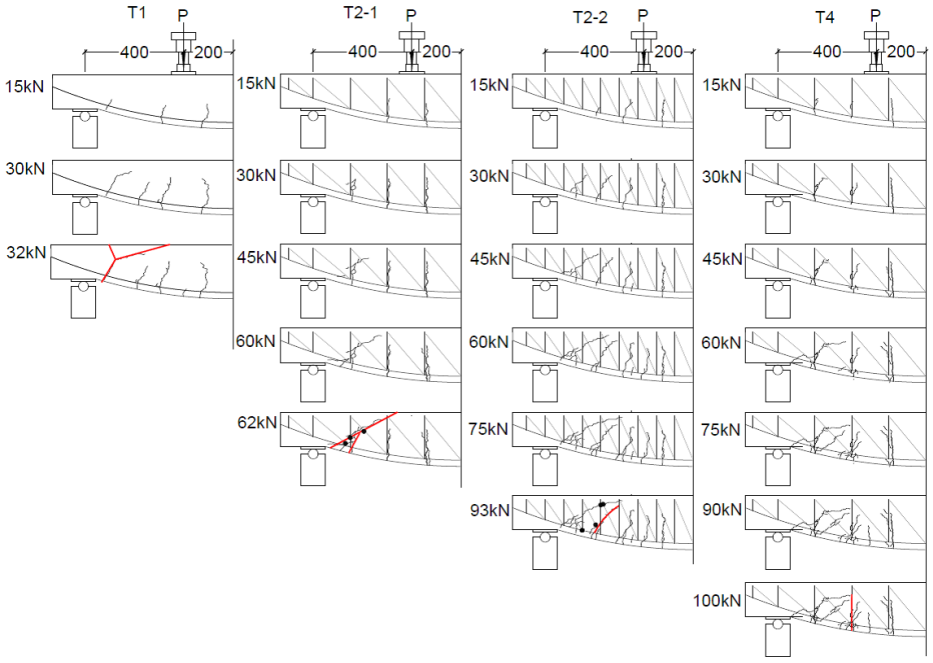


Figure 5-18: Crack development of specimen TP1, TP2 and TP4

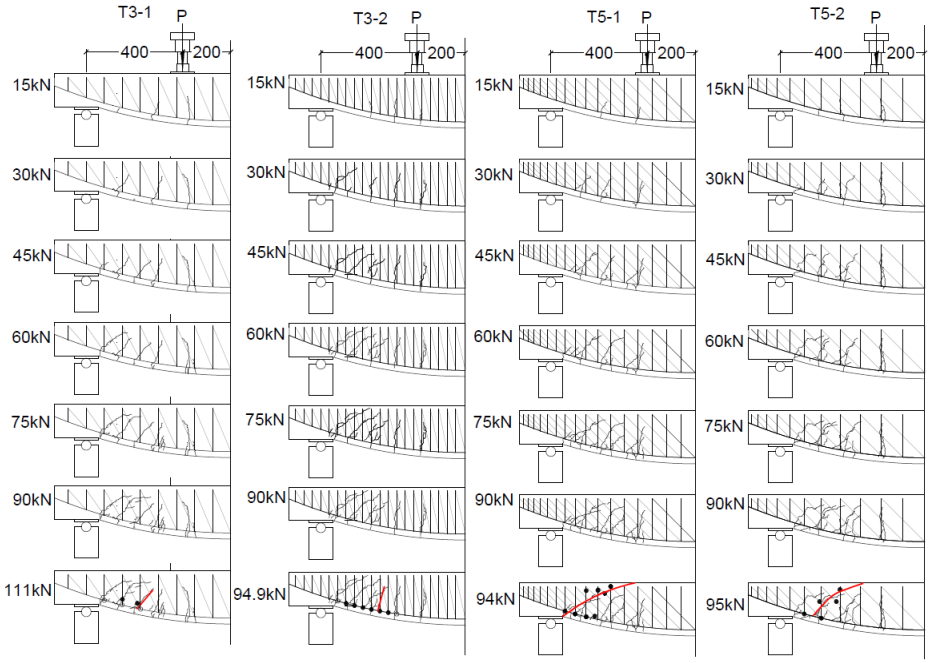


Figure 5-19: Crack development of specimen TP3 and TP5

## 5.6 Analysis and discussion

In this section, the test results are analysed and interpreted. The contributing factors to the shear performance of the specimens including the shear reinforcement ratios, shear reinforcement patterns and geometry are examined. The behaviours of the specimens are also compared with the prismatic beams (Chapter 4). The validity of proposed revisions on ACI 440.1, CSA S806 and MCFT model in Chapter 3 is calibrated against the test results.

### 5.6.1 Shear reinforcement ratio

As expected, higher shear reinforcement ratio results in higher ultimate capacity. As shown in Table 5.5, the ultimate shear capacity of TP2-1 is 96% higher than the reference specimen TP1. Whilst the ultimate shear capacity of TP4 (designed for flexural failure) was not obtained from the test due to the unexpected end slip failure, it is still 217% higher than the reference.

Combining the strain data (Table 5.7), the material properties (Table 5.1) and the arrangement (Figure 5-7) of W-FRP shear links, the shear contribution W-FRP shear reinforcement at the failure load was obtained, as shown in Table 5.8. The value of $V_u$ was calculated as two-thirds of the applied load, based on the test setup. Since not all the shear links of specimen TP3-2 were gauged, the strains of the two that were not recorded were taken as the average strain of the adjacent links.

Table 5.8: Shear contribution of W-FRP

| Specimen | Shear reinforcement ratio $\rho_{fv}$ (%) | Shear contribution $V_f$ (kN) | Ultimate shear capacity $V_u$ (kN) | $V_f/V_u$ |
|---|---|---|---|---|
| TP1 | - | 0 | 21.1 | - |
| TP2-1 | 0.25 | 18.3 | 41.2 | 0.44 |
| TP2-2 | 0.25 | 37.5 | 61.7 | 0.61 |
| TP3-1 | 0.50 | 36.8 | 63.1 | 0.58 |
| TP3-2 | 0.50 | 54.4 | 73.3 | 0.74 |
| TP4 | 0.75 | 37.0 | 66.8 | 0.55 |
| TP5-1 | 0.50 | 45.5 | 62.7 | 0.73 |
| TP5-2A | 0.30 | 29.4 | 63.3 | 0.46 |

With the same W-FRP shear reinforcement pattern, the values of $V_f$ and $V_f/V_u$ of TP4

are 101% and 25% greater than TP2-1 respectively. With a similar pattern to TP5-2, the values of $V_f$ and $V_f/V_u$ of TP5-1 are 55% and 56% larger than TP5-2 respectively.

As specimen TP4 did not fail in shear, there was a potential for the shear reinforcement to carry more shear force. Regardless of the premature end slip flexural failure, TP4 had a higher ultimate capacity than all of the specimens except for T3-2. The variable-depth beams reinforced with a certain amount of W-FRP reinforcement could have sufficient shear capacity as the prismatic beams do when the anchorage is secured.

The failure mode of specimens is also influenced by the reinforcement ratio. The specimens with a shear reinforcement ratio higher than 0.3% all exhibited concrete crushing at about 80kN. The sufficient shear reinforcement allowed the concrete to crush before the shear reinforcement ruptured. However, the shear reinforcement of specimens with lower shear reinforcement ratio (TP1 and TP2-1) ruptured before the concrete crushing and both the specimens failed with lower applied loads.

The specimens with the same shear reinforcement ratio had varying shear performance and the shear reinforcement exhibited difference shear contributions (Table 5.8). With different shear reinforcement ratio, specimens TP2-2 and TP3-1 exhibited similar shear performance. The specimen comparisons in this section demonstrate that in addition to the shear reinforcement ratio, there could be more factors that influenced the shear performance. This will be further discussed in section 5.6.2 and 5.6.3.

### 5.6.2 W-FRP patterns

This section presents the analysis of the influence W-FRP patterns on the shear performance. There are three main factors: corner strength, shear reinforcement arrangement and the confinement of concrete.

#### 5.6.2.1 Corner strength of W-FRP shear links

As tested by Spadea et al. (2017a), the corner strength of W-FRP shear links varied along with the cross-section area, as shown in Table 4.15. With same shear reinforcement ratio, W-FRP reinforcement having different corner strengths delivered different shear performances to the specimens. As shown in section 5.2.4, the shear links of specimens TP2-2 and TP3-2 have smaller cross-section area than specimens TP2-1 and TP3-1 respectively. The higher ultimate shear capacities of TP2-2 and TP3-2 compared with TP2-1 and TP3-1 respectively, demonstrate the influence of corner strength of W-FRP.

The influence of corner strengths of the W-FRP shear links are highlighted by the higher rupture strains in shear links of smaller cross-section area (Table 5.7 and Figure 5-20). The average strain of the vertical shear links in TP3-2 is 60% larger than those in TP3-1; the average strain of the diagonal links of TP3-2 is 81% larger than those in TP3-1 at the failure loads. The diagonal and vertical links of TP2-2 have approximately 100% higher average strains than that of TP2-1.

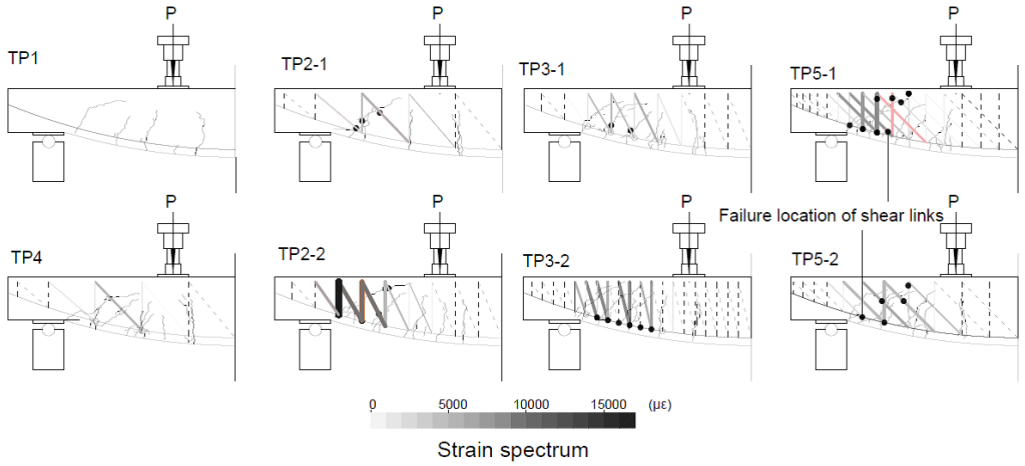


Figure 5-20: Strain of shear links and cracking patterns of specimens at failure load

The higher average strain of shear links in TP2-2 and TP3-2 at failure is one of the reasons for the higher shear contribution of the W-FRP reinforcement. The higher corner strength of W-FRP of smaller cross-section area in denser patterns (see Figure 5-20) allows that the shear links carry higher tensile strains at failure and hence provide higher shear contribution. With the same shear reinforcement ratio, shear contribution of the W-FRP shear reinforcement in TP2-2 is more than 104% higher than in TP2-1 (Table 5.8). The shear contribution of W-FRP in TP3-2 is 50% higher than in TP3-1. With the higher shear contribution of W-FRP, the specimen TP2-2 had 50% more shear capacity and the failure mode was changed from DT to SC compared to TP2-1. Similar to group TP2, specimen TP3-2 had 17% higher shear capacity than TP3-1.

The larger cross-section area of W-FRP shear reinforcement in T3-1 results in a lower corner strength than in T2-2. Although the shear reinforcement ratio of TP3-1 is larger than TP2-2, the lower corner strength of W-FRP shear links could be the reason for the similar shear contributions of W-FRP (Table 5.8) and hence the similar shear performance of the two specimens.

#### 5.6.2.2 Arrangement of W-FRP shear links

The arrangement of the W-FRP shear links is seen to influence the shear performance. As shown in Figure 5-18 and Figure 5-19, the denser patterns of W-FRP shear reinforcement resulted in denser cracking patterns in the specimens. Hence, there is a higher probability that more shear links will cross a major shear crack. For the specimen TP2-1 and TP4, there was only one major shear crack going across three shear links (S3, S4 and S5). However, for specimens with denser patterns, two to four shear cracks developed in the shear span. In these specimens, more shear links went across the shear cracks and as a result, the shear behaviour of the specimens was remarkably different.

Unlike steel shear links, which can theoretically reach their yielding point prior to shear failure, FRP shear links always have different strain values and hence some links cannot be fully utilised due to their linear elastic properties. The denser patterns of W-FRP result in a smaller angle difference between adjacent links, which leads to smaller differences in the relative angles between the shear links and the shear cracks. This could create similar strains between the adjacent links, which indicates that between one diagonal link and its adjacent vertical link, the one with lower strain could be utilised more efficiently when the one link with higher strain ruptures.

As shown in Figure 5-20, the small angle difference between adjacent links results in smaller strain difference. Since the rupturing is more likely to occur on the links with high strains, the two adjacent links that encountered the maximum average strain in each specimen and their strain difference are shown in Table 5.9, in which the number in the brackets is the shear link number as shown in Figure 5-7. The values of $\epsilon_{fm}/\epsilon_{fa}$ of specimens TP2-2 and TP3-2 are very close to 1 and are smaller than TP2-1 and TP3-1 respectively. However, for specimens TP2-1, TP4, TP5-1 and TP5-2, the diagonal links were arranged with approximately 45° and the resulting strain difference between adjacent links is larger.

There is only one exception, TP3-1, where the maximum strain of shear links was recorded in link S4 and S8 had the second largest strain. This variation could be caused by the different cracking development. When the shear links S8 and S7 of TP3-1 are used for calculation as for TP2-2, the value of $\epsilon_{fm}/\epsilon_{fa}$ is 114%, which also supports the argument that a smaller angle difference between adjacent links results a in smaller strain difference.

Table 5.10 shows the shear contribution of the diagonal and vertical links, where $V_f$ is the total shear contribution of shear reinforcement as shown in Table 5.8. When

$V_{f,D}/V_f$ is larger than 0.5, the diagonal links are more effective than the vertical ones.

Table 5.9: Comparison of shear links with maximum strains and their adjacent links

| Specimen | Load (kN) | Strain of links with maximum strain $\epsilon_{fm}(\%)$ | Strain of the adjacent vertical link $\epsilon_{fa}$ (%) | Difference $\epsilon_{fm}/\epsilon_{fa}$ |
|---|---|---|---|---|
| TP2-1 | 61.9 | 0.51 (S3) | 0.44 (S4) | 1.15 |
| TP2-2 | 92.6 | 1.07 (S8) | 1.01 (S7) | 1.06 |
| TP3-1 | 94.9 | 0.57 (S4) | 0.29 (S5) | 1.96 |
| TP3-2 | 110.8 | 0.89 (S6) | 0.81 (S5) | 1.11 |
| TP4 | 100.3 | 0.54 (S3) | 0.14 (S4) | 3.68 |
| TP5-1 | 94.0 | 0.81 (S9) | 0.53 (S8) | 1.50 |
| TP5-2 | 94.9 | 0.73 (S5) | 0.62 (S6) | 1.18 |

Table 5.10: Shear contribution of diagonal and vertical links

| Specimen | Load (kN) | Shear contribution of diagonal links $V_{f,D}$ (kN) | Shear contribution of vertical links $V_{f,V}$ (kN) | $V_{f,D}/V_f$ | $V_{f,V}/V_f$ |
|---|---|---|---|---|---|
| TP2-1 | 61.9 | 10.1 | 8.2 | 0.55 | 0.45 |
| TP2-2 | 92.6 | 21.2 | 16.3 | 0.56 | 0.44 |
| TP3-1 | 94.9 | 23.6 | 13.1 | 0.64 | 0.36 |
| TP3-2 | 110.8 | 32.5 | 21.9 | 0.59 | 0.41 |
| TP4 | 100.3 | 29.2 | 7.8 | 0.78 | 0.22 |
| TP5-1 | 94.0 | 18.9 | 26.2 | 0.41 | 0.59 |
| TP5-2 | 94.9 | 16.7 | 12.7 | 0.56 | 0.44 |

For specimens TP2-2, TP3-1 and TP3-2, the diagonal links have large angles to the horizontal axis and larger strains than the vertical ones. The shear contributions of the diagonal links in these specimens are more effective than the vertical links in shear carrying (Table 5.8). The diagonal links contributed 56% to 64% of the total shear contribution of shear reinforcement. With an angle of approximately 45 degrees, the total shear contribution of the diagonal links in TP2-1, TP5-1 and TP5-2 is similar to that of the vertical ones, but the average strain of the diagonal links is greater than the vertical links, as shown by $V_{f,D}/V_f$ varying from 0.41 to 0.56 in Table 5.10. There is only one exception TP4, which could have been due to one single diagonal shear link S3 contributing to about 54% of shear contribution provided by all the shear links crossing the shear crack.

With the analysis above, it can be seen that when the W-FRP shear reinforcement has the constant spacing between the vertical links, a denser pattern can result in more

shear link crossing the shear cracks, smaller strain difference between adjacent links and increased effectiveness of the diagonal links. All these factors contribute to improved shear performance of the specimens with denser W-FRP pattern in each group.

#### 5.6.2.3 Confinement of concrete

For confinement reinforcement, both cross-section area and spacing influence the confined concrete strength (Afifi et al., 2015). When the confinement reinforcement ratio is the same, a smaller spacing results in higher confined concrete strength. All the shear compression failures of the specimens were initiated by concrete crushing, which indicates that the concrete performance may limit the shear performance. From observation of the testing, the W-FRP shear reinforcement may have different confinement effects on the compression zone concrete.

This perspective is supported by the fact that among these specimens, TP3-2 which had the densest shear links and a higher load of concrete crushing at about 100kN and thus, has the best ultimate capacity of 110kN. However, the concrete of TP3-2 has neither best deformability or stiffness, as shown by the ascending branch of the load-strain curves in Figure 5-21.

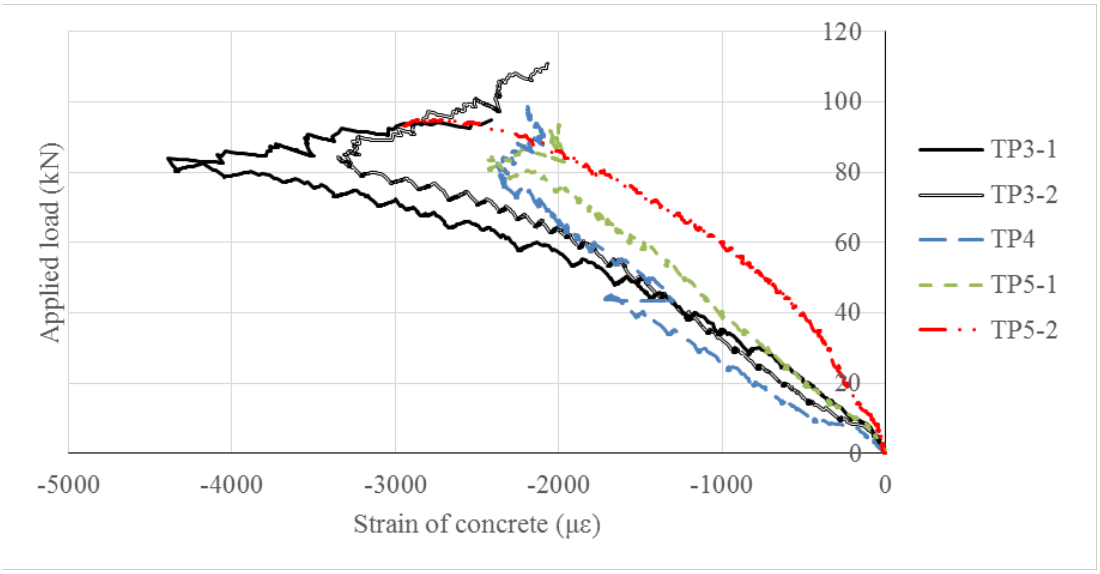


Figure 5-21: Load strain relations of concrete

There are large variations of concrete strain data and hence, the present data cannot validate the influence of the confinement provided by W-FRP shear reinforcement.

The unexpected descending branch of the four specimens shows that in addition to flexure, there may be other factors influencing the performance of concrete. Thus, further investigations need to be conducted to explain the concrete performance of the specimens and to demonstrate the confinement influence of W-FRP.

### 5.6.3 Contribution of the longitudinal bars

As presented in section 3.2.3.1, the shear contribution of the inclined longitudinal bars can be taken as the vertical component of tensile force, which is created by both flexure and shear (additional tensile force). As the shear cracks in the specimens develop from the support area towards the loading point, the shear contribution of the longitudinal bars can be calculated based on their strains at the support area. However, the strain data (Table 5.6 and Figure 5-9) only shows the strains in the longitudinal bars at the loading point, as presented in section 5.4.2. Consequently, the shear contribution of longitudinal bars ($V_t$) and concrete ($V_c$) are considered together as the difference between the applied shear force and shear contribution of shear reinforcement (Table 5.8) as shown in Table 5.11.

Table 5.11: Shear contribution of inclined longitudinal bars and concrete

| Specimen | Ultimate capacity $P_u$ (kN) | Applied shear force $V_u$ (kN) | Shear contribution of longitudinal bars and concrete $V_t$+$V_c$ (kN) | $(V_c+V_t)/V_u$ |
|---|---|---|---|---|
| TP1 | 31.6 | 21.1 | 21.1 | 1.00 |
| TP2-1 | 61.9 | 41.2 | 22.9 | 0.55 |
| TP2-2 | 92.6 | 61.7 | 24.2 | 0.39 |
| TP3-1 | 94.9 | 63.1 | 26.3 | 0.42 |
| TP3-2 | 110.0 | 73.3 | 18.8 | 0.25 |
| TP4 | 100.0 | 66.8 | 29.7 | 0.44 |
| TP5-1 | 94.0 | 62.7 | 17.2 | 0.27 |
| TP5-2 | 94.9 | 63.3 | 33.9 | 0.54 |

Since the shear cracks develop from the support area, the flexural tensile force of longitudinal bars is neglected. The additional tensile force of these bars is related to the applied shear force, the shear contribution of shear links and angle of the concrete strut as shown in Equation 2.28 from CSA-S806 (2012). As all the specimens have the same geometry and the concrete area at each cross section is the same, the concrete shear contribution $V_c$ is assumed as the same. The following analysis focuses on the influence of the applied shear force and shear contribution of the W-FRP shear reinforcement.

As expected from the design procedures in section 3.2.3.1, the shear contribution of the longitudinal bars increases with the applied load. Comparing specimens TP1, TP2-1 and TP2-2 at their failure loads (Table 5.11), the shear contribution of the longitudinal bars increases along with the applied shear force following the assumption that $V_c$ is constant. As discussed in section 5.6.1, the higher reinforcement ratio helps to increase the ultimate capacity. Consequently, the higher ultimate capacity results in higher resistance of the longitudinal bars, which can be seen through the comparison of specimens TP1, TP2-1 and TP4 (Table 5.11).

In addition to the ultimate capacity, the shear contribution of the longitudinal bars is also influenced by the shear reinforcement patterns (section 5.6.2). Following Equation 2.28 (CSA-S806, 2012), the additional tensile force would be effectively reduced by $V_f$, which influences the load distribution in the longitudinal bars and the shear reinforcement. Therefore, shear links with a smaller cross-section area and smaller spacing result in higher shear contribution of shear reinforcement (see section 5.6.2.1) and hence lower shear contribution of flexural reinforcement. This could explain why despite specimens TP3-2 and TP5-1 reaching relatively high ultimate capacity, their values of $V_t$+$V_c$ are smaller than most of the others, as shown in Table 5.11.

In addition to the positive effect to shear, high tensile force in the longitudinal bars could lead to premature end slip failure, as revealed by TP4. This tensile force in longitudinal bars at the support makes the anchorage strength also important in the design of variable-depth beams. However, it is a topic of additional research beyond the scope of this chapter and it will be discussed in Chapter 6.

### 5.6.4 Prediction examination

In section 5.2.3, the flexural capacity predictions of the specimens are 87kN following ACI-440.1R (2015) and 93kN following CSA-A23.3-4 (2004). Both the predictions are conservative. The shear performance of the specimens are compared to the predictions for total applied load from the proposed revised codified methods ($P_{v,ACI}$ and $P_{v,CSA}$) and the revised MCFT model ($P_{v,MCFT}$) in Table 5.12.

The governing factor of the codified predictions is the strain limits: 0.4% for ACI 440.1 and 0.5% for CSA S806 (see section 5.2.4). By considering the shear contributions of inclined longitudinal bars, predictions of the revised ACI 440.1 are conservative ($P_{exe.}/P_{ACI}$=1.45) with the least standard deviation (0.25) With the variable angle truss model and higher design strength of W-FRP shear links, the revised CSA S806

give unconservative predictions ($P_{exe.}/P_{CSA}$=0.89) with a smaller deviation (0.13). Through comparison of the test results and predictions, it emerges that the codes cannot differentiate the varying shear reinforcement patterns with same reinforcement ratio, as the same predictions were made for each specimen in group TP2 and TP3. Hence optimisation of W-FRP arrangement cannot be taken into account in the codified designs.

Table 5.12: Shear prediction examination

| Specimen | $P_{exp.}$. | $P_{v,ACI}$ | $P_{v,CSA}$ | $P_{v,MCFT}$ | $\frac{P_{exp.}}{P_{v,ACI}}$ | $\frac{P_{exp.}}{P_{v,CSA}}$ | $\frac{P_{exp.}}{P_{v,MCFT}}$ |
|---|---|---|---|---|---|---|---|
| TP1 | 31.6 | 20.1 | 34.6 | - | 1.57 | 0.91 | - |
| TP2-1 | 61.9 | 50.4 | 84.8 | 40.9 | 1.23 | 0.73 | 1.51 |
| TP2-2 | 92.6 | 50.4 | 84.8 | 65.2 | 1.84 | 1.09 | 1.42 |
| T3-1 | 94.9 | 80.2 | 123.7 | 93.7 | 1.18 | 0.77 | 1.01 |
| T3-2 | 110.0 | 80.2 | 123.7 | 137.1 | 1.37 | 0.89 | 0.80 |
| T4 | 100.0 | 110.4 | 156.3 | 126.4 | 0.91* | 0.64* | 0.79* |
| TP5-1 | 94.0 | 74.1 | 116.5 | 124.0 | 1.27 | 0.81 | 0.76 |
| TP5-2 | 94.9 | 56.6 | 93.2 | 80.7 | 1.68 | 1.02 | 1.18 |
| Average | | | | | 1.45 | 0.89 | 1.11 |
| Standard deviation | | | | | 0.25 | 0.13 | 0.31 |

Where * indicates that the predictions of T4 were removed from the calibrations and standard deviation calculation owing to its failure mode. All partial safety factors are set to 1.00 in these comparisons.

The revised MCFT model shows more accurate predictions ($P_{exe.}/P_{MCFT}$=1.11, SD=0.31) than the two codified methods. Moreover, by incorporating the actual corner strength of shear links, it is possible to provide unique predictions for specimens T2-1/T2-2 and T3-1/T3-2. The W-FRP patterns are recognised by the model and it shows the potential to optimise the patterns based on the different corner strengths (Table 5.1).

Aside from the advantages of the MCFT model, unconservative predictions have been made for TP3-2 and TP5-1. The unconservative predictions could be caused by choosing the actual corner strength, obtained from testing of single W-FRP links, as the design strength. However, it has been seen that the average failure strains of the shear links in Table 5.7 are not as high as expected. The test results of a single shear link are not representative of the actual performance of multiple shear links in concrete. Directly using the corner strength of W-FRP could therefore be unconservative in shear design.

### 5.6.5 Material saving

The tapered geometry of the specimens not only contributes to the shear resistance but also saves a proportion of material usage. Compared with previous experimental research on prismatic beams (Chapter 4), two out of the three tapered beams, the shear reinforcement ratio of which was lower than specimen P2, had slightly better performance as shown in Table 5.13. A saving of 19% concrete still has been achieved. As the geometry of the variable depth specimens being limited by the length of the longitudinal bars due to the short dimensions of the specimens, higher concrete saving could be achieved in full-scale beams. For most of the cases, tapered beams had higher capacities than prismatic beams (Chapter 4).

Table 5.13: Comparison of tapered beams and prismatic beams

| Tapered specimen | $\rho_{ft}$ (%) | Concrete volume ($10^{-3}m^3$) | $V_u$ (kN) | Prismatic specimen | $\rho_{ft}$ (%) | Concrete volume ($10^{-3}m^3$) | $V_u$ (kN) |
|---|---|---|---|---|---|---|---|
| TP1 | 0 | 29.5 | 21.1 | P1 | 0 | 36.3 | 19.5 |
| TP2-1 | 0.25 | 29.5 | 41.2 | P2 | 0.31 | 36.3 | 60.4 |
| TP2-2 | 0.25 | 29.5 | 61.7 | | | | |
| TP3-1 | 0.50 | 29.5 | 63.1 | | | | |
| TP3-2 | 0.51 | 29.5 | 73.3 | | | | |
| TP5-1 | 0.45 | 29.5 | 62.7 | | | | |
| TP5-2 | 0.30 | 29.5 | 63.3 | | | | |
| TP4 | 0.75 | 29.5 | 66.8 | P3 | 0.84 | 36.3 | 74.3 |

Where $\rho_{ft}$ is the shear reinforcement ratio of tapered beams; $\rho_{fp}$ is the shear reinforcement ratio of prismatic beams and $V_u$ is the shear force in shear span at ultimate capacity.

For the specimens with no shear reinforcement, i.e. TP1, had a similar shear capacity with P1. For the under-reinforced specimens (Table 5.13), compared with prismatic beams (P2), the tapered beams had lower, similar or higher shear reinforcement ratios. For all the tapered specimens with similar or higher shear reinforcement ratios, their shear capacity was higher than P2. In the case of the variable depth beams with lower shear reinforcement ratios, TP2-1 had lower shear capacity but TP2-2 had a similar shear capacity to P2. Regarding the over reinforced specimens, TP4 had a lower bending capacity than P1 because of the lower concrete strength and premature end slip failure of longitudinal bars.

With all the comparisons, the goal of achieving low carbon emissions and embodied

energy was unlocked by optimising the geometry and the W-FRP patterns. Materials were saved without reducing structural performance in most cases which was highlighted by the lower reinforcement ratio of TP2-2 and TP5-2.

## 5.7 Conclusions

In this chapter, the experimental research of W-FRP reinforced beams with variable depth geometry has been presented. Eight tapered beams with four shear reinforcement ratios and six shear reinforcement patterns were designed and tested under three-point bending. The contributing factors to shear have been analysed and the validity of proposed revisions to the codified design methods and MCFT design in Chapter 3 is examined. The variable-depth geometry has also been analysed regarding the material saving aspect. The experimental research in this chapter supports the following conclusions:

- The W-FRP shear reinforcement ratio can effectively influence the performance of the specimens. Both the shear contributions of W-FRP $V_f$ and the ratio of $V_f$ to the ultimate shear capacity $V_u$ increase with the shear reinforcement ratio, when other influencing factors are excluded, as revealed by the comparisons of TP1/TP2-1/TP4 and TP5-1/TP5-2.

- The patterns of W-FRP shear reinforcement influence the performance of the specimens in two aspects: corner strength and arrangement. Smaller cross section of W-FRP results in higher corner strength. The denser arrangements of W-FRP can create denser cracking patterns, smaller strain difference between adjacent links and more effective diagonal links. The influence of patterns implies that the W-FRP can be optimised to achieve less material use or higher capacity which has been highlighted by the 50% higher shear capacity of T2-2 when compared with T2-1.

- The shear contribution of the inclined longitudinal bars relates to the ultimate capacity and it is also influenced by the shear contributions of shear reinforcement, which can effectively reduce the additional tensile force and thereby change the load distribution between flexural and shear reinforcement.

- Compared with the prismatic beams in Chapter 4, the variable depth beam specimens have achieved a saving of 19% concrete without compromising the performance of the specimens.

- The examination of the proposed design methods in Chapter 3 shows that that the

revised MCFT had the best correlation ($P_{exe.}/P_{MCFT}$=1.11, SD=0.31) with the test results and it could be used to optimise the pattern of W-FRP by adopting the actual corner strength of W-FRP links. The codified design cannot differentiate the W-FRP patterns.

The research of this Chapter has been published in journal paper 'Yang, Y., Orr, J., Spadea, S. (2018). Shear behaviour of variable-depth concrete beams with Wound Fibre Reinforced Polymer shear reinforcement, Journal of Composites for Construction (accepted).'. In the next Chapter, experimental research of fabric formed T beam specimens is presented to further investigate the contributing factors to shear performance of W-FRP reinforced beams with variable-depth geometries.

# Chapter 6

# Structural behaviour of fabric formed concrete T beams reinforced with W-FRP

## 6.1 Introduction

In order to investigate the structural behaviour of full-scale fabric formed beams, eleven T beam specimens reinforced with W-FRP shear reinforcement were designed and tested, based on the investigations into W-FRP shear reinforcement patterns in Chapter 5. Three main contributing factors to shear were considered in the shear design: the geometry, W-FRP shear reinforcement and anchorage. The manufacturing of W-FRP cages was improved with an automated winding machine and flexible fabric formwork was used to cast the T beam specimens.

The structural behaviour of the specimens and the contributing factors to shear considered in the design are analysed. An equation is proposed to establish the relations between the tensile force in longitudinal bars and the contributing factors. Finally, the predictions of revised codified design methods from ACI-440.1R (2015) and CSA-S806 (2012) and the revised MCFT model are examined.

## 6.2 Test design

Following the experimental research and analysis of tapered beam tests (Chapter 5), investigations into W-FRP reinforced fabric formed T beams was conducted to understand how the W-FRP shear reinforcement, anchorage, and geometry influence the structural behaviour.

With different geometries (subsection 6.2.3), shear designs (subsection 6.2.4), and anchorage designs (subsection 6.2.5), the specimens were classified into six groups from T1 to T6. The contributing factors that were investigated in each specimen are shown in Table 6.1.

Table 6.1: Design purpose of specimens

| Specimen | Expected failure mode | Design purpose |
|---|---|---|
| T1 | Shear failure | Reference specimen with no W-FRP |
| T2-1 | Shear failure | W-FRP and anchorage |
| T2-2 | Shear failure | W-FRP and anchorage |
| T2-1R | Shear failure | W-FRP and anchorage |
| T2-2R | Shear failure | W-FRP and anchorage |
| T3-1 | Shear failure | W-FRP and anchorage |
| T3-2 | Shear failure | W-FRP and anchorage |
| T4-1 | Flexural failure | W-FRP and geometry |
| T4-2 | Shear failure | W-FRP, anchorage and geometry |
| T5 | Flexural failure | W-FRP and anchorage |
| T6 | Flexural failure | W-FRP, anchorage and geometry |

Group T1, T2, T2R, T3 and T5 had the same geometry but different shear and anchorage designs to investigate their influence. T2R was a revised version of T2, with improved anchorage. Group T4 and T6 had different geometries with other groups to understand the influence of geometry. Within each group, the two specimens were designed to show the influence of W-FRP patterns.

In this section, design details of the specimens, including the test setup, material properties, geometries, flexural design, shear design and anchorage design, are presented.

### 6.2.1 Test setup

All the specimens were designed as simply supported T beams, 4m in length with a clear span of 3m to simulate a prefabricated T beam in practice. In order to simulate

realistic geometry (e.g. overhangs to support the facade), a protruding end of 500mm beyond the support was included. This also worked as the anchorage zone for the longitudinal bars. In order to simulate an approximation to uniformly distributed load, five hydraulic jacks at spacings of 500mm were used to apply the load. The test setup design is shown in Figure 6-1.

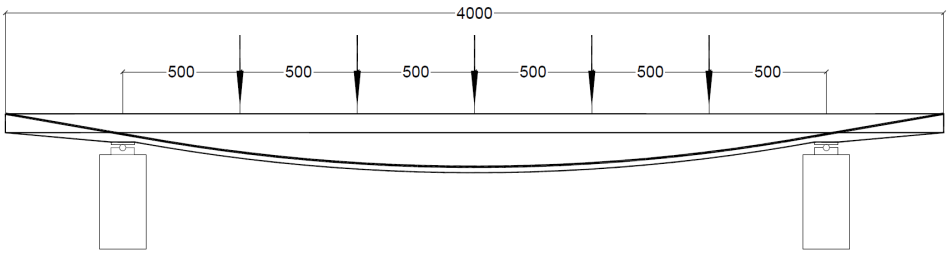


Figure 6-1: Designed test setup

### 6.2.2 Material property

W-FRP and Aslan bars that were used in the prismatic beams (Chapter 4) and tapered beams (Chapter 5) were adopted as the flexural and shear reinforcement in the T beam specimens. All the specimens were designed with C45/55 concrete. The material properties of the longitudinal bars and W-FRP shear reinforcement (Spadea et al., 2017a) are shown in Table 6.2.

Table 6.2: Material properties of flexural and shear reinforcement

| Reinforcement | $A_f$ (mm$^2$) | $f_{fu}$ (MPa) | $f_{fb}$ (MPa) | $\epsilon_b$ (%) | $E_f$ (GPa) |
|---|---|---|---|---|---|
| W-FRP shear links | 4.3 | 1537 | 957 | 0.87 | 109 |
| | 8.6 | 1503 | 745 | 0.69 | 108 |
| | 12.8 | 1484 | 715 | 0.67 | 107 |
| | 17.1 | 1487 | 695 | 0.65 | 107 |
| | 21.4 | 1426 | 654 | 0.62 | 106 |
| | 25.7 | 1384 | 623 | 0.64 | 105 |
| Longitudinal bars | 71.3 | 2648 | - | 1.85 | 143 |

Where $A_f$ is the cross section area of the reinforcement; $f_{fu}$ is tensile strength of the reinforcement; $f_{fb}$ is the corner strength of W-FRP shear reinforcement; $\epsilon_b$ is the strain at the corner strength and $E_f$ is the elastic modulus of the reinforcement.

### 6.2.3 Geometry and flexural design

The T-beam specimens were designed with a flange width of 800mm to simulate the effective flange width as the result of the beam and slab construction in practice, following BS-EN-1992-1-1 (2004), Figure 6-2.

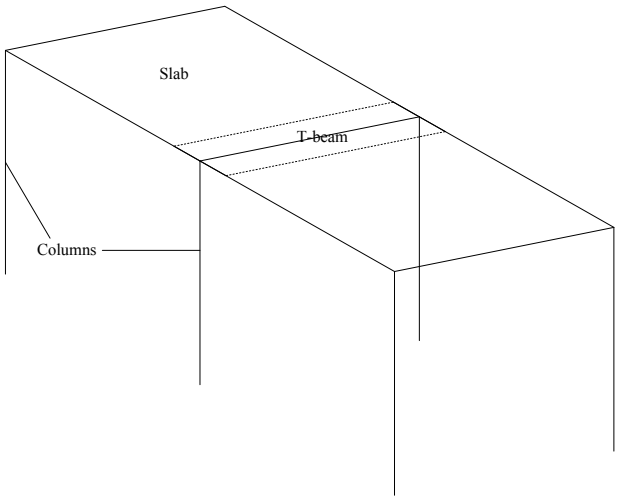


Figure 6-2: Beam and slab construction

The flange depth was designed to be 80mm to simulate the normal slab depth in actual structures, whilst the web width was designed to be 200mm to simulate the width of a normal beam with a 3m clear span. At the mid-span, considering that the web width actually is irrelevant to bending after cracking, the width was reduced to 100mm. Consequently, the web width of the specimens was designed as varying from 100mm at mid-span to 200mm at the supports as shown in Figure 6-3. The larger web width at the supports were used to provide higher shear contribution of concrete.

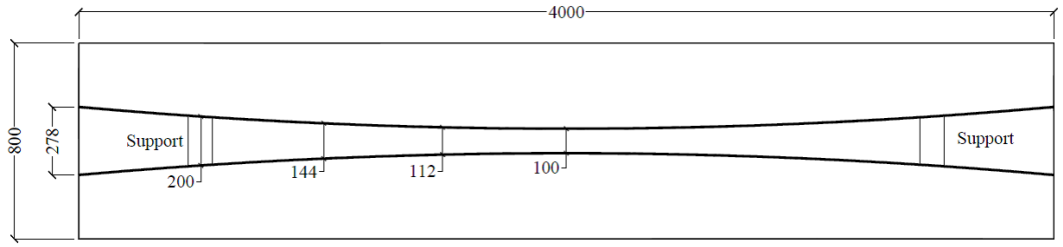


Figure 6-3: Flange and web design

#### 6.2.3.1 Ultimate limit state flexural design

Following the design process specified in Chapter 3, ultimate limit state design was conducted first with a dead load of 2.4kN/m and a live load of 7.5kN/m. The dead load was calculated as the weight of the equivalent prismatic beam of the final design (see section 6.2.6), which has 250mm depth, 200mm web width, 800mm flange width and 80mm flange depth. The enlarged dead load results in conservative design under the ultimate limit state. The live load is taken as $2.5\,\mathrm{kN\,m^{-2}}$ and the T beam is assumed to support a 3m wide slab strip.

Three ⌀10mm Aslan carbon bars were used as the longitudinal reinforcement, along the total beam length (except for T2, see section 6.2.5). The effective depth at mid-span was calculated as 140mm under the ultimate limit state, with a balanced failure mode: simultaneous concrete crushing and longitudinal bars rupture. The effective depths of the remaining cross sections were calculated by providing the exact flexural strength required by the design loading profile with a balanced failure mode following the design procedures (section 3.2.1). The geometry after ultimate limit state (ULS) design is shown in Figure 6-4, where the ultimate capacity of the designed specimen is calculated based on the balanced failure mode.

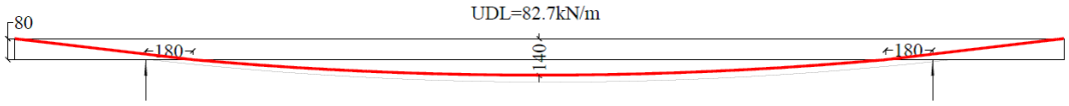


Figure 6-4: Geometry of ULS design

#### 6.2.3.2 Service limit state flexural design

The service limit state design was conducted to control the displacement of the specimens at service. The geometries of the specimens were revised by directly increasing the depth of the cross sections rather than prestressing the longitudinal bars to save the cost of anchorage, time and labour in beam construction. Following the displacement calculation method in section 3.2.2, the depth of each cross section was revised until the mid-span displacement was controlled to be equal to $l/240$ (ACI-440.1R, 2015).

The geometries of the specimens were revised with a rationalised mid-span depth of 250mm and a cover depth of 20mm. The profile of the web was revised to ensure the final bending failure would occur at the mid-span and simplified as a parabola. A depth of 120mm was selected at the supports, as shown in Figure 6-5, Geometry I.

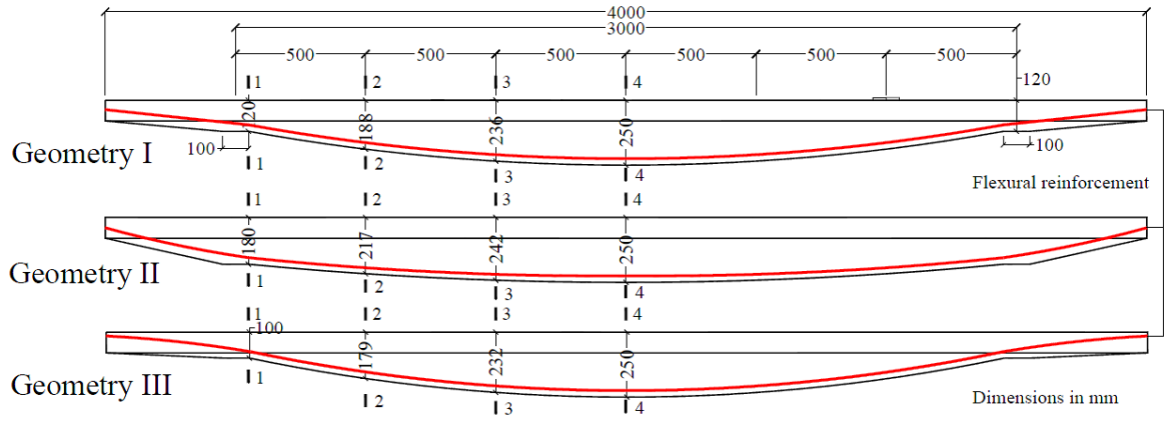


Figure 6-5: Specimen geometry

During testing, it was found that the geometry is related to the end slip failure of the longitudinal bars (see section 6.5.2). Hence, in order to investigate the influence of geometry, further two geometries, II and III, were designed with the respective support depth of 180mm and 100mm (Figure 6-5).

After the SLS design, the geometries were determined of the specimens and flexural capacities (total applied load) were rechecked following the codes and guidelines (ACI-440.1R (2015) and CSA-S806 (2012)) on the four cross sections as shown in Figure 6-5 and Figure 6-6. The corresponding bending strength of these cross sections was calculated. The flexural capacity of specimens was determined by the minimum total applied load under the test setup (Figure 6-1), as shown in Table 6.3, in which $M_{cs,ACI}$ is the nominal bending strength of the cross sections following ACI-440.1R (2015) and $P_{u,ACI}$ is the corresponding ultimate flexural capacity; $M_{cs,CSA}$ is the nominal bending strength of the cross sections following CSA-S806 (2012) and $P_{u,CSA}$ is the corresponding ultimate flexural capacity.

Table 6.3: Flexural predictions of the specimens

| Specimen | $M_{cs,ACI}$ (kNm) | | | | $P_{u,ACI}$ (kN) | $M_{cs,CSA}$ (kNm) | | | | $P_{u,CSA}$ (kN) |
|---|---|---|---|---|---|---|---|---|---|---|
| | 1-1 | 2-2 | 3-3 | 4-4 | | 1-1 | 2-2 | 3-3 | 4-4 | |
| Geomtry I | 37 | 79 | 111 | 118 | 263 | 40 | 87 | 109 | 116 | 258 |
| Geometry II | 73 | 100 | 114 | 118 | 263 | 83 | 100 | 112 | 116 | 258 |
| Geometry III | 27 | 73 | 109 | 118 | 263 | 29 | 82 | 107 | 116 | 258 |

In the calculations, the effective width of the three geometries was taken as 800mm

which was the minimum value calculated from BS-EN-1992-1-1 (2004), ACI-440.1R (2015). The flexural capacity was governed by cross-section 4-4 (mid-span) following CSA-S806 (2012) and the flexural capacity predictions of the specimens in all three geometries were 258kN total applied load, as all the three geometries have the same mid-span depth. In the ACI-440.1R (2015) predictions, it was also section 4-4 that governed the flexural prediction (263kN total applied load) for the three geometries.

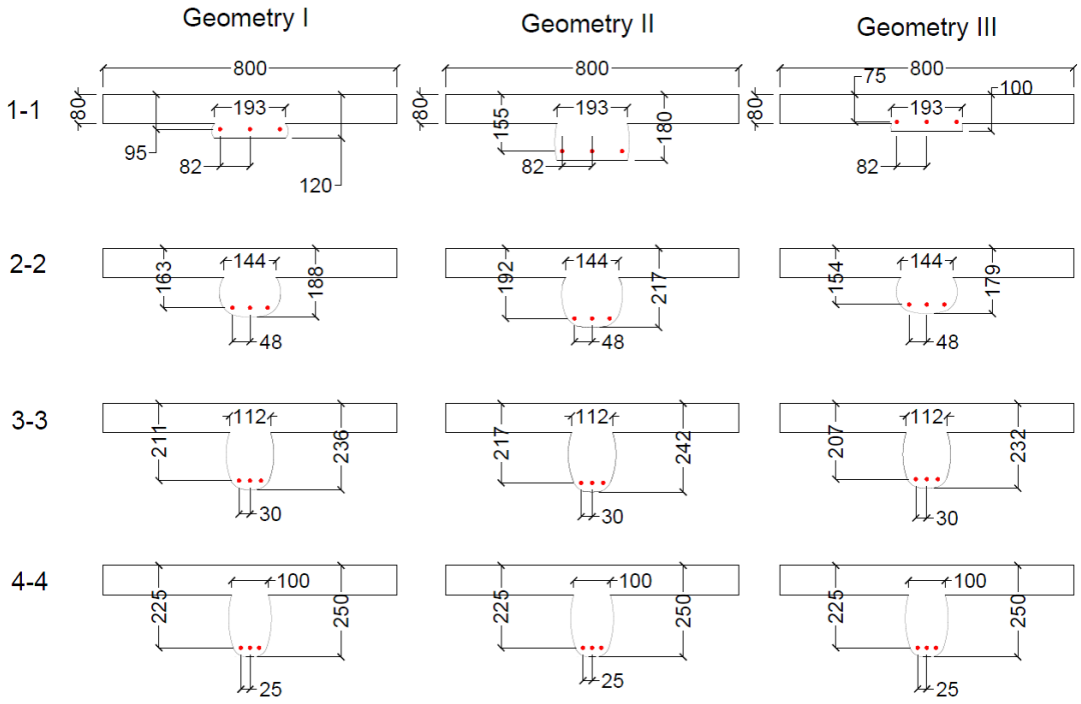


Figure 6-6: Cross sections used for flexural predictions

### 6.2.4 Shear design

In order to investigate the influence of W-FRP shear reinforcement, three levels of shear reinforcement ratios and four types of reinforcement patterns were designed for the specimens. In this subsection, the design details of the shear reinforcement are presented.

#### 6.2.4.1 Shear design

Specimen T1 was designed as the reference specimen without shear reinforcement. The shear links of group T2 and T2R were designed with constant angles (65° and 90°) to the

horizontal axis and variable spacings between the links. The angle difference between adjacent links was reduced to 30° degrees based on the analysis of chapter 5. The shear designs of T1 and T2 are shown in Figure 6-7 and those of T2R are illustrated in Figure 6-8 with group T3.

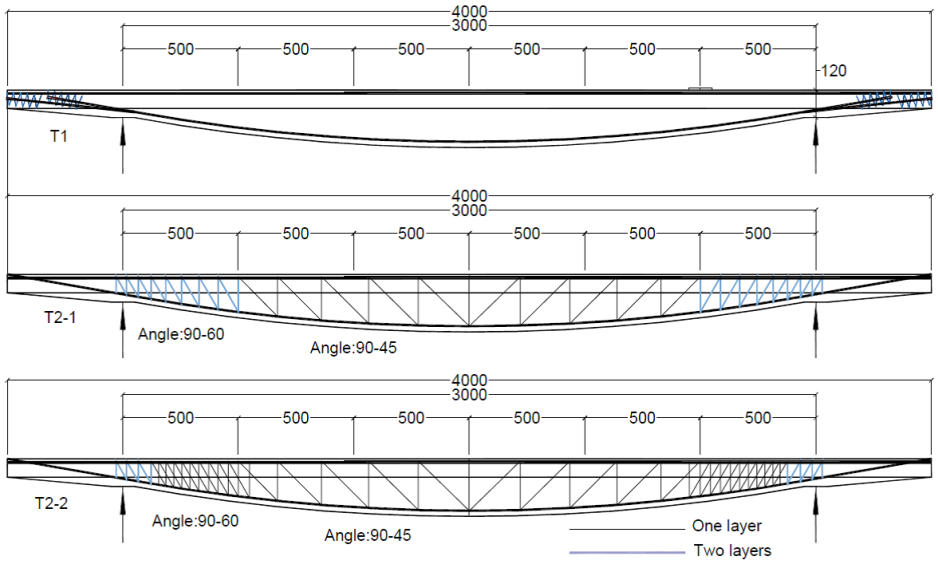


Figure 6-7: Shear design of groups T1 and T2

T2-1 and T2-1R were designed with shear links with a cross-section area of 8.56 mm$^2$ (two layers of 50k carbon fibres). As smaller cross section of W-FRP can increase the corner strength, the cross-section area of the shear links in T2-2 and T2-2R was designed as 4.28 mm$^2$ and the spacings between the shear links was designed as half of those in T2-1 and T2-2R to investigate the influence of the shear reinforcement patterns. As a result, the T2 and T2R specimens all had the same shear reinforcement ratio of 0.34% (calculated according to Equation 3.7).

As analysed in the prismatic beam tests and the tapered beam tests, it has been shown that the inclined W-FRP shear links could be more efficient than the vertical ones. Consequently, the shear reinforcement in specimens of group T3 was designed with the same reinforcement ratio as that of T2 and T2R but with patterns comprising all inclined shear links with constant angles of 60° and 45° to the horizontal axis as shown in Figure 6-8. The two shear reinforcement patterns of all diagonal links in T3-1 and T3-2 were designed to provide comparisons with group T2 and T2R. The shear links of T3-1 were designed with a cross-section area of 8.56 mm$^2$ and the shear links of T3-2 were designed with half of the cross-section area as well as the spacing of the shear

links in T3-1.

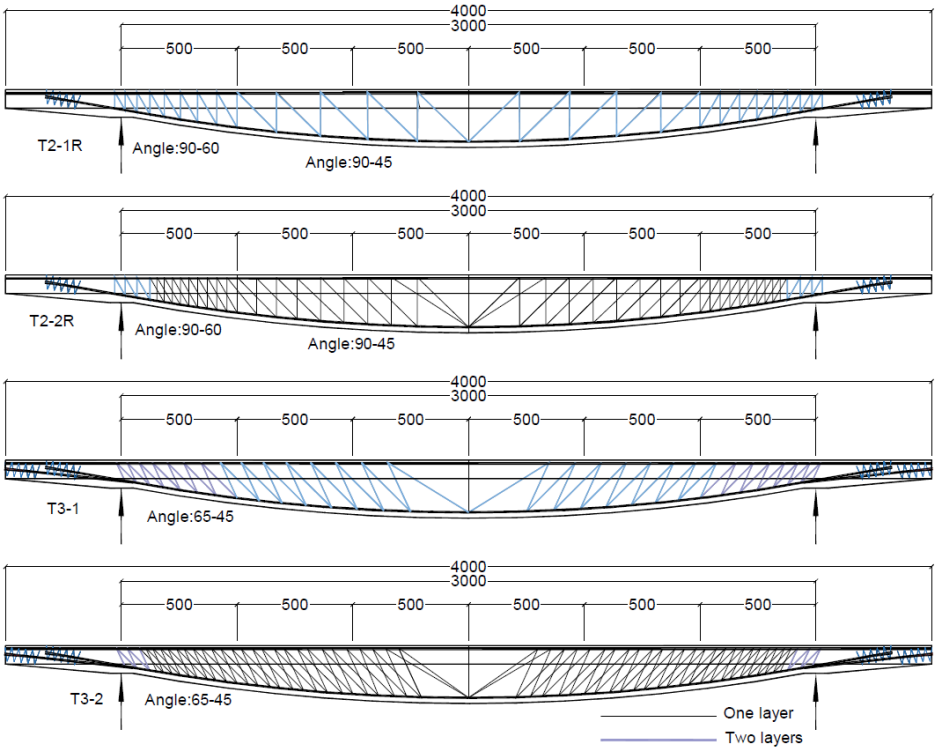


Figure 6-8: Shear design of groups T2R and T3

The shear reinforcement of T4-2 was designed with the same pattern (with constant angles of 60° and 45°) and cross section area (8.56 $mm^2$) with T3-1, as shown in Figure 6-9. However, due to the geometry difference, the spacings between shear links were larger, resulting in a lower shear reinforcement ratio, 0.26% (Equation 3.7).

Specimens T4-1, T5 and T6 were designed with higher shear reinforcement ratios and the same shear reinforcement pattern as T3-1 to avoid shear failure, as shown in Figure 6-9. The shear links of the three specimens had a cross-section area of 21.4 $mm^2$, which were composed of five layers of 50k carbon fibre tows. The resulting reinforcement ratios (Equation 3.7) of these three specimens were 0.65%, 0.85% and 0.87% respectively, due to the different geometries.

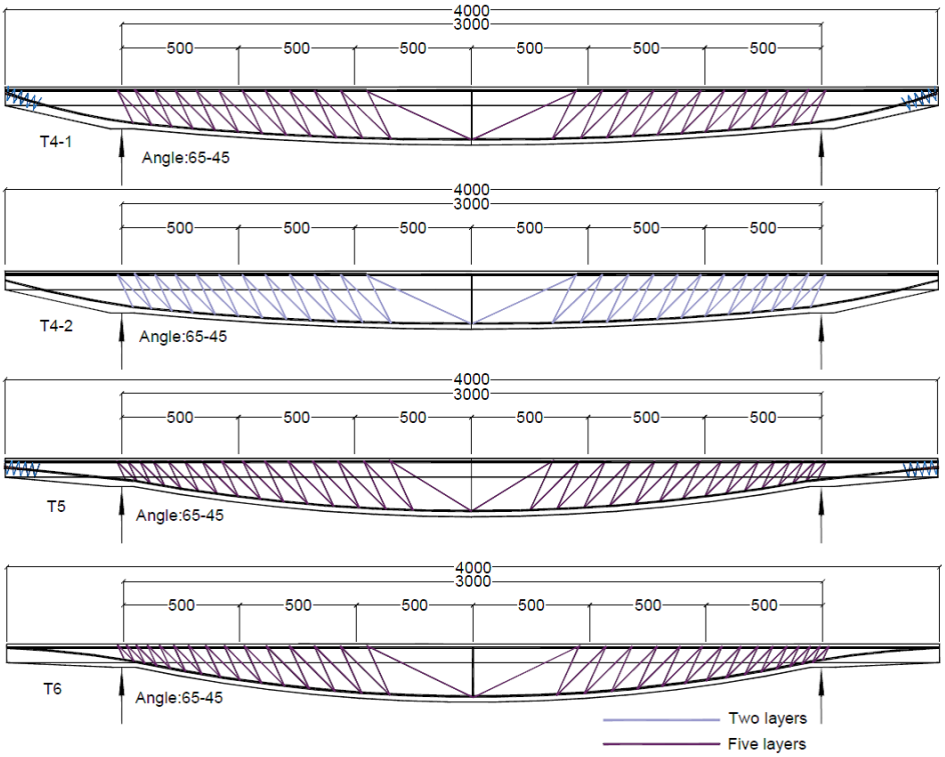


Figure 6-9: Shear design of groups T4, T5 and T6

The shear capacities of the T beam specimens were predicted using the design procedures presented in Chapter 3 (revised ACI-440.1R (2015), CSA-S806 (2012) and the MCFT model (Vecchio and Collins, 1988)). The calculation program is formulated to 'Matlab' codes in Appendix A, which incorporates the influence of the diagonal longitudinal bars, variable-depth geometries, corner strength of shear reinforcement and inclined shear reinforcement. The predictions of shear capacity (total applied load) are shown in Table 6.4.

In the MCFT calculation, the shear stress was assumed to be carried by two parts of each cross section: the compression zone in the flange and the tension zone within the web width. Following the typical shear stress distribution of a cross section from the variable depth beam (see section 2.4.2.2), the shear stress distribution in the compression zone was assumed as a concaved parabola. For simplification, the area of shear stress distribution in the compression zone was calculated as one-third of the depth of compression zone multiplied by the maximum shear stress at the neutral axis. The prediction of the revised MCFT model had variations for the specimens in the same testing group of T2, T2R and T3, which was caused by the different design strain

in shear links having different cross section area, which has been discussed in Chapter 5.

Table 6.4: Shear predictions of T beams

| Specimen | Shear predictions (kN) | | |
|---|---|---|---|
| | $V_{u,ACI}$ | $V_{u,CSA}$ | $V_{u,MCFT}$ |
| T1 | 33 | 47 | - |
| T2-1 | 105 | 200 | 108 |
| T2-2 | 105 | 200 | 173 |
| T2-1R | 105 | 200 | 108 |
| T2-2R | 105 | 200 | 173 |
| T3-1 | 105 | 200 | 108 |
| T3-2 | 105 | 200 | 173 |
| T4-1 | 221 | 301 | 267 |
| T4-2 | 111 | 199 | 104 |
| T5 | 213 | 303 | 273 |
| T6 | 193 | 295 | 245 |

### 6.2.5 Anchorage design

Specimen T2-1 and T2-2 were designed first. In the original design, no additional anchorage was installed at the end of the flexural bars. The middle one of the three flexural bars was not extended to the support to save material as two flexural bars can provide sufficient tensile force to resist bending moment at the support area, Figure 6-10. This arrangement of flexural reinforcement and no anchorage design was named as Anchorage I.

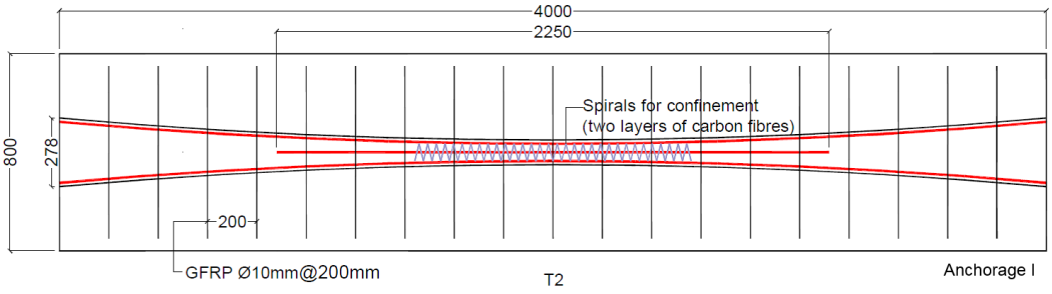


Figure 6-10: Arrangement of anchorage and distributed bars in flange of group T2

Both T2-1 and T2-2 failed in the end slip of longitudinal bars. In order to ensure anchorage strength, all longitudinal bars were extended beyond the support and a

splayed anchorage (section 2.4.3) was installed at the end of each longitudinal bar for the other specimens.

Following the research of splayed anchorage from Kostova (2016), the design details of the splayed anchorage are shown in Figure 6-11. The end of each bar was notched over a 100mm length. A wedge of 4° made of carbon plate was used to splay the notch.

A CFRP helix of 150mm length, 60mm diameter and 30mm spacing was fabricated to provide confinement to the splayed anchorage and to prevent the wedges from being pulled out. The spirals were fabricated using two layers of 50k carbon fibres and Tyfo S two-component epoxy, which have been used in the W-FRP shear reinforcement fabrication. Another helix made of the same material (Figure 6-11) was designed to confine the concrete at mid-span as shown in Figure 6-10 and Figure 6-12.

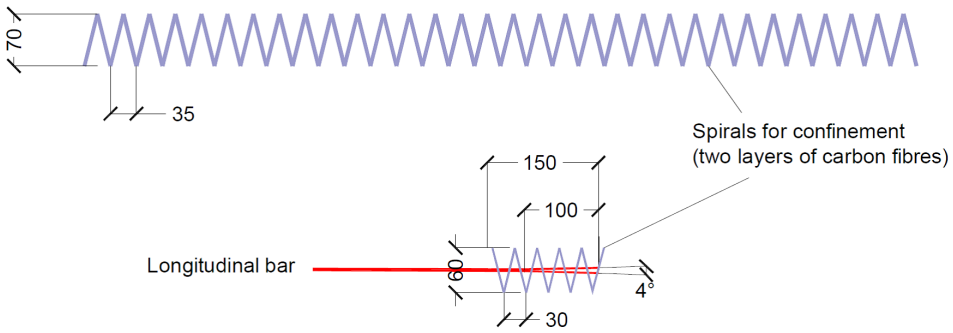


Figure 6-11: Splayed anchorage and spirals design

The other four types of different anchorage designs (Anchorage II, III, IV and V), shown in Figure 6-12, were to examine the influence of anchorage strength. The distributed bars (GFRP ⌀10mm) were arranged as the flexural reinforcement of the overhanging flange. The spacing of 200mm was chosen following the specification of the minimum reinforcement ratio for a structural slab (0.0014) in ACI-318 (2008).

In accordance with the prediction model of splayed anchorage strength (Equation 2.31), the strengths of the designed splayed anchorage including the bonding length were calculated as shown in Table 6.5 in which $F_{bs}$ is the ultimate tensile strength of the side bars; $F_{bm}$ is the ultimate tensile strength of the middle bars, whilst $\epsilon_{bs}$ and $\epsilon_{bm}$ are the ultimate strains of the side bars and middle bars respectively.

Table 6.5: Anchorage strength of longitudinal bars

| Anchorage type | Specimens | $F_{bs}$ (kN) | $F_{bm}$ (kN) | $\epsilon_{bs}$ (%) | $\epsilon_{bm}$ (%) |
|---|---|---|---|---|---|
| I | T2 | 103 | - | 0.99 | - |
| II | T1, T3 | 185.4 | 154.6 | 1.64 | 1.37 |
| III | T2R | 154.6 | 154.6 | 1.37 | 1.37 |
| IV | T4-1, T5 | 185.4 | 185.4 | 1.64 | 1.64 |
| V | T4-2, T6 | 103 | 103 | 0.99 | 0.99 |

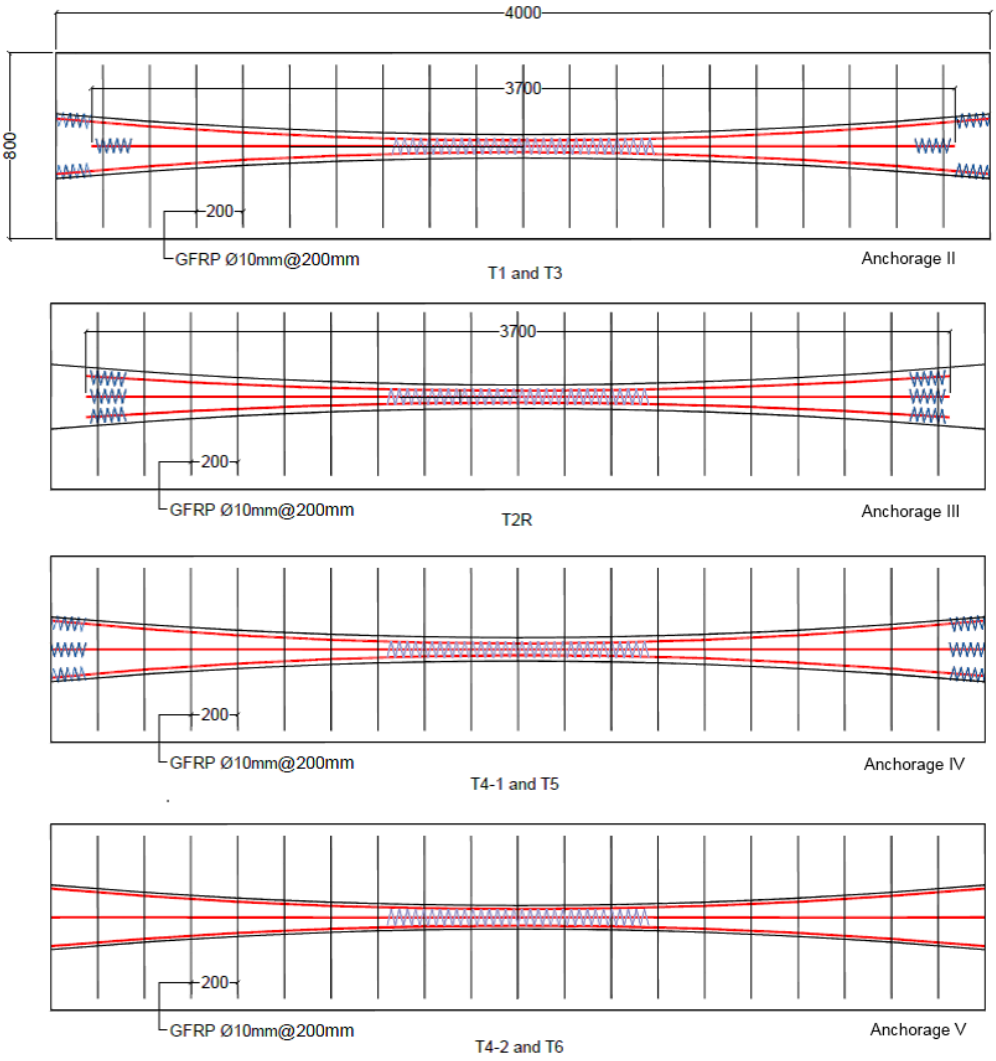


Figure 6-12: Arrangement of Anchorage II, III, IV and V

### 6.2.6 Design summary

Following the designs of the test setup, material property, geometry, shear reinforcement and anchorage, the details of the specimens are summarised in Table 6.6.

Table 6.6: Design summary of specimens

| Specimen | $d_s$ (mm) | $d_m$ (mm) | Flexural bars (mm) (CFRP) | $\rho_{fv}$ (%) | $\alpha$ (°) | $A_{fv}$ ($mm^2$) | Anchorage Type | Expected Failure |
|---|---|---|---|---|---|---|---|---|
| T1 | 120 | 250 | 3⌀10 | 0.00 | - | 0.00 | II | Shear |
| T2-1 | 120 | 250 | 3⌀10 | 0.34 | 60/90 | 8.56 | I | Shear |
| T2-2 | 120 | 250 | 3⌀10 | 0.34 | 60/90 | 4.28 | I | Shear |
| T2-1R | 120 | 250 | 3⌀10 | 0.34 | 60/90 | 8.56 | III | Shear |
| T2-2R | 120 | 250 | 3⌀10 | 0.34 | 60/90 | 4.28 | III | Shear |
| T3-1 | 120 | 250 | 3⌀10 | 0.34 | 45/65 | 8.56 | II | Shear |
| T3-2 | 120 | 250 | 3⌀10 | 0.34 | 45/65 | 4.28 | II | Shear |
| T4-1 | 180 | 250 | 3⌀10 | 0.64 | 45/65 | 21.40 | IV | Flexural |
| T4-2 | 180 | 250 | 3⌀10 | 0.26 | 45/65 | 8.56 | V | Shear |
| T5 | 120 | 250 | 3⌀10 | 0.85 | 45/65 | 21.40 | IV | Flexural |
| T6 | 100 | 250 | 3⌀10 | 0.87 | 45/65 | 21.40 | V | Flexural |

Where $d_s$ is the depth of the supports; $d_m$ is the depth at the mid-span; $\rho_{fv}$ is the shear reinforcement ratio in the shear span; $\alpha$ is the angle of the shear links to the horizontal axis and $A_{fv}$ is the cross section area of the shear links.

## 6.3 Specimen fabrication

### 6.3.1 Flexible formwork

In line with the literature in section 2.2.2, fabric formwork with a keel (Orr, 2012) was designed, as shown in Figure 6-13. The formwork was constructed using plywood and woven fabrics. The woven fabrics were stapled onto the plywood to form the flange of the specimens and the keels to control the depth of the different cross-sections of the beams. All the specimens were formed using fabric formwork.

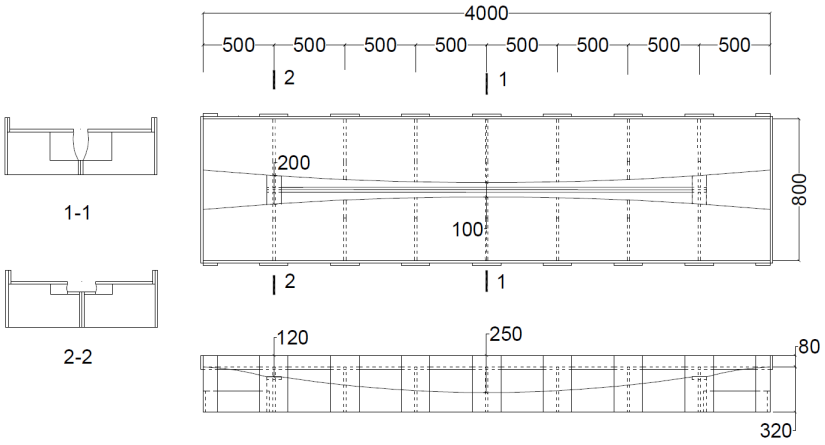


Figure 6-13: Design of fabric formwork

### 6.3.2 Automatic winding and W-FRP cage

An automated winding machine was developed in order to improve the hand-winding fabrication of W-FRP cages. The resulting cages were precisely produced with consistent quality, as shown in Figure 6-14. The winding machine was composed of a controlling computer, a winding mandrel and a resin tank.

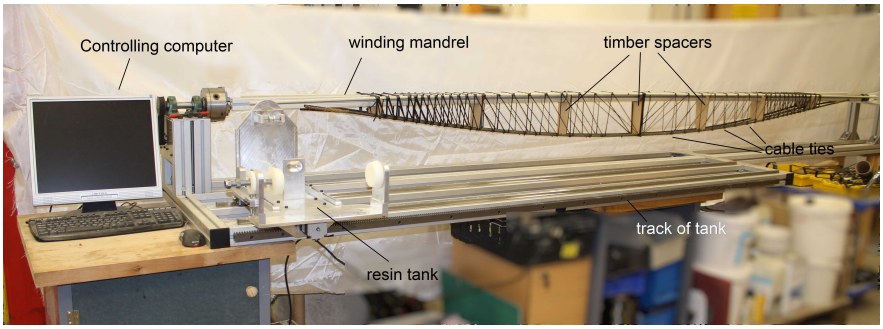


Figure 6-14: Automated winding machine

In the automated winding, instructions were given by the computer with the programmed codes. In the programmed codes, the horizontal coordinates of the winding position and the angle coordinates of mandrel rotation were calculated following the flexural design in section 6.2.3 and shear design in section 6.2.4. The mandrel was used to assemble the longitudinal bars and enable the winding process by rotation. The resin tank was used to coat the carbon fibres with epoxy resin before winding around the longitudinal bars and carrying the carbon fibre tows to the horizontal coordinates of

the winding. When each shear link was wound, the resin tank moved to the calculated horizontal coordinate and then the mandrel rotated following the angle coordinates.

With two people operating it, on average the winding process took four hours per cage, including preparation, automated winding and cleaning. All the cages of the specimens were wound following these winding procedures. After the winding, all the cages were placed under laboratory conditions for 72 hours to be cured. A cured cage is shown in Figure 6-15.

Figure 6-15: W-FRP cage after curing

### 6.3.3 Splayed anchorage fabrication

The splayed anchorages were fabricated before the automated winding of the W-FRP cages. The wedges made of carbon plate with a 4° angle were cut and inserted in the notched bar ends (section 6.2.5). As suggested by Kostova (2016), a sand coating was made for the splayed anchorage to increase the friction between the concrete and anchorages. Samples of the splayed bars are shown in Figure 6-16 (a).

The spirals used for the splayed anchorage were fabricated by winding the wet fibres around a plastic tube with outer diameter of 60mm, whilst the spirals for concrete confinement at the mid-span of each specimen were fabricated using a plastic tube with outer diameter of 70mm. The resulting splayed anchorage samples are shown in Figure 6-16 (b). The spirals were fastened on the flexural reinforcement using cable ties to stay in place during casting.

During the test of T3-1, although the splayed anchorage was installed, failure occurred due to end slip failure of the longitudinal bars. In order to avoid the same type of failure in specimen T3-2, an additional mechanical anchorage was installed on each protruding

end of the longitudinal bars in T3-2 as shown in Figure 6-17. The mechanical anchorage was made of a 50mm long steel tube. The protruding part of the longitudinal bars was covered with epoxy (HIT-RE 500) and the steel tube was screwed on the protruding bar.

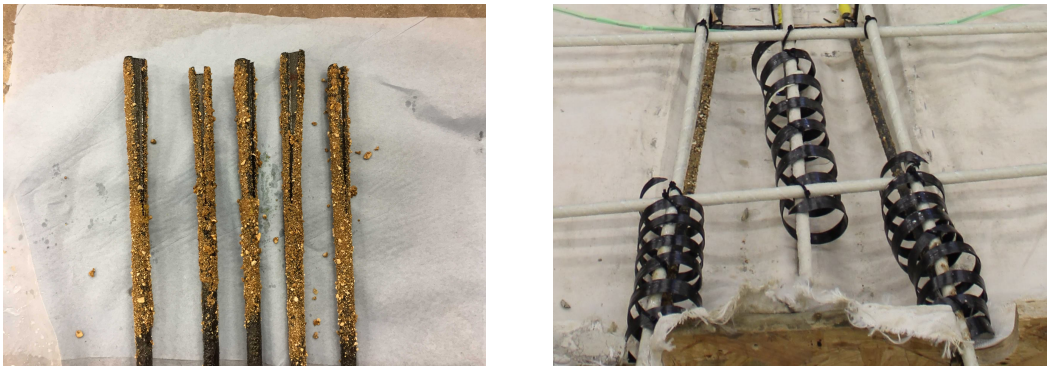

(a) Splayed bars of T2R (b) Splayed anchorage for T2R

Figure 6-16: Fabrication of splayed anchorage

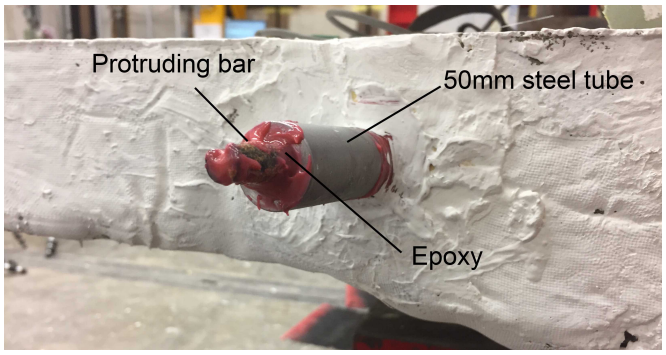


Figure 6-17: An additional anchorage installed in T3-2

### 6.3.4 Casting

After fabrication of W-FRP cages, preparation of fabric formwork and installation of strain gauges on the shear links, the specimens were ready for casting. The fabric formwork and W-FRP cage of T2-1 before casting are shown in Figure 6-18. Group T2 was cast using ready-mix concrete. Due to the low quality of the ready-mix concrete in group T2 at 28 days (section 6.4.3), the concrete in all the remaining specimens was mixed in the concrete laboratory of the University of Bath.

All these specimens were proposed to be tested at 10 days and hence the mix recipe was designed to achieve the target concrete strength (C45/55), as shown in Table 6.7.

Dragon Alfa CEM I 42.5 cement, saturated river sand and crushed 10mm aggregate were adopted as the materials for mixing. Ten cubes and five cylinders were made for the concrete strength testing.

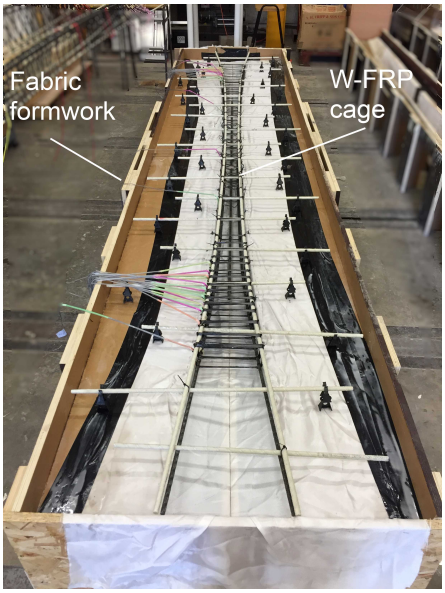


Figure 6-18: Fabric formwork and W-FRP cage of T2-1 before casting

Table 6.7: Concrete mix design

| Quantities ($m^3$) | Cement (kg) | Water (kg) | Aggregate (kg) | Sand (kg) |
|---|---|---|---|---|
| 1 | 620 | 210 | 710 | 865 |

### 6.3.5 Summary

This section presents the fabrication process of the specimens. Fabric formwork has been designed and fabricated following the literature (Orr, 2012) and the specimen designs. A new automated production method has been developed, by which W-FRP cages with standard quality were produced. Splayed anchorages were installed on the specimens following the work of Kostova (2016). Finally, the specimens were cast and cured for 10 days (28 days for T2) in laboratory conditions before testing.

## 6.4 Test program

### 6.4.1 Test setup

All the specimens were tested under seven-point bending to simulate an approximation to uniformly distributed load. The test rig was set on the strong floor as shown in Figure 6-19. Rigid steel frames with loading jacks were fixed on the strong floor and the specimens were simply supported on bridge bearings.

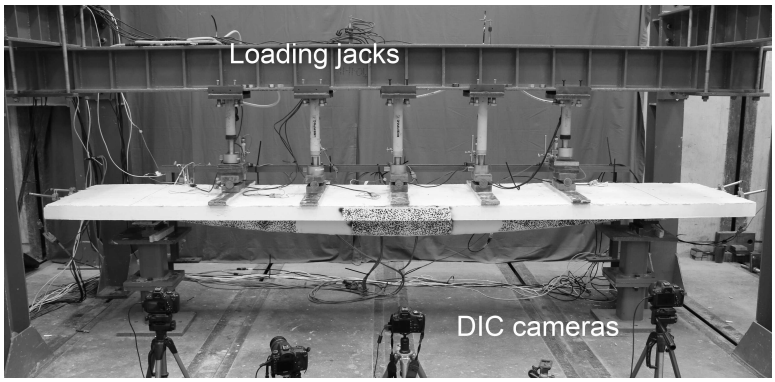


Figure 6-19: Test setup

### 6.4.2 Instrumentation and conventions

As shown in Figure 6-20, load cells, displacement transducers (LVDTs) and strain gauges were placed on the specimens. Supports are denoted by A and B. The five loading jacks were denoted by P1 to P5 from support A to support B. Under each loading jack, a load cell was used to record the applied load. Displacement transducers placed on each jack were denoted by T1 to T5. Transducers were also placed on the intentionally protruded reinforcement at the two ends of the specimens to record the bar slip. The bar-slip transducers were denoted as T6 and T7 at support A and T8 and T9 at support B.

Strain gauges were installed on flexural reinforcement, shear reinforcement and the concrete surface. The gauges on the longitudinal bars in Figure 6-20 were placed symmetrically in four locations. Label 'F' denotes the flexural bars strain gauge. Label 'A' and 'B' denotes the side of support A and support B respectively. Label 'M' and 'S' denotes the middle bar and two side bars on which the strain gauges were installed. Strain gauges were also installed at the middle of one leg of the shear links in the

two shear spans (between the support and the adjacent loading jack). The shear link strain gauges were denoted as 'SA'and 'SB' to show the shear links at support A and support B. Three concrete strain gauges were installed on the top surface of the flange at 100mm away from loading point P3, P4 and P5, being denoted as CS1, CS2 and CS3 respectively.

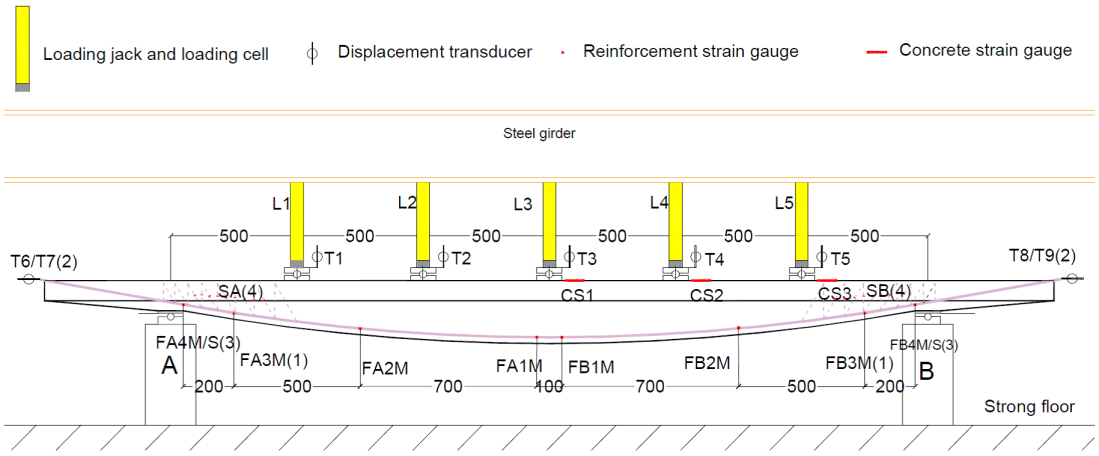


Figure 6-20: Instrumentation locations

The numbers in brackets denote the four minor differences in the instrumentation positioning between the different specimens due to the progressive testing schedule, as shown in Figure 6-20. For T2-1 and T2-2, all the gauges on the longitudinal bars were installed on the side bars and none was installed at the locations of FA3M, FB3M, FA4M and FB4M. For T2-1R and T2-2R, no bar slip was measured from T6 to T9 because no longitudinal bars protruded. The number of shear reinforcement gauges varied for the different specimens due to the different shear designs (section 6.2.4).

As shown in Figure 6-19, DIC speckle patterns were painted on the surface of the shear span and mid-span, whilst five cameras were set 2m away from the speckled surface to record the movement of speckle patterns, thus allowing for the analysis of the performance of the specimens.

### 6.4.3 Material properties

Five concrete cubes and three cylinders cast with each specimen were tested on the testing day to determine the concrete strength as shown in Table 6.8. The material properties of the flexural and shear reinforcement are shown in Table 6.2. Actual material properties are used in all subsequent analysis.

Table 6.8: Concrete strength

| Specimen | Cylinder strength $f_c$ (MPa) | SD (MPa) | COV (%) | Cube strength $f_{c,cube}$ (MPa) | SD (MPa) | COV (%) |
|---|---|---|---|---|---|---|
| T1 | 40.6 | 3.3 | 8.2 | 50.0 | 4.3 | 8.6 |
| T2-1 | 28.4 | 3.4 | 11.9 | 31.6 | 1.1 | 3.3 |
| T2-2 | 28.4 | 3.4 | 11.9 | 31.6 | 1.1 | 3.3 |
| T2-1R | 37.6 | 3.1 | 8.1 | 41.3 | 1.9 | 4.7 |
| T2-2R | 42.0 | 5.6 | 13.4 | 47.9 | 1.6 | 3.4 |
| T3-1 | 44.0 | 3.2 | 7.4 | 44.2 | 2.4 | 5.4 |
| T3-2 | 47.1 | 1.6 | 3.5 | 49.1 | 3.4 | 6.8 |
| T4-1 | 44.0 | 1.4 | 3.3 | 48.3 | 1.3 | 2.7 |
| T4-2 | 47.5 | 1.1 | 2.3 | 55.1 | 2.7 | 5.0 |
| T5 | 49.2 | 2.2 | 4.4 | 53.7 | 1.9 | 3.5 |
| T6 | 51.8 | 1.1 | 2.2 | 52.7 | 1.7 | 3.3 |

## 6.5 Test results and interpretations

### 6.5.1 Test results summary

All the specimens were tested to failure under displacement control at increments of 10kN applied load (2kN for each jack). Three different types of failure modes (shear failure, flexural failure and end slip failure) were observed across all the tests, as shown in Table 6.9.

Table 6.9: Test results summary

| Specimen | Failure load (kN) | Deflection at failure load (mm) | Failure Mode |
|---|---|---|---|
| T1 | 101 | 45 | Shear failure |
| T2-1 | 153 | 100 | End slip |
| T2-2 | 160 | 109 | End slip |
| T2-1R | 188 | 80 | Shear |
| T2-2R | 222 | 100 | End slip |
| T3-1 | 226 | 95 | End slip |
| T3-2 | 253 | 120 | Flexural |
| T4-1 | 279 | 107 | Flexural |
| T4-2 | 217 | 90 | End slip |
| T5 | 261 | 117 | Flexural |
| T6 | 233 | 110 | Flexural |

### 6.5.2 Failure mode, ultimate capacity and stiffness

#### 6.5.2.1 Shear failure specimens

Specimens T1 and T2-1R were designed for shear failure, and both failed in shear. For these two specimens, the first shear crack was observed on the web in the shear span at approximately 60kN, which initiated at approximately 50mm away from the edge of the support plate. At 101kN, the shear cracks in T1 developed in the flange horizontally and separated the beams into two parts with 45mm mid-span displacement, as shown in Figure 6-21. T2-1R failed at 188kN total applied load with 80mm mid-span displacement due to the rupture of W-FRP shear reinforcement. The shear failure of T2-1R is shown in Figure 6-22.

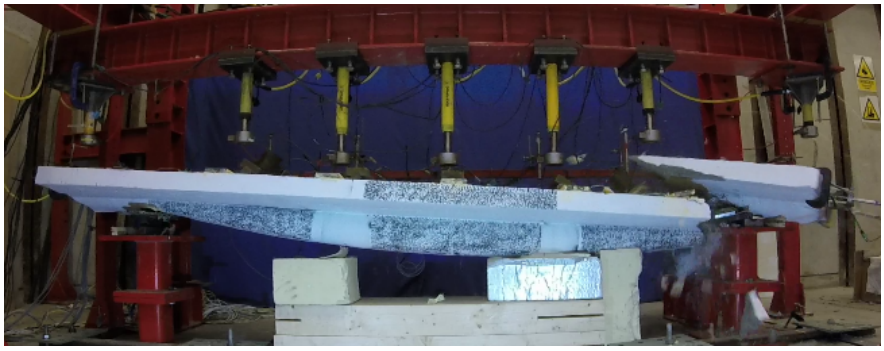

Figure 6-21: Shear failure in T1

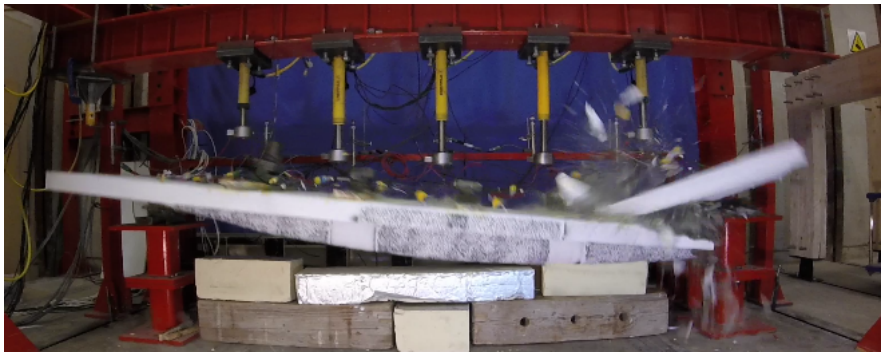

Figure 6-22: Shear failure in T2-1R

The specimens which failed in shear (T1 and T2-1R) exhibited near-linear load-displacement relations during the tests, as shown in Figure 6-23. Before shear crack formation, the stiffness of T1 and T2-1R had been similar. After the shear crack formation, the stiffness of T1 was 24% lower than T2-1R. Having no shear reinforcement, T1 developed larger shear crack width than T2-1R and hence a larger displacement. The W-FRP

shear reinforcement of T2-1R enabled a shear capacity of 188kN, 86% higher than T1 (101kN). When the displacement reached 12.5mm ($l/240$ limit required by ACI-440.1R (2015)), the total load applied to T1 and T2-1 reached 35kN, as shown in Figure 6-23.

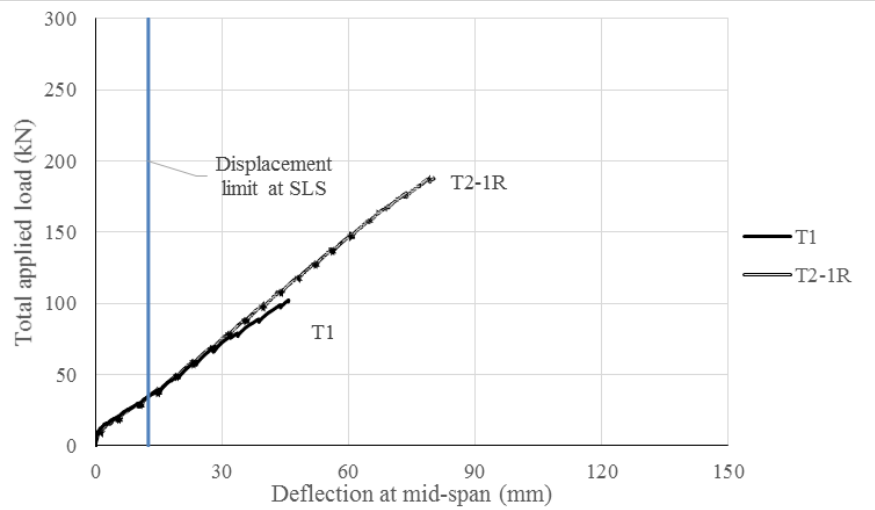


Figure 6-23: Load - deflection comparisons in T1 and T2-1R

#### 6.5.2.2 Flexural failure specimens

Specimen T3-2 was designed to fail in shear but failed in flexure. Similar to the shear failure specimens, the first bending crack was observed at mid-span at approximately 20kN and the first shear crack was observed in the shear span at approximately 80kN. Under increasing load, loud noises were heard from side B of T3-2 under 220kN of applied load and the longitudinal bars at side B slipped. The concrete beneath P5 started to crush and T3-2 reached the failure load of 253kN with the end slip of longitudinal bars at side B, rupture at mid-span (Figure 6-24) and 120mm displacement at mid-span.

T4-1, T5 and T6 were designed to fail in flexure, and all failed in flexure. With a very similar crack development to T3-2, T4-1 failed at 279kN (107mm mid-span displacement) with the longitudinal bars rupture at mid-span (Figure 6-25). T5 also failed in flexure with longitudinal bar rupture at mid-span at 261kN (117mm mid-span displacement), as shown in Figure 6-26. T6 failed in flexure at 233kN (110mm mid-span displacement) which was caused by concrete crushing under jack P5 (Figure 6-27) at 220kN. This flexural failure could be caused by a casting flaw located near loading jack P5 that voids and honeycombs were found at the flange surface. The longitudinal bars

and shear links were ruptured because of the bending failure (Figure 6-28). Zero bar slip was recorded at the ends of T4-1, T5 and T6.

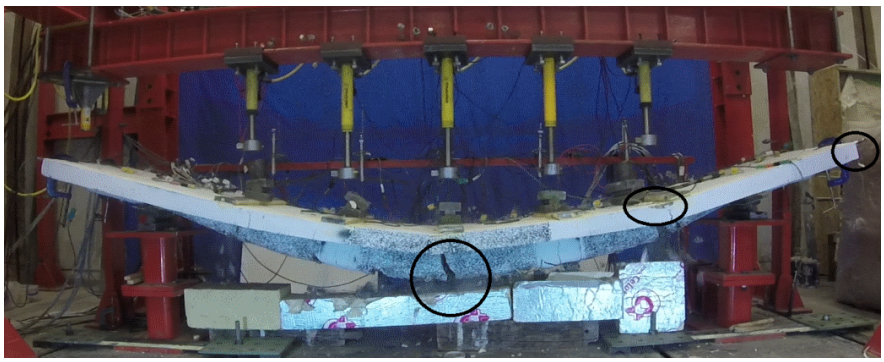

Figure 6-24: Flexural failure in T3-2


Figure 6-25: Flexural failure in T4-1

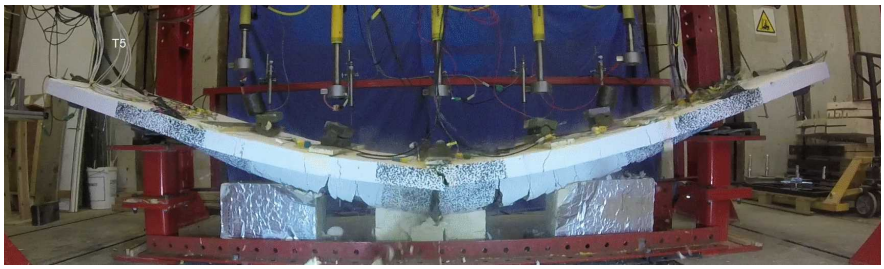


Figure 6-26: Flexural failure in T5

With the greatest support depth (180mm), T4 exhibited the highest stiffness in comparison to the other three bending failure specimens. As shown in Figure 6-29, T3-2 and T6 had similar stiffness reduction after 220kN. The stiffness reduction of T3-2 could have been caused by the slip of the longitudinal bars at 220kN. The stiffness reduction was caused by concrete crushing (see Figure 6-27 and Figure 6-28) under loading jack P5, which confirmed the flexure failure of T6. The load applied to T3-2, T4-1, T5 and

T6 reached 35kN, 41kN, 30kN and 30kN respectively when the mid-span displacement reached 12.5mm ($l/240$), as shown in Figure 6-29.

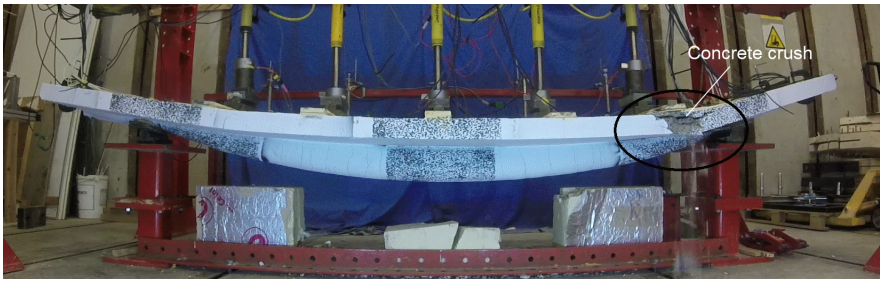


Figure 6-27: Flexural failure in T6

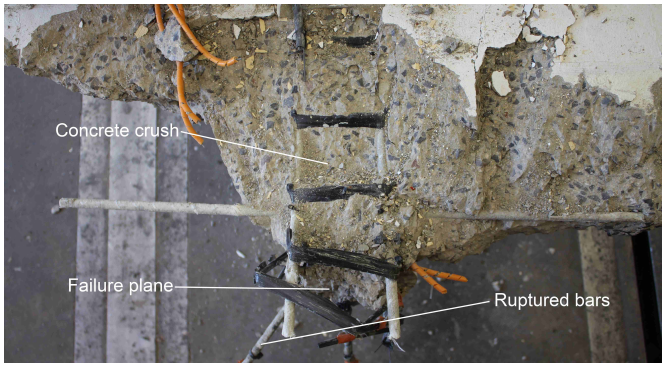


Figure 6-28: Failure plane in T6

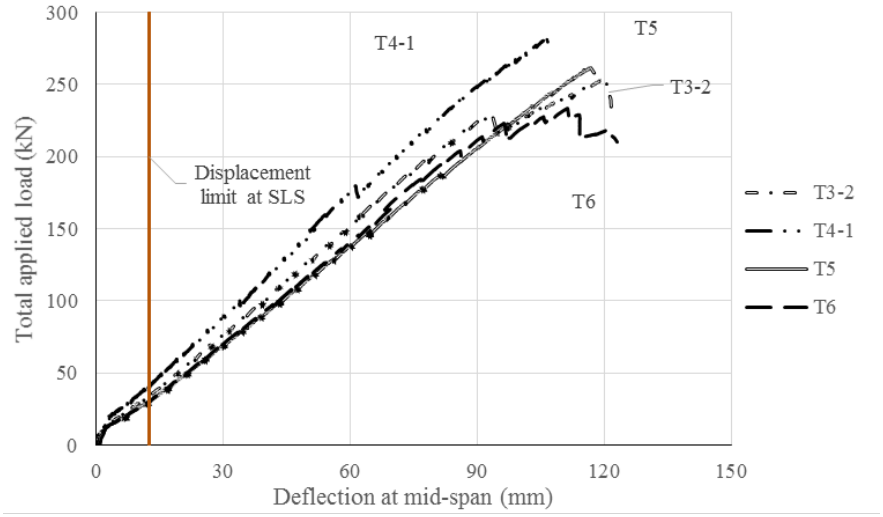


Figure 6-29: Load - deflection comparisons in the flexural failure specimens

#### 6.5.2.3 End slip failure specimens

Group T2 was designed to fail in shear but failed in end slip of the longitudinal bars. T2-1 and T2-2 encountered flexural cracks on the web of mid-span at 20kN. At about 50kN, the first shear crack propagated in the shear span (about 50mm from the edge of support). At 150kN, noises were heard from the support B and then T2-1 failed under large curvature (Figure 6-30). The protruding longitudinal bars in the anchorage zone were pulled into the concrete flange at side B (Figure 6-31 b). Concrete crushing under P5 in T2-2, which could have been caused by the low concrete strength, occurred after 150kN (Figure 6-31 a) and T2-2 failed at 160kN at side B (Figure 6-31 b).


Figure 6-30: End slip failure in T2-1 and T2-2

T2-2R, T3-1 and T4-2 were also designed to fail in shear but failed in end slip of longitudinal bars. Loud noises were heard during the test of T2-2R at 200kN. No end slip of longitudinal bars was observed from T2-2R because all the longitudinal bars were inside of the beam. At approximately 220kN, the width of the major shear crack of T2-2R at side A was over 10mm by visual observation (Figure 6-32). T2-2R failed in end slip at side B at 223kN applied load. Loud noises were heard during the test of T3-1 at 200kN. T3-1 failed in end slip at side B at 226kN applied load (Figure 6-32). For specimen T4-2, the first noise was heard at about 140kN. At every 20 to 30kN load increment, more noises of shear link rupture were heard. Under the load of 217kN, the longitudinal bars were pulled into the flange at B side and the specimen failed in end slip of longitudinal bars (Figure 6-32).

(a) Concrete crushing in T2-2 (b) End slip of longitudinal bar

Figure 6-31: Failure of concrete and end slip of longitudinal bar

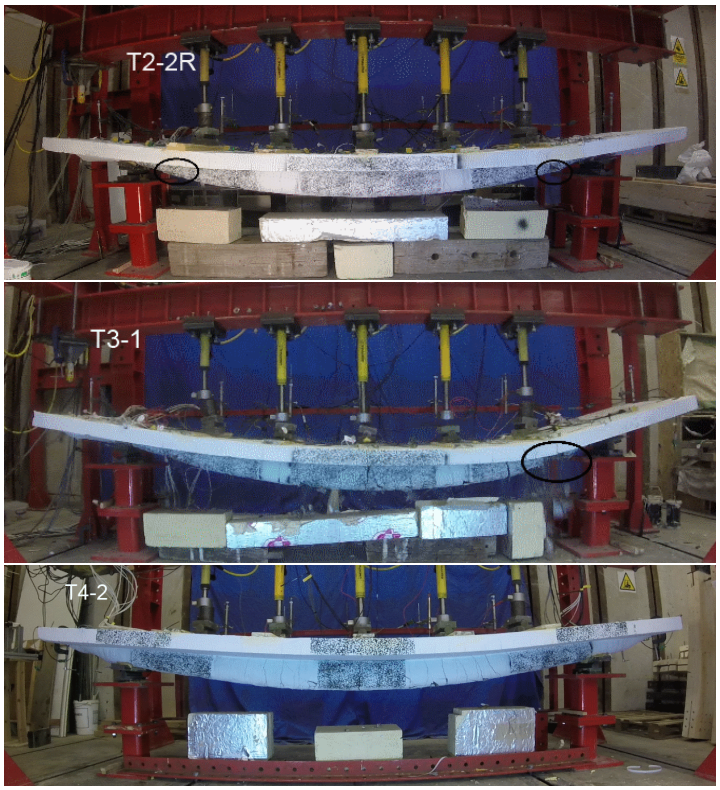


Figure 6-32: End slip failure in T2-2R, T3-1 and T4-2

Amongst the specimens that failed in end slip, group T2 also had the lowest stiffness as shown in Figure 6-33. The lower stiffness before 90kN of applied load could be caused by not extending all longitudinal bars to the support. The stiffness of group T2 decreased 30% after 90kN of applied load. Since no bar slip was found for the two

protruding longitudinal bars in T2-1 and T2-2 at 90kN, the stiffness reduction might have been caused by end slip of the middle bar at about 90kN. The load applied to T2-1, T2-2, T2-2R, T3-1 and T4-2 reached 33kN, 32kN, 32kN, 34kN and 36kN respectively when the mid-span displacement reached 12.5mm ($l/240$), as shown in Figure 6-33.

Specimens T2-2R, T3-1 and T4-2 had the similar stiffness before the end slip occurred. Similar stiffness reduction for T2-2R, T3-1 and T3-2 (Figure 6-33 and Figure 6-29) after 200kN could have been caused by the end slip of the longitudinal bars since the end slip in T3-1 and T3-2 occurred at the same load of stiffness change. At the failure load, specimens T2-1, T2-2, T2-2R, T3-1 and T4-2 had respective mid-span displacement of 100mm, 109mm, 100mm, 95mm and 90mm as shown in Table 6.9.

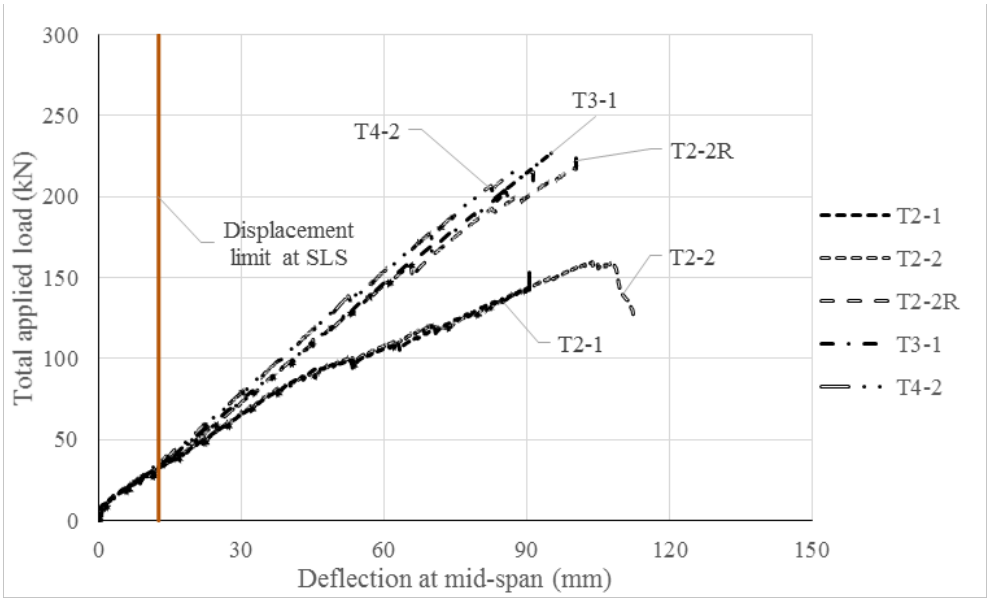


Figure 6-33: Load - deflection comparisons in the end slip failure specimens

### 6.5.3 Longitudinal bars

The load-strain curves for the longitudinal bars near the support in shear failure specimens are shown in Figure 6-34. The longitudinal bars of T1 had similar performance to that of T2-1R before 70kN. After the shear cracks formed at 70kN (side B), the slopes of the load-strain curves in T1 are lower than T2-1R which correlates with similar slope difference in stiffness (Figure 6-23).

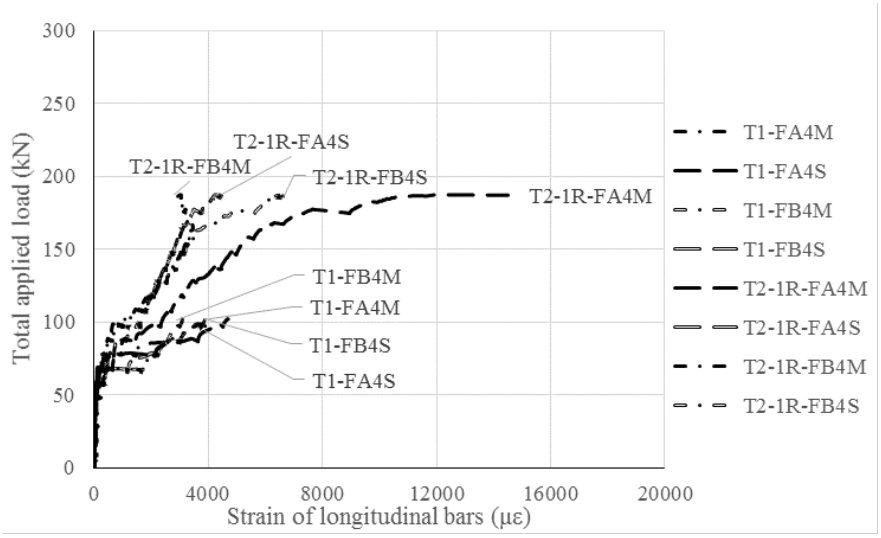


Figure 6-34: Strain in longitudinal bars near the supports in the shear failure specimens

The longitudinal bars in T4-1 had lower strains than the other specimens (Figure 6-35) which was also correlated against the largest stiffness of T4 (Figure 6-29). The larger support depth of T4-1 could be the reason for the smaller tensile force in the longitudinal bars compared with T5 and T6, which had similar shear reinforcement and anchorage designs. The strain data in T5 exhibited a large variation at the two side of the beam. The longitudinal bars at side A of T5 carried higher strain than all the other bars under the same load. The longitudinal bars in T3-2 exhibited similar strains with T5 (side B) and T6.

Similar correlations against the stiffness (Figure 6-29) were found in the load - strain curves of longitudinal bars at the supports (Figure 6-36). Group T2, which had the lowest stiffness, exhibited the largest strains in longitudinal bars under the same load whilst the other specimens had relatively similar strains before 200kN.

The plateaus in the load-strain curves (between 200kN and the failure load in Figure 6-36) occurred at the same load of the loud noises heard from the tests, which indicate that the tensile force carried by the longitudinal bars at the supports increased abruptly to very high values with little load increment. This could be the reason for the end slip failures in T2-1, T2-2, T2-2R, T3-1, T4-2 and T3-2. In addition, for the listed specimens, some of the strain gauges on the longitudinal bars at the support were lost before the failure loads and therefore the actual tensile force carried by longitudinal bars could have been larger than what the data showed.

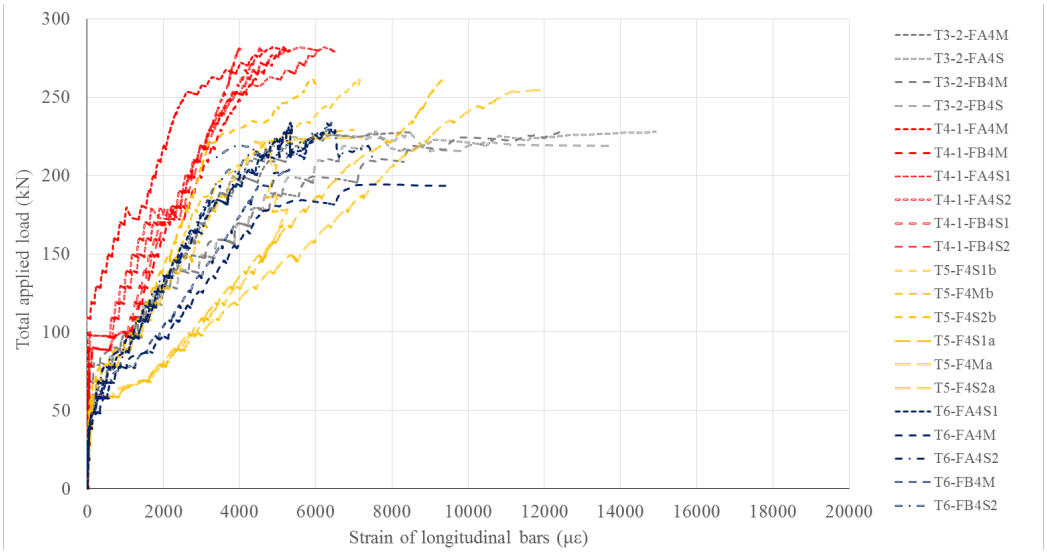


Figure 6-35: Strain in longitudinal bars near the supports in the flexural failure specimens

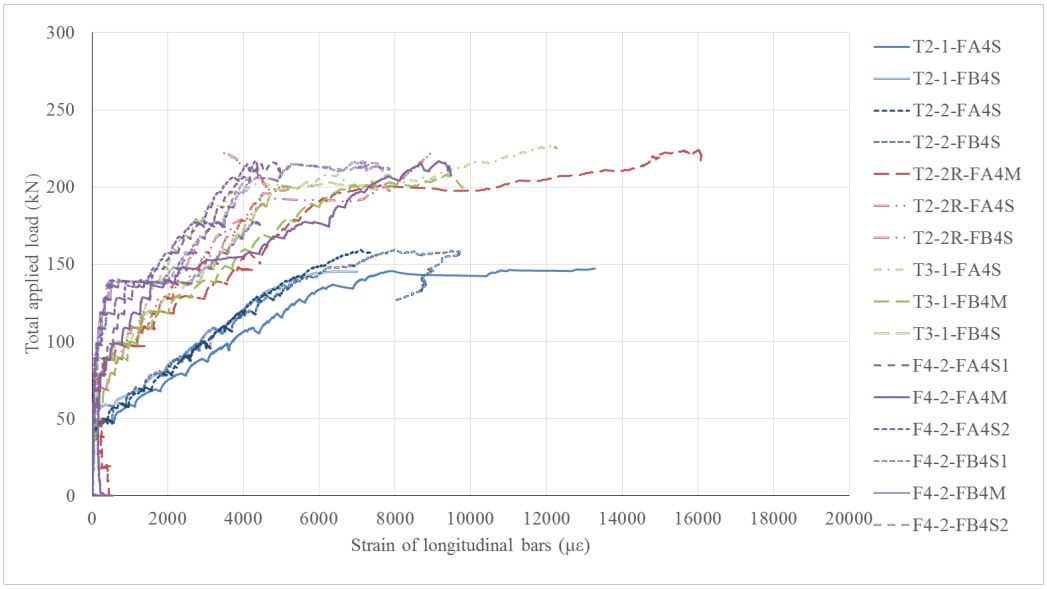


Figure 6-36: Strains in longitudinal bars near the support in the end slip failure specimens

### 6.5.4 Shear reinforcement

#### 6.5.4.1 Summary of the strain in W-FRP shear links

Table 6.10 summarises the minimum strain, maximum strain and average strain in the shear links (vertical and diagonal) of the shear span in all the specimens at the specified

loads.

As the loss of strain gauges on shear links in different pairs of specimens varied, for ease of comparison, the load in Table 6.10 is set as a value before gauge loss in either specimens. As specimens T4-1 and T4-2 failed at very different applied loads, two different loads were specified. For group T3, which had all diagonal links, the diagonal links at 65° to the horizontal axis are denoted as the vertical links in Table 6.10. The summary of shear links data shows that the diagonal links worked more efficiently than the vertical links on average, with the ratio $\epsilon_{d,ave.}/\epsilon_{v,ave.}$ varying from 1.3 to 2.8.

Table 6.10: Shear reinforcement performance in all specimens

| Specimen | Load (kN) | $\epsilon_{d,min}$ (%) | $\epsilon_{d,ave.}$ (%) | $\epsilon_{d,max}$ (%) | $\epsilon_{v,min}$ (%) | $\epsilon_{v,ave.}$ (%) | $\epsilon_{v,max}$ (%) | $\epsilon_{d,ave.}/\epsilon_{v,ave.}$ |
|---|---|---|---|---|---|---|---|---|
| T2-1 | 148 | 0.07 | 0.44 | 0.66 | 0.06 | 0.28 | 0.64 | 1.6 |
| T2-2 | 148 | 0.13 | 0.45 | 0.81 | 0.02 | 0.28 | 0.54 | 1.6 |
| T2-1R | 177 | 0.29 | 0.68 | 0.89 | 0.12 | 0.48 | 0.79 | 1.4 |
| T2-2R | 177 | 0.15 | 0.74 | 1.10 | 0.12 | 0.39 | 0.67 | 2.1 |
| T3-1 | 200 | 0.40 | 0.59 | 0.76 | 0.15 | 0.46 | 0.63 | 1.3 |
| T3-2 | 200 | 0.53 | 0.74 | 1.10 | 0.05 | 0.56 | 0.90 | 1.3 |
| T4-1 | 250 | 0.33 | 0.63 | 0.81 | 0.08 | 0.36 | 0.61 | 1.8 |
| T4-2 | 200 | 0.28 | 0.61 | 0.90 | 0.05 | 0.38 | 0.69 | 1.6 |
| T5 | 250 | 0.29 | 0.45 | 0.58 | 0.14 | 0.22 | 0.34 | 2.0 |
| T6 | 200 | 0.28 | 0.41 | 0.63 | 0.07 | 0.15 | 0.22 | 2.8 |

Where $\epsilon_{d,min}$ is the minimum strain recorded from all the diagonal links; $\epsilon_{d,ave.}$ is the average strain of all the diagonal links; $\epsilon_{d,max}$ is the maximum strain recorded from all the diagonal links; $\epsilon_{v,min}$ is the minimum strain recorded from all the vertical links; $\epsilon_{v,ave.}$ is the average strain of all the vertical links and $\epsilon_{v,max}$ is the maximum strain recorded from all the vertical links.

#### 6.5.4.2 Ruptured shear links

Shear link rupture was found in the shear failure specimens and also the end slip failure specimens. For example, the width of the major shear crack of T2-2R reached over 10mm by visual observation (see Figure 6-32) and the links across this major shear crack seem to be ruptured in the inspection after the test. A signal that shear links had ruptured was that the strain reading increased or decreased abruptly.

Using these proxy characteristics, the ruptured shear links were identified. All the end

slip failure specimens encountered shear link rupture during the tests and most of the rupture happened at the load of end slip of longitudinal bars, which means the loud noises heard during the tests could have been caused by the shear link rupture and the end slip of longitudinal bars.

In T2-2R and T3-1, shear link rupture occurred at 200kN applied load. In T3-2, the rupture of shear links occurred at 220kN applied load. In T4-2, the strain in shear links increased abruptly at 140kN of applied load, which is the same load when the first noise was heard. Although the strain recording continued, rupture of the ungauged leg of shear links might have happened and consequently increased the strain of the gauged leg.

## 6.6 Analysis and discussion

In this section, analysis and discussion of the T-beam tests are presented. The test data is processed to show the shear contributions of flexural and shear reinforcement. Then the contributing factors to the structural performance of the specimens are analysed, including the shear reinforcement, geometry and anchorage design. Following the analysis of the specimens, an equation of tensile force in longitudinal bars is proposed to establish the interactive relation between the shear reinforcement, geometry and anchorage. The predictions from the revised design methods (see Chapter 3) are examined.

### 6.6.1 Contribution of flexural and shear reinforcement to shear capacity

#### 6.6.1.1 Assumptions

The specimens were divided by a major shear crack in the shear span into two parts. The vertical component of tensile force in the flexural reinforcement and W-FRP shear reinforcement crossing the major shear crack contributed to resist the applied shear force. Assumptions are made for the shear contribution calculation of the flexural and shear reinforcement.

- The calculation location is selected at the observed shear crack near the support for end slip failure specimens, and flexural failure specimens so that the strain of longitudinal bars at the shear crack can be taken as the strain near the support.

- For shear failure specimens, the actual shear crack that caused failure is selected for calculation whilst the strain in the longitudinal bars near the supports are also used for calculation because most of the gauges at the middle of shear span stopped working prior to the failure of the specimens.
- Only the shear links crossing the selected shear crack are used for shear contribution calculation. It is assumed that the recorded strain is the average strain along the shear link.
- Considering that not all longitudinal bars and shear link legs were gauged, the strain of the ungauged reinforcement is assumed to be the same as the gauged reinforcement at the symmetrical location.
- If a strain gauge was lost during testing, the shear contribution of the corresponding reinforcement is neglected. This could result in underestimation of the shear contribution of reinforcement.
- Due to support rotation under the applied load, the angle of flexural and shear reinforcement to horizontal axis were changed during the tests. It is assumed that the rotation of the support can be calculated using the displacement of the loading jack P1/P5 and their distance to the support.

Following the assumptions, the tensile force carried by flexural and shear reinforcement can be calculated using their material properties (Table 6.2). The shear contribution is calculated as the vertical component of the resulting tensile force.

#### 6.6.1.2 Shear contribution calculation

The cracking pattern in T1 is plotted with the strain of the flexural and shear reinforcement in Figure 6-37, where the actual shear cracks are highlighted with the bold line and the load for each step is the total applied load. A symmetrical major shear crack is assumed on side A in T1 for the shear contribution calculation.

The cracking pattern and strain of reinforcement in T2-1R is shown in Figure 6-38. A symmetrical major shear crack is assumed on side A for the shear contribution calculation. In T2-1R, shear links SA1D, SA2V and SA3D are selected for the shear calculation on side A, whilst shear links SB1D, SB2V and SB3D are selected on side B.

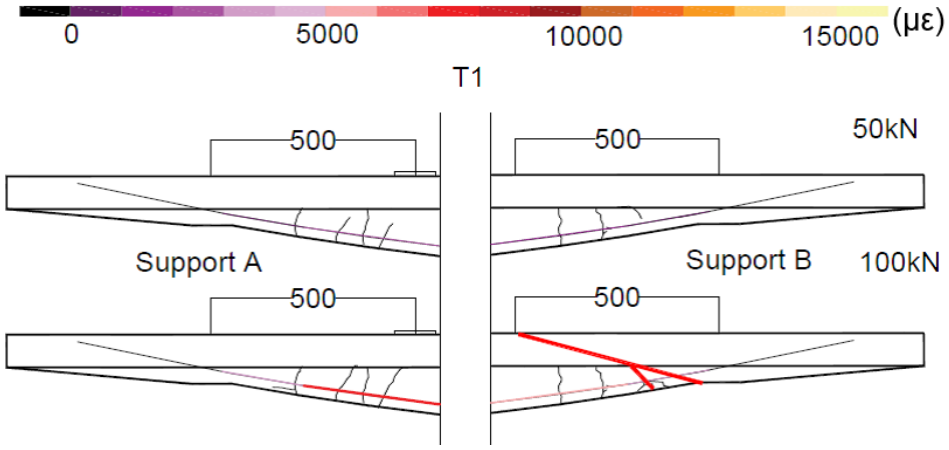


Figure 6-37: Strain in shear reinforcement and crack patterns in T1

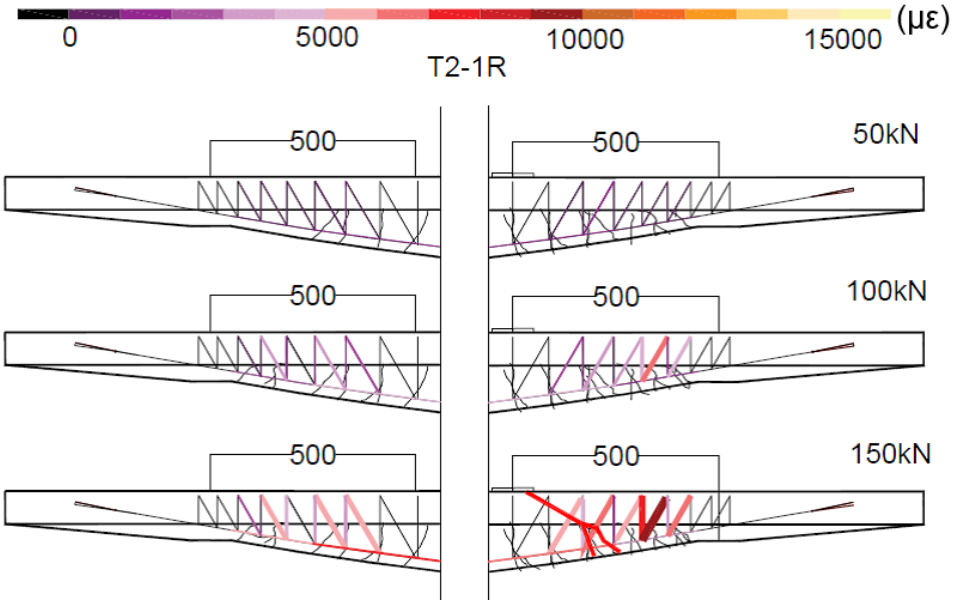


Figure 6-38: Strain in shear reinforcement and crack patterns in T2-1R

Following the assumptions, the shear contribution of flexural reinforcement $T_{fv}$, the shear contribution of shear reinforcement $T_{vv}$ and the total shear contribution of reinforcement $V_r$ are calculated and shown in Table 6.11, in which $P$ is the total applied load before strain gauges were lost and $V_a$ is the shear force in the shear span, calculated as half of $P$. The ratios $T_{vv}/V_a$, $T_{fv}/V_a$ and $V_r/V_a$ are calculated and shown in the brackets in Table 6.11. $T_{fv}$ and $T_{vv}$ are plotted against the applied shear force, as shown in Figure 6-39 and Figure 6-40 respectively.

Table 6.11: Load and shear resistance of reinforcement in T1 and T2-1R

| Specimen | $P$ (kN) | $T_{vv}$ (kN) | $T_{vv}/V_a$ | $T_{fv}$ (kN) | $T_{fv}/V_a$ | $V_r$ (kN) | $V_r/V_a$ |
|---|---|---|---|---|---|---|---|
| T1 (side A) | 102 | - | - | 28.1 | 0.55 | 28.1 | 0.55 |
| T1 (side B) | 102 | - | - | 22.6 | 0.44 | 22.6 | 0.44 |
| T2-1R (side A) | 187 | 34.4 | 0.37 | 59.0 | 0.63 | 93.5 | 0.99 |
| T2-1R (side B) | 187 | 37.5 | 0.40 | 42.5 | 0.45 | 80.1 | 0.85 |

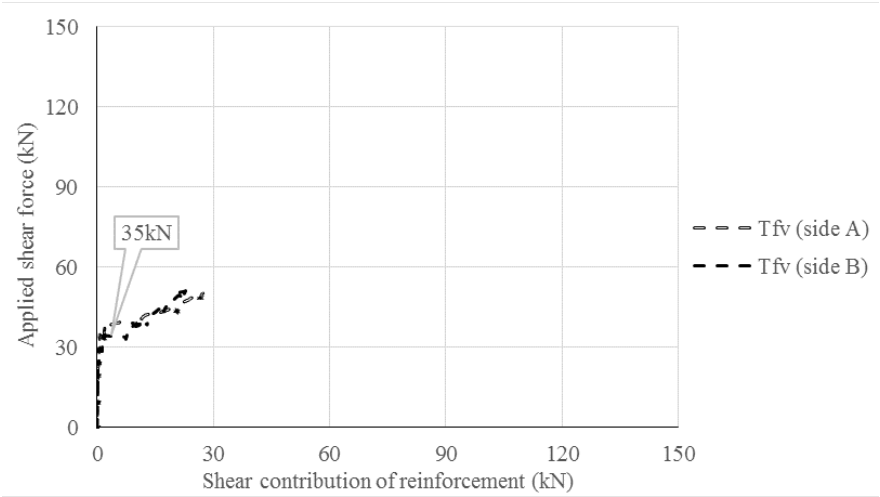


Figure 6-39: Comparison of load and shear resistance in T1

In specimen T1, the calculation results in Table 6.11 and Figure 6-39 show that the longitudinal bars begin to carry applied shear force after the shear crack formation at 70kN (section 6.5.2). At the failure load (102kN), the longitudinal bars contributed 28.1kN shear resistance at the shear span A and 22.6kN shear resistance at the shear span B which respectively accounts for 55% and 44% ($T_{fv}/V_a$) of the applied shear force (51kN).

In specimen T2-1R, both the shear reinforcement and the longitudinal bars carried the applied shear force. After the shear cracking formation at 70kN, the total shear contributions of flexural and shear reinforcement ($V_r$) account for an increasing proportion of the applied shear force (Figure 6-40) with the increasing total applied load. At the failure load, the total shear contribution of reinforcement $V_r$ (93.5kN) is very close to the applied shear force (94kN) on side A, whilst $V_r/V_a$ reaches about 85% on side B as shown in Table 6.11. The longitudinal bars carried larger proportions of applied shear force than the shear reinforcement on both side A and side B, as shown in Table 6.11 and Figure 6-40.

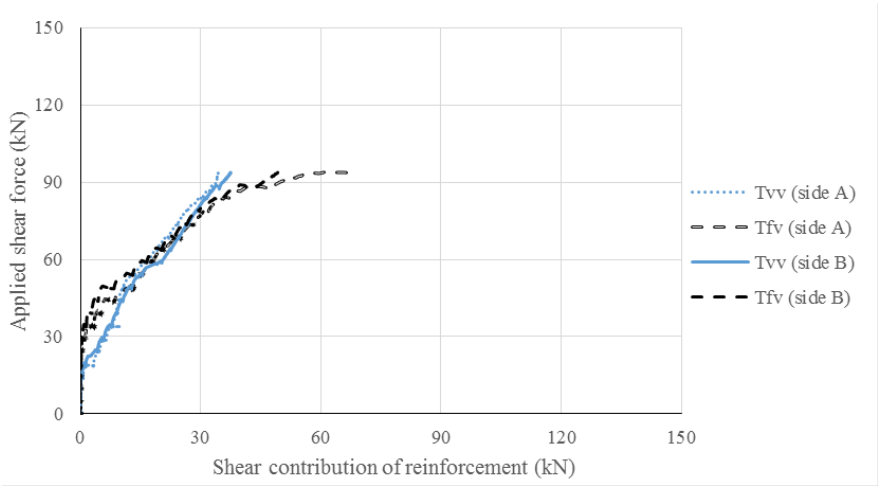


Figure 6-40: Comparison of load and shear resistance in T2-1R

The cracking patterns in T4-1, T5 and T6 are plotted with the strain of the flexural and shear reinforcement in Figure 6-41, Figure 6-42 and Figure 6-43, where the highlighted bold lines are the actual shear cracks used to conduct shear contribution calculation.

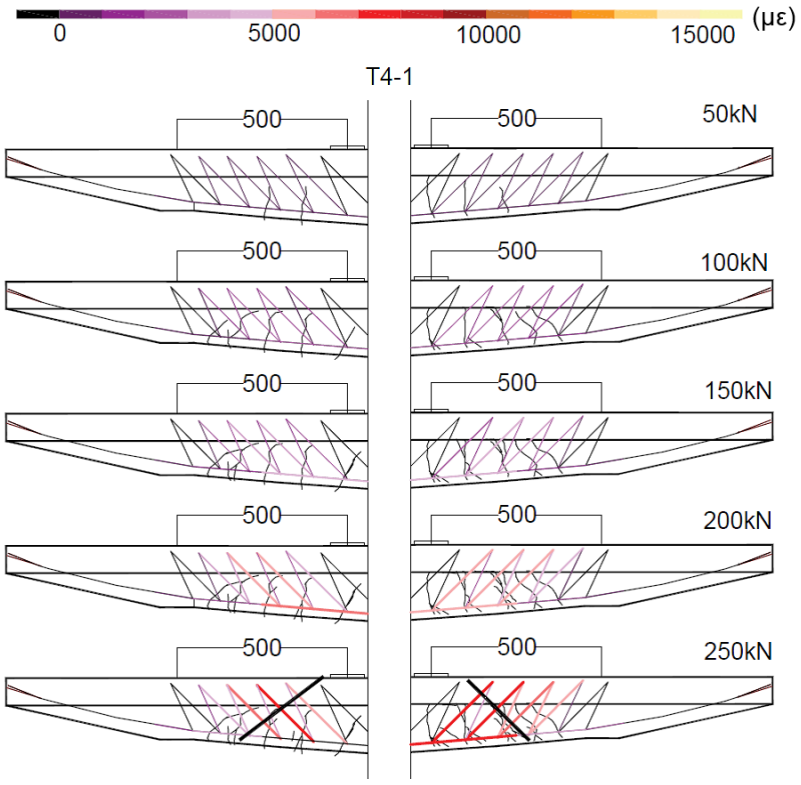


Figure 6-41: Strain in shear reinforcement and crack patterns in T4-1

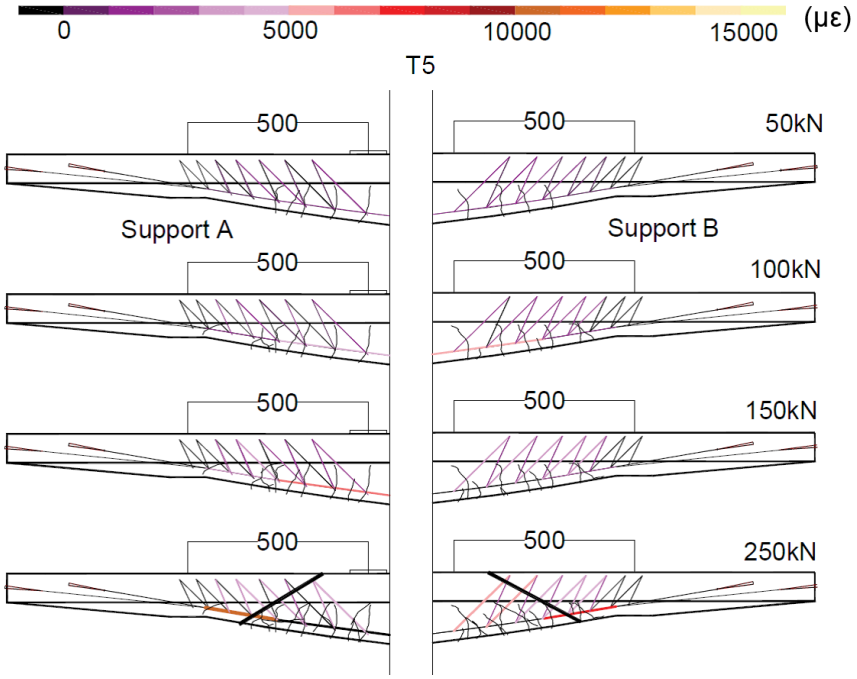


Figure 6-42: Strain in shear reinforcement and crack patterns in T5

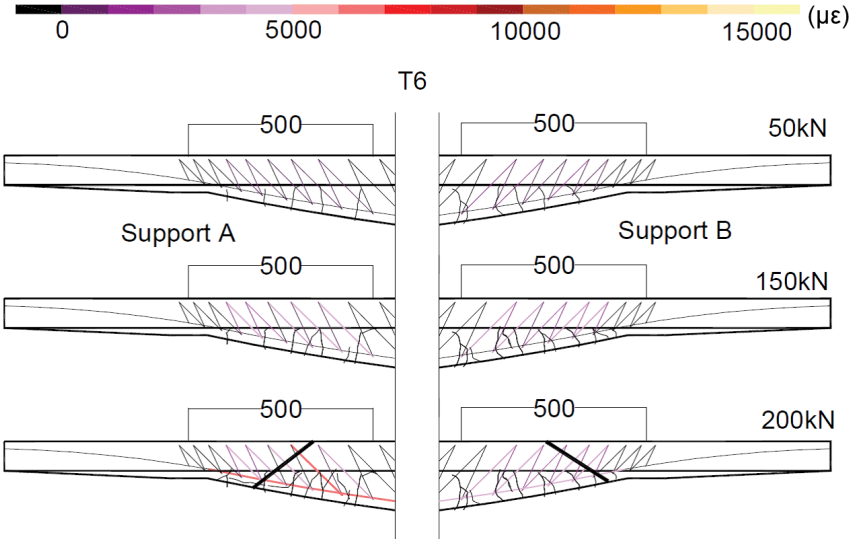


Figure 6-43: Strain in shear reinforcement and crack patterns in T6

Following the same method, the shear contribution calculation of the reinforcement in T4-1, T5 and T6 is conducted. The calculation results at the load before the loss the strain gauges in longitudinal bars are shown in Table 6.12. $V_a$, $T_{fv}$, $T_{vv}$ and $V_r$ are plotted against the total applied load, as shown in Figure 6-44, Figure 6-45 and Figure

6-46, respectively.

The calculation results show that the longitudinal bars and shear links carried most of the applied shear force after the shear crack formation. Compared to T2-1R, the W-FRP shear reinforcement accounts for a higher proportion of the total shear resistance. In T4-1, $T_{vv}/V_a$ reaches 74% of the applied shear force at 279kN. Due to the data variation of longitudinal bars, in T5, the value of $T_{vv}/V_a$ also varies at side A (26%) and side B (42%). $T_{vv}/V_a$ in T6 reaches 31% on side A and 37% on sided B at 213kN. Accordingly, the values of $T_{fv}/V_a$ are different in these specimens. The different values of $T_{vv}/V_a$ and $T_{fv}/V_a$ could have been caused by the geometry difference. The further analysis focusing on geometry is presented in section 6.6.3.

Table 6.12: Load and shear resistance of reinforcement in T4-1, T5 and T6

| Specimen | $P$ (kN) | $T_{vv}$ (kN) ($T_{vv}/V_a$) | $T_{fv}$ (kN) ($T_{fv}/V_a$) | $V_r$ (kN) ($V_r/V_a$) |
|---|---|---|---|---|
| T4-1 (side A) | 279 | 103.3 (0.74) | 26.7 (0.19) | 130.0 (0.94) |
| T4-1 (side B) | 279 | 103.0 (0.74) | 35.2 (0.25) | 138.2 (1.00) |
| T5 (side A) | 258 | 33.8 (0.26) | 101.2 (0.78) | 134.9 (1.04) |
| T5 (side B) | 258 | 55.1 (0.42) | 71.0 (0.55) | 126.1 (0.98) |
| T6 (side A) | 213 | 32.9 (0.31) | 59.2 (0.56) | 92.1 (0.86) |
| T6 (side B) | 213 | 39.0 (0.37) | 60.2 (0.57) | 99.2 (0.94) |

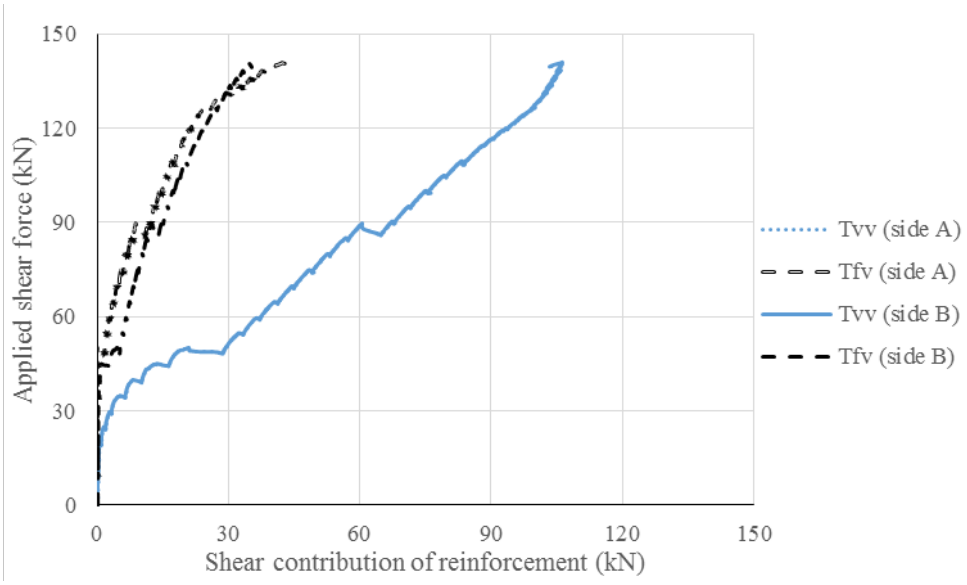


Figure 6-44: Comparison of load and shear resistance in T4-1

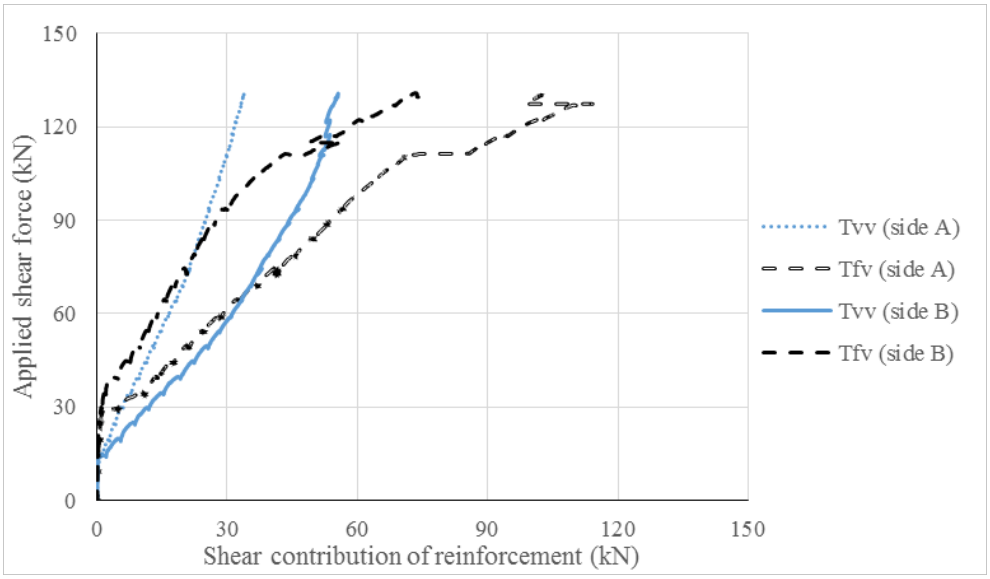


Figure 6-45: Comparison of load and shear resistance in T5

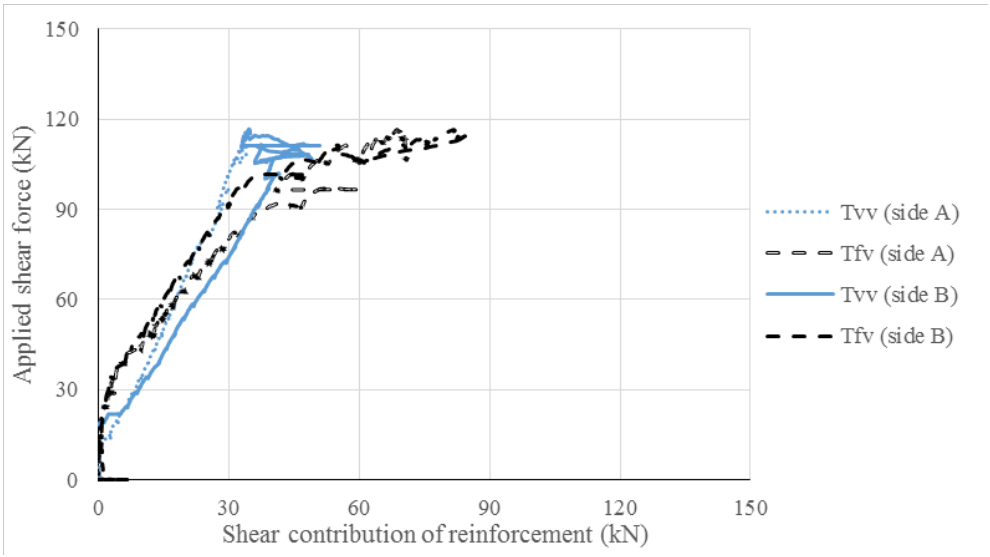


Figure 6-46: Comparison of load and shear resistance in T6

The specimens that failed in end slip of longitudinal bars (T2-1, T2-2, T2-2R, T3-1 and T4-2) are compared together with specimen T3-2 because T3-2 also encountered end slip of longitudinal bars and all these specimens shared a similar shear reinforcement ratio. The cracking patterns in these specimens are plotted with the strain of the flexural and shear reinforcement before the failure in Figure 6-47. The major shear cracks used to conduct shear contribution calculation are highlighted by bold lines.

The shear contribution of reinforcement in the specimens that failed in end slip is

compared with the applied shear force in Table 6.13, where P is the applied load selected for ease of comparison and the ratios $T_{vv}/V_a$, $T_{fv}/V_a$, and $V_r/V_a$ are shown in the brackets.

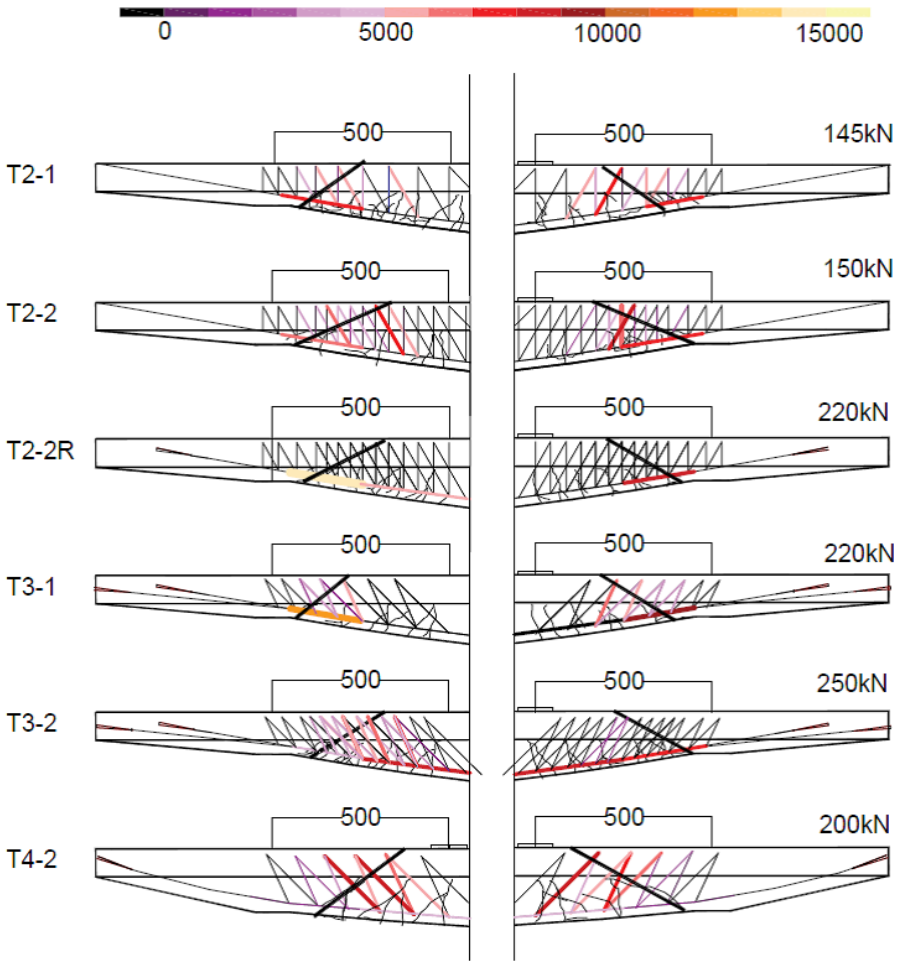


Figure 6-47: Shear links strains and crack patterns in end slip failure specimens

The specified load is taken as the load before the shear links rupture and for ease of comparison, it is set as the same for group T2 and the other testing groups. $V_a$, $T_{fv}$, $T_{vv}$ and $V_r$ are plotted against the total applied load, as shown in Figure 6-48, Figure 6-49, Figure 6-50, Figure 6-51, Figure 6-52 and Figure 6-53, respectively.

As shown in Table 6.13, the shear reinforcement and longitudinal bars account for most of the shear resistance in the end slip failure specimens. With the exception of T4-2, the value of $T_{vv}/V_a$ in most of these specimens is below 50%. Specimen T4-2 exhibits a uniquely high value of $T_{vv}$ and ratio of $T_{vv}/V_a$, which could be caused by the different

geometry (section 6.6.3).

Table 6.13: Load and shear resistance of reinforcement in end slip failure specimens

| Specimen | $P$(kN) | $T_{vv}$ (kN) ($T_{vv}/V_a$) | $T_{fv}$ (kN) ($T_{fv}/V_a$) | $V_r$ (kN) ($V_r/V_a$) |
|---|---|---|---|---|
| T2-1 (side A) | 145 | 20.7 (0.28) | 44.1 (0.61) | 64.8 (0.89) |
| T2-1 (side B) | 145 | 27.4 (0.38) | 40.3 (0.55) | 67.7 (0.93) |
| T2-2 (side A) | 145 | 34.2 (0.47) | 25.9 (0.35) | 60.1 (0.82) |
| T2-2 (side B) | 145 | 37.4 (0.51) | 34.9 (0.48) | 72.3 (0.99) |
| T2-2R (side A) | 188 | 44.1 (0.47) | 38.9 (0.40) | 83.0 (0.88) |
| T2-2R (side B) | 188 | 44.3 (0.47) | 35.7 (0.38) | 80.0 (0.86) |
| T3-1 (side A) | 188 | 32.3 (0.34) | 25.7 (0.27) | 58.1 (0.62) |
| T3-1 (side B) | 188 | 38.5 (0.41) | 35.7 (0.38) | 74.2 (0.79) |
| T3-2 (side A) | 188 | 46.0 (0.49) | 27.2 (0.29) | 74.2 (0.80) |
| T3-2 (side B) | 188 | 32.1 (0.34) | 38.3 (0.41) | 70.4 (0.75) |
| T4-2 (side A) | 188 | 53.5 (0.57) | 35.1 (0.38) | 88.5 (0.94) |
| T4-2 (side B) | 188 | 49.7 (0.51) | 27.7 (0.29) | 77.4 (0.82) |

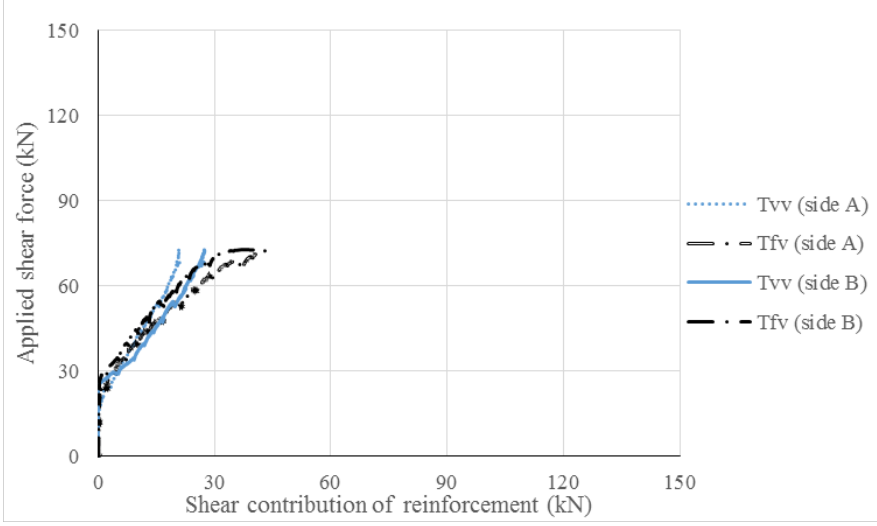


Figure 6-48: Comparison of load and shear resistance in T2-1

In addition, the W-FRP reinforcement design also influences the value of $T_{vv}/V_a$ when the shear reinforcement ratio is similar. Specimens T2-1, T2-1R (Table 6.11) and T3-1, which are designed with the same cross section area of shear links, exhibit very similar value of $T_{vv}/V_a$ whilst specimens T2-2, T2-2R and T3-2 exhibit higher value of $T_{vv}/V_a$ on average. The higher shear contribution of W-FRP shear reinforcement in T2-2, T2-2R and T3-2 could be caused by the W-FRP pattern (see section 6.6.2).

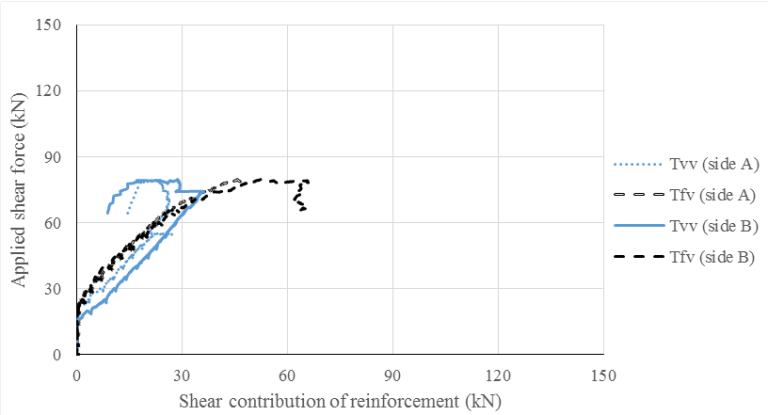


Figure 6-49: Comparison of load and shear resistance in T2-2

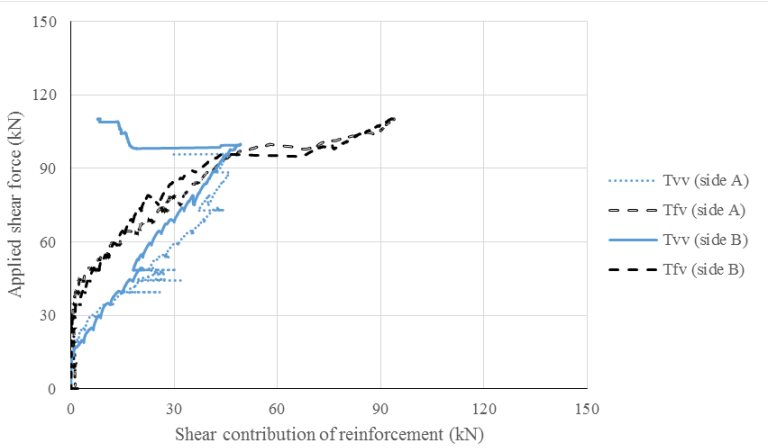


Figure 6-50: Comparison of load and shear resistance in T2-2R

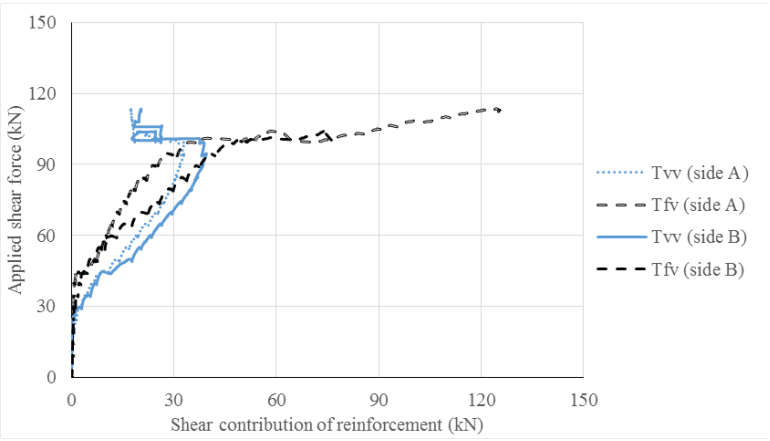


Figure 6-51: Comparison of load and shear resistance in T3-1

In contrast to the specimens that failed in either shear or flexure, all the specimens that failed in end slip of the longitudinal bars demonstrate load transmission from the shear links to the longitudinal bars after the shear link rupture. The value of $T_{fv}/V_a$ is below 0.5 before the shear reinforcement rupture, as shown in Table 6.13. However, at the failure load, the value of $T_{fv}/V_a$ reached over 0.9 in specimen T2-2 (Figure 6-49), T2-2R (Figure 6-50), T3-1 (Figure 6-51) and T3-2 (Figure 6-52).

Consequently, the shear link rupture did not result in shear failure. Although $T_{vv}$ decreases abruptly, the tensile force in the longitudinal bars increases abruptly at the same time, such that $V_r$ does not decrease. With the longitudinal bars carrying most of the applied shear force, the high tensile force in longitudinal bars results in end slip.

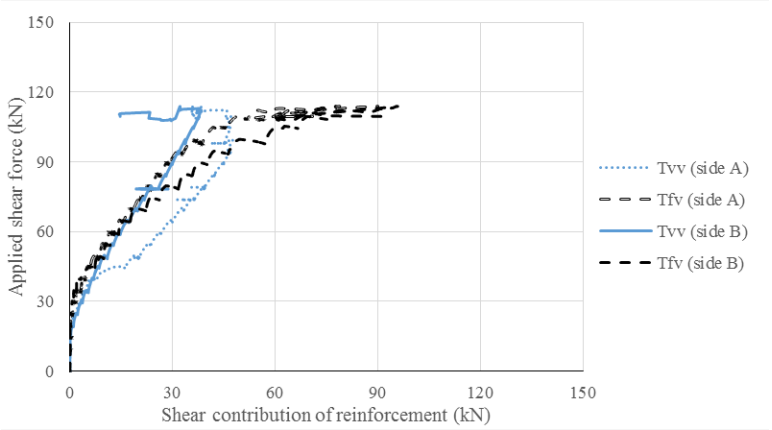


Figure 6-52: Comparison of load and shear resistance in T3-2

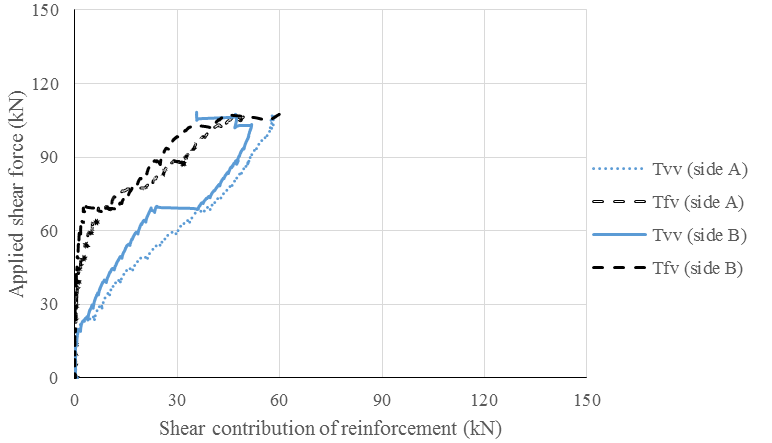


Figure 6-53: Comparison of load and shear resistance in T4-2

### 6.6.2 Shear reinforcement

In this section, the performance of shear reinforcement is analysed based on the previous shear contribution calculations in section 6.6.1. Excluding the influencing factors including geometry and anchorage, two groups of comparison are used to show the influence of shear reinforcement ratio and shear reinforcement pattern.

#### 6.6.2.1 Shear reinforcement ratio

Specimens T3-1 and T5 had the same shear reinforcement pattern, geometry and similar anchorage. The comparison of T1, T3-1 and T5 shows that the shear contribution of the W-FRP shear reinforcement increased from 0kN (T1, Table 6.11) to 38.5kN (T3-1, Figure 6-51) and 55.1kN (T5, Figure 6-45) before longitudinal bars slipped on side B. The ratio of $T_{vv}/V_a$ also increased from 0 (T1, Figure 6-39) to 41% (T3-1, Figure 6-51) and 42% (T5, Figure 6-45) on the failure side B.

Shear capacity was enhanced by the contribution from the flexural reinforcement. At failure of T1, the shear contribution of flexural reinforcement was 22.6kN (Table 6.11). Cooperated with the shear reinforcement, flexural reinforcement contributed 35.7kN to shear in T3-1 (Table 6.13) at the failure load. With the largest shear reinforcement ratio, the longitudinal bars of T5 contributed 71kN of shear resistance at the failure load (Table 6.12).

A higher shear reinforcement ratio also restrained the tensile force development in the longitudinal bars. Figure 6-54 shows that at failure, the tensile strain of longitudinal bars decreased along with the increasing shear reinforcement ratio under the same load. The higher the shear reinforcement ratio results in higher shear contribution and hence, the lower additional tensile force.

Consequently, the total tensile force in longitudinal bars decreases as the shear reinforcement ratio increases, with the same flexural tensile force, same geometry and the same load. It is also expected that the higher tensile strain in the longitudinal bars of T1 is the reason for the lower stiffness when compared to T2-1R, as the strain of flexural reinforcement affects the curvature of the cross-sections.

In addition, the high shear reinforcement ratio of T5 led to no rupture of the shear reinforcement, which means that there was no load transmission from shear reinforcement to longitudinal bars, as happened in specimen T3-1. Hence, when T5 failed, the tensile force in the longitudinal bars was controlled to a relatively lower level compared to T3-1.

Consequently, T5 was able to fail in flexure whilst the shear reinforcement rupture in T3-1 caused end slip failure.

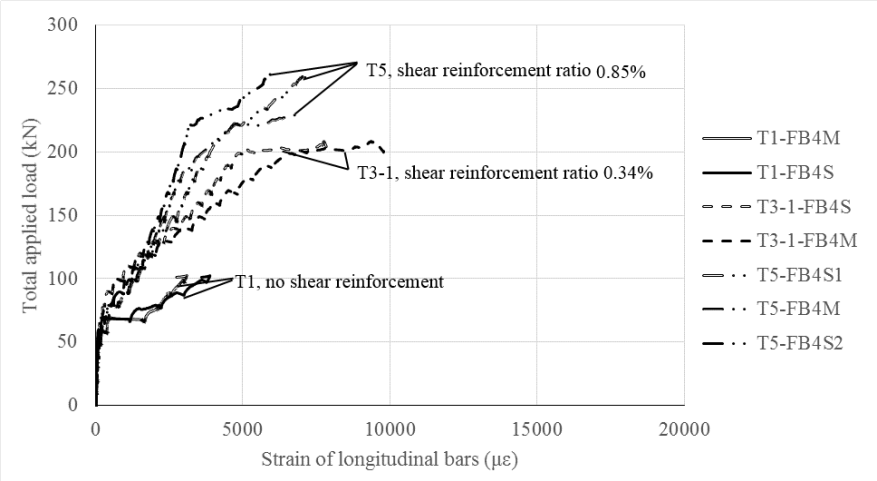


Figure 6-54: Tensile strain of longitudinal bars of T1, T3-1 and T5 at support B

#### 6.6.2.2 Shear reinforcement pattern

The influence of shear reinforcement pattern is highlighted through the comparisons amongst the four specimens in groups T2R and T3 which had the same geometry and shear reinforcement ratio. Variation in rupture of W-FRP reinforcement in the two specimens of group T2R and T3 may occur due to: (i) the cross-section area and (ii) the angle of W-FRP links. Smaller cross section area results in larger ratio of radius of the corner to effective diameter and hence higher corner strength, Equation 2.29.

As shown in Table 6.2, the W-FRP shear links that are composed of one layer of 50k carbon fibres, have a failure stress of 957MPa at the corners, which is 28% higher than the shear links composed of two layers of carbon fibres (745MPa) and 37% higher than those composed of five layers of carbon fibres (654MPa). With smaller cross-section area, the shear links in specimens T2-2R and T3-2 had higher ruptures load at the corners than those in T2-1R and T3-2 (Table 6.14).

In addition to the higher corner strength obtained from the single shear link tests (Spadea et al., 2017a), the W-FRP shear links of smaller cross-section area have better average performance in the specimens, as shown in Table 6.10 (page 151).

The average strain of diagonal shear links in T2-2R (0.74%) was 8% higher than T2-1R (0.68%) and for T3-2 (0.74%), it was 25% higher than T3-1 (0.59%). On average, the

resulting shear contribution of shear reinforcement increases from 36kN (38% of the applied force) in T2-1R to 44kN (47% of the applied force) in T2-2R. For group T3, the shear contribution of shear reinforcement increases from 35.4kN (37% of the applied shear force) in T3-1 to 39kN (41% of the applied shear force).

Table 6.14: Comparisons of shear reinforcement patterns in groups T2R and T3

| Specimen | Applied load of shear reinforcement rupture (kN) | Cross section area of shear reinforcement (mm2) | Orientations of shear reinforcement (degrees) | Shear reinforcement ratio |
|---|---|---|---|---|
| T2-1R | 188 | 8.6 | 60/90 | 0.34% |
| T2-2R | 200 | 4.3 | 60/90 | 0.34% |
| T3-1 | 200 | 8.6 | 45/65 | 0.34% |
| T3-2 | 220 | 4.3 | 45/65 | 0.34% |

The comparison shows that the W-FRP shear links of smaller cross-section area can be utilised more efficiently. Consequently, having the same shear reinforcement ratio, specimens T2-2R and T3-2 have higher loads of shear link rupture than T2-1R and T3-1, respectively.

The different loads of shear reinforcement rupture in group T2R and group T3 are also influenced by the shear reinforcement angle. The smaller angle difference between the vertical and diagonal links could result in a situation where the shear crack opening led to similar strains in the adjacent links at two angles. Therefore, the rupture of shear links with high strain difference between adjacent links could be avoided and the shear links can be utilised more efficiently before their rupture.

The average strains of diagonal links (45 degrees) and vertical links (65 degrees) of T3 ($\epsilon_{d,ave.}/\epsilon_{v,ave.}$=1.3) are smaller than T2R ($\epsilon_{d,ave.}/\epsilon_{v,ave.}$=1.4 for T2-1R and $\epsilon_{d,ave.}/\epsilon_{v,ave.}$=2.1 for T2-2R) as shown in Table 6.10. The uneven distribution of load between FRP shear links is caused by the linear tensile property of FRP and it has been also discussed in the tapered beam tests in section 5.6.2.2.

In addition, the larger angles of the shear links in group T3 can reduce the influence of non-axial forces in the shear links. The all-diagonal links in T3 have a higher probability to be perpendicular to the diagonal shear cracks than those in T2R. Hence, these links could have been more likely failing in axial tension, while vertical links and diagonal links at 60° were more vulnerable due to their low strength when loaded transversely (section 2.3.3.2 on page 18).

### 6.6.3 Geometry

Excluding the influence of the shear reinforcement and anchorage, the influence of geometry is analysed in three aspects: stiffness, shear carrying mechanism and the concrete usage, by comparing specimens T4-1, T5 and T6.

#### 6.6.3.1 Stiffness

As specified in section 3.2.2 of Chapter 3, the displacement of the specimens can be calculated using the equivalent moment of inertia approach (Bischoff and Gross, 2010b). Assuming the specimens are divided into segments along the beam axis, their displacement can be calculated as the double integral of the curvature of each segment. Theoretically, larger tensile strain in the longitudinal bars means larger curvature of the corresponding cross section. Therefore, the influence of geometry on stiffness can be analysed on the strain of longitudinal bars.

As presented in section 6.5.2, specimen T4-1 had the largest stiffness, compared with T5 and T6 (Figure 6-29). Accordingly, the average slope of the load-strain curves in longitudinal bars near the support (Figure 6-55) has a positive correlation to the depth of the support in these specimens.

One reason for the different strains in the longitudinal bars along the beam axis is the flexural tensile force. Under the same load, the effective depth of each cross-section in T4-1 is larger than T5 and T6. Hence the tensile force carried by the longitudinal bars is lower due to the larger lever arm.

The other reason for the strain difference in Figure 6-55 could be the additional tensile force caused by shear, which is more significant near the support. The larger effective depth at the support of T4-1 results in the larger angle of concrete strut, Figure 6-56. According to Equation 2.28 in CSA-S806 (2012), reducing the angle of concrete strut can result in larger additional tensile force. Although the additional tensile force does not necessarily increase the curvature of the cross-section, it could create a tension force on the cross-section that results in larger displacement at the mid-span.

As a result of smaller flexural tensile force and additional tensile force, T4-1 had lower tensile strains in longitudinal bars. Therefore the stiffness of T4-1 is larger than the other two specimens.

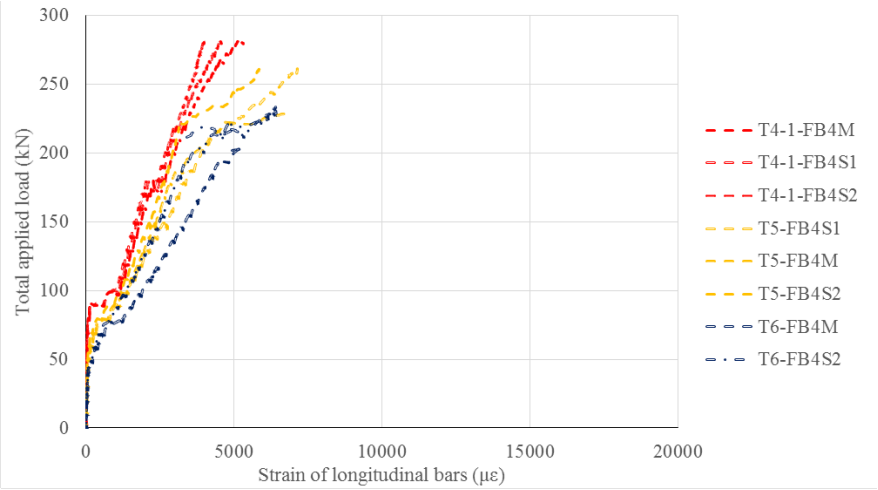


Figure 6-55: Tensile strain of longitudinal bars of T4-1, T5 and T6

Following the research of Hashemian (2012), variable depth geometry results in lower stiffness of beams. Besides, FRP reinforced beams have lower stiffness than steel reinforced beams due to lower elastic modulus of FRP bars. Displacement under service limit state becomes the governing factor in the geometry design of the specimens (see section 6.2.3).

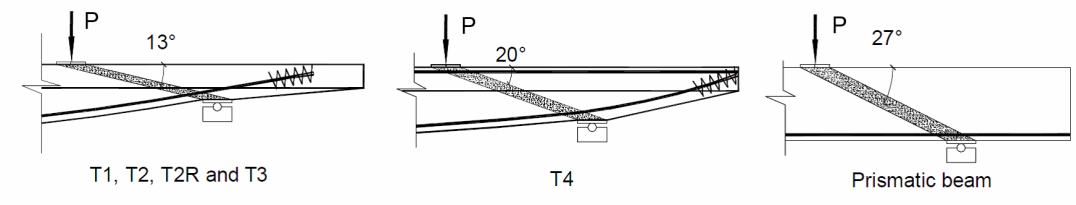


Figure 6-56: Influence of geometry on additional tensile force

#### 6.6.3.2 Shear carrying mechanism

In the specimens that were transversely under-reinforced, the variable-depth geometry enabled the possibility of load transmission. As presented in section 6.6.1.2, all the specimens that failed in end slip of longitudinal bars exhibited load transmission from the shear reinforcement to the flexural reinforcement when the shear reinforcement was ruptured gradually.

The load transmission allowed these specimens to fail in two steps: shear reinforcement rupture and end slip of longitudinal bars. Consequently, the specimens had larger

capacity and deformability than the load to the shear reinforcement rupture. It might be better to allow the beams to fail in this way since flexural failure is also brittle anyway.

In addition, the critical factor that determined the ultimate capacity was changed from shear to anchorage. With sufficient anchorage strength and appropriate support depth, the under-reinforced specimens could be able to reach their flexural capacity, as happened in T3-2. This provides a new approach to minimise the material usage in the flexibly formed beams.

For all the specimens, the different geometries resulted in variation in load distribution in flexural and shear reinforcement before shear link rupture. As presented in Table 6.12 in section 6.6.1.2, with the support depth increasing from 100mm to 180mm, $T_{vv}/V_a$ of the flexural failure specimens increased from 37% in T6 to 43% in T5 and to 74% in T4-1 on side B.

The comparison of the shear contributions of longitudinal bars and shear reinforcement at the failure side (B) in T4-1, T5 and T6 (Figure 6-57) also confirms the geometry influence on the load distribution in flexural and shear reinforcement.

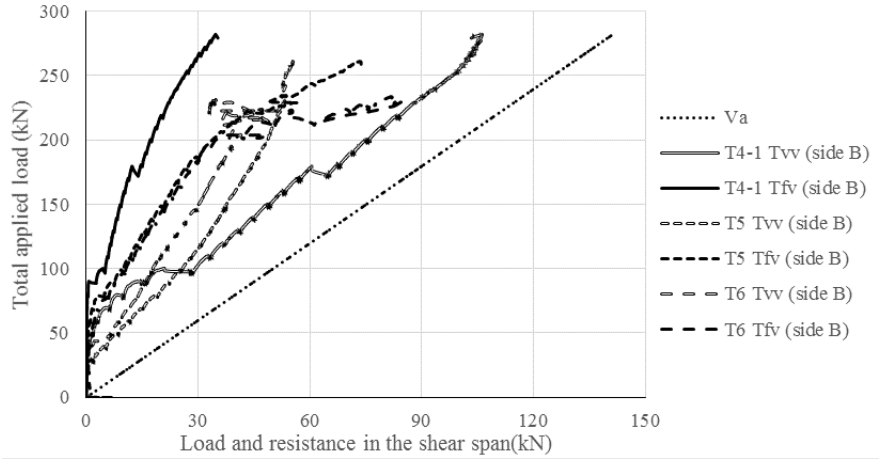


Figure 6-57: Shear contributions of reinforcements of T4-1, T5 and T6

The geometry influences the load distribution in these three specimens in three ways: angle of concrete strut, angle of flexural reinforcement and stiffness. As shown in Figure 6-56, smaller depth at support results in the smaller angle of concrete strut and the larger angle of flexural reinforcement, both of which result in larger additional tensile force following Equation 2.28 (CSA-S806, 2012). In addition, carrying the same tensile force, flexural reinforcement at a larger angle can provide a larger vertical

component of the tensile force. The specimen having smaller support depth exhibited larger displacement under the same load and hence the angle of flexural reinforcement and concrete strut near supports will encounter corresponding change due to the displacement. With largest support depth, the shear contribution of flexural reinforcement in specimen T4-1 was the smallest amongst the three over-reinforced specimens.

#### 6.6.3.3 Concrete saving

In addition to the influence on structural performance of the specimens, the variable-depth geometries (I, II and III) exhibits different concrete saving, compared with equivalent prismatic T beams, for which the same mid-span depth (250mm), flange width (800mm), flange depth (80mm), length (4000mm) and clear span (3000mm) are adopted. In order to simulate the normal web width of a T beam, as discussed in section 6.2.3, the web width is set as 200mm.

The concrete consumption for the geometry designs adopted in the specimens are compared with the equivalent prismatic T beam in Table 6.15, in which $Q_{c,web}$ is the concrete used in the web; $Q_{c,flange}$ is the concrete used in the flange and $Q_c$ is the total concrete usage. The ratio of the three parameters is calculated as the relative values compared to the equivalent prismatic T beams (taken as 1.00).

Table 6.15: Comparison of concrete consumptions

| Geometry | $Q_{c,web}$ $(m^3)$ | $Q_{c,flange}$ $(m^3)$ | $Q_c$ $(m^3))$ | Ratio of $Q_{c,web}$ | Ratio of $Q_{c,flange}$ | Ratio of $Q_c$ |
|---|---|---|---|---|---|---|
| I | 0.056 | 0.256 | 0.312 | 0.42 | 1.00 | 0.80 |
| II | 0.080 | 0.256 | 0.336 | 0.59 | 1.00 | 0.85 |
| III | 0.048 | 0.256 | 0.305 | 0.36 | 1.00 | 0.77 |
| Prismatic T-beam | 0.136 | 0.256 | 0.392 | 1.00 | 1.00 | 1.00 |

Due to the optimisation of the width and depth of the web, the three geometries of the specimens have a much smaller web. The ratio of $Q_{c,web}$ varies from 0.36 to 0.59 along with the increasing depth of the web, indicating up to 64% of concrete saving. The resulting total concrete usage of the specimens varies from 77% to 85% of the equivalent prismatic beam.

For this research, it is the flange design that limits the concrete saving because the flange was designed to simulate the slab construction in practice. Considering that the flange under neutral axis was cracked, there is potential to optimise the flange design

to achieve a higher ratio of concrete saving.

### 6.6.4 Anchorage

In this section, the influence of anchorage design is analysed in three aspects: stiffness, failure mode and ultimate capacity.

#### 6.6.4.1 Stiffness, failure modes and ultimate capacities

The influence of anchorage designs on the stiffness and ultimate capacities is highlighted by the premature end slip failure of group T2. As discussed in section 6.5.2.3, the stiffness reduction under approximately 90kN of applied load could be caused by the end slip of the middle longitudinal bar, which was not extended to the end of the specimens. Although there was no direct evidence that can confirm the end slip of the middle bar, the loss of one bar in the tension zone could feasibly result in abrupt stiffness change.

Compared with the other specimens, under the same applied load, only two longitudinal bars in group T2 carried even larger tensile force due to the lower stiffness of T2. As shown in Figure 6-36, under 150kN of applied load, the tensile strain of longitudinal bars in group T2 already reached approximately $7000\mu\epsilon$. However, for the other specimens (except for T4-2 due to the different geometry), it was over 200kN of applied load when the tensile strain in the longitudinal bars near the support reached $7000\mu\epsilon$.

With no splayed anchorage installed, the anchorage strength of group T2 was lower (Table 6.5). The higher applied load in the longitudinal bars (Figure 6-36) and lower resistance (anchorage strength) resulted in end slip failure of group T2, under the lowest applied load amongst all transversely-reinforced specimens.

In addition, the significance of anchorage is highlighted by end slip failure in specimens of group T2R and T3. For the specimens, T2-2R, T3-1, T3-2, which did not fail in shear, the same rupture of shear reinforcement and the consequent load transmission resulted in all the applied shear force being carried by the longitudinal bars.

Therefore, the anchorage strength became the critical factor which determined the ultimate capacity and failure mode of the specimens. It has rarely been seen in the literature that prismatic beams can maintain their capacity after shear link rupture.

This indicates that the W-FRP reinforced specimens may have an advantage of gradual failure compared with FRP-reinforced prismatic beams.

With higher anchorage strength, the ultimate capacity can be improved after the shear link rupture. The splayed anchorage of specimens T2-2R and T3-1 was not able to provide enough anchorage strength for the two specimens to achieve flexural failure. T2-2R and T3-1 failed in end slip of longitudinal bars under approximately 220kN of applied load. With additional mechanical anchorage, the anchorage strength of T3-2 was improved so that T3-2 failed in flexure at the largest ultimate capacity (253kN) across all three specimens.

#### 6.6.4.2 Anchorage design assessment

For transversely under-reinforced specimens (T2, T2-2R, T3-1, and T3-2), the splayed anchorage was crucial to the ultimate capacities only when the shear reinforcement in the shear span were ruptured. The consequent load transmission resulted in very large tensile force in the longitudinal bars (Figure 6-36) (see section 6.6.1.2). The splayed anchorage was thus the key factor that determined the ultimate capacity and failure mode.

For specimens T1, T4-1, T5 and T6, the splayed anchorage was not that critical to the performance, due to the low tensile force in longitudinal bars near the support. For the transversely over-reinforced specimens (T4-1, T5 and T6), the tensile force in longitudinal bars was controlled to a relatively low level (less than $7500\mu\epsilon$ in Figure 6-55) because of the large shear contributions of the shear reinforcement (Table 6-44). For T1, which had no shear reinforcement, the tensile strain of longitudinal bars was less than $5000\mu\epsilon$ as shown in Figure 6-34 because of the low ultimate capacity.

Based on the initial design of the specimens, the tensile force in longitudinal bars at the supports can be calculated following the codified Equation 3.2 in section 3.2.3.1 of Chapter 3. At the load of flexural failure predicted by ACI-440.1R (2015) and CSA-S806 (2012) (Table 6.3), the flexural tensile force is assumed to be zero due to zero bending moment. The shear contribution of shear reinforcement ($V_f$) is calculated following Equation 3.5 and Equation 3.6. The resulting predictions of tensile force in the longitudinal bars are compared with the design anchorage strength (Table 6.5) in Table 6.16.

Table 6.16: Anchorage strength calibration

| Specimen | $F_{bs}$ (kN) | $F_{bm}$ (kN) | $R_a$ (kN) | $F_{a,ACI}$ (kN) | $F_{a,CSA}$ (kN) | $\frac{R_a}{F_{a,ACI}}$ | $\frac{R_a}{F_{a,CSA}}$ |
|---|---|---|---|---|---|---|---|
| T1 | 185.4 | 154.6 | 525.4 | 171.0 | 167.7 | 3.07 | 3.15 |
| T2 | 103.0 | - | 206.0 | 152.0 | 137.7 | 1.35 | 1.49 |
| T2R | 154.6 | 154.6 | 463.8 | 152.0 | 137.7 | 3.05 | 3.36 |
| T3 | 185.4 | 154.6 | 525.4 | 152.0 | 137.7 | 3.45 | 3.81 |
| T4-1 | 185.4 | 184.4 | 556.2 | 116.0 | 103.4 | 4.80 | 5.53 |
| T4-2 | 103.0 | 103.0 | 309.0 | 148.6 | 132.8 | 2.08 | 2.32 |
| T5 | 185.4 | 185.4 | 556.2 | 123.6 | 100.2 | 4.50 | 5.54 |
| T6 | 103.0 | 103.0 | 309.0 | 131.2 | 116.9 | 2.35 | 2.64 |

Where $F_{bs}$ is the side bar anchorage strength prediction; $F_{bm}$ is the middle bar anchorage strength prediction $R_a$ is the total anchorage strength that equals to $2F_{bs}+F_{bm}$; $F_{a,ACI}$ and $F_{a,CSA}$ are the predictions of total tensile force in longitudinal bars at the support following ACI 440.1 and CSA S806 respectively.

The comparisons in Table 6.16 show that anchorage strength predictions of the specimens (except for T2) exceed twice the total tensile force in the longitudinal bars. The two code and guideline underestimate the tensile force in longitudinal bars at the support.

According to the analysis in this section, it is seen that the accurate prediction of tensile force development in the longitudinal bars is a critical factor that governs the validity of anchorage design. Following the accurate bar force prediction, the anchorage safety can be ensured by choosing appropriate techniques, such as the splayed anchorage and mechanical anchorage.

### 6.6.5 Tensile force in longitudinal bars

As analysed in section 6.6.2 and section 6.6.3, shear reinforcement layout and geometry influence the tensile force in the longitudinal bars, whilst the effectiveness of anchorage (section 6.6.4) is dependent on the tensile force in the longitudinal bars. In this section, an equation is proposed to calculate the tensile force in longitudinal bars in the beams having variable depth geometry, based on the analysis of the contributing factors to the performance of the specimens (shear reinforcement, geometry and anchorage).

Taking a cut in the shear span of the specimen following the direction of concrete strut, the free body above the concrete strut is shown in Figure 6-58. By taking moments about Point A, the tensile force in longitudinal bars near the support can be calculated

as Equation 6.1, in which $\beta$ is the angle of bars to the horizontal axis. In Equation 6.1, the moment about Point A created by the aggregate interlock along with the shear crack and the small difference of locations of $T_f$ and $V_a$ are neglected. The influence of shear reinforcement is considered by $T_{vh}$ and $T_{vv}$. Geometry is considered by incorporating the angle of concrete strut $\theta$ and flexural reinforcement $\beta$.

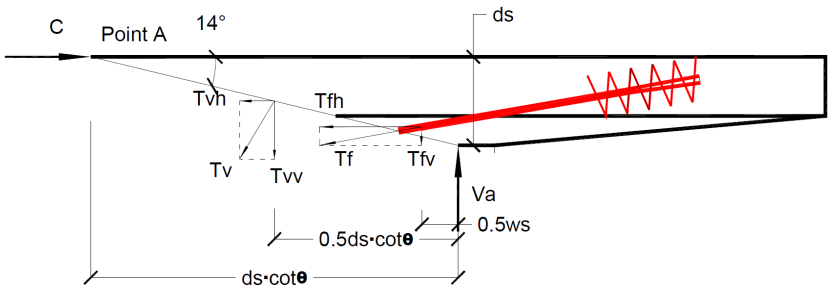


Figure 6-58: Equilibrium of tested specimens at the support

Where $C$ is the compression force in the concrete; $T_v$ is the tensile force in the shear reinforcement; $T_{vh}$ and $T_{vv}$ are the horizontal and vertical component of $T_v$, respectively; $T_f$ is the tensile force in the longitudinal bars; $T_{fh}$ and $T_{fv}$ are the horizontal and vertical component of $T_f$, respectively; $d_s$ is the depth of the support; $V_a$ is the reaction force of the support, which is also equal to the applied shear force; $\theta$ is the angle of the concrete strut and $w_s$ is the width of the support. The angle of the concrete strut is calculated as the tangent of the ratio of shear span to support depth.

$$T_f = \frac{(V_a - T_{vv}/2)\cot\theta - T_{vh}/2}{(1 + \tan\beta\cot\theta)\cos\beta} \tag{6.1}$$

Whilst a similar expression (Equation 3.2) is used in the codified equations CSA-S806 (2012) to specify the additional tensile force, some of the influencing factors in Equation 6.1 are replaced with empirical values based on prismatic beams. For example, in Equation 2.28 CSA-S806 (2012), $\cot\theta$ is set as a constant value of 1.3. However, the angle of the concrete strut in variable-depth beam could be much smaller and hence the value of $\cot\theta$ could be much larger as shown in Figure 6-56. The simplifications of the code and guideline could result in inaccurate tensile force prediction in the specimen as discussed in section 6.6.4.

In particular, the displacement of the variable depth beam is not considered by the codified equations, as in prismatic beams, the shear contribution of the longitudinal bars is normally neglected. However, the displacement of the specimens under loads

(section 6.6.1.1 and section 6.6.3) changed the angle of the concrete strut and flexural reinforcement to the horizontal axis, as shown in Figure 6-59. The rotation of the supports is equivalent to reducing the support depth. Whilst the variation in geometry could result in different the shear contributions of the longitudinal bars, as discussed in section 6.6.3.

Considering the displacement, Equation 6.1 can also be adopted to calculate the tensile force in the longitudinal bars, whilst the values of $\theta$ and $\beta$ are set as the actual angles in Figure 6-59. Using Equation 6.1, the relation between the tensile force in the longitudinal bars and the contributing factors to the structural performance of the specimens is established. The validity of Equation 6.1 will be examined through the modelling of the specimens, presented in Chapter 7.

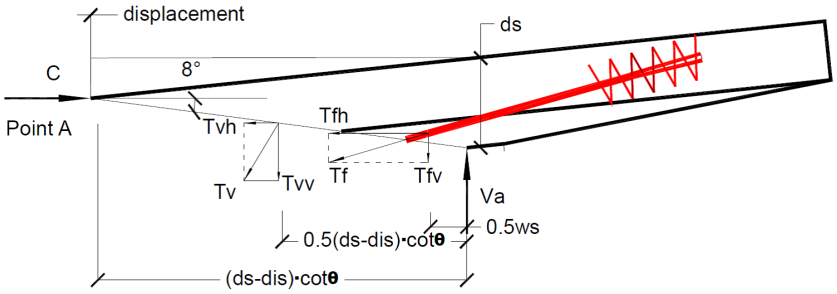


Figure 6-59: Equilibrium of tested specimens at the support with displacement

### 6.6.6 Prediction examination

The flexural (Table 6.3) and shear predictions (Table 6.4) following the revised codified methods and the revised MCFT model are compared with the test results, as shown in Table 6.17, The predictions are calculated following the proposed revisions as presented in Chapter 3. In Table 6.17, the average ratio of the test results to the corresponding predictions and their standard deviation are only taken for the transversely reinforced specimens, with the exception of group T2 due to their premature end slip failure.

As shown in Table 6.17, the revised CSA S806 provides the most accurate predictions ($P_{u,exp.}/P_{u,CSA}$=1.06), with the least standard deviation (0.12). The revised MCFT predictions are conservative, but compared to the revised ACI 440.1, the MCFT predictions are closer to the test results ($P_{u,exp.}/\ P_{u,MCFT}$=1.46 with SD=0.46). The revised ACI 440.1 makes the most conservative predictions with the largest standard deviation ($P_{u,exp.}/P_{u,ACI}$=1.76 with SD=0.47).

Table 6.17: Comparisons between codified methods and test results

| Specimen | $P_{u,ACI}$ (kN) | $P_{u,CSA}$ (kN) | $P_{u,MCFT}$ (kN) | $P_{u,exp.}$ (kN) | $\frac{P_{u,exp.}}{P_{u,ACI}}$ | $\frac{P_{u,exp.}}{P_{u,CSA}}$ | $\frac{P_{u,exp.}}{P_{u,MCFT}}$ |
|---|---|---|---|---|---|---|---|
| T1 | 33(S) | 47(S) | - | 101(S) | 3.06 | 2.14 | - |
| T2-1 | 105(S) | 200(S) | 108(S) | 153(E) | 1.45 | 0.77 | 1.42 |
| T2-2 | 105(S) | 200(S) | 173(S) | 160(E) | 1.52 | 0.80 | 0.92 |
| T2-1R | 105(S) | 200(S) | 108(S) | 188(S) | 1.79 | 0.94 | 1.74 |
| T2-2R | 105(S) | 200(S) | 173(S) | 222(E) | 2.11 | 1.11 | 1.28 |
| T3-1 | 105(S) | 200(S) | 108(S) | 226(E) | 2.15 | 1.13 | 2.09 |
| T3-2 | 105(S) | 200(S) | 173(S) | 253(B) | 2.41 | 1.26 | 1.46 |
| T4-1 | 221(S) | 258(B) | 267(B) | 279(B) | 1.26 | 1.08 | 1.08 |
| T4-2 | 111(S) | 199(S) | 104(S) | 217(E) | 1.95 | 1.09 | 2.08 |
| T5 | 213(S) | 258(B) | 273(B) | 261(B) | 1.22 | 1.01 | 1.01 |
| T6 | 193(S) | 258(B) | 245(S) | 233(B) | 1.20 | 0.90 | 0.95 |
| | | | | Average | 1.76 | 1.06 | 1.46 |
| | | | | SD | 0.47 | 0.12 | 0.46 |

Where $P_{u,ACI}$ is the ultimate capacity (in total applied load) prediction of the revised ACI 440.1; $P_{u,CSA}$ is the the ultimate capacity prediction of the revised CSA S806; $P_{u,MCFT}$ is the the ultimate capacity prediction of the revised MCFT model; $P_{u,exp.}$ is the ultimate capacity of the specimens; S, E and B are denoted as shear failure, end slip failure and bending failure, respectively.

#### 6.6.6.1 Limitations: shear contribution of longitudinal bars

The ratio of the shear contribution provided by the longitudinal bars to the applied shear force is shown in Table 6.18, in which, $\frac{T_{fv}}{V_a}$ is the average ratio of the shear contribution of the longitudinal bars to the applied shear force in the specimens, from Table 6.11, Table 6.12 and Table 6.13; $\frac{T_{fv,ACI}}{V_{u,ACI}}$, $\frac{T_{fv,CSA}}{V_{u,CSA}}$, $\frac{T_{fv,MCFT}}{V_{u,MCFT}}$ are the ratios of shear contribution of longitudinal bars to the maximum applied shear force, predicted by the revised ACI 440.1, the revised CSA S806 and the revised MCFT model, respectively.

Whilst the predictions of ultimate capacity are conservative, the shear contribution of the longitudinal bars are under-estimated by the three design methods, especially for the specimens that had geometry I and III (T1, T2, T2R, T3, T5 and T6), compared with the test data ($\frac{T_{fv}}{V_a}$), Table 6.18. There are two main reasons for the inaccurate predictions of the shear contribution provided by the longitudinal bars: (i) the empirical equations of additional tensile force from CSA S806 and (ii) the omission of the support

rotation as discussed in section 6.6.5.

Table 6.18: Shear contribution of longitudinal bars

| Specimen | $\frac{T_{fv}}{V_a}$ | $\frac{T_{fv,ACI}}{V_{u,ACI}}$ | $\frac{T_{fv,CSA}}{V_{u,CSA}}$ | $\frac{T_{fv,MCFT}}{V_{u,MCFT}}$ |
|---|---|---|---|---|
| T1 | 0.50 | 0.28 | 0.28 | - |
| T2, T2R, T3 | 0.54 | 0.22 | 0.24 | 0.20 |
| T4-1 | 0.22 | 0.10 | 0.11 | 0.09 |
| T4-2 | 0.17 | 0.10 | 0.12 | 0.09 |
| T5 | 0.55 | 0.21 | 0.23 | 0.20 |
| T6 | 0.56 | 0.25 | 0.29 | 0.25 |

As discussed in section 6.6.5, the empirical factor 1.3 ($\cot\theta$) in Equation 2.28 assumes the angle of the concrete strut to be 52°. This value of $\theta$ might work for normal prismatic beams since the additional tensile force rarely governs the design of normal beams. The concrete strut angle of the specimens could be considerably smaller than prismatic beams. The value of $\cot\theta$ could reach 4.3 when $\theta$ is assumed to be 13 degrees, as shown in Figure 6-56. Hence, when the geometry of the specimens is more similar to a prismatic beam (T4), the difference between $\frac{T_{fv}}{V_a}$ and the predictions are smaller, as shown in Table 6.18.

The displacement of the loading jacks P1 and P5 of the transversely reinforced specimens varied from 45mm to 80mm at the failure load. The displacement resulted in the rotation at the support varying from 5° to 9° and the angle of the concrete strut and longitudinal bars changed correspondingly. Consequently, the shear contribution of the longitudinal bars would be even larger, due to the changed value of $\cot\theta$ and $\sin\beta$ considering the displacement.

Finally, neither of the revised codified design methods can simulate the development of the tensile force in longitudinal bars during the loading process. Therefore, following the three methods, only the tensile force in the longitudinal bars at the failure can be calculated. However, as discussed in section 6.6.4.2, it is critical to understand the development of tensile force. Further revision is required to address this issue.

#### 6.6.6.2 Limitations: shear reinforcement pattern

In addition to the under-estimation of the shear contribution of longitudinal bars, the codified design methods are unable to recognise the different patterns of shear reinforcement. The design strain is set as 0.4% in ACI-440.1R (2015) and 0.5% in

CSA-S806 (2012), which results in the same prediction of the two specimens in groups T2, T2R and T3 (Table 6.17). The different corner strengths of shear links with different cross sections (Table 6.2) are neglected.

In contrast to the codified methods, the corner strength of the shear links from previous tests (Spadea et al., 2017a) is adopted for in the shear design of revised MCFT model. The variation of predictions for the specimens in the same testing group is achieved. However, using the actual corner strength from the test of single shear link in the shear design of revised MCFT may result in unconservative predictions as the average strain of W-FRP shear links (Table 6.10) in the specimens is lower than the single link test data (Table 6.2), when the shear contribution of flexural reinforcement is considered correctly.

## 6.7 Conclusions

In this chapter, investigations into flexibly formed concrete T-beams reinforced with W-FRP reinforcement has been presented. Eleven T beams were designed with different geometries, shear reinforcement and anchorages to investigate their influences. All the specimens were tested under seven-point bending until failure. The test results have been analysed based on the test results and the contributing factors to shear considered in the design are examined. The the predictions using the proposed revisions to ACI-440.1R (2015), CSA-S806 (2012) and MCFT model have been examined. The research in this chapter has supported the following conclusions:

1. All the three factors considered in the design: W-FRP reinforcement, geometry, and anchorage have shown great influence on the shear capacity and stiffness of the specimens.

2. Both shear reinforcement ratio and patterns influence the structural behaviour of specimens by changing the shear contribution of shear links and the load distribution between flexural and shear reinforcement. The pattern of specimen T3-2 has been shown as the best of those tested for the maximum corner strength.

3. The optimised geometry reduces the stiffness due to the increased the tensile force in flexural reinforcement. Both flexural tensile force created by bending moment and additional tensile force created by shear increase with smaller support depth.

4. The inclined flexural reinforcement is able to carry similar shear force to W-FRP shear reinforcement and high tensile force in longitudinal bars could result in a

two-step end slip failure mode, which enables higher deformability than the direct shear failure.

5. In all specimens, a 15% to 23% of concrete saving has been achieved compared with the equivalent T beam. The concrete saving in web achieves 41% to 64%.

6. The effectiveness of the anchorage is dependent on the tensile force in longitudinal bars. Equation 6.1 is proposed to describe the interactive relations between geometry, shear reinforcement and the tensile force in longitudinal bars near the support.

7. The prediction examination shows that the revised CSA S806 leads to the best correlation with the test results whilst the revised ACI 440.1R and MCFT model are conservative.

8. The revised codified methods underestimate the shear contribution of the longitudinal bars, which resulting in end slip failure. The different arrangements of W-FRP shear reinforcement patterns cannot be recognised.

Based on the knowledge acquired from this Chapter, further development of design methodology of W-FRP reinforcement beams with optimised geometry are presented in Chapter 7.

# Chapter 7

# Modelling and design guidance

**Structural performance of flexibly formed T beam**

## 7.1 Introduction

This chapter presents modelling and parametric analysis of the flexibly formed concrete T beams tested in Chapter 6, as development of the revised codified designs and revised MCFT presented in Chapter 3. Since the codified methods cannot simulate the whole loading process, a model is built based on the MCFT model (Vecchio and Collins, 1986) incorporating the analysis results of the T beam specimens to simulate the structural performance of the specimens.

The new model is used to conduct parametric analysis by changing the critical parameters including geometry and shear reinforcement ratio to achieve the optimal design of flexibly formed T beams reinforced with W-FRP. Based on the results of this Chapter and proposed design methodology in Chapter 3, design guidance is given.

## 7.2 Simulation model

### 7.2.1 Modeling procedures

To simulate the tests, there are four aspects to describe the structural performance of the specimens: i) flexural capacity; ii) load-deflection curve; iii) shear capacity and iv) shear contribution of the flexural reinforcement.

The flexural capacity is calculated following the procedures presented in section 3.2.1 of Chapter 3 and therefore no further details are given here. The load-deflection relations of the specimens are calculated following an equivalent moment inertia approach used for beams with variable stiffness, which is developed by Bischoff and Gross (2010a) (see section 3.2.2). The shear capacity and the tensile force in longitudinal bars near the support are calculated together based on MCFT model (Vecchio and Collins, 1986) and Equation 6.1 which has been proposed in the analysis of T beam specimens (Chapter 6). Considering the four aspects, the simulation process is conducted with the following procedures and further details are introduced in the following subsections:

1. Input the specimen design details including the beam geometry, reinforcement and concrete details (see section 7.2.2).

2. Divide the beam into numerous equally spaced cross sections. Calculate the bending strength of each cross-section and the equivalent moment of inertia.

3. Calculate the ultimate capacity (total load) under the test setup of the T beam specimens using the bending strength of each cross-section (see section 7.2.3). Calculate the displacement of each section following approach of Bischoff and Gross (2010a) (see section 7.2.4) at each loading step.

4. Conduct MCFT calculation by iterating the shear contribution of longitudinal bars calculated by Equation 6.1 and the shear contribution of concrete and shear reinforcement calculated by MCFT until the summation of these two parts is equal to the applied shear force (see section 7.2.5).

5. Output the calculation results: failure load, failure mode, failure location.

### 7.2.2 Input

The dimensions of the model (clear span, effective flange width, flange depth, web width, web depth) are taken here to be the same as the specimens. The specimens have 800mm flange width whilst the support is only 200mm wide. As the applied load is transferred to the support, a limited width of the flange works to resist flexure, following the Saint Venant (1856) principle. In normal prismatic beams, the reaction force is transferred to the surface of flange at a distance of effective depth $d$ (ACI-318, 2008), considering the 45° concrete strut. However, as discussed in section 6.6.3, the concrete strut angle may be different in fabric formed T beam specimens (also see the assumption in section 7.2.5). Therefore, the effective flange width near the support is determined by the concrete strut and the flange dimensions, as shown in Figure 7-1. The variable web width and effective depth of each cross-section along the beam axis are described by Equation 7.1 and Equation 7.2 respectively, in which $D_s$ is the depth at the support.

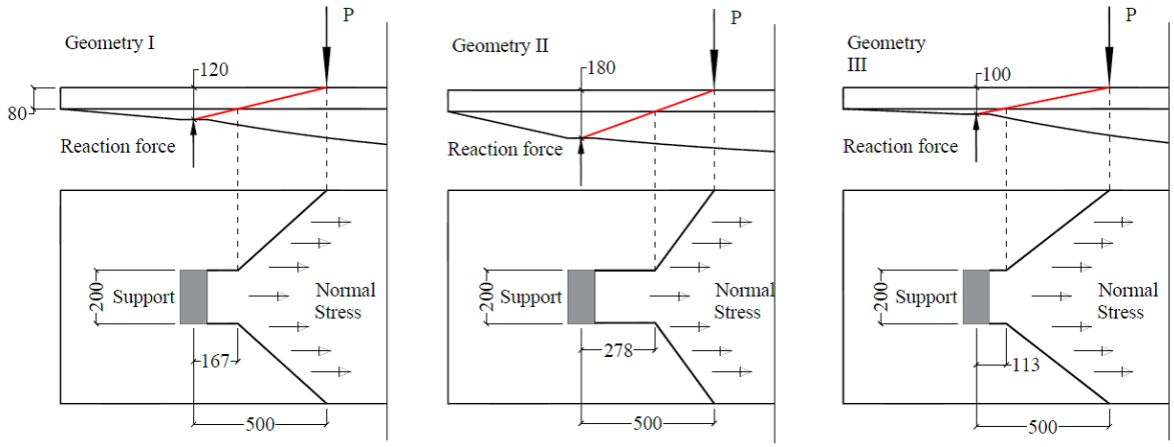


Figure 7-1: Assumed effective flange width

$$b_w = 2(50(\frac{x - 1500}{1500})^2 + 50) \tag{7.1}$$

$$d = 250 - (250 - D_s)(\frac{x - 1500}{1500})^2 - 25 \tag{7.2}$$

The flexural reinforcement and concrete properties used are taken from test results. The cross-section area of the flexural reinforcement is 212 $mm^2$, the tensile properties are shown in Table 6.2 in Chapter 6. The concrete properties are shown in Table 6.8

in Chapter 6.

For the shear reinforcement, although Spadea et al. (2017a) have already tested the single W-FRP shear link under tension, it could be unconservative to adopt the test results directly because the average performance of shear links in the specimens (Table 6.10) is lower than the test results from shear link tests (Table 6.2). Given that failure strain of shear links can influence calculation results of MCFT significantly, the failure strain of shear links for different cross-sectional areas is acquired from the actual tests. From all specimens including the prismatic beams (Chapter 4), variable depth beams (Chapter 5) and the T beams (Chapter 6), only the shear links composed of less than three layers of carbon fibre tows (50K) have ruptured. The average rupture strain of shear links composed of one layer and two layers of carbon fibre tows are adopted as the input. The statistics of these shear links are shown in Table 7.1.

Table 7.1: Average rupture strain of shear reinforcement in specimens

| Layer of 50K carbon fibres | Cross section area ($mm^2$) | Average rupture strain $\epsilon_r$ | SD |
|---|---|---|---|
| 1 | 4.28 | 0.51% | 0.15% |
| 2 | 8.56 | 0.62% | 0.30% |

The average strain of shear reinforcement rupture shown in Table 7.1 is calculated as the summation of rupture strains of vertical links and the vertical component of strains of diagonal links divided by the number of shear links. Using the average rupture strain could make the predictions conservative. The reason for adopting the vertical strain is that the shear reinforcement ratio calculated following Equation 3.7 only counts the spacing of vertical links and the diagonal links are considered as vertical links with a factor related to the angle. The MCFT calculation also assumes the shear reinforcement to be vertical.

The average rupture strain of links with a cross-section of $4.28\,mm^2$ will be used in the simulation of specimens T2-2R, T3-2 and the ratio between the average rupture strain and single shear link test result (Table 6.2) is 0.75. The calculation result for $8.56\,mm^2$ shear links are used in the simulation of T2-1R, T3-1 and T4-2 and the ratio between calculation result and single link test result (Table 6.2) is 0.73. Therefore a factor of 0.74 is used to account for the rupture strain of the shear links with five layers of carbon fibre tows, which are used in specimens T4-1, T5 and T6.

### 7.2.3 Flexural capacity

As presented in the calculation procedures in section 7.2.1, after the beam model is divided into sections, the bending strength of each section can be calculated based on the equilibrium of the cross-section and the model input. The approach to calculating bending strength of a cross section is presented in section 3.2.1 of Chapter 3.

The model considers two types of flexural failure: concrete crushing and longitudinal reinforcement rupture. The bending strength of each cross-section is taken as the lesser of the two. The total applied load, which is required to reach the bending strength of each cross-section, is calculated based on the seven-point bending test setup. The section which governs the flexural failure is output as the failure location and the minimum total applied load is output as the flexural capacity.

### 7.2.4 Load-displacement curve

The load-displacement relation is important to FRP reinforced concrete structure due to the lower stiffness of FRP reinforcement. It is even more critical to the variable depth beam since the displacement can increase the tensile force of inclined longitudinal bars at the support as discussed in section 6.6.3. Therefore, the model should accurately simulate the load-displacement curves of the specimens. Following the calculation procedures based on the equivalent moment of inertia approach from Bischoff and Gross (2010a) in the section 3.2.2 of Chapter 3, the load-displacement relations of the specimens can be calculated.

With the load-displacement relation for each of the cross section, the angle of the longitudinal bars to the horizontal axis near the support $\alpha_{rd}$ can be calculated, equals to the summation of initial angle of longitudinal bars $\alpha_r$ and the angle changed by the displacement of the loading jack next to the supports $\alpha_d$ (see section 6.6.5).

### 7.2.5 MCFT calculation and tensile force of longitudinal bars

The MCFT model used to predict the shear performance of the specimens is adopted and the calculation method is presented in section 3.2.3, Chapter 3. The tensile force of the longitudinal bars at the edge of the support plates $T$ is calculated with the following procedure:

1. Calculate the horizontal normal strain $\epsilon_n$ and applied shear stress $\upsilon_a$ at the mid-depth of the selected cross section as the initial input for MCFT calculation. The shear contribution of flexural reinforcement is excluded from this step.

2. Conduct MCFT calculation to obtain the stress and strain state of the shear links. Compare the strain of shear links $\epsilon_{fy}$ with the rupture strain $\epsilon_r$ specified in section 7.2.2.

3. Where $\epsilon_{fy}$ is lower than $\epsilon_r$, use $\upsilon_a$ and the cross section property to calculate the shear resistance provided by the cross section $F_v$. Otherwise, $F_v$ is regarded as zero and output shear failure. Then calculate the horizontal component of tensile force carried by shear reinforcement $F_h$.

4. Calculate the value of $T$ with Equation 6.1 in section 6.6.5 of Chapter 6 and its vertical component $T_v$.

5. Calculate the total shear resistance $V_u$ as $T_v$+$F_v$.

6. Where the difference ($C$) between $V_u$ and applied shear force $V_a$ is larger than the specified error range, recalculate the value of $\upsilon_a$ by reducing the shear resistance of longitudinal bars $T_v$ from the applied shear force $V_a$.

7. Iterate from step 2 until $C$ is lower than error range.

8. Repeat the calculation for each loading step.

There are a few assumptions in the calculation of the tensile force of longitudinal bars and its vertical component. First, as discussed in section 3.2.3.2 of Chapter 3, the typical shear stress distribution of a cross-section in a beam with the variable depth geometry is shown in Figure 7-2. The shear stress distribution in the compression zone is a concave curve. The area of the shaded shear stress in compression zone is simplified as one-third of the depth of compression multiplied by the maximum shear stress for simplification. The resulting maximum shear stress on the cross-section can be calculated directly with the applied shear force and the cross-section properties.

The second assumption is that the load is transferred from the loading jack next to the support through a straight concrete strut as shown in Figure 7-3. The discussion in section 3.2.3 shows that the tensile force in longitudinal bars near the support area changes along with the variation of support depth from 100mm (T6) to 180mm (T4-1). MCFT assumes the angle of the concrete strut is the same with shear crack. However, the actual shear crack angles do not change much as shown in section 6.6.1 of Chapter

6. Therefore, the concrete strut is assumed as a straight line linking the loading point and the support to address the variation of the concrete strut for different specimens.

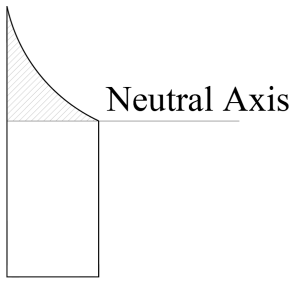


Figure 7-2: Typical shear stress distribution of a variable depth beam

The third assumption is that the shear cracking starts to develop at the bottom of the beam, 50mm from the edge of the support. Given that the model calculates the tensile force in longitudinal bars at the gauge location, the corresponding cross section should be adopted in the MCFT calculation. However, the shear cracks in the specimens were not developed from the edge support. The distance of 50mm is an approximate distance from the point where the shear cracks started to develop to the gauge location in the longitudinal bars from the tests. The resulting cross-section used for MCFT calculation is 100mm+$l/2$ away from the centre of the support, as shown in Figure 7-3, where $l$ is the horizontal projection length of the shear crack calculated from MCFT. Consequently, the shear resistance of shear reinforcement is no longer at the middle of the concrete strut. Equation 6.1 in section 6.6.5, which has been proposed to calculate the tensile force of longitudinal bars $T$, is rewritten as Equation 7.3, where $V_a$ is the applied shear force; $a_v$ is the length of shear span; $\theta$ is the angle of shear crack and $\theta_0$ is the angle of the concrete strut.

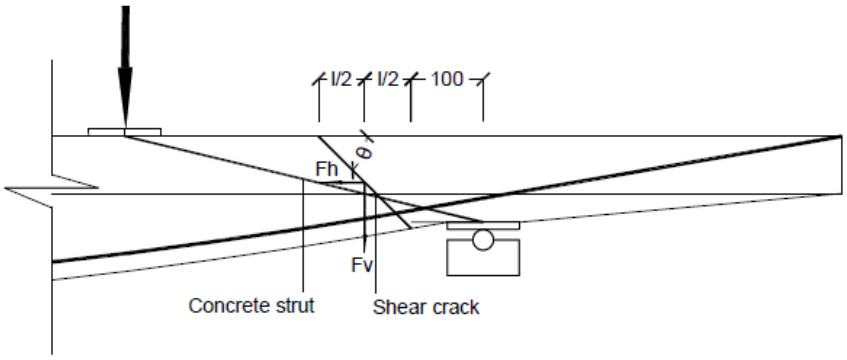


Figure 7-3: Concrete strut and assumed shear crack

$$T = \frac{(V_a - F_v(a_v - 100 - l/2) - F_h l \tan\theta/2/a_v)\cot\theta_0}{(\cot\theta_0 \tan\alpha_{rd} * (a_v - 50)/a_v + 1)\cos\alpha_{rd}} \tag{7.3}$$

Finally following Equation 3.7, which is used to calculate the shear reinforcement ratio as presented in section 3.2.3.4, the horizontal component of tensile force carried by the diagonal links is assumed as Equation 7.4, where $\alpha_1$ and $\alpha_2$ are the angles of the diagonal and vertical shear reinforcement to the horizontal axis.

$$F_h = F_v \frac{((\sin\alpha_1 + \cos\alpha_1)\cos\alpha_1 + (\sin\alpha_2 + \cos\alpha_2)\cos\alpha_2)}{((\sin\alpha_1 + \cos\alpha_1)\sin\alpha_1 + (\sin\alpha_2 + \cos\alpha_2)\sin\alpha_2)} \tag{7.4}$$

## 7.3 Validity examination

This section presents the validity examination of the model presented in section 7.2. The load-displacement relations of the specimens are compared with the modelling results. The comparison of the structural performance (the shear failure loads, the strains of longitudinal bars, and shear resistance of longitudinal bars) are made between the modelling results and test results.

### 7.3.1 Load-displacement relation

Using the equivalent moment of inertia approach from Bischoff and Gross (2010a), the load-displacement curves of the specimens of three geometries are calculated. As all the specimens have different concrete strength from cylinder test, the model adopts the concrete strength in design, 45MPa. The effective flange width used in the flexural capacity calculation is also used to calculate the cross-section properties.

The load-displacement curves of specimens of the geometry I (T1, T2R, T3 and T5), geometry II (T4-1 and T4-2), and geometry III (T6) (see section 6.2.3) at the mid-span are compared with the simulation results, as shown in Figure 7-4, Figure 7-5 and Figure 7-6, where the simulations stop at the calculated flexural capacities of the specimens. Since about half of the specimens encountered end slip of the longitudinal bars after 200kN of the applied load, the load-displacement comparison before the debonding is compared in Table 7.2. The test results are taken as average value when there are several specimens having the same geometry.

As shown in Table 7.2, the model gives a good simulation of the initial stiffness of

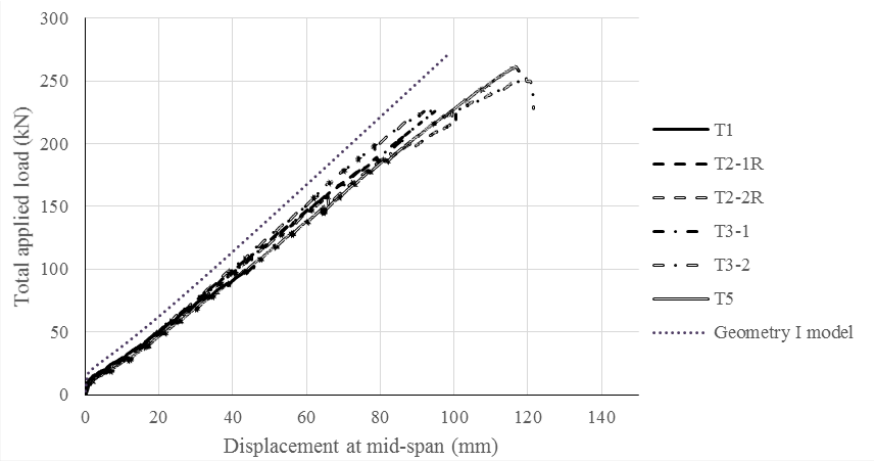


Figure 7-4: Load-displacement comparisons of geometry I

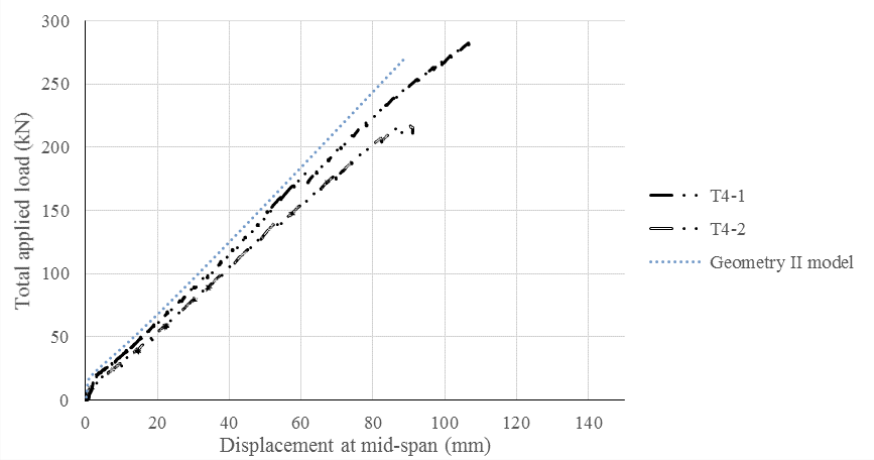


Figure 7-5: Load-displacement comparisons of geometry II

specimens. The maximum difference between model and tests is 15% from the geometry I. The best simulation comes from specimen T6 which has the geometry III with a displacement difference of 10% at 200kN of the applied load. However, after 200kN, the simulation model has a larger difference from the test results as the model only considers the tensile strain of longitudinal bars created by the bending moment. The concrete crushing, the opening of shear cracks, and the additional tensile force created by shear could increase the displacement but they are not considered in the model. Consequently, the model results show larger stiffness than the specimens after 200kN.

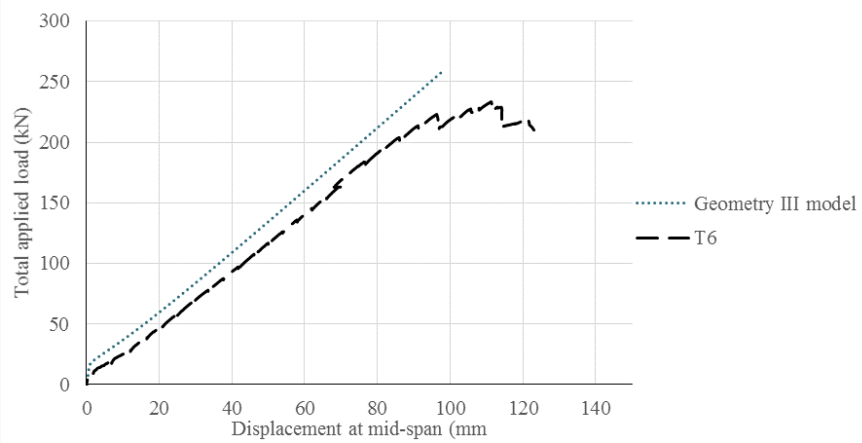


Figure 7-6: Load-displacement comparisons of geometry III

Table 7.2: Load-deflection comparison between model and tests

| Specimen | Load (kN) | Test displacement (mm) | Model displacement (mm) | Difference (%) |
|---|---|---|---|---|
| Geometry I | 200 | 85.3 | 72.5 | 15.0 |
| Geometry II | 200 | 75.5 | 65.4 | 13.3 |
| Geometry III | 200 | 84.3 | 75.4 | 10.5 |

### 7.3.2 Structural performance simulation

Using the verified load-displacement relations, the tensile force in the longitudinal bars is calculated as specified by the procedures in section 7.2.5. At the same time, the response of shear links under applied load is also calculated with the shear resistance of longitudinal bars. To simulate each specimen, the actual concrete strength of each specimen is used (Table 6.8).

Two simulation results are calculated by the model. Using Model I, the predictions of failure is calculated with the rupture strain of shear links in Table 7.1. Model II is used to acquire the design rupture strain of shear links when the perfect prediction is made for the under-reinforced specimens.

As shown in Figure 7-7, the average strain in longitudinal bars at the gauge location in T2-1R calculated using Model I and Model II is compared with strain gauge data. For Model I, between 0kN to 100kN of the applied load, there is a large difference between model and test because in actual test only when there was a crack developed, the longitudinal bars started to carry large tensile force. Between 100kN to 131kN of

the applied load, Model I has a good correlation with the test results. At 131kN, there is a plateau in the model curve, which is caused by the rupture of shear links. The shear failure load is 30% lower than the actual failure load from the test, indicating the shear prediction is conservative. For Model II, when the model input of rupture strain in shear links is set as 0.65%, the plateau occurs at the same load of shear link rupture in T2-1R. Between 100kN to 187kN, the strain in the longitudinal bars are simulated well by Model II.

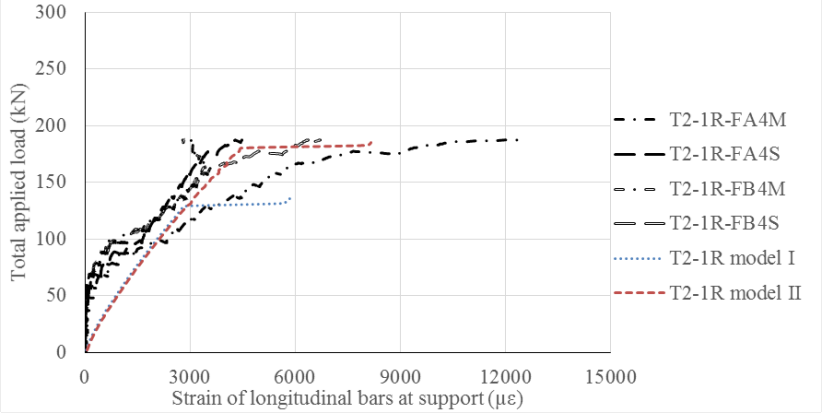


Figure 7-7: Comparison of strains of flexural reinforcement of T2-1R

The shear contribution of longitudinal bars calculated with Model I and II is also compared with test data as shown in Figure 7-8, which shares very similar characteristics with the strain curve in Figure 7-7. Since in the actual test, the longitudinal bars started to carry tensile force after shear cracks developed, there is a difference between the model and test results in the initial part of the curves.

Similar calculation results are found from Model I and Model II of T3-1R as shown in Figure 7-9 and Figure 7-10. However, due to the reinforcement pattern of the 45-degree diagonal links and 65-degree vertical links, the models of T3-1 can provide a higher horizontal component of the tensile force in the shear reinforcement than those of T2-1R. Therefore, the longitudinal bars of T3-1 carried lower shear force under the same load than T2-1R, according to Equation 7.3. With the same strength of shear reinforcement, Model I of T3-1 failed at 122kN in shear, 39% lower than the load of shear link rupture in the test. For Model II, if the model fails in shear at the same load observed from the test, the rupture strain in shear links reaches 0.67%. Consequently, both the strain in longitudinal bars and the resulting shear resistance are well simulated.

With the higher rupture strain of shear links, the Model I of T2-2R (Figure 7-7) is more accurate than those of T2-1R and T3-1. The load of shear link rupture in Model

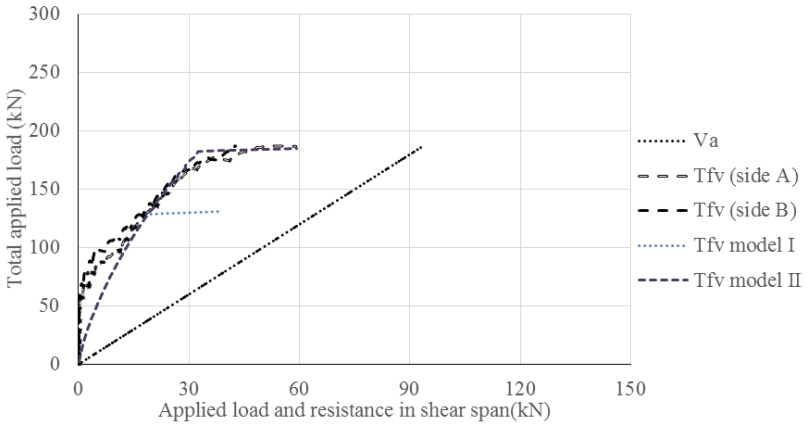


Figure 7-8: Comparison of shear resistance of flexural reinforcement of T2-1R

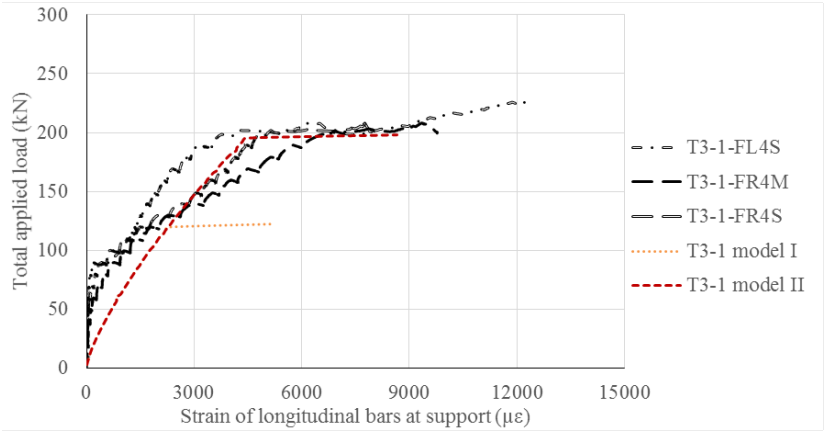


Figure 7-9: Comparison of strains of flexural reinforcement of T3-1

I of T2-2R is 181kN, which is 10% lower than the actual load of shear links rupture. For Model II, when the rupture load of shear links is accurately simulated, the rupture strain is 0.70%, similar to 0.62% as shown in Table 7.1. Overall, Model I and II of T2-2R have good simulations of the tensile strain and shear resistance (Figure 7-8) of the flexural reinforcement after 100kN.

Similar model results are found in T3-2, as shown in Figure 7-9 and Figure 7-10. With the same reason of patterns with T3-1, the Model I of T3-2 has a lower load of shear links rupture at 174kN, 21% lower than the test results. If the rupture strain of shear links is set as 0.74%, the Model II encounters the same load of shear link rupture as that in tests. Model II has very good simulations of tensile strain and shear resistance of longitudinal bars through the loading process.

For the specimens that failed in end slip, the plateaus in the strain curves (Figure 7-9,

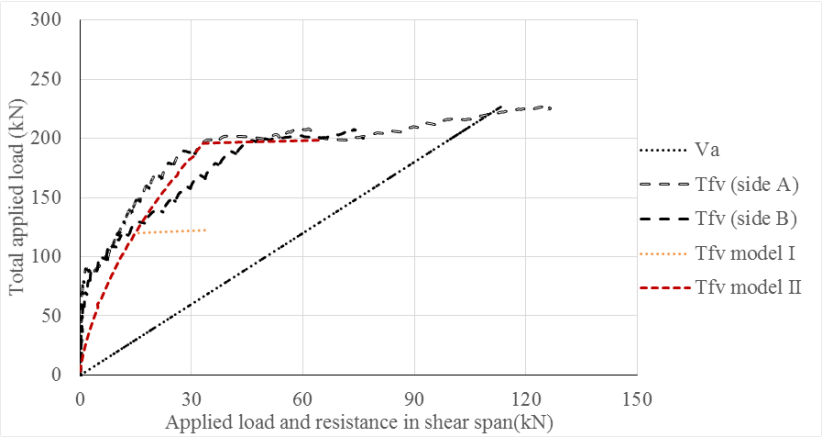


Figure 7-10: Comparison of shear resistance of flexural reinforcement of T3-1

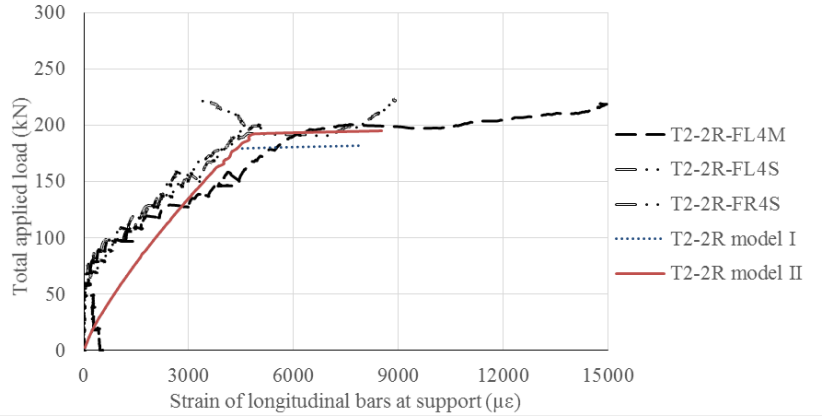


Figure 7-11: Comparison of strains of flexural reinforcement of T2-2R

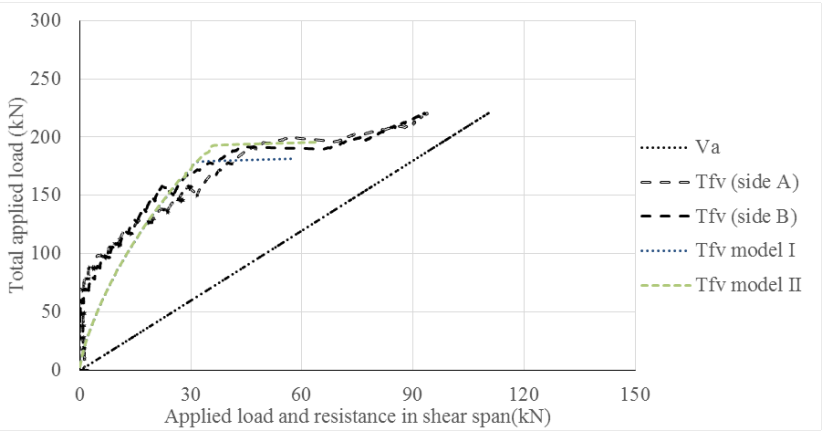


Figure 7-12: Comparison of shear resistance of flexural reinforcement of T2-2R

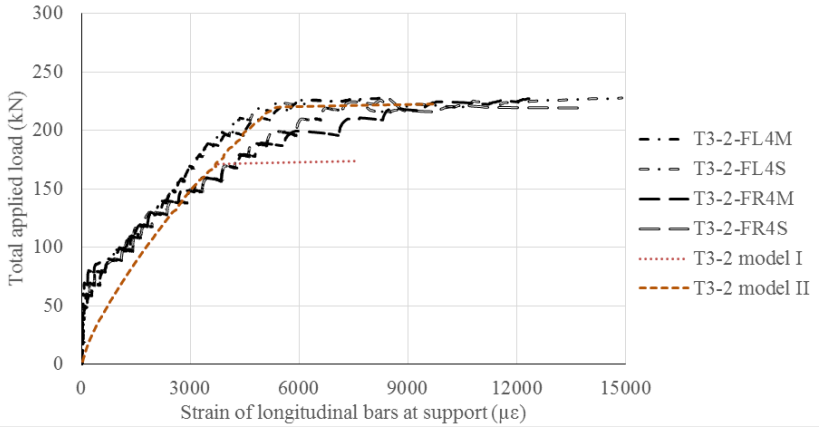


Figure 7-13: Comparison of strains of flexural reinforcement of T3-2

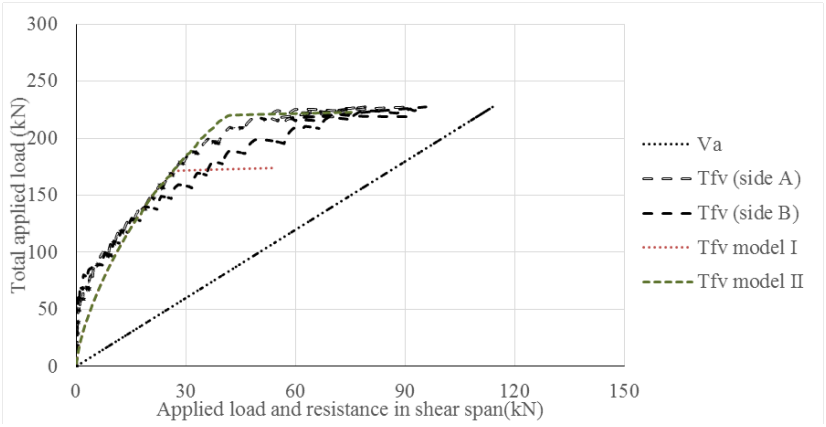


Figure 7-14: Comparison of shear resistance of flexural reinforcement of T3-2

Figure 7-11 and Figure 7-13) and the shear resistance curves (Figure 7-10, Figure 7-12 and Figure 7-14) of Model II explain the reason for the high strain in longitudinal bars after the shear link rupture. The shear reinforcement works as an important component to restrain the tensile force of longitudinal bars. When the shear links rupture, only the longitudinal bar can resist the applied shear force and balance the load transferred to the support.

With the support depth increasing, the shear reinforcement will carry more shear force as the angle of flexural reinforcement becomes smaller and shear contribution provided by the flexural reinforcement becomes lower. As shown in Figure 7-15 and Figure 7-16, the shear links rupture in Model I of T4-2 at 108kN. The simulation curve of longitudinal bar strain (Figure 7-15) shares similar trend with the test data. For Model II, the rupture strain of shear links is calculated as 0.64%.

During the test of specimen T4-2, the first sound of FRP rupture was heard at approximately 140kN, which correlates to the load of strain plateau of the test data. Although there is no proof showing the shear link rupture as the strain continued growing until final failure, it is likely that one of the links not being gauged gave out the sound as discussed in Chapter 6. Under this assumption, the load of shear link rupture in the Model I of T4-2 is 23% lower than test result.

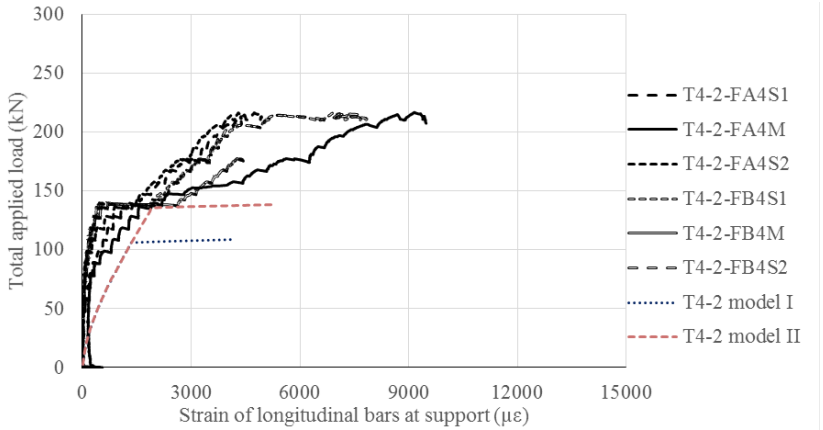


Figure 7-15: Comparison of strains of flexural reinforcement of T4-2

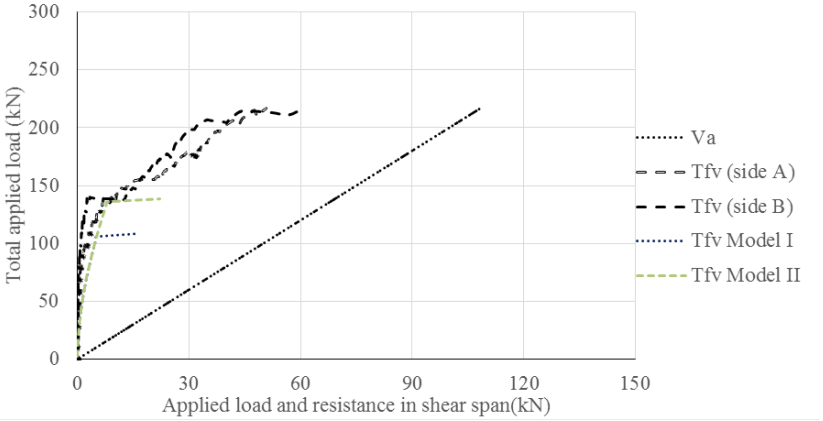


Figure 7-16: Comparison of shear resistance of flexural reinforcement of T4-2

For Model I of the transversely under-reinforced specimens, the rupture load of shear reinforcement is underestimated due to the rupture strain obtained from test data statistics. In specimens T2-1R, T2-2R, T3-1, T3-2, and T4-2, the underestimation of rupture load of W-FRP reaches 30%, 10%, 39%, 21%, and 23% respectively. For Model II, in order to accurately simulate the rupture load of shear links in different specimens, the rupture strain of shear links is calculated. The strain varies from 0.65% to 0.70% for shear links made of two layers of 50K carbon fibre tows and from 0.67% to 0.74%

for those made of one layer of carbon fibre tows.

In the testing, rupture of a single shear link does not necessarily cause shear failure. The load was transferred from the ruptured links to the longitudinal bars. However, the model cannot simulate the gradual rupture of shear links and consequently, the rupture of shear links directly leads to shear failure because the abrupt increase of shear contribution provided by flexural reinforcement cannot replace the loss of shear reinforcement if the tensile force of flexural reinforcement is calculated by Equation 7.3.

When the specimens are transversely over-reinforced, Model I has excellent correlations with the strain and shear contribution of longitudinal bars. Given that all these specimens did not encounter shear link rupture, there is no need to use Model II to find the rupture strain of shear link. For specimen T4-1, the simulation of flexural reinforcement strain correlates well with most the strain data curves after 100kN as shown in Figure 7-17. T4-1 is predicted to fail in flexure at the mid-span under 271kN of the applied load, which has only 3% difference from the test data. With good simulation of tensile force of longitudinal bars, the simulation of the shear contribution of longitudinal bars also correlates well to test results.

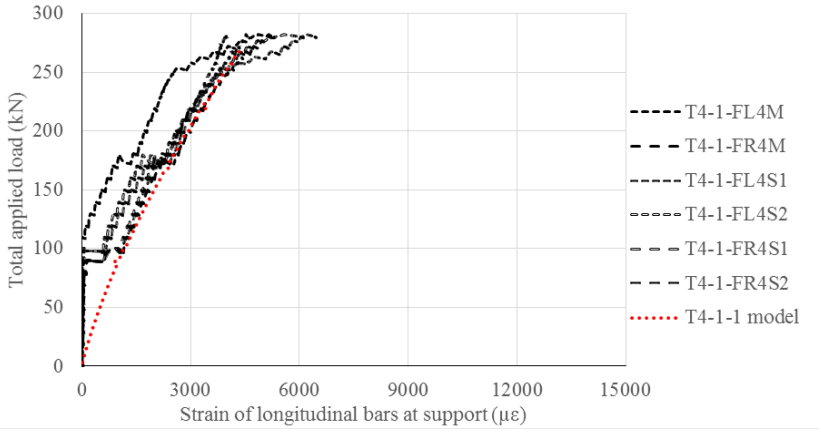


Figure 7-17: Comparison of strains of flexural reinforcement of T4-1

For specimen T5, there are larger variations between the strain test data from the two supports as shown in Figure 7-19. As the data from side A are higher than the strain data from all other specimens failed in flexure, therefore, the simulation results are only compared with data obtained from side B support. The model of T5 has a good simulation of the strain development in longitudinal bars. With no shear link rupture, T5 is predicted to fail in flexure at mid-span at 271kN, 3% larger than the test results. Similar to the strain data, the shear contribution carried by the flexural reinforcement

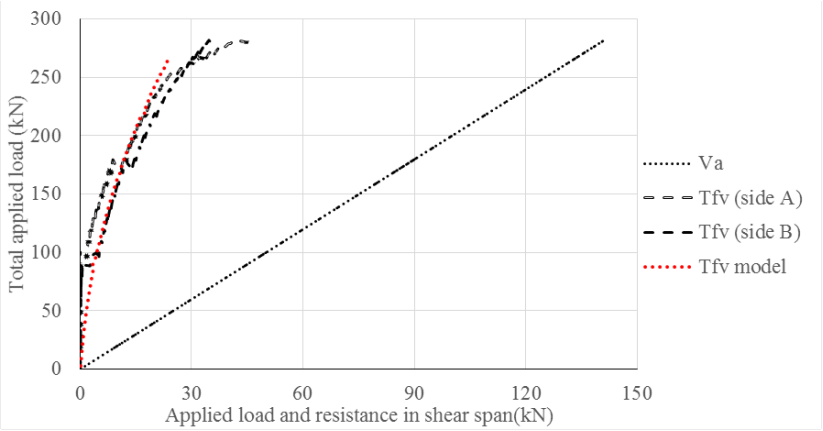


Figure 7-18: Comparison of shear contribution of flexural reinforcement of T4-1

simulation is also accurate at support B (Figure 6-20).

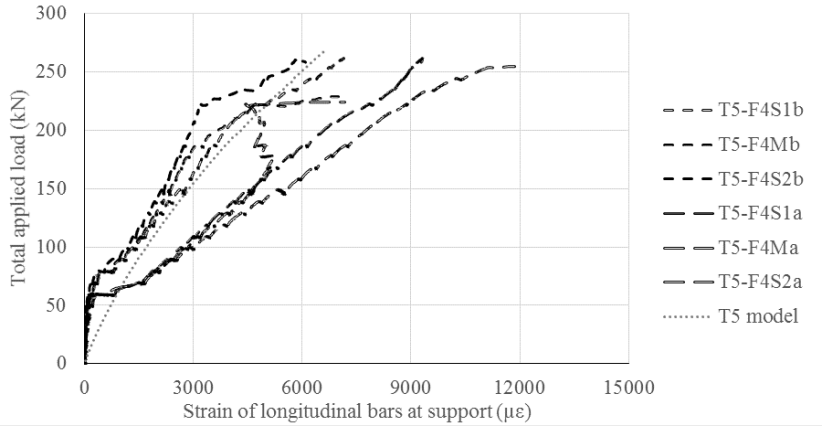


Figure 7-19: Comparison of strains of flexural reinforcement of T5

For specimen T6, the simulation of flexural reinforcement strain correlates well with the strain data curves after 100kN as shown in Figure 7-21. However, the failure mode of T6 is predicted as a flexural failure at mid-span at 271kN, which is 18% larger than the test results and is at the wrong location. This could be caused by the flaw in the casting, which located near loading jack P5 as presented in section 6.5.2.

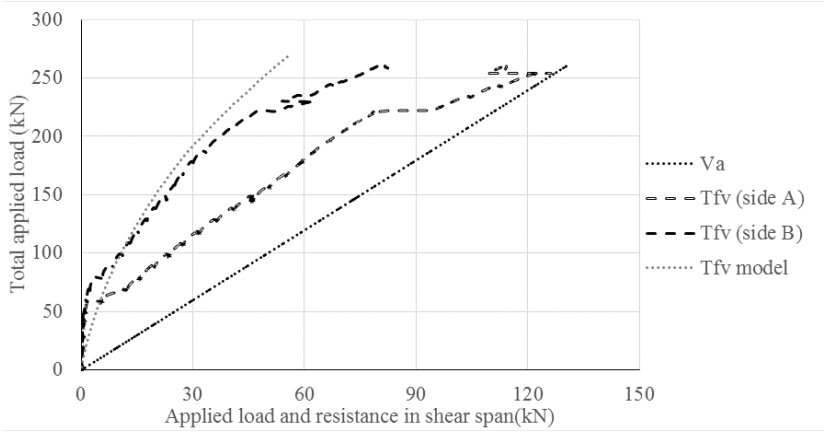


Figure 7-20: Comparison of shear contribution of flexural reinforcement of T5

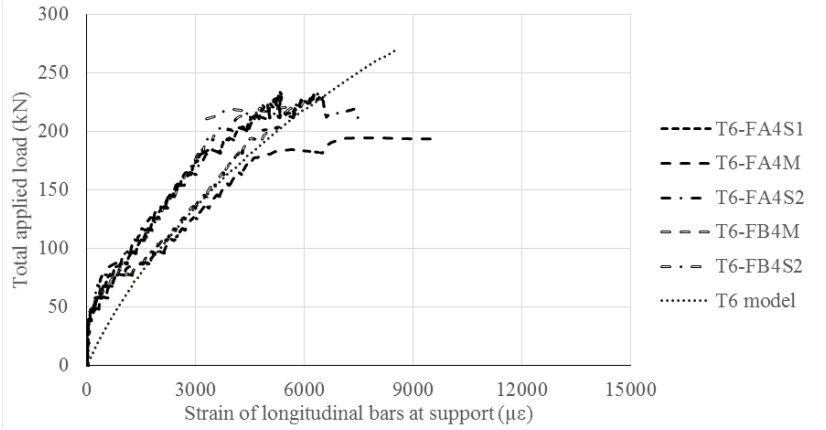


Figure 7-21: Comparison of strains of flexural reinforcement of T6

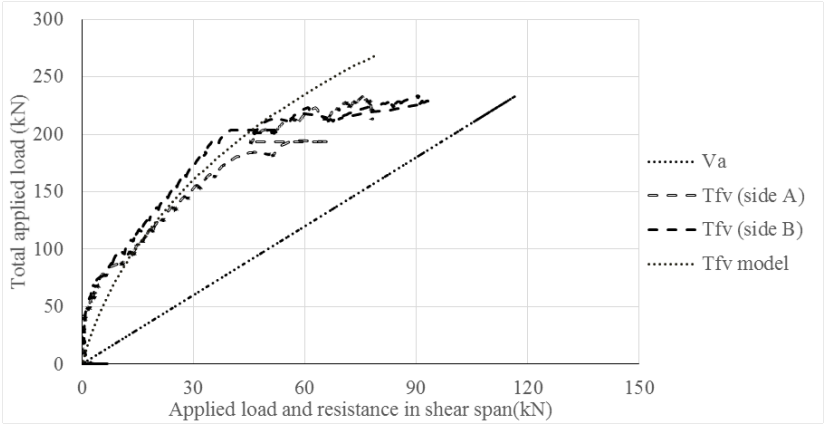


Figure 7-22: Comparison of contribution of flexural reinforcement of T6

### 7.3.3 Summary

This section presents the validity examination of the simulation model. The model shows good correlation with the load-displacement curves from tests with a maximum 15% difference of deflection at 200kN from the test data.

In the simulation of structural performance, the model shows great validity for the transversely over-reinforced specimens. For T4-1, T5 and T6, the strain and shear contribution simulations correlate with the test data well. The ultimate capacity predictions of T4-1 and T5 have a difference of only 3% from the test results and for T6, the difference reaches to 17% due to the wrong failure location prediction.

For Model I of the under-reinforced specimens, due to the conservative rupture strain of shear links obtained from test data statistics, the prediction for the shear links rupture are conservative. For T2-1R, T3-1 and T4-2, the difference of shear link rupture load between tests and the model reaches up to 39%. Whilst the simulations of the specimens with shear links of $4.28\,\mathrm{mm}^2$ (T2-2 and T3-2) are more accurate with the difference up to 21%.

For Model II of the under-reinforced specimens, different design strains of shear links, which can result in accurate simulations of the load of shear link rupture in the specimens, are calculated. The strain varies from 0.65% to 0.70% for shear links made of two layers of 50K carbon fibre tows and from 0.67% to 0.74% for those made of one layer of carbon fibre tows.

The modelling of under-reinforced specimens also explains the reason for the debonding failure: the gradual rupture of shear links in the tests transferred the applied shear force to the flexural reinforcement. However, the model cannot simulate the gradual rupture of the shear links. The output at the load of shear links rupture is shear failure.

The model can be used for further parametric analysis. By varying the geometry, the model can accurately predict the tensile force and shear contribution of flexural reinforcement. By varying the shear reinforcement, the Model I can conservatively predict the shear performance for under-reinforced specimens whilst Model II can give accurate predictions using the rupture strain of shear links obtained.

## 7.4 Parametric analysis

This section presents the parametric analysis of the geometry, shear reinforcement ratio with the model verified in section 7.3. By varying the two parameters, the structural performance of different design cases is investigated. With the study of parametric analysis, an optimal design case is acquired, which minimises the material usage without compromising structural performance.

### 7.4.1 Geometry

The parametric analysis of geometry is conducted with varied profiles of the effective depth of each cross-section (Equation 7.2) by changing the support depth from 80mm to 250mm. The 80mm support depth is set to simulate the case that the flange is placed on the support directly. The 250mm support depth is to simulate the geometry of prismatic T beam with constant depth along the beam axis. The concrete strength is set as 45MPa. To exclude the influence of shear reinforcement, the shear reinforcement ratio of T5 is used to ensure the strength of shear reinforcement.

The load-displacement relations at the mid-span of the modelling are plotted against applied load as shown in Figure 7-23. When the support depth changes from 250mm to 80mm, the stiffness of the specimens changes from 3.17kN/mm (calculated as the slope of the curve) to 2.25kN/mm. When the support depth is 80mm, the flexural failure location is changed from the mid-span to 300mm away from the support due to concrete crushing and the resulting failure load is 232kN of the total applied load.

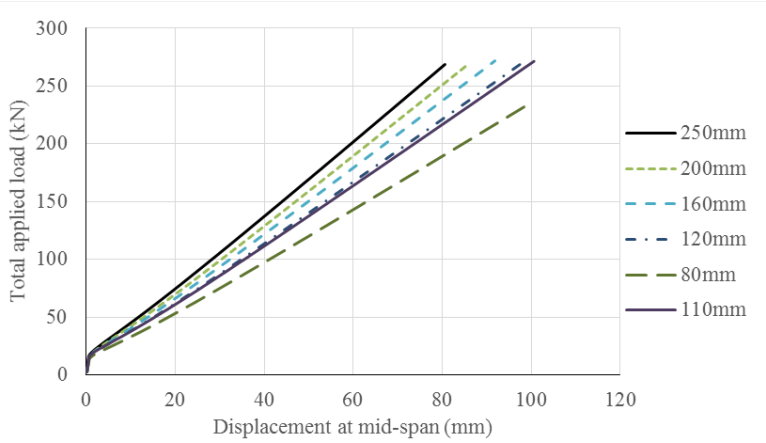


Figure 7-23: Load-displacement relations with varying support depth

The average tensile strains of the flexural reinforcement at the support area are plotted against applied load as shown in Figure 7-24. The resulting shear resistance of the flexural reinforcement is plotted against applied load in Figure 7-25. Both the average tensile strain and the shear resistance of the flexural reinforcement increase non-linearly with the total applied load. Due to the non-linear increase of the angle of flexural reinforcement to the horizontal axis, the difference of the shear resistance of flexural reinforcement (Figure 7-25) between different cases is even larger than the difference of average strains shown in Figure 7-24. When the support depth decreases, the angle of flexural reinforcement increases as shown in Table 7.3.

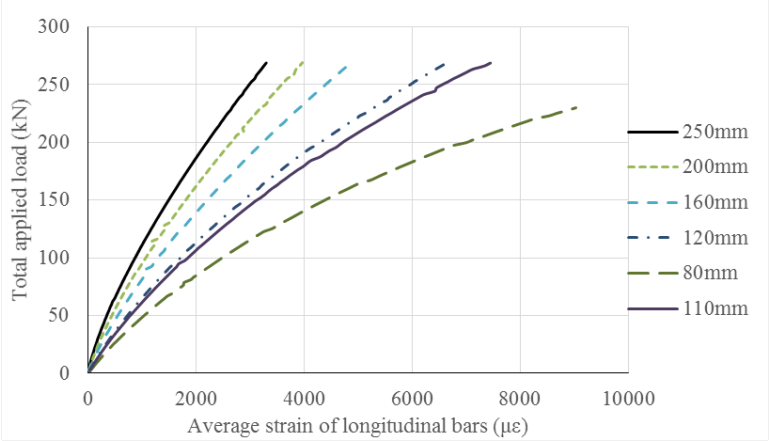


Figure 7-24: Tensile strains of flexural reinforcement with varying support depth

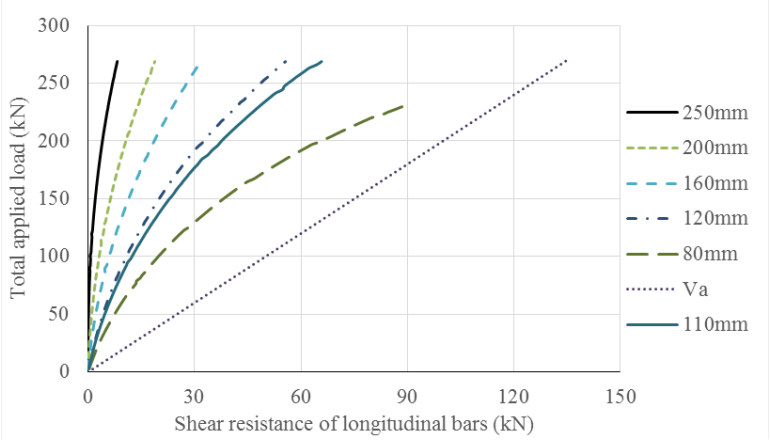


Figure 7-25: Shear contribution of flexural reinforcement with varying support depth

In Figure 7-24 and Figure 7-25, another design case of 110mm is added to show the minimum support depth of the geometry for which the flexural failure occurs at mid-span. This case minimises the concrete usage without compromising the flexural

capacity. The average strain of longitudinal bars is 7400 $\mu\epsilon$ which indicates that in this case with the bonding length of 500mm, the longitudinal bars will not debond.

For simply supported prismatic beams, the tensile force of flexural reinforcement at the support is normally regarded as zero and the shear resistance is normally neglected. However, it is seen from Figure 7-24 that the flexural reinforcement of prismatic beam case (250mm) has 3200 $\mu\epsilon$ at the flexural failure load and a shear resistance of 8.2kN. The tensile strains and shear resistance is mainly caused by the increasing displacement.

When the support depth is 80mm, the average tensile strain of the flexural reinforcement reaches 9000 $\mu\epsilon$ and the resulting shear contribution reaches 88.6kN. The non-linear relations between $\beta$ and $T_v/V_a$ confirms the discussion presented in the section 6.6.3 of Chapter 6 that the geometries can influence the tensile force of longitudinal bars and the stiffness changed by the geometry can influence the tensile force of longitudinal bars.

Table 7.3: Modeling results of varying support depth at failure load

| Support depth | Angle of flexural reinforcement (degrees) | Shear contribution of flexural reinforcement $T_v$ (kN) | Applied shear force $V_a$ (kN) | $T_v/V_a$ |
|---|---|---|---|---|
| 250mm | 0.0 | 8.2 | 135 | 0.06 |
| 200mm | 3.7 | 18.7 | 135 | 0.14 |
| 160mm | 6.7 | 31.7 | 135 | 0.24 |
| 120mm | 9.6 | 55.6 | 135 | 0.41 |
| 80mm | 12.5 | 88.3 | 116 | 0.77 |
| 110mm | 10.4 | 65.8 | 135 | 0.49 |

### 7.4.2 Shear reinforcement ratio

A parametric analysis of shear reinforcement ratio is conducted based on the Model II of T3-2, the shear reinforcement of which exhibited the largest rupture load. The support depth is revised to 110mm, which results in minimised concrete usage. The concrete strength is set as 45MPa. The analysis aims to investigate the minimum shear reinforcement ratio that results in flexural failure. It is assumed that all the shear links in this model are only composed of one layer of 50K carbon fibres. Therefore the rupture strain of shear links used in the model is set as 0.74%, as discussed in section 7.3.2.

It is possible that the flexural reinforcement carries all the applied shear force after the

rupture of shear links. Therefore, after the shear link rupture, the tensile force carried by flexural reinforcement is assumed to carry all applied load to simulate the end slip failure specimens. The failure criteria then will be changed that the tensile force of flexural reinforcement is larger than the anchorage strength (Table 6.16).

The shear reinforcement ratio of the model increases from 0.3% at increments of 0.03% until no rupture of the shear reinforcement is found. The calculation results of the average tensile strain of longitudinal bars are shown in Figure 7-26, where the plateaus show the rupture loads of shear links. The load of shear failure increases with the higher shear reinforcement ratio. When the shear reinforcement reaches 0.39%, shear link rupture is avoided and the model fails in flexure at the mid-span.

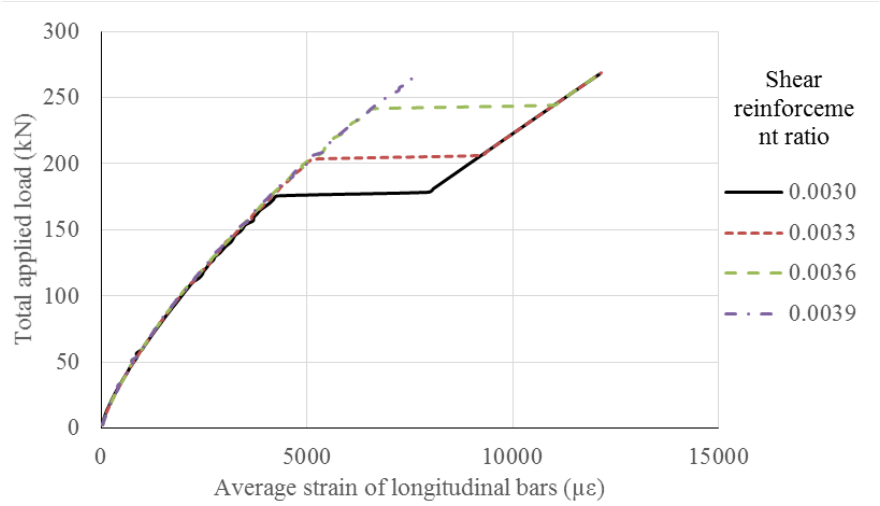


Figure 7-26: Tensile strains of flexural reinforcement with varying shear reinforcement ratio

Having the same shear reinforcement pattern of T5, the model has the same average tensile strain of flexural reinforcement of 7400 $\mu\epsilon$, when the shear reinforcement does not rupture, as shown in Figure 7-26 and Figure 7-24. This tensile force of flexural reinforcement calculated by this strain is lower than the anchorage strength of three longitudinal bars with 500mm bonding length as observed from the tests. The flexural reinforcement can provide 65.8kN of shear contribution, which is 49% of the applied shear force.

When the shear reinforcement is lower than 0.39%, the shear reinforcement rupture transfers the load to flexural reinforcement at the load of shear link rupture. If the shear links rupture gradually as assumed, it is possible that the model fails with a higher load through end slip of longitudinal bars. When adopting the same anchorage design

of T4-2, which has no splayed anchorage installed (Table 6-17 in the section 6.2.5), the longitudinal bars will encounter end slip at the strain of 0.99%. The resulting prediction of failure load at shear reinforcement ratio 0.36% reaches 244kN and the shear link rupture causes the end slip of longitudinal bars. For the cases with a shear reinforcement ratio of 0.30% and 0.33%, the predictions will be end slip failure at 222kN.

Although it is good to have a higher ultimate capacity than the load of shear link rupture by using the flexural reinforcement to carry all the applied shear force, the test of T2-1R also shows that it is possible that the T beam fails in shear directly when all the shear link crossing the shear crack rupture at the same time. Therefore it is better to use the load of shear links rupture as the prediction for design and the higher failure load of debonding could be regarded as safety reservation in practice.

Using flexural reinforcement to carry all applied shear force results in lower capacity than the flexural capacity. To increase this ultimate capacity, addition anchorage is required to improve the anchorage strength, which leads to additional cost. For the simplification of manufacturing, it is not recommended to have under-reinforced beams with additional anchorage installed.

However, the ultimate capacities of the specimens were much higher than the design under ultimate capacities as service limit state governs the final design. Compromising the ultimate capacity is not critical in design. Therefore, when the beams are required not to fail in brittle way, it is better to install additional splayed anchorages to have two-step end slip failure.

Another method to increase the load of end slip failure is to add the flexural reinforcement bars. The resulting stiffness of the beam will be higher, which leads to a lower tensile force of longitudinal bars. With a larger area of flexural reinforcement, the average strain of the flexural reinforcement will be lower. Both the two factors can increase the load of end slip failure. However, increasing the usage of flexural reinforcement also indicates higher cost whilst the flexural capacity does not necessarily increase because the flexural failure could be controlled by cross-sections other than the mid-span. Finally, adding bars is not the optimal case minimising the material usage.

### 7.4.3 Optimal case

With the analysis of section 7.4.1 and section 7.4.2, under 271kN total applied load (UDL=90kN/m), the model predicts that the optimal design case of a simply supported

flexibly formed T beam reinforced with W-FRP shear reinforcement would have a support depth of 110mm. The shear reinforcement ratio should reach 0.39% and the shear reinforcement pattern of T3-2 should be used. The design details of the optimal case are shown in Figure 7-27. With this design, the specimen is predicted to fail in flexure with no shear reinforcement rupture or end slip of flexural reinforcement.

The volume of concrete usage of this design case is calculated and compared with the equivalent prismatic T beams (Table 6.15) as shown in Table 7.4. The comparison shows that 61% of concrete in the web is saved and for the total usage, 21% of saving is achieved.

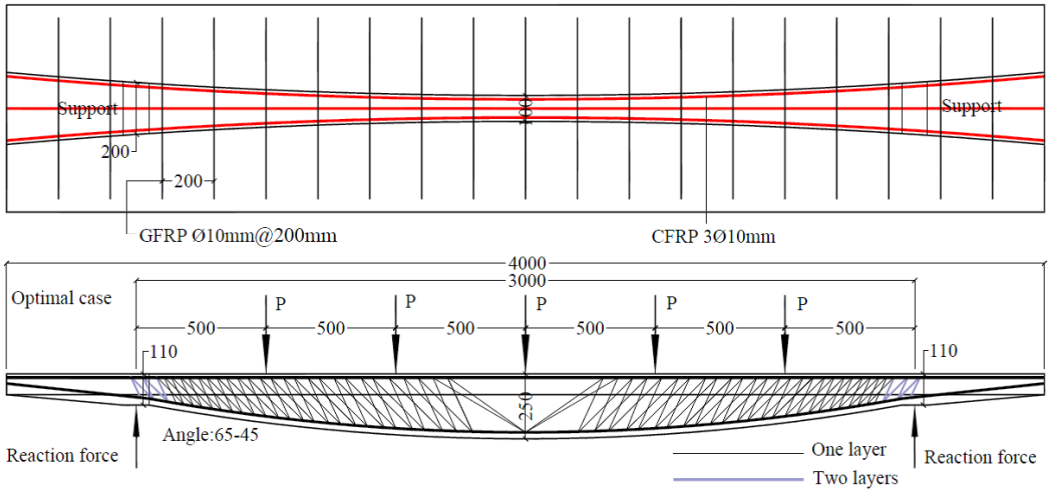


Figure 7-27: Design details of the optimal case

Table 7.4: Comparison of concrete usage

| Design case | $Q_{c,web}$ $(m^3)$ | $Q_{c,flange}$ $(m^3)$ | $Q_c$ $(m^3))$ | Ratio of $Q_{c,web}$ | Ratio of $Q_{c,flange}$ | Ratio of $Q_c$ |
|---|---|---|---|---|---|---|
| Optimal | 0.053 | 0.256 | 0.308 | 0.39 | 1.00 | 0.79 |
| Prismatic T-beam | 0.136 | 0.256 | 0.392 | 1.00 | 1.00 | 1.00 |

However, it should be noted that the geometry of this design case is the optimum one revised from the tested T beam specimens (Chapter 6), the design of which was governed by service limit state. Much more concrete can be saved when service limit state design is not allowed to govern the final design. As shown in Figure 6-4, the mid-span depth of the design is reduced to 140mm when a balanced failure mode is assumed. If the design load (2.4kN/m dead load and 7.5kN/m live load) is used to

conduct ultimate limit state design, the top slab itself is capable of carrying the design load, which results in 35% total concrete saving.

In addition, as shown in Table 7.4, the flange concrete use has not been optimised as the flange was designed to simulate the standard slab depth in actual buildings. Using fabric formwork also provides the opportunity to form optimised T beam flange as there is a great proportion of concrete in the flange not resisting flexure. Even higher concrete saving can be achieved if flange optimisation is conducted.

### 7.4.4 Summary

This section presents the parametric analysis of the modelling. The geometry and shear reinforcement ratio are selected as the varying parameter for their significant influence on the structural performance of the specimens. An optimal design case is acquired to minimise the material usage.

When varying the geometry, the tensile strain and shear contribution of flexural bars increase with the decreasing support depth. Without reducing the flexural capacity, the minimum support depth is calculated as 110mm and the resulting shear contribution is calculated as 65.8kN, 49% of the applied shear force when the shear reinforcement pattern of T5 is adopted.

The optimal case is acquired through the parametric analysis to minimise the shear reinforcement and concrete usage. Up to 69% of concrete in the web is saved compared with the equivalent prismatic T beam.

## 7.5 Design guidance

Based on the analysis of test results (Chapter 6), the successful modelling of test results and the parametric analysis, guidance is given to design a simply supported and W-FRP reinforced beam with optimised geometry in this section.

As the codified design methods (ACI-440.1R, 2015; CSA-S806, 2012) have shown accurate prediction of bending strength, the flexural design procedures presented in section 3.2.1 can be used for optimising the geometry of beams to minimise concrete use.

The load-displacement relation is important to FRP reinforced concrete beams. For

beams with variable-depth geometry, the displacement is critical in the shear design by influencing the shear contribution of longitudinal bars. The proposed effective moment of inertia approach from Bischoff and Gross (2010a) (section 3.2.2) has shown great validity in the modelling of test results. Using this approach, the load-displacement relations of the beam that has the optimised geometry in flexural design can be determined. The depth of each cross-section of the optimised geometry in flexural design needs to be revised, to meet the requirement of displacement limit.

After the geometry has been revised based on load-displacement relations, the bending strength of each section needs to be checked to make sure that flexural failure occurs at a favourable location, such as mid-span.

With the optimised beam geometry, the shear design can be conducted based on the Model II, built in this Chapter, instead of using the design procedures proposed in section 3.2.3. Equation 7.3, which has been shown valid in modelling of the test results, should be used to simulate the tensile force of longitudinal bars of the beams, instead of Equation 3.2, since the prediction calibration in Chapter 6 has shown the codified method to consider the inclined longitudinal bars is not appropriate for variable-depth beams. Instead of directly adopting the corner strength of W-FRP reinforcement from single link tests (Spadea et al., 2017a), design strength of W-FRP shear links at reduced strains (see section 7.3.2) shall be used to consider the lower strength of multiple shear links in concrete.

Based on the flexural, load-displacement and shear design, the structural performance of the designed beam can be determined. Different from prismatic beams, the optimised beam in geometry and shear reinforcement can still have large tensile force at the support area. An appropriate bonding length is required to ensure the beam does not failing prematurely due to end slip of longitudinal bars. Alternatives, such as splayed anchorage, can be installed to have the required anchorage strength (see Table 6-17).

Following this design process, the geometry of the specimens is normally governed by service limit state. The design service load could be over-estimated and limits of the displacement from different design codes and guidelines vary.

Whilst service limit state design is helpful to protect non-structural elements and create comfortable feelings of displacement, the SLS governed design consumes much more concrete than the ULS design. The resulting ultimate capacity of design is significantly higher than the design requirement. Great potential saving of concrete can be achieved if the limitations of service limit state design can be extended.

## 7.6 Conclusion

This chapter presents the modelling and parametric analysis of the flexibly formed T beams tested in Chapter 6. The details of the simulation model are presented first with the calculation approaches and assumptions. The validity of the model is examined by comparing the load-displacement relations at the mid-span and structural performance of specimens between simulation results and test results. A further parametric analysis is conducted by varying the geometry and shear reinforcement ratio. An optimal design case with minimised material usage is acquired. The research in this chapter supports the following conclusions:

1. Using the equivalent moment of inertia approach developed by (Bischoff and Gross, 2010a), the load-displacement relations of the specimens are well simulated with the model. The difference of deflection between the simulation and test results varies from 10% to 15%.

2. Using the actual material properties of the specimens, the simulation results correlate well with the structural performance of transversely over-reinforced specimens. Conservative predictions of the shear performance of the transversely under-reinforced specimens are made using the rupture strain of shear links from test data (Model I).

3. Using Model II for the under-reinforced specimens, in order to accurately simulate the load of shear link rupture in the specimens, the design rupture strains of shear links vary from 0.65% to 0.7% for shear links made of two layers of 50K carbon fibre tows and from 0.67% to 0.74% for those made of one layer of carbon fibre tows.

4. The shear reinforcement rupture in the modelling results in an abrupt increase of the strain of longitudinal bars, which explains the reason for the debonding failure of the specimens. The vertical resistance of flexural reinforcement increases with the decreasing support depth at the flexural failure load.

5. An optimum design case, which uses the minimum amount of material to achieve the maximum structural performance, has been obtained based on the parametric analysis. The optimum design case can save up to 69% of concrete used in the web and save 21% concrete for the total concrete usage.

# Chapter 8

# Conclusion and future work

## 8.1 Introduction

In this research, theoretical, experimental and analytical work has been undertaken to investigate fabric formed concrete beams reinforced with W-FRP in three aspects: i) the W-FRP reinforcing system, ii) structural behaviour of W-FRP reinforced concrete beams and iii) the design and optimisation methods. All these three aspects have been answered to achieve the original objectives defined in Chapter 1, which help to remove the obstacles in the way of building sustainable and durable concrete structures using flexible formwork. In the following sections, conclusions from the course of this dissertation are presented in brief to provide the summary of the work that has been undertaken in each chapter. This dissertation has not addressed every feasible aspect of the flexibly formed concrete structures reinforced with W-FRP and acknowledges that there are questions requiring future work.

## 8.2 Conclusions

The defined objectives of this research have been achieved and the work undertaken in this thesis supports the following main conclusions:

- A W-FRP reinforcing system has been investigated to address the difficulty of using steel reinforcement in fabric formed concrete structures, the production of which addresses constructibility through the use of an automated winding machine. The resulting W-FRP reinforcement cages are light-weight, easily transported, easy to position in formwork and more importantly, adaptive to any beam geometry created by fabric formwork.

- The experimental research undertaken has demonstrated that i) the structural behaviour of the beam specimens reinforced with W-FRP is influenced by designs of geometry, W-FRP shear reinforcement, and anchorage; ii) the W-FRP patterns can be optimised to achieve higher shear performance without increasing material usage and iii) the inclined flexural reinforcement has shown significant influence on the shear carrying mechanism.

- The proposed revisions to the MCFT model are shown to be better able to accurately predict the shear performance of the tested specimens than codified design method. Based on MCFT, a simulation model has been established to demonstrate the accurate behaviour of the 'T beams' in the full loading process and to explore the optimum design case by parametric analysis. Design guidance and instructions are provided for designers to design and predict W-FRP reinforced beams with any geometry under any loading condition.

- Compared with equivalent beams with the same flexural capacity, fabric formed T beam specimens have shown a significant advantage in minimising concrete use (up to 23%), without compromising the structural behaviour and creating additional costs of time and labour. Hence the objective of reducing carbon emissions and embodied energy in concrete structures can be achieved. Further optimisation of the T beam flange can result in even higher concrete saving ratio. Capitalising on flexible fabric formwork and W-FRP shear reinforcement, constructing more sustainable concrete structures has been demonstrated to be feasible, economical and practical.

### 8.2.1 W-FRP shear reinforcement and W-FRP reinforced concrete

The experimental research in Chapter 4, Chapter 5 and Chapter 6 has shown the structural behaviour of the W-FRP reinforced beams with prismatic and variable depth geometries. A summary of the key conclusions made throughout each of these Chapters is given as follows:

1. In the prismatic beam specimens (P series), W-FRP shear links have carried up to 90% of shear force. In the non-prismatic specimens (TP series and T series), higher shear reinforcement ratio has increased the shear capacity by improving the shear contribution of shear reinforcement and flexural reinforcement as the bar force is related to the applied load.

2. In the testing of the P, TP, and T series of beam specimens, the W-FRP shear reinforcement rupture has been found at the corner and straight portion of the stirrups. This may be caused by both the weaker corner strength and the deformation in the non-axial direction, respectively. Both types of rupture have shown that the average rupture strength of W-FRP does not reach the corner strength obtained by testing a single W-FRP shear link in isolation.

3. The diagonal W-FRP links have exhibited higher rupture strains than the adjacent vertical links. On average, the diagonal shear links have shown higher contributions to shear than the vertical links, indicating potential in optimising W-FRP patterns to achieve higher shear capacity or less material use.

4. By optimising the pattern of W-FRP reinforcement, higher corner strength, denser cracking patterns, smaller strain difference between adjacent links and less influence from the non-axial direction of links have been achieved. Without increasing W-FRP use, the shear capacity of TP3-2 has been enhanced by 50% compared to TP2-1 and specimen T3-2 has shown 17% improvement in the load of shear link rupture than T2-1R.

5. Three types of failure mode have been observed in the P, TP and T series of testing: shear failure, flexural failure and end slip failure. The end slip failures have been shown as the results of the high tensile force in the inclined longitudinal bars, which is initiated by the non-prismatic geometry and the gradual rupture of W-FRP shear links.

6. The inclined longitudinal bars of the T beam specimens have shown significant contributions in carrying shear. Influenced by geometry and shear reinforcement,

the flexural reinforcement has shown the ability to carry over 50% of applied shear force before shear link rupture and over 90% after gradual rupture of shear links, due to the load transmission.

7. The influence of geometry on the stiffness and shear carrying mechanisms is seen, as the tapered geometry results in lower stiffness and higher shear contribution from flexural reinforcement. Most importantly, the variable-depth geometry could allow the two-step failure with better deformability to occur and avoid the brittle shear failure, which is the most significant difference between beams with optimised geometry and the prismatic beams.

8. Anchorage strength has been shown as one of the governing factors to the structural performance of simply supported non-prismatic beams due to the high tensile force in flexural reinforcement. The splayed anchorage has shown the effectiveness to enhance the shear capacity and deformability of under-reinforced fabric formed T beams after the shear link rupture.

### 8.2.2 Design and optimisation

The proposed design methodology in Chapter 3 has been assessed by examining the predictions of the experimental research. Based on the experimental research, an MCFT model has been built to simulate the test results and conduct a parametric analysis. A summary of the key conclusions from the theoretical work in this dissertation is given as follows:

1. ACI-440.1R (2015) and CSA-S806 (2012) have shown great validity in predicting the flexural capacity of the T beam specimens, with less than 6% difference from the flexural capacity of the T beam specimens.

2. Using specified failure strains of FRP shear reinforcement gives the codified shear design using ACI-440.1R (2015) and CSA-S806 (2012) extremely conservative shear predictions that cannot differentiate between W-FRP patterns. For standard structural design, conservative shear predictions might be favourable, as FRP is a brittle material. For structural optimisation to minimise the material usage, the proposed MCFT model has shown an advantage to accurately predict the shear performance.

3. The codified design has also underestimated the tensile force in flexural reinforcement by using an empirical angle of concrete strut without considering the influence

of displacement, resulting in the underestimation of the shear contribution. In addition, the codified design has not shown the ability to consider the two-step failure of the specimens and the end slip failure of flexural reinforcement.

4. A new MCFT based model has been built to accurately simulate the structural behavior of the T beam specimens in full loading process by considering rupture strain and pattern of W-FRP links, shear stress distribution caused by variable-depth geometry, the contribution from flexural reinforcement and the influence of displacement on angle of flexural reinforcement.

5. The revised MCFT model can simulate the two-step failure of under-reinforced T beam specimens: shear link rupture and end slip of flexural bars. Although it is possible to rely on only flexural reinforcement to carry all the shear after shear link rupture, it is not recommended as installing additional anchorage will complicate the fabrication of fabric formed beams and the enhanced ultimate capacity will not exceed the flexural capacity.

6. Combining the simulation model and the proposed design procedures, designers can design the concrete beams reinforced with W-FRP, which use the minimum concrete volume and W-FRP shear reinforcement, and predict the structural performance of a given W-FRP reinforced beam.

### 8.2.3 Concrete saving

1. Compared with the P series specimens, the variable depth beams (TP series) have achieved 19% concrete saving without compromising the shear performance.

2. The optimised geometries of T beam specimens have shown 17% to 23% concrete saving compared to the equivalent prismatic T beam. Excluding the flange, the concrete saving of the web in Geometry I, II and III has reached 58%, 41% and 64%.

3. As Geometry III has resulted in flexural failure occurring near the support, the optimum design case has been explored based on the simulation model, which controls flexural failure at the mid-span, showing 61% concrete saving in web and 21% concrete saving in total.

## 8.3 Future work

This research has investigated the structural performance of W-FRP reinforced concrete beams of different geometries, formed by traditional and fabric formworks. A design tool has been developed to design an optimised W-FRP reinforced beam in concrete and reinforcement use and to accurately predict the structural behaviour of these beams. However, there are still many aspects that require improvement and further investigation.

### 8.3.1 W-FRP shear reinforcement

In this research, there are two ways of arranging W-FRP reinforcement in the variable-depth beams (TP series and T series): maintaining the angle of diagonal links and spacing between vertical links. With the flexibility of W-FRP, unlimited ways of arranging the flexible fibres can be explored in concrete elements with any geometry. Further investigations should be undertaken to explore the possibilities.

In addition, as only carbon fibres have been adopted to produce W-FRP shear reinforcement, further investigations into W-FRP reinforcement composed of glass fibres, aramid fibres and basalt fibres are required to explore their behaviour to achieve further beneficial effects, such as lower cost.

The automated winding machine introduced in Chapter 6 is a laboratory prototype. Further investigations can be undertaken to improve the winding machine to the industrial production level. The ability of large-scale production is also a critical factor in pushing prefabricated optimised structures in construction.

### 8.3.2 W-FRP reinforced concrete

In this research, except for the W-FRP prismatic beams, for each design of shear reinforcement, only one specimen was tested due to limited time and funding. As variations could occur in experimental research, further repetitions are required to establish the consistency of the test results.

The fabric formed T beams have exhibited a unique end slip failure mode but this failure mode has not occurred in all under-reinforced specimens. There has been no quantification of shear design to demonstrate how to control the shear links to rupture

gradually, hence resulting in the end slip failure. Further investigations should be undertaken into the boundary between shear failure and the end slip failure.

Although in the testing of W-FRP reinforced beams, it has been concluded the W-FRP can provide additional confinement in compression zone concrete, there has been insufficient data support to quantify this confining effect. Further experimental research in W-FRP confined beam elements could potentially address this question. This aspect could also be applied in W-FRP confined columns, pillars and joints.

The experimental research has shown that the rupture strain of W-FRP in concrete beams is lower than individual corner strength. Statistical rupture strains have been acquired for the simulation model and have resulted in conservative simulation results. Further research, such as Hofbeck push-off testing (Hofbeck et al., 1969), is required to establish the relationship between the strength of single W-FRP shear link and behaviour of multiple W-FRP links in concrete structures.

Service limit state design controlled the geometry of the T beam specimens. The effective depth of the beams has been increased massively to meet the displacement limit requirement from the codes and guidelines. Much more concrete saving could have been achieved if only ultimate limit state design is considered. Further investigations should focus on the significance of service limit design and if the service limit state design is critical, more approaches, such as pre-stressing concrete, should be examined to save more concrete.

The flange of the T beam specimens has been shown as the primary contributor to concrete use. With the web being optimised by over 60%, the total concrete saving only reaches over 20%. Further efforts should focus on optimising the flange of the fabric formed T beams. There could be a great potential to save concrete from the flange, where the concrete in tension zone does not carry much of the applied load.

### 8.3.3 Design and optimisation

The model built in Chapter 7 has shown a good simulation of the structural performance of the fabric formed T beam specimens. However, as there are many assumptions and simplifications, many aspects can be improved.

Using the effective moment of inertia approach (Bischoff and Gross, 2010a), the stiffness reduction caused by concrete crushing and end slip of flexural reinforcement cannot be simulated. Using the classical equations of the MCFT model, the concrete contribution

to shear before shear cracks developed cannot be simulated. The assumption of concrete strut is not necessarily correct but with this assumption the simulation results were satisfying. Further work should be undertaken to investigate more about the concrete strut and the calculation of bar force of flexural reinforcement. The model can only simulate the gradual rupture of W-FRP shear links, resulting in the difficulty of differentiation of shear failure and end-slip failure. Further improvement should be undertaken to simulated the structural behaviour of simply supported and fabric formed T beams reinforced with W-FRP.

In addition, the design methodology and simulations in this thesis focus on the simply supported beams under uniformly distributed loads. However, in practical construction, there could be more complex cases, such as continuous beams under multiple loading cases. Although the design method presented in this thesis cannot be directly used in such complex cases, it can be further developed.

Considering multiple loading cases, the flexural design and geometry optimisation could also be conducted following the method shown in Chapter 3 but as the joint of beams and columns is different from the conventional ones, further investigations need to be undertaken.

The displacement calculation of continuous beams could be much more complicated than the simply supported beams, further work needs to be undertaken to accurately calculate the displacement of FRP reinforced continuous beams with variable depth geometry. With this aim being achieved, the bar force of flexural reinforcement can be predicted using the proposed equations and the shear contribution of flexural reinforcement can be given.

## 8.4 Summary

This Chapter presents the main conclusions drawn throughout the research of this dissertation. The performance of W-FRP reinforcement, structural behaviour of W-FRP reinforced concrete beams with prismatic and variable-depth geometries, the advantage of fabric formed beams reinforced with W-FRP and design methodology have been shown.

This research has shown that W-FRP presents a novel alternative to steel reinforcement for fabric formed concrete beams that enable structurally optimised designs. Through a series of design, testing and analysis, the structural performance of W-FRP reinforced

beams have been understood and the design methodology has been developed, which can facilitate construction of sustainable concrete structures with minimum material use.

# References


BS-1881-125:2013 (2013). *Testing concrete. Methods for mixing and sampling fresh concrete in the laboratory.* British Standard Institution.

ACI-318 (2008). 'Building code requirements for structural concrete (ACI 318-08) and commentary'. In: American Concrete Institute.

ACI-440.1R (2015). 'ACI 440.1R-15: Guide for the design and construction of concrete reinforced with FRP bars'. In: American Concrete Institute.

Afifi, M. Z., H. M. Mohamed, and B. Benmokrane (2015). 'Theoretical stress–strain model for circular concrete columns confined by GFRP spirals and hoops'. In: *Engineering Structures* 102, pp. 202–213.

Agarwal, B. D., L. J. Broutman, and K. Chandrashekhara (2017). *Analysis and performance of fiber composites.* John Wiley & Sons.

Ahmed, E. A., B. Benmokrane, and P. Eng (2009a). 'Characterization and Strength Evaluation of the Headed GFRP Bars'. In: *University of Sherbrooke, Technical report submitted to Pultrall Inc*, pp. 1–21.

Ahmed, E. A., A. K. El-Sayed, E. El-Salakawy, and B. Benmokrane (2009b). 'Bend strength of FRP stirrups: Comparison and evaluation of testing methods'. In: *Journal of composites for construction* 14.1, pp. 3–10.

Bailiss, J. (2006). 'Fabric-formed concrete beams: Design and analysis'. In: *MEng Thesis, Department of Architecture and Civil Engineering, Bath, University of Bath.*

Bakis, C. E., L. C. Bank, V. Brown, E. Cosenza, J. Davalos, J. Lesko, A. Machida, S. Rizkalla, and T. Triantafillou (2002). 'Fiber-reinforced polymer composites for construction State of the art review'. In: *Journal of composites for construction* 6.2, pp. 73–87.

Balduzzi, G., M. Aminbaghai, E. Sacco, J. Fssl, J. Eberhardsteiner, and F. Auricchio (2016). 'Non-prismatic beams: a simple and effective Timoshenko-like model'. In: *International Journal of Solids and Structures* 90, pp. 236–250.

Barcelo, L., J. Kline, G. Walenta, and E. Gartner (2014). 'Cement and carbon emissions'. In: *Materials and structures* 47.6, pp. 1055–1065.

Bentz, E. C. (2000). *Sectional analysis of reinforced concrete members*. University of Toronto Toronto.

Bentz, E. C., F. J. Vecchio, and M. P. Collins (2006). 'Simplified modified compression field theory for calculating shear strength of reinforced concrete elements'. In: *ACI Structural Journal* 103.4, p. 614.

Bischoff, P. H. and S. P. Gross (2010a). 'Design approach for calculating deflection of FRP-reinforced concrete'. In: *Journal of Composites for Construction* 15.4, pp. 490–499.

– (2010b). 'Equivalent moment of inertia based on integration of curvature'. In: *Journal of Composites for Construction* 15.3, pp. 263–273.

Boden, T., G. Marland, and R. Andres (2013). *Global, Regional, and National Fossil-Fuel CO2 Emissions. Carbon Dioxide Information Analysis Center (CDIAC), Oak Ridge National Laboratory, US Department of Energy, Oak Ridge, Tenn., USA*.

Calladine, C. R. (2013). *Engineering Plasticity: The Commonwealth and International Library: Structures and Solid Body Mechanics Division*. Elsevier.

Chen, C., G. Habert, Y. Bouzidi, and A. Jullien (2010). 'Environmental impact of cement production: detail of the different processes and cement plant variability evaluation'. In: *Journal of Cleaner Production* 18.5, pp. 478–485.

Cosenza, E., G. Manfredi, and R. Realfonzo (2002). 'Development length of FRP straight rebars'. In: *Composites Part B: Engineering* 33.7, pp. 493–504.

CSA-A23.3-4 (2004). 'Design of concrete structure'. In: Canadian Standard Association.

CSA-S6 (2006). *Canadian highway bridge design code*. Canadian Standards Association.

CSA-S806 (2012). *Design and construction of building structures with fibre-reinforced polymers*. Canadian Standards Association.

Darby, A., T. Ibell, S. Tallis, and C. Winkle (2007). 'End anchorage for internal FRP reinforcement'. In: *FRPRCS-8, July*, pp. 16–18.

Eligehausen, R., E. P. Popov, and V. V. Bertero (1982). 'Local bond stress-slip relationships of deformed bars under generalized excitations'. In:

BS-EN-12390-1 (2012). 'Testing hardened concrete Shape, dimensions and other requirements for specimens and moulds'. In: *British Standards Institute, London*.

BS-EN-1992-1-1 (2004). 'Eurocode 2 : design of concrete structures Part 1-1: General rules and rules for buildings'. In: British Standards Institution.

BS-EN-ISO-527-4 (1997). *Plastics: Determination of Tensile Properties. Test Conditions for Isotropic and Orthotropic Fibre-reinforced Plastic Composites*. British Standards Institution.

BS-EN-ISO-527-5 (1997). *Plastics. Determination of tensile properties. Test conditions for unidirectional fibre-reinforced plastic composites.* British Standards Institution.

FIB (2010). 'Model Code for concrete structures'. In: *Ostfildern, Germany: Document Competence Center Siegmar Kstl EK.*

FIB-bulletin-40 (2007). *FRP reinforcement in RC structures. Technical report.*

Flower, D. J. and J. G. Sanjayan (2007). 'Green house gas emissions due to concrete manufacture'. In: *The international Journal of life cycle assessment* 12.5, p. 282.

Focacci, F., A. Nanni, and C. E. Bakis (2000). 'Local bond-slip relationship for FRP reinforcement in concrete'. In: *Journal of composites for construction* 4.1, pp. 24–31.

Garbett, J., A. Darby, and T. J. Ibell (2010). 'Optimised beam design using innovative fabric-formed concrete'. In: *Advances in Structural Engineering* 13.5, pp. 849–860.

Garbett, J. (2008). 'Bone growth analogy for optimising flexibly fomed concrete beams'. In: *MEng Thesis, Dept for Architecture and Civil Engineering, Bath, University of Bath.*

Grant, W. (2013). 'Shear capacity of concrete beams reinforced with continuous rectangular CFRP spirals'. In: *MEng Thesis, Dept for Architecture and Civil Engineering, Bath, University of Bath.*

Hashemian, F. K. (2012). *Structural behaviour and optimization of moment-shaped reinforced concrete beams.* University of Manitoba (Canada).

Hawkins, W. J., M. Herrmann, T. J. Ibell, B. Kromoser, A. Michaelski, J. J. Orr, R. Pedreschi, A. Pronk, H. R. Schipper, P. Shepherd, et al. (2016). 'Flexible formwork technologies–a state of the art review'. In: *Structural Concrete* 17.6, pp. 911–935.

Hofbeck, J., I. Ibrahim, and A. H. Mattock (1969). 'Shear transfer in reinforced concrete'. In: *Journal Proceedings.* Vol. 66. 2, pp. 119–128.

Hognestad, E., N. W. Hanson, and D. McHenry (1955). 'Concrete stress distribution in ultimate strength design'. In: *Journal Proceedings.* Vol. 52. 12, pp. 455–480.

Hoult, N., E. Sherwood, E. C. Bentz, and M. P. Collins (2008). 'Does the use of FRP reinforcement change the one-way shear behavior of reinforced concrete slabs?' In: *Journal of Composites for Construction* 12.2, pp. 125–133.

Huijben, F. (2016). 'Vacuumatic formwork: a novel granular manufacturing technique for producing topology-optimised structures in concrete'. In: *Granular Matter* 18.2, p. 23.

Huntzinger, D. N. and T. D. Eatmon (2009). 'A life-cycle assessment of Portland cement manufacturing: comparing the traditional process with alternative technologies'. In: *Journal of Cleaner Production* 17.7, pp. 668–675.

Ibell, T., A. Darby, and S. Denton (2009). 'Research issues related to the appropriate use of FRP in concrete structures'. In: *Construction and Building Materials* 23.4, pp. 1521–1528.

Ibell, T., J. Orr, K. Kostova, A. Darby, and M. Evernden (2013). 'Extraordinary possibilities for future concrete structures'. In: *The IES Journal Part A: Civil & Structural Engineering* 6.4, pp. 239–248.

Janssen, B. (2011). 'Double curved precast load bearing concrete elements'. In:

Jourawski, D. (1856). 'Remarques sur la rsistance d'un corps prismatiques et d'une pice compose en bois ou en tle de fer une force perpendiculaire leur longeur'. In: *Annales des Ponts et Chausses* 12.2. cited By 30, pp. 328–351.

Kani, G. (1964). 'The riddle of shear failure and its solution'. In: *Journal Proceedings*. Vol. 61. 4, pp. 441–468.

Karbhari, V. M. and Y. Gao (1997). 'Composite jacketed concrete under uniaxial compressionVerification of simple design equations'. In: *Journal of materials in civil engineering* 9.4, pp. 185–193.

Kostova, K. Z. (2016). 'Design and constructability of fabric-formed concrete elements reinforced with FRP materials'. PhD thesis. University of Bath.

Kostova, K., T. Ibell, A. Darby, and M. Evernden (2017). 'Innovative structural forms of concrete structures using fabric formwork'. In: *IABSE Symposium Report*. Vol. 108. 1. International Association for Bridge and Structural Engineering, pp. 72–73.

Kotsovos, M. D. and M. Pavlovic (1999). *Ultimate limit-state design of concrete structures: a new approach*. Thomas Telford.

Lam, L. and J. Teng (2003a). 'Design-oriented stress-strain model for FRP-confined concrete'. In: *Construction and building materials* 17.6-7, pp. 471–489.

– (2003b). 'Design-oriented stress-strain model for FRP-confined concrete in rectangular columns'. In: *Journal of Reinforced Plastics and Composites* 22.13, pp. 1149–1186.

Lee, C., M. Ko, and Y. Lee (2013). 'Bend strength of complete closed-type carbon fiber-reinforced polymer stirrups with rectangular section'. In: *Journal of Composites for Construction* 18.1, p. 04013022.

Lee, S. H. (2011). 'Study of construction methodology and structural behaviour of fabric-formed form-efficient reinforced concrete beam'. In:

Lilienthal, L. (1899). *Louis wilhelm gustav lilienthal*. US Patent 619,769. URL: `https://www.google.co.uk/patents/US619769`.

Lillistone, D. and C. Jolly (1997). 'Concrete-filled fibre reinforced plastic circular columns'. In: *Composite ConstructionConventional and Innovative, Innsbruck, IABSE*.

– (2000). 'An innovative form of reinforcement for concrete columns using advanced composites'. In: *Structural Engineer* 78.23/24.

Lubliner, J., J. Oliver, S. Oller, and E. Onate (1989). 'A plastic-damage model for concrete'. In: *International Journal of solids and structures* 25.3, pp. 299–326.

Malvar, L. J. (1994). *Bond stress-slip characteristics of FRP rebars*. Tech. rep. Naval Facilities Engineering Service Center Port Hueneme CA.

Mander, J. B., M. J. Priestley, and R. Park (1988). 'Theoretical stress-strain model for confined concrete'. In: *Journal of structural engineering* 114.8, pp. 1804–1826.

Mehta, K. P. (2001). 'Reducing the environmental impact of concrete'. In: *Concrete international* 23.10, pp. 61–66.

Mehta, P. K. (2002). 'Greening of the concrete industry for sustainable development'. In: *Concrete international* 24.7, pp. 23–28.

Mohamed, H. M., M. Z. Afifi, and B. Benmokrane (2014). 'Performance evaluation of concrete columns reinforced longitudinally with FRP bars and confined with FRP hoops and spirals under axial load'. In: *Journal of Bridge Engineering* 19.7, p. 04014020.

Morsch, E. (1908). 'Der Eisenbeton'. In: *Verlag von Konrad Wittwer, Stuttgart*, pp. 44–46.

Naik, T. R. (2008). 'Sustainability of concrete construction'. In: *Practice Periodical on Structural Design and Construction* 13.2, pp. 98–103.

Nervi, P. L. (1956). *Structures*. FW Dodge Corp.

Oden, J. T. and E. A. Ripperger (1981). *Mechanics of elastic structures*. Hemisphere Pub. Corp.

Orr, J., A. Darby, T. Ibell, and M. Evernden (2011a). 'Fibre reinforced polymer grids as shear reinforcement in fabric formed concrete beams'. In:

Orr, J., T. Ibell, A. Darby, and M. Evernden (2014). 'Shear behaviour of non-prismatic steel reinforced concrete beams'. In: *Engineering Structures* 71, pp. 48–59.

Orr, J. (2012). 'Flexible formwork for concrete structures'. PhD thesis. University of Bath.

Orr, J. J., A. P. Darby, T. J. Ibell, M. Evernden, and M. Otlet (2011b). 'Concrete structures using fabric formwork'. In:

Orr, J., A. Darby, T. Ibell, and M. Evernden (2011c). 'Innovative reinforcement for fabric formed concrete structures'. In: *10th International Symposium on Fiber Reinforced Polymer Reinforcement for Concrete Structures (FRPRCS-10)*. University of Bath.

– (2012). 'Optimisation and durability in fabric cast'Double T'beams'. In: *Second International Conference on Flexible Formwork (icff2012)*. University of Bath.

Ottosen, N. S. (1979). 'Constitutive model for short-time loading of concrete'. In: *Journal of the Engineering Mechanics Division ASCE* 105, pp. 127–141.

Ozbakkaloglu, T., J. C. Lim, and T. Vincent (2013). 'FRP-confined concrete in circular sections: Review and assessment of stress–strain models'. In: *Engineering Structures* 49, pp. 1068–1088.

Paglietti, A. and G. Carta (2009). 'Remarks on the current theory of shear strength of variable depth beams'. In: *Open Civil Engineering Journal* 3, pp. 28–33.

Peters, B. (2014). 'Additive Formwork: 3D Printed Flexible Formwork'. In:

Razaqpur, A. G. and S. Spadea (2014). 'Shear strength of FRP reinforced concrete members with stirrups'. In: *Journal of Composites for Construction* 19.1, p. 04014025.

Richart, F. E., A. Brandtzaeg, and R. L. Brown (1928). *A study of the failure of concrete under combined compressive stresses*. Tech. rep. University of Illinois at Urbana Champaign, College of Engineering. Engineering Experiment Station.

Ritter, W. (1899). 'Die bauweise hennebique (hennebiques construction method)'. In:

Rousakis, T. C., A. I. Karabinis, and P. D. Kiousis (2007). 'FRP-confined concrete members: Axial compression experiments and plasticity modelling'. In: *Engineering Structures* 29.7, pp. 1343–1353.

El-Sayed, A. K., E. El-Salakawy, and B. Benmokrane (2007). 'Mechanical and structural characterization of new carbon FRP stirrups for concrete members'. In: *Journal of Composites for Construction* 11.4, pp. 352–362.

El-Sayed, A. K. and K. Soudki (2010). 'Evaluation of shear design equations of concrete beams with FRP reinforcement'. In: *Journal of composites for construction* 15.1, pp. 9–20.

Scrivener, K. L. and E. M. Gartner (1987). 'Microstructural gradients in cement paste around aggregate particles'. In: *MRS Online Proceedings Library Archive* 114.

Seible, F., R. Burgueno, M. Abdallah, and R. Nuismer (1995). 'Advanced composite carbon shell systems for bridge columns under seismic loads'. In: *Proceedings of the National Seismic Conference on Bridges and Highways*. San Diego, California, p. 16.

Shooshtari, A. and R. Khajavi (2010). 'An efficient procedure to find shape functions and stiffness matrices of nonprismatic Euler–Bernoulli and Timoshenko beam elements'. In: *European Journal of Mechanics-A/Solids* 29.5, pp. 826–836.

Spadea, S., J. Orr, and K. Ivanova (2017a). 'Bend-strength of novel filament wound shear reinforcement'. In: *Composite Structures* 176, pp. 244–253.

Spadea, S., J. Orr, A. Nanni, and Y. Yang (2017b). 'Wound FRP shear reinforcement for concrete structures'. In: *Journal of Composites for Construction* 21.5, p. 04017026.

Spoelstra, M. R. and G. Monti (1999). 'FRP-confined concrete model'. In: *Journal of composites for construction* 3.3, pp. 143–150.

Tallis, S. (2005). 'Wedging effects in the anchorage of FRP reinforcing bars'. In: *MEng Thesis, Dept for Architecture and Civil Engineering, Bath, University of Bath.*

Tayfur, Y. R. (2016). 'Optimisation for serviceability of fabric-formed concrete structures'. PhD thesis. University of Bath.

Teychenne, D. C., R. E. Franklin, H. C. Erntroy, and B. Marsh (1975). *Design of normal concrete mixes*. HM Stationery Office.

Thirion, C. (2013). 'Putting the Material in the Right Place: Investigations Into the Sustainable Use of Structural Materials to Reduce the Embodied Environmental Impact of Building Structures'. PhD thesis. University College London.

Timoshenko, S. (1956). *Strength of Materials.-2: Advanced Theory and Problems*. Van Nostrand.

USGS (2018). *Mineral commodity summaries 2018*. Tech. rep. US Geological Survey.

Vecchio, F. J. and M. P. Collins (1986). 'The modified compression-field theory for reinforced concrete elements subjected to shear.' In: *ACI J.* 83.2, pp. 219–231.

– (1988). 'Predicting the response of reinforced concrete beams subjected to shear using modified compression field theory'. In: *ACI Structural Journal* 85.3, pp. 258–268.

Veenendaal, D. (2008). 'Evolutionary optimisation of fabric formed structural elements'. In: *Master's Thesis* 1223, p. 1224.

Veenendaal, D., J. Coenders, J. Vambersky, and M. West (2011a). 'Design and optimization of fabric-formed beams and trusses: evolutionary algorithms and form-finding'. In: *Structural concrete* 12.4, pp. 241–254.

Veenendaal, D., M. West, and P. Block (2011b). 'History and overview of fabric formwork: using fabrics for concrete casting'. In: *Structural Concrete* 12.3, pp. 164–177.

Venant, B. d. S. (1856). 'Memoire sur la torsion des prisms'. In: *Mem. div. sav. Acad. Sci* 14, pp. 233–560.

Waller, J. (1934). *Method of building with cementitious material applied to vegetable fabrics*. US Patent 1,955,716. URL: `https://www.google.co.uk/patents/US1955716`.

– (1955). *Method of forming reinforced concrete arched structures*. US Patent 2,705,826. URL: `https://www.google.co.uk/patents/US2705826`.

West, M. (2016). *The fabric formwork book: Methods for building new architectural and structural forms in concrete*. Routledge.

Whitehead, P. A. (2002). 'Shear strength of concrete containing fibre-reinforced-plastic reinforcement'. PhD thesis. University of Bath.

Winkle, C. (2005). 'The use of helical reinforcement to anchor FRP reinforcing bars'. In: *MEng Thesis, Dept for Architecture and Civil Engineering, Bath, University of Bath*.

Yang, Y., J. Orr, T. Ibell, and A. Darby (2015). 'Shear strength theories for beams of variable depth'. In: *Proceedings of IASS Annual Symposia*. Vol. 2015. 1. International Association for Shell and Spatial Structures (IASS), pp. 1–11.

Yin, P., L. Huang, L. Yan, and D. Zhu (2016). 'Compressive behavior of concrete confined by CFRP and transverse spiral reinforcement. Part A: experimental study'. In: *Materials and Structures* 49.3, pp. 1001–1011.

# Appendix A

# Prediction model for experimental research

The 'Matlab' codes used to predict the shear capacities of the specimens in experimental research are presented in this appendix. For each method, the code for only one specimen is shown. For other specimens, the codes can be acquired by changing the user defined parameters.

## Prismatic beams in Chapter 4

1. 'Matlab' codes for ACI-440.1R (2015) prediction:

```
%width and depth
b=110;dm=195;
%longitudinal bars
Ef=125000;efu=0.0175;ffu=Ef*efu;Af=142.5;
%concrete strength and factors
fc=35;
Ec=22*(fc/10)^0.33*1000;
b1=0.85-0.05*(fc-28)/7;%concrete factor
if b1<0.65,
    b1=0.65;
end
ecu=0.003;
%bending capacity calculation point
a=488;
du=dm; %effective depth at the loading point
```

```
%calculate the nominal flexural strength (Mn) of critical section
pfb=0.85*b1*fc/ffu*(Ef*ecu)/(Ef*ecu+ffu);
pf=Af/b/du;
if pf>pfb,
    ff=((Ef*ecu)^2/4+0.85*b1*fc/pf*Ef*ecu)^0.5-0.5*Ef*ecu;
    Mn=pf*ff*(1-0.59*pf*ff/fc)*b*du^2;
else
    Mn=Af*ffu*(du-b1/2*(ecu/(ecu+efu))*d);
end

%applied load calculation according to nominal flexural strength
Pu=Mn/a*2;
C=(Af*ff)/(0.85*b1*fc*b);

% material property of shear links
Efv=107000;efvu=0.004;ffvu=Efv*efvu;
Afv=12.84;
%%%cross section area of shear links, this should be changed for different specimens;
s=180;
%%%%%%%%%%%%spacing
%shear reinforcement ratio%%%%%%%%%%%%%%%%%%%%%%%%%%%%
pfv=Afv*2/b/s*(1+sin(pi/4)+cos(pi/4));

%critical section
av=50;
%%%%%% 50mm from middle of the support
dv=dm;
%%%%%%%
pf2=Af/b/dv;
%reinforcement raito of critical cross section

%shear contribution of concrete
nf=Ef/Ec;
k=(2*pf2*nf+(pf2*nf)^2)^0.5-pf2*nf;
c=k*dv;
Vc=0.4*(fc)^0.5*b*c;
%shear contribution of shear reinforcement;
Vf=pfv*ffvu*b*dv;

%shear resistance of concrete and shear reinforcement
Vu=Vc+Vf;

Pvu=Vu*2;
%%%%total applied load
```

2. ‘Matlab’ codes for CSA-S806 (2012) predictions:

```
clear all
%width and depth
b=110;dm=195;
%longitudinal bars
Ef=125000;efu=0.0175;ffu=Ef*efu;Af=142.5;
%concrete strength and factors
fc=35;
Ec=22*(fc/10)^0.33*1000;
a1=0.85-0.0015*fc;
if a1<0.67,
    a1=0.67;
end
b1=0.97-0.0025*fc;%concrete factor
if b1<0.67,
    b1=0.67;
end
ecu=0.0035;
%bending capacity calculation point
a=488;
du=dm; %effective depth at the loading point

%calculate the nominal flexural strength (Mn) of critical section
pf=Af/b/du;
ff=((Ef*ecu)^2/4+a1*b1*fc/pf*Ef*ecu)^0.5-0.5*Ef*ecu;
c=Af*ff/(a1*fc*b1*b);
Mn=Af*ff*(du-b1*c/2);


%applied load calculation according to nominal flexural strength
Pu=Mn/a*2;
C=(Af*ff)/(0.85*b1*fc*b);%depth of compression zone

% material property of shear links
Efv=107000;efvu=0.005;ffvu=Efv*efvu;

Afv=0;%%%%%%%%%cross section area of shear links;
s=180;%%%%%%%%%%%%%spacing
%shear reinforcement ratio%%%%%%%%%%%%%%%%%%%%%%%%%%%%%
pfv=Afv*2/b/s*(1+sin(pi/4)+cos(pi/4));

%critical section
```

```
av=a;
dv=0.9*dm;
pf2=Af/b/dv;%reinforcement raito of critical cross section

%shear contribution of concrete
k3=(dv/av)^0.5;
k4=1+(Ef*pf2)^(1/3);
Vc=0.05*k3*k4*(fc)^(1/3)*b*dv;

if Vc>0.22*(fc)^0.5*b*dv,
    Vc=0.22*(fc)^0.5*b*dv;
else
    if Vc<0.11*(fc)^0.5*b*dv,
        Vc=0.11*(fc)^0.5*b*dv;
    end
end
%%arch effect
ka=2.5/(av/dv);
if ka<1,
    ka=1;
else
    if ka>2.5,
        ka=2.5;
    end
end
Vc=Vc*ka;

%member size
ks=750/(450+dv);
if ks<1,
    Vc=Vc*ks;
end




Mv=1;%calculate the applied shear force when Th is assumed;
Vv=1/a;

el=(Mv/dv+(Vv))/2/(Ef*Af);
theta=30+7000*el;%angle of compressive stress in concrete
ko=cot(theta/180*pi);
Vf=pfv*ffvu*b*dv*ko;
Vu=Vf+Vc;
while abs(Vu-Vv)>10,
    Vv=Vv+1;
```

```
    Mv=Vv*a;%calculate the applied shear force when Th is assumed;
    el=(Mv/dv+(Vv))/2/(Ef*Af);
    theta=30+7000*el;%angle of compressive stress in concrete
    ko=cot(theta/180*pi);
    Vf=pfv*ffvu*b*dv*ko;
    Vu=Vf+Vc;
end

if theta>60,
    theta=60;
else
    if theta<30,
        theta=30;
    end
end
ko=cot(theta/180*pi);
Vf=pfv*ffvu*b*dv*ko;
Vu=Vf+Vc;
Pvu=Vu*2;
```

3. 'Matlab' codes for MCFT Vecchio and Collins (1986) predictions:

```
b=110;Ef=124000;efu=0.0181;ffu=Ef*efu;b1=0.8;ecu=0.0033;Af=142.5;d=195;

Efv=107000;efvu=0.013868;ffvu=Efv*efvu;
t=0.000001;
fyx=efu*Ef;fyy=efvu*Efv;fc=-35;smx=180;smy=175;fcr=0.33*(-fc)^0.5;
ec=-0.0035;Ec=22*(-fc/10)^0.33*1000;ecr=fcr/Ec;agg=10;
psx=Af/b/d;
psy=0.0031;
e1=0.00000001;
c1=2;n=0;c2=1;

syms x ef Mu
[Mu,ef,x]=solve(b1*(-fc)*b*x==Af*Ef*ef,
b1*(-fc)*b*x*(d-x/2)==Mu, x*ef==(d-x)*ecu);
ef=ef(ef>0);
x=x(x>0);
Mu=Mu(Mu>0);
x=eval(x);
Mu=eval(Mu);
ef=eval(ef);

Vm=Mu/488;
```

```
ex=(ef+ecu)/2-ecu;

while abs(c1)>0.1,
if e1>ecr,
    fc1=fcr/(1+(200*e1)^0.5);
else
    fc1=Ec*e1;
end
A=-Efv*psy*(e1-ex);
B=-t;
C=Efv*e1*psy+fc1;
a=((-B-(B^2-4*A*C)^0.5)/2/A);
theta=atan(a);
rxy=2*(e1-ex)*tan(theta);
ey=e1-(e1-ex)*tan(theta)^2;
e2=ex-(e1-ex)*tan(theta)^2;
if -e2+ec>0,
    c2=0;
    break
end
fcx=fc1-t/tan(theta);
fcy=fc1-t*tan(theta);
fc2=fc1-t*(tan(theta)+1/tan(theta));

if 1/(0.8-0.34*e1/ec)<1,
    fc2max=fc*(1/(0.8-0.34*e1/ec));
else
    fc2max=fc;
end

fc2a=fc2max*(2*(e2/ec)-(e2/ec)^2);

c1=fc2-fc2a;
if abs(c1)>0.1,
    e1=e1+0.000001;
end
n=n+1;
end

%judge if the reinforcement yield or what


if ey<efvu,
    fsy=ey*Efv;
else
```

```
    c2=0;
70    break

72 end
if ex<efu,
74    fsx=ex*Ef;
else
76    c2=0;
    break
78
end
80
dfc1=fc1-psy*(fyy-fsy);
82 s=1/(sin(theta)/smx+cos(theta)/smy);
w=e1*s;
84 vcimax=(-fc)^0.5/(0.31+24*w/(agg+16));
if dfc1<=0,
86    vci=0;
    fci=0;
88 else
    F=dfc1/tan(theta)-0.18*vcimax;
90    if F<=0,
        fci=0;
92        vci=dfc1/tan(theta);
    else
94        D=0.82/vcimax;
        E=1/tan(theta)-1.64;
96        fci=(-E-(E^2-4*D*F)^0.5)/2/D;
        vci=(fci+dfc1)/tan(theta);
98    end
end
100
fsycr=fsy+(fc1+fci-vci*tan(theta))/psy;
102 fsxcr=fsx+(fc1+fci+vci/tan(theta))/psx;

104 %check failure mode
kc=1.64-1/tan(theta);
106 if kc<0,
    kc=0;
108 end


110
fm1=vcimax*(0.18+0.3*kc^2)*tan(theta)+psy*(fyy-fsy)-fc1;
112 fm2=(-fc2max+fc2);
fm3=(fyx-fsxcr);
114 fm4=(fyy-fsycr);
```

```
116
118 while ffvu*0.452>fsycr,
120 t=t+0.01;
122
    e1=0.000001;
124
    c1=2;n=0;c2=1;
126
    while abs(c1)>0.1,
128 if e1>ecr,
        fc1=fcr/(1+(200*e1)^0.5);
130 else
        fc1=Ec*e1;
132 end
    A=-Efv*psy*(e1-ex);
134 B=-t;
    C=Efv*e1*psy+fc1;
136 a=((-B-(B^2-4*A*C)^0.5)/2/A);
    theta=atan(a);
138 rxy=2*(e1-ex)*tan(theta);
    ey=e1-(e1-ex)*tan(theta)^2;
140 e2=ex-(e1-ex)*tan(theta)^2;
    if -e2+ec>0,
142     c2=0;
        break
144 end
    fcx=fc1-t/tan(theta);
146 fcy=fc1-t*tan(theta);
    fc2=fc1-t*(tan(theta)+1/tan(theta));
148
    if 1/(0.8-0.34*e1/ec)<1,
150     fc2max=fc*(1/(0.8-0.34*e1/ec));
    else
152     fc2max=fc;
    end
154
    fc2a=fc2max*(2*(e2/ec)-(e2/ec)^2);
156
    c1=fc2-fc2a;
158 if abs(c1)>0.1,
        e1=e1+0.000001;
160 end
```

```
n=n+1;
end

%judge if the reinforcement yield or what




if ey<efvu,
    fsy=ey*Efv;
else
   break;
end
fsx=0;

dfc1=fc1-psy*(fyy-fsy);
s=1/(sin(theta)/smx+cos(theta)/smy);
w=e1*s;
vcimax=(-fc)^0.5/(0.31+24*w/(agg+16));
if dfc1<=0,
    vci=0;
    fci=0;
else
    F=dfc1/tan(theta)-0.18*vcimax;
    if F<=0,
        fci=0;
        vci=dfc1/tan(theta);
    else
        D=0.82/vcimax;
        E=1/tan(theta)-1.64;
        fci=(-E-(E^2-4*D*F)^0.5)/2/D;
        vci=(fci+dfc1)/tan(theta);
    end
end

fsycr=fsy+(fc1+fci-vci*tan(theta))/psy;
fsxcr=fsx+(fc1+fci+vci/tan(theta))/psx;

%check failure mode
kc=1.64-1/tan(theta);
if kc<0,
    kc=0;
end

fm1=vcimax*(0.18+0.3*kc^2)*tan(theta)+psy*(fyy-fsy)-fc1;
fm2=(-fc2max+fc2);
```

```
fm3=(fyx-fsxcr);
fm4=(fyy-fsycr);

end

%calculate the reinforcement
Vu=t*b*d;
Pvu=Vu*2;
```

## Variable depth beams in Chapter 5

1. 'Matlab' codes for ACI-440.1R (2015) prediction:

```
%width and depth
b=110;dm=195;
%longitudinal bars
Ef=144000;efu=0.0181;ffu=Ef*efu;Af=142.5;
%concrete strength and factors
fc=28;
Ec=22*(fc/10)^0.33*1000;
b1=0.85-0.05*(fc-28)/7;%concrete factor
if b1<0.65,
    b1=0.65;
end
ecu=0.003;
%bending capacity calculation point
a=400;
du=195-2.7116*(600-a)^2/10000; %effective depth at the loading point

%calculate the nominal flexural strength (Mn) of critical section
pfb=0.85*b1*fc/ffu*(Ef*ecu)/(Ef*ecu+ffu);
pf=Af/b/du;
if pf>pfb,
    ff=((Ef*ecu)^2/4+0.85*b1*fc/pf*Ef*ecu)^0.5-0.5*Ef*ecu;
    Mn=pf*ff*(1-0.59*pf*ff/fc)*b*du^2;
else
    Mn=Af*ffu*(du-b1/2*(ecu/(ecu+efu))*d);
end

%applied load calculation according to nominal flexural strength
Pu=Mn/a*1.5;

```

```
% material property of shear links
Efv=107000;efvu=0.004;ffvu=Efv*efvu;
%shear reinforcement ratio%%%%%%%%%%%%%%%%%%%%%%%%%%%%%%
pfv=0.00;

%critical section
av=50;
dv=195-2.7116*(600-av)^2/10000;
pf2=Af/b/dv;%reinforcement raito of critical cross section

%shear contribution of concrete
nf=Ef/Ec;
k=(2*pf2*nf+(pf2*nf)^2)^0.5-pf2*nf;
c=k*dv;
Vc=0.4*(fc)^0.5*b*c;
%shear contribution of shear reinforcement;
Vf=pfv*ffvu*b*dv;

%shear resistance of concrete and shear reinforcement
Vv=Vc+Vf;


%shear contribution of longitudinal bars
tana=2*2.7116*(600-av)/10000;
at=atan(tana);

Thf=1;%assume the flexural tensile force at the critical cross section
Vtf=tana*Thf;%calculate the vertical component
Mv=Thf*(dv-Thf/(0.85*fc*b)/2);%calculate the bending moment
Va=Mv/(av);%calculate the applied shear force when Th is assumed;
Ftd=1.3*(Va-0.5*Vf-Vtf);
Vt=tana*(Thf+Ftd*cos(at));%calculate the vertical component


Vu=(Vt+Vv);%calculate the total shear resistance;
C0=abs(Va-Vu);%the difference between applied load and shear resistance
%iteratation to find the answer.
while C0>10,
    Thf=Thf+1;
    Vtf=tana*Thf;%calculate the vertical component
Mv=Thf*(dv-Thf/(0.85*fc*b)/2);%calculate the bending moment
Va=Mv/(av);%calculate the applied shear force when Th is assumed;
Ftd=1.3*(Va-0.5*Vf-Vtf);
Vt=tana*(Thf+Ftd*cos(at));%calculate the vertical component


```

```
Vu=(Vt+Vv);%calculate the total shear resistance;
C0=abs(Va-Vu);%the difference between applied load and shear resistance
%iteratation to find the answer.
end

Pvu=Vu*1.5;
```

2. 'Matlab' codes for CSA-S806 (2012) predictions:

```
clear all
%width and depth
b=110;dm=195;
%longitudinal bars
Ef=144000;efu=0.0181;ffu=Ef*efu;Af=142.5;
%concrete strength and factors
fc=28;
Ec=22*(fc/10)^0.33*1000;
a1=0.85-0.0015*fc;
if a1<0.67,
    a1=0.67;
end
b1=0.97-0.0025*fc;%concrete factor
if b1<0.67,
    b1=0.67;
end
ecu=0.0035;
%bending capacity calculation point
a=400;
du=195-2.7116*(600-a)^2/10000; %effective depth at the loading point

%calculate the nominal flexural strength (Mn) of critical section
pf=Af/b/du;
ff=((Ef*ecu)^2/4+a1*b1*fc/pf*Ef*ecu)^0.5-0.5*Ef*ecu;
c=Af*ff/(a1*fc*b1*b);
Mn=Af*ff*(du-b1*c/2);


%applied load calculation according to nominal flexural strength
Pu=Mn/a*1.5;

% material property of shear links
Efv=107000;efvu=0.005;ffvu=Efv*efvu;
%shear reinforcement ratio%%%%%%%%%%%%%%%%%%%%%%%%%%%%
pfv=0.00;
```

```
36
%critical section
38 av=50;
dv=(195-2.7116*(600-av)^2/10000)*0.9;
40 pf2=Af/b/dv/0.9;%reinforcement raito of critical cross section

42 %shear contribution of concrete
k3=(dv/0.9/a)^0.5;
44 if k3>1,
    k3=1;
46 end

48 k4=1+(Ef*pf2)^(1/3);
Vc=0.05*k3*k4*(fc)^(1/3)*b*dv;
50
if Vc>0.22*(fc)^0.5*b*dv,
52     Vc=0.22*(fc)^0.5*b*dv;
else
54     if Vc<0.11*(fc)^0.5*b*dv,
           Vc=0.11*(fc)^0.5*b*dv;
56     end
end
58 %%arch effect
ka=2.5*(dv/0.9/a);
60 if ka<1,
    ka=1;
62 else
    if ka>2.5,
64         ka=2.5;
    end
66 end
Vc=Vc*ka;
68
%member size
70 ks=750/(450+dv/0.9);
if ks<1,
72     Vc=Vc*ks;
end
74
%shear contribution of longitudinal bars
76 tana=2*2.7116*(600-av)/10000;
at=atan(tana);
78 %shear contribution of shear reinforcement;

80 Thf=1;%assume the flexural tensile force at the critical cross section
Vtf=tana*Thf;%calculate the vertical component
```

```
Mv=Thf*dv;%calculate the bending moment

Va=Mv/(av);%calculate the applied shear force when Th is assumed;

Vfa=1;
Ftd=1.3*(Va-0.5*Vfa-Vtf);% additional tensile force
Vt=tana*(Thf+Ftd*cos(at));%calculate the vertical component
el=(Mv/dv+(Va-Vt))/2/(Ef*Af);
theta=30+7000*el;%angle of compressive stress in concrete
ko=cot(theta/180*pi);
Vf=pfv*ffvu*b*dv*ko;
while abs(Vf-Vfa)>1,
    Vfa=Vfa+1;
    Ftd=1.3*(Va-0.5*Vfa-Vtf);% additional tensile force
    Vt=tana*(Thf+Ftd*cos(at));%calculate the vertical component
    el=(Mv/dv+(Vf-Vt))/2/(Ef*Af);
    theta=30+7000*el;%angle of compressive stress in concrete
    ko=cot(theta/180*pi);
    Vf=pfv*ffvu*b*dv*ko;
end

Vu=(Vt+Vf+Vc);%calculate the total shear resistance;
C0=abs(Va-Vu);%the difference between applied load and shear resistance
%iteratation to find the answer.
while C0>100,
Thf=Thf+100;
Vtf=tana*Thf;%calculate the vertical component
Mv=Thf*(dv-Thf/(a1*fc*b)/2);%calculate the bending moment

Va=Mv/(av);%calculate the applied shear force when Th is assumed;

Vfa=1;
Ftd=1.3*(Va-0.5*Vfa-Vtf);% additional tensile force
Vt=tana*(Thf+Ftd*cos(at));%calculate the vertical component
el=(Mv/dv+(Vf-Vt))/2/(Ef*Af);
theta=30+7000*el;%angle of compressive stress in concrete
ko=cot(theta/180*pi);
Vf=pfv*ffvu*b*dv*ko;
while abs(Vf-Vfa)>1,
    Vfa=Vfa+1;
    Ftd=1.3*(Va-0.5*Vfa-Vtf);% additional tensile force
    Vt=tana*(Thf+Ftd*cos(at));%calculate the vertical component
    el=(Mv/dv+(Vf-Vt))/2/(Ef*Af);
    theta=30+7000*el;%angle of compressive stress in concrete
    ko=cot(theta/180*pi);
    Vf=pfv*ffvu*b*dv*ko;
```

```
end

Vu=(Vt+Vf+Vc);%calculate the total shear resistance;
C0=abs(Va-Vu);%the difference between applied load and shear resistance
end

Pvu=Vu*1.5;
```

3. 'Matlab' codes for MCFT Vecchio and Collins (1986) predictions:

```
b=110;Ef=144000;efu=0.0181;ffu=Ef*efu;b1=0.8;ecu=0.0033;Af=142.5;d=195;
Efv=107000;efvu=0.00668;ffvu=Efv*efvu;cp=50;
t=0.000001;%the shear stress at the calculation point
fyx=efu*Ef;fyy=efvu*Efv;fc=-28;smx=180-2.7116*(600-cp)^2/10000;
smy=150;fcr=0.33*(-fc)^0.5;ec=-0.0035;Ec=22*(abs(fc)/10)^0.33*1000;ecr=fcr/Ec;agg=10;

psy=0.0025; %%%%%%%%%%%%%%%%%%%%SELF DEFINED
e1=0.00000001;
c1=2;
n=0;c2=1;%concrete crush parameters
c3=10;
tana=2*2.7116*(600-cp)/10000;%the angle of inclined flexural reinforcement
at=atan(tana);

du=195-2.7116*(600-400)^2/10000;

syms x ef Mu
[Mu,ef,x]=solve(b1*(-fc)*b*x==Af*Ef*ef,
b1*(-fc)*b*x*(du-x/2)==Mu, x*ef==(du-x)*ecu);
ef=ef(ef>0);
x=x(x>0);
Mu=Mu(Mu>0);
x=eval(x);
Mu=eval(Mu);
ef=eval(ef);


P=Mu/400*3/2;%shear force according to max bending moment
Vm=P*2/3;%assign the shear force as Vm
V=Vm;

while abs(c3)>5,

Mc=V*cp;%The calculation section's moment 150 is the distance away from support
```

```
dc=195-2.7116*(600-cp)^2/10000;
%The effective depth of the calculation section which is 150mm from the support;
%calculate the concrete strain/the tensile force/the compression force
psx=Af/b/dc;
syms xc efc ecc

[ecc,efc,xc]=solve(b1*Ec/2*(-ecc)*b*xc==Af*Ef*efc, b1*Ec/2*(-ecc)*b*xc*
(dc-xc/2*b1)==Mc, xc*efc==(dc-xc)*(-ecc));
efc=efc(efc>0);
xc=xc(xc>0);
ecc=ecc(ecc<0);
xc=eval(xc);
ecc=eval(ecc);
efc=eval(efc);


Cc=b1*Ec/2*(-ecc)*b*xc;%the compression force of the compression area
efc=Cc/Ef/Af;
Vf=1;




Tl=efc*Af*Ef;
Tv=Tl*tana;%vertical component of tensile force of flexural reinforcement
Ftd=1.3*(V-0.5*Vf-Tv);
ex=efc+Ftd/Ef/Af;

while abs(c1)>0.1,
if e1>ecr,
    fc1=fcr/(1+(200*e1)^0.5);
else
    fc1=Ec*e1;
end
A=-Efv*psy*(e1-ex);
B=-t;
C=Efv*e1*psy+fc1;
a=((-B-(B^2-4*A*C)^0.5)/2/A);
theta=atan(a);
rxy=2*(e1-ex)*tan(theta);
ey=e1-(e1-ex)*tan(theta)^2;
e2=ex-(e1-ex)*tan(theta)^2;
if -e2+ec>0,
    c2=0;
    break
end
```

```
fcx=fc1-t/tan(theta);
fcy=fc1-t*tan(theta);
fc2=fc1-t*(tan(theta)+1/tan(theta));

if 1/(0.8-0.34*e1/ec)<1,
    fc2max=fc*(1/(0.8-0.34*e1/ec));
else
    fc2max=fc;
end

fc2a=fc2max*(2*(e2/ec)-(e2/ec)^2);

c1=fc2-fc2a;
if abs(c1)>0.1,
    e1=e1+0.000001;
end
n=n+1;
end

%judge if the reinforcement yield or what


if ey<efvu,
    fsy=ey*Efv;
else
    c2=0;
   break

end
if ex<efu,
    fsx=ex*Ef;
else
    c2=0;
   break

end

dfc1=fc1-psy*(fyy-fsy);
s=1/(sin(theta)/smx+cos(theta)/smy);
w=e1*s;
vcimax=(-fc)^0.5/(0.31+24*w/(agg+16));
if dfc1<=0,
    vci=0;
    fci=0;
else
    F=dfc1/tan(theta)-0.18*vcimax;
```

```
    if F<=0,
        fci=0;
        vci=dfc1/tan(theta);
    else
        D=0.82/vcimax;
        E=1/tan(theta)-1.64;
        fci=(-E-(E^2-4*D*F)^0.5)/2/D;
        vci=(fci+dfc1)/tan(theta);
    end
end

fsycr=fsy+(fc1+fci-vci*tan(theta))/psy;
fsxcr=fsx+(fc1+fci+vci/tan(theta))/psx;

%check failure mode
kc=1.64-1/tan(theta);
if kc<0,
    kc=0;
end


fm1=vcimax*(0.18+0.3*kc^2)*tan(theta)+psy*(fyy-fsy)-fc1;
fm2=(-fc2max+fc2);
fm3=(fyx-fsxcr);
fm4=(fyy-fsycr);



while ffvu>fsycr,

t=t+0.01;


e1=0.000001;

c1=2;n=0;c2=1;

while abs(c1)>0.1,
if e1>ecr,
    fc1=fcr/(1+(200*e1)^0.5);
else
    fc1=Ec*e1;
end
A=-Efv*psy*(e1-ex);
B=-t;
C=Efv*e1*psy+fc1;
```

```
a=((-B-(B^2-4*A*C)^0.5)/2/A);
theta=atan(a);
rxy=2*(e1-ex)*tan(theta);
ey=e1-(e1-ex)*tan(theta)^2;
e2=ex-(e1-ex)*tan(theta)^2;
if -e2+ec>0,
    c2=0;
    break
end
fcx=fc1-t/tan(theta);
fcy=fc1-t*tan(theta);
fc2=fc1-t*(tan(theta)+1/tan(theta));

if 1/(0.8-0.34*e1/ec)<1,
    fc2max=fc*(1/(0.8-0.34*e1/ec));
else
    fc2max=fc;
end

fc2a=fc2max*(2*(e2/ec)-(e2/ec)^2);

c1=fc2-fc2a;
if abs(c1)>0.1,
    e1=e1+0.000001;
end
n=n+1;
end

%judge if the reinforcement yield or what




if ey<efvu,
    fsy=ey*Efv;
else
   break;
end
if ex<efu,
    fsx=ex*Ef;
else
    c2=0;
   break

end
```

```
dfc1=fc1-psy*(fyy-fsy);
s=1/(sin(theta)/smx+cos(theta)/smy);
w=e1*s;
vcimax=(-fc)^0.5/(0.31+24*w/(agg+16));
if dfc1<=0,
    vci=0;
    fci=0;
else
    F=dfc1/tan(theta)-0.18*vcimax;
    if F<=0,
        fci=0;
        vci=dfc1/tan(theta);
    else
        D=0.82/vcimax;
        E=1/tan(theta)-1.64;
        fci=(-E-(E^2-4*D*F)^0.5)/2/D;
        vci=(fci+dfc1)/tan(theta);
    end
end

fsycr=fsy+(fc1+fci-vci*tan(theta))/psy;
fsxcr=fsx+(fc1+fci+vci/tan(theta))/psx;

%check failure mode
kc=1.64-1/tan(theta);
if kc<0,
    kc=0;
end

fm1=vcimax*(0.18+0.3*kc^2)*tan(theta)+psy*(fyy-fsy)-fc1;
fm2=(-fc2max+fc2);
fm3=(fyx-fsxcr);
fm4=(fyy-fsycr);

end

%calculate the shear reinforcement capacity
Vf=t*b*xc/2+(dc-xc)*b*t;
Vv=Tv+1.3*(V-0.5*Vf-Tv)*sin(at);

c3=Vf+Vv-V;

if Vf+Vv<V,
    V=0.9*V;
else
    V=1.1*V;
```

```
end

end
 if c3<0,
    V=V/0.9;
else
    V=V/1.1;
end


P=V*3/2;
```

## Fabric formed T beams in Chapter 6

1. 'Matlab' codes for ACI-440.1R (2015) prediction:

```
%width and depth
b=800;
%longitudinal bars
Ef=144000;efu=0.0181;ffu=Ef*efu;Af=142.5/2*3;
%concrete strength and factors
fc=40;
Ec=22*(fc/10)^0.33*1000;
b1=0.85-0.05*(fc-28)/7;%concrete factor
if b1<0.65,
    b1=0.65;
end
ecu=0.003;
%bending capacity calculation point
a=1000; %calculation point_distance from support%%%%%%%%
%%%%%%%%%%%%%%%%%%%%%%%%%%%defined by the user
ds=100; %the depth of supports%%%%%%%%%%%%
%%%%%%%%%%%%%%%%%%defined by the user
cc=20; %cover depth
du=250-(250-ds)/1500^2*abs(a-1500)^2-cc-10/2;
%effective depth at the loading point
bfe=750; %%(b/2-300/1500^2*abs(a-1500)^2)*2;
%%%%%%%%%effective width of flange
bwe=(50/1500^2*abs(a-1500)^2+50)*2;


%calculate the nominal flexural strength (Mn) of critical section
pfb=0.85*b1*fc/ffu*(Ef*ecu)/(Ef*ecu+ffu);
```

```
pf=Af/bfe/du;
if pf>pfb,
    ff=((Ef*ecu)^2/4+0.85*b1*fc/pf*Ef*ecu)^0.5-0.5*Ef*ecu;
    Mn=pf*ff*(1-0.59*pf*ff/fc)*bfe*du^2;
else
    Mn=Af*ffu*(du-b1/2*(ecu/(ecu+efu))*du);
end

%applied load calculation according to nominal flexural strength

if a<500,
        Pu=2*Mn/a;
    else
        if a<1000,
            Pu=Mn/(0.5*a-1/5*(a-500));
        else
            if a<1500,
                Pu=Mn/(0.5*a-1/5*(a-1000)-1/5*(a-500));
            else
                if a<2000,
                    Pu=Mn/(0.5*a-1/5*(a-1500)-1/5*(a-1000)-1/5*(a-500));
                else
                    if a<2500,
                       Pu=Mn/(0.5*a-1/5*(a-2000)-1/5*(a-1500)-1/5*(a-1000)-1/5*(a-500));
                    else
                        Pu=Mn/(0.5*a-1/5*(a-2500)-1/5*(a-2000)-1/5*(a-1500)-
                        1/5*(a-1000)-1/5*(a-500));
                    end
                end
            end
        end
    end

% material property of shear links
Efv=107000;efvu=0.004;ffvu=Efv*efvu;
%shear reinforcement ratio%%%%%%%%%%%%%%%%%%%%%%%%%%%%
pfv=0.0026;

%critical section
av=50;
dv=250-(250-ds)/1500^2*abs(av-1500)^2-cc-10/2;

pf2=Af/bfe/dv;%reinforcement raito of critical cross section
bw=(50/1500^2*abs(av-1500)^2+50)*2;%%%%%%%%%%%%the width of web
%shear contribution of concrete
nf=Ef/Ec;
```

```
k=(2*pf2*nf+(pf2*nf)^2)^0.5-pf2*nf;
c=k*dv;
Vc=0.4*(fc)^0.5*bw*c;
%shear contribution of shear reinforcement;
Vf=pfv*ffvu*bw*dv;

%shear resistance of concrete and shear reinforcement
Vv=Vc+Vf;


%shear contribution of longitudinal bars
tana=2*(250-ds)/1500^2*abs(1500-av);
at=atan(tana);

Thf=1;%assume the flexural tensile force at the critical cross section
Vtf=tana*Thf;%calculate the vertical component
Mv=Thf*(dv-Thf/(0.85*fc*bfe)/2);%calculate the bending moment
Va=Mv/(av);%calculate the applied shear force when Th is assumed;
Ftd=1.3*(Va-0.5*Vf-Vtf);
Vt=tana*(Thf+Ftd*cos(at));%calculate the vertical component


Vu=(Vt+Vv);%calculate the total shear resistance;
C0=abs(Va-Vu);%the difference between applied load and shear resistance
%iteratation to find the answer.
while C0>10,
    Thf=Thf+1;
    Vtf=tana*Thf;%calculate the vertical component
Mv=Thf*(dv-Thf/(0.85*fc*bfe)/2);%calculate the bending moment
Va=Mv/(av);%calculate the applied shear force when Th is assumed;
Ftd=1.3*(Va-0.5*Vf-Vtf);
Vt=tana*(Thf+Ftd*cos(at));%calculate the vertical component


Vu=(Vt+Vv);%calculate the total shear resistance;
C0=abs(Va-Vu);%the difference between applied load and shear resistance
%iteratation to find the answer.
end

Pvu=Vu*2;
```

2. 'Matlab' codes for CSA-S806 (2012) predictions:

```
%width and depth
```

```
bfm=800;
%longitudinal bars
Ef=144000;efu=0.0181;ffu=Ef*efu;Af=142.5/2*3;
%concrete strength and factors
fc=40;
Ec=22*(fc/10)^0.33*1000;
a1=0.85-0.0015*fc;
if a1<0.67,
    a1=0.67;
end
b1=0.97-0.0025*fc;%concrete factor
if b1<0.67,
    b1=0.67;
end
ecu=0.0035;
%bending capacity calculation point
a=500; %calculation point%%%%%%%%%%%%%%%%%%%%
%%%%%%%%%%%%%defined by the user
ds=100; %the depth of supports%%%%%%%%%%%%%%%%%
%%%%%%%%%%%defined by the user
cc=20; %cover depth
du=250-(250-ds)/1500^2*abs(a-1500)^2-cc-10/2;
%effective depth at the loading point
b=750; %%%(bfm/2-300/1500^2*abs(a-1500)^2)*2;
%%%%%%%%%%%effective flange width

%calculate the nominal flexural strength (Mn) of critical section
pfb=0.85*b1*fc/ffu*(Ef*ecu)/(Ef*ecu+ffu);
pf=Af/b/du;
if pf>pfb,
    ff=((Ef*ecu)^2/4+a1*b1*fc/pf*Ef*ecu)^0.5-0.5*Ef*ecu;
    c=Af*ff/(a1*fc*b1*b);
    Mn=Af*ff*(du-b1*c/2);
else
    Mn=Af*ffu*(du-b1/2*(ecu/(ecu+efu))*du);
end


%applied load calculation according to nominal flexural strength
if a<500,
        Pu=2*Mn/a;
    else
        if a<1000,
            Pu=Mn/(0.5*a-1/5*(a-500));
        else
            if a<1500,
```

```
            Pu=Mn/(0.5*a-1/5*(a-1000)-1/5*(a-500));
        else
            if a<2000,
                Pu=Mn/(0.5*a-1/5*(a-1500)-1/5*(a-1000)-1/5*(a-500));
            else
                if a<2500,
                    Pu=Mn/(0.5*a-1/5*(a-2000)-1/5*(a-1500)-1/5*(a-1000)-1/5*(a-500));
                else
                    Pu=Mn/(0.5*a-1/5*(a-2500)-1/5*(a-2000)-1/5*(a-1500)-1/5*
                    (a-1000)-1/5*(a-500));
                end
            end
        end
    end
end

% material property of shear links
Efv=107000;efvu=0.005;ffvu=Efv*efvu;
%shear reinforcement ratio%%%%%%%%%%%%%%%%%%%%%%%%%%%%
pfv=0.0087;

%critical section
av=50;
dv=(250-(250-ds)/1500^2*abs(av-1500)^2-cc-10/2)*0.9;
b=(bfm/2-300/1500^2*abs(av-1500)^2)*2;
pf2=Af/b/dv;%reinforcement raito of critical cross section
bw=(50/1500^2*abs(av-1500)^2+50)*2;
%shear contribution of concrete
k3=(dv/av)^0.5;
k4=1+(Ef*pfv)^(1/3);
Vc=0.05*k3*k4*(fc)^(1/3)*bw*dv;

if Vc>0.22*(fc)^0.5*bw*dv,
    Vc=0.22*(fc)^0.5*bw*dv;
else
    if Vc<0.11*(fc)^0.5*bw*dv,
        Vc=0.11*(fc)^0.5*bw*dv;
    end
end
%%arch effect
ka=2.5/(dv/av);
if ka<1,
    ka=1;
else
    if ka>2.5,
        ka=2.5;
```

```
    end
end
Vc=Vc*ka;

%member size
ks=750/(450+dv);
if ks<1,
    Vc=Vc*ks;
end

%shear contribution of longitudinal bars
tana=2*(250-ds)/1500^2*abs(1500-av);
at=atan(tana);
%shear contribution of shear reinforcement;

Thf=1;%assume the flexural tensile force at the critical cross section
Vtf=tana*Thf;%calculate the vertical component
Mv=Thf*(dv-Thf/(a1*fc*b)/2);%calculate the bending moment

Va=Mv/(av);%calculate the applied shear force when Th is assumed;

Vfa=1;
Ftd=1.3*(Va-0.5*Vfa-Vtf);% additional tensile force
Vt=tana*(Thf+Ftd*cos(at));%calculate the vertical component
el=(Mv/dv+(Va-Vt))/2/(Ef*Af);
theta=30+7000*el;%angle of compressive stress in concrete
ko=cot(theta/180*pi);
Vf=pfv*ffvu*bw*dv*ko;
while abs(Vf-Vfa)>1,
    Vfa=Vfa+1;
    Ftd=1.3*(Va-0.5*Vfa-Vtf);% additional tensile force
    Vt=tana*(Thf+Ftd*cos(at));%calculate the vertical component
    el=(Mv/dv+(Vf-Vt))/2/(Ef*Af);
    theta=30+7000*el;%angle of compressive stress in concrete
    ko=cot(theta/180*pi);
    Vf=pfv*ffvu*bw*dv*ko;
end

Vu=(Vt+Vf+Vc);%calculate the total shear resistance;
C0=abs(Va-Vu);%the difference between applied load and shear resistance
%iteratation to find the answer.
while C0>100,
Thf=Thf+100;
Vtf=tana*Thf;%calculate the vertical component
Mv=Thf*(dv-Thf/(a1*fc*b)/2);%calculate the bending moment

```

```
Va=Mv/(av);%calculate the applied shear force when Th is assumed;

Vfa=1;
Ftd=1.3*(Va-0.5*Vfa-Vtf);% additional tensile force
Vt=tana*(Thf+Ftd*cos(at));%calculate the vertical component
el=(Mv/dv+(Vf-Vt))/2/(Ef*Af);
theta=30+7000*el;%angle of compressive stress in concrete
ko=cot(theta/180*pi);
Vf=pfv*ffvu*bw*dv*ko;
while abs(Vf-Vfa)>1,
    Vfa=Vfa+1;
    Ftd=1.3*(Va-0.5*Vfa-Vtf);% additional tensile force
    Vt=tana*(Thf+Ftd*cos(at));%calculate the vertical component
    el=(Mv/dv+(Vf-Vt))/2/(Ef*Af);
    theta=30+7000*el;%angle of compressive stress in concrete
    ko=cot(theta/180*pi);
    Vf=pfv*ffvu*bw*dv*ko;
end

Vu=(Vt+Vf+Vc);%calculate the total shear resistance;
C0=abs(Va-Vu);%the difference between applied load and shear resistance
end

Pvu=Vu*2;
```

3. 'Matlab' codes for MCFT Vecchio and Collins (1986) predictions:

```
b=800;Ef=144000;efu=0.0181;ffu=Ef*efu;b1=0.8;ecu=0.0033;Af=142.5/2*3;
Efv=107000;cp=50;%%%%%%%%%%shear calculation point at support
efvu=0.0087;%%%%%%%%%%DEFINE THE CORNER STRENGTH
ffvu=Efv*efvu;
cm=1500;%%%%%%%bending calculation at mid-span
t=0.000001;%the shear stress at the calculation point
ds=120;%%%%%%%%%%%%%%%%%%%%%%%%%%%%support depth
bfe=(b/2-300/1500^2*abs(cm-1500)^2)*2;%%%%%%%%%effective width of flange
fyx=efu*Ef;fyy=efvu*Efv;fc=-40;
smx=250-(250-ds)/1500^2*abs(cp-1500)^2-25;
smy=150;fcr=0.33*(-fc)^0.5;ec=-0.0035;
Ec=22*(abs(fc)/10)^0.33*1000;
ecr=fcr/Ec;agg=10;

psy=0.0034; %%%%%%%%%%%%%%%%%%SELF DEFINED
e1=0.00000001;
c1=2;
```

```
n=0;c2=1;%concrete crush parameters
c3=10000;
tana=2*(250-ds)/1500^2*abs(1500-cp);
at=atan(tana);%the angle of inclined flexural reinforcement


du=250-(250-ds)/1500^2*abs(cm-1500)^2-25;

syms x ef Mu
[Mu,ef,x]=solve(b1*(-fc)*bfe*x/2==Af*Ef*ef, b1*(-fc)*bfe*x/2*(du-b1*x/2)==Mu,
x*ef==(du-x)*ecu);
ef=ef(ef>0);
x=x(x>0);
Mu=Mu(Mu>0);
x=eval(x);
Mu=eval(Mu);
ef=eval(ef);


if cm<500,
        Pu=2*Mu/cm;
    else
        if cm<1000,
            Pu=Mu/(0.5*cm-1/5*(cm-500));
        else
            if cm<1500,
                Pu=Mu/(0.5*cm-1/5*(cm-1000)-1/5*(cm-500));
            else
                if cm<2000,
                    Pu=Mu/(0.5*cm-1/5*(cm-1500)-1/5*(cm-1000)-1/5*(cm-500));
                else
                    if cm<2500,
                       Pu=Mu/(0.5*cm-1/5*(cm-2000)-1/5*(cm-1500)-1/5*
                       (cm-1000)-1/5*(cm-500));
                    else
                        Pu=Mu/(0.5*cm-1/5*(cm-2500)-1/5*(a-2000)-1/5*
                        (cm-1500)-1/5*(cm-1000)-1/5*(cm-500));
                    end
                end
            end
        end
end


%shear force according to max bending moment
Vm=Pu/2;%assign the shear force as Vm
```

```
V=Vm;

while abs(c3)>100,

Mc=V*cp;
%The calculation section's moment 150 is the distance away from support
dc=250-(250-ds)/1500^2*abs(cp-1500)^2-25;
%The effective depth of the calculation section
%which is 150mm from the support;
%calculate the concrete strain/the tensile force/the compression force
bfe=(b/2-300/1500^2*abs(cp-1500)^2)*2;
bw=(50/1500^2*abs(cp-1500)^2+50)*2;
psx=Af/bw/dc;
syms xc efc ecc

[ecc,efc,xc]=solve(b1*Ec*(-ecc)*bfe*xc/2==Af*Ef*efc,
b1*Ec*(-ecc)*bfe*xc/2*(dc-xc/2*b1)==
Mc, xc*efc==(dc-xc)*(-ecc));
efc=efc(efc>0);
xc=xc(xc>0);
ecc=ecc(ecc<0);
xc=eval(xc);
ecc=eval(ecc);
efc=eval(efc);

Cc=b1*Ec*(-ecc)*bfe*xc/2;%the compression force of the compression area
efc=Cc/Ef/Af;
Vf=1;




Tl=efc*Af*Ef;
Tv=Tl*tana;%vertical component of tensile force of flexural reinforcement
Ftd=1.3*(V-0.5*Vf-Tv);
ex=efc+Ftd/Ef/Af;

while abs(c1)>0.1,
if e1>ecr,
    fc1=fcr/(1+(200*e1)^0.5);
else
    fc1=Ec*e1;
end
A=-Efv*psy*(e1-ex);
B=-t;
C=Efv*e1*psy+fc1;
```

```
a=((-B-(B^2-4*A*C)^0.5)/2/A);
theta=atan(a);
rxy=2*(e1-ex)*tan(theta);
ey=e1-(e1-ex)*tan(theta)^2;
e2=ex-(e1-ex)*tan(theta)^2;
if -e2+ec>0,
    c2=0;
    break
end
fcx=fc1-t/tan(theta);
fcy=fc1-t*tan(theta);
fc2=fc1-t*(tan(theta)+1/tan(theta));

if 1/(0.8-0.34*e1/ec)<1,
    fc2max=fc*(1/(0.8-0.34*e1/ec));
else
    fc2max=fc;
end

fc2a=fc2max*(2*(e2/ec)-(e2/ec)^2);

c1=fc2-fc2a;
if abs(c1)>0.1,
    e1=e1+0.000001;
end
n=n+1;
end

%judge if the reinforcement yield or what


if ey<efvu,
    fsy=ey*Efv;
else
    c2=0;
   break

end
if ex<efu,
    fsx=ex*Ef;
else
    c2=0;
   break

end
```

```
dfc1=fc1-psy*(fyy-fsy);
s=1/(sin(theta)/smx+cos(theta)/smy);
w=e1*s;
vcimax=(-fc)^0.5/(0.31+24*w/(agg+16));
if dfc1<=0,
    vci=0;
    fci=0;
else
    F=dfc1/tan(theta)-0.18*vcimax;
    if F<=0,
        fci=0;
        vci=dfc1/tan(theta);
    else
        D=0.82/vcimax;
        E=1/tan(theta)-1.64;
        fci=(-E-(E^2-4*D*F)^0.5)/2/D;
        vci=(fci+dfc1)/tan(theta);
    end
end

fsycr=fsy+(fc1+fci-vci*tan(theta))/psy;
fsxcr=fsx+(fc1+fci+vci/tan(theta))/psx;

%check failure mode
kc=1.64-1/tan(theta);
if kc<0,
    kc=0;
end


fm1=vcimax*(0.18+0.3*kc^2)*tan(theta)+psy*(fyy-fsy)-fc1;
fm2=(-fc2max+fc2);
fm3=(fyx-fsxcr);
fm4=(fyy-fsycr);



while ffvu>fsycr,

t=t+0.01;


e1=0.000001;

c1=2;n=0;c2=1;
```

```
while abs(c1)>0.1,
if e1>ecr,
    fc1=fcr/(1+(200*e1)^0.5);
else
    fc1=Ec*e1;
end
A=-Efv*psy*(e1-ex);
B=-t;
C=Efv*e1*psy+fc1;
a=((-B-(B^2-4*A*C)^0.5)/2/A);
theta=atan(a);
rxy=2*(e1-ex)*tan(theta);
ey=e1-(e1-ex)*tan(theta)^2;
e2=ex-(e1-ex)*tan(theta)^2;
if -e2+ec>0,
    c2=0;
    break
end
fcx=fc1-t/tan(theta);
fcy=fc1-t*tan(theta);
fc2=fc1-t*(tan(theta)+1/tan(theta));

if 1/(0.8-0.34*e1/ec)<1,
    fc2max=fc*(1/(0.8-0.34*e1/ec));
else
    fc2max=fc;
end

fc2a=fc2max*(2*(e2/ec)-(e2/ec)^2);

c1=fc2-fc2a;
if abs(c1)>0.1,
    e1=e1+0.000001;
end
n=n+1;
end

%judge if the reinforcement yield or what




if ey<efvu,
    fsy=ey*Efv;
else
   break;
```

```
end
if ex<efu,
    fsx=ex*Ef;
else
    c2=0;
   break

end

dfc1=fc1-psy*(fyy-fsy);
s=1/(sin(theta)/smx+cos(theta)/smy);
w=e1*s;
vcimax=(-fc)^0.5/(0.31+24*w/(agg+16));
if dfc1<=0,
    vci=0;
    fci=0;
else
    F=dfc1/tan(theta)-0.18*vcimax;
    if F<=0,
        fci=0;
        vci=dfc1/tan(theta);
    else
        D=0.82/vcimax;
        E=1/tan(theta)-1.64;
        fci=(-E-(E^2-4*D*F)^0.5)/2/D;
        vci=(fci+dfc1)/tan(theta);
    end
end

fsycr=fsy+(fc1+fci-vci*tan(theta))/psy;
fsxcr=fsx+(fc1+fci+vci/tan(theta))/psx;

%check failure mode
kc=1.64-1/tan(theta);
if kc<0,
    kc=0;
end

fm1=vcimax*(0.18+0.3*kc^2)*tan(theta)+psy*(fyy-fsy)-fc1;
fm2=(-fc2max+fc2);
fm3=(fyx-fsxcr);
fm4=(fyy-fsycr);

end

%calculate the shear reinforcement capacity
```

```
Vf=t*b*xc/3+(dc-xc)*bw*t;
Vv=Tv+1.3*(V-0.5*Vf-Tv)*sin(at);

c3=Vf+Vv-V;

if Vf+Vv<V,
    V=0.9*V;
else
    V=1.1*V;
end

end
 if c3<0,
    V=V/0.9;
else
    V=V/1.1;
end


P=V*2;
```

# Appendix B

# Simulation model and parametric analysis model

This appendix presents the simulation model used for simulating the tests of fabric formed T beams and the parametric analysis. Only the model used for T2-1R is presented and models for the other specimens can be acquired by changing the user defined parameters. The 'Matlab' codes for the simulation model of T2-1R is shown as follows:

```
%%%%geometry
L=3000;bwm=100;bf=800;df=80;
%%%%%%%%%%%%%% depth at the support
Ds=120;
%%%%%reinforcement
Ef=144000;efu=0.0185;ffu=Ef*efu;
db=10;
%%%%concrete
fcu=37.6;b1=0.8;
ecu=0.0035;Ec=22*(fcu/10)^0.33*1000;



%%%%% horizontal section cuts
y1=linspace(0,3000,100);%the calculation section
dx=L/99;
Af=zeros(1,100);%%%%%reinforcement area
bw=zeros(1,100);%%%%%%%%webwidth
D=zeros(1,100);%%%%%%%%depth
d=zeros(1,100);%%%%%effective depth
```

```
xu=zeros(1,100);%%%%%%%%%%compression zone depth before cracking
Ig=zeros(1,100);%%%%%%%%second moment of area before cracking
xc=zeros(1,100);%%%%%%%%%%compression zone depth after cracking
Icr=zeros(1,100);%%%%%%%%%second moment of area after cracking
Mcr=zeros(1,100);%%%%%%%%moment of cracking
Ma=zeros(1,100);%%%%%%%%applied moment
nf=Ef/Ec;%%%%%%%%modulus ratio of reinforcement and concrete
bfe=zeros(1,100);
Mu0=zeros(1,100);
UDLu0=zeros(1,100);
s2=500;
angle=atan(Ds/s2);
s1=(Ds-df)*cot(angle);









for i=1:100
    bw(i)=(50/1500^2*abs(y1(i)-1500)^2+50)*2;%%%%%%%web width of each section


        Af(i)=213;%%%%%%%% cross section aea of reinforcement

        D(i)=250-(250-Ds)/1500^2*abs(y1(i)-1500)^2;%%%%%%%%%%hight of
        each section (including concrete cover 25mm)
        d(i)=D(i)-25;
    if y1(i)<s1,
        bfe(i)=200; %%%width of the support
    else
        if y1(i)<s2,
            bfe(i)=(100+(y1(i)-s1)/(s2-s1)*300)*2;
        else
            if y1(i)<(3000-s2),
                bfe(i)=bf;
            else
                if y1(i)<(3000-s1),
                    bfe(i)=(100+((3000-y1(i))-s1)/(s2-s1)*300)*2;
                else
                    bfe(i)=200;
                end
            end
        end
     end
        xu(i)=(bfe(i)*df^2/2+bw(i)*(D(i)-df)*(D(i)-df)/2+(nf-1)*
```

```
        Af(i)*d(i))/(df*bfe(i)+bw(i)*(D(i)-df)+(nf-1)*Af(i));
68      %%%%%uncracked centroid
        Ig(i)=bfe(i)*df^3/12+bfe(i)*df*(xu(i)-df/2)^2+bw(i)*(D(i)-df)^3/12+bw(i)*(D(i)-df)*
70      (xu(i)-(D(i)+df)/2)^2+(nf-1)*Af(i)*(d(i)-xu(i))^2;
        %%%uncracked moment of inertia
72      xc(i)=(((nf*Af(i))^2+2*nf*Af(i)*d(i)*bfe(i))^0.5-nf*Af(i))/
        bfe(i);%%%%%%%%%%compression zone
74      Icr(i)=bfe(i)*xc(i)^3/3+(nf)*Af(i)*(d(i)-xc(i))^2;
        Mcr(i)=0.62*(fcu)^0.5*Ig(i)/(D(i)-xu(i));
76
    Mu0(i)=min(ffu*Af(i)*(d(i)-xc(i)/2),b1*fcu*bfe(i)*xc(i)*(d(i)-xc(i)/2));
78   if y1(i)<500,
       UDLu0(i)= Mu0(i)/0.5/L/y1(i);
80  else
      if y1(i)<1000,
82        UDLu0(i)=Mu0(i)/(0.5*(1*L)*y1(i)-(1*L)/5*(y1(i)-500));
      else
84        if y1(i)<1500,
            UDLu0(i)=Mu0(i)/(0.5*(1*L)*y1(i)-(1*L)/5*(y1(i)-1000)-(1*L)/5*(y1(i)-500));
86        else
            if y1(i)<2000,
88            UDLu0(i)=Mu0(i)/(0.5*(1*L)*y1(i)-(1*L)/5*(y1(i)-1500)-(1*L)/5*
              (y1(i)-1000)-(1*L)/5*(y1(i)-500));
90          else
              if y1(i)<2500,
92              UDLu0(i)=Mu0(i)/(0.5*(1*L)*y1(i)-(1*L)/5*(y1(i)-2000)-(1*L)/5*
                (y1(i)-1500)-(1*L)/5*(y1(i)-1000)-(1*L)/5*(y1(i)-500));
94            else
                UDLu0(i)=Mu0(i)/(0.5*(1*L)*y1(i)-(1*L)/5*(y1(i)-2500)-(1*L)/5*
96              (y1(i)-2000)-(1*L)/5*(y1(i)-1500)-(1*L)/5*(y1(i)-1000)-(1*L)/5*(y1(i)-500));
              end
98          end
        end
100   end
    end
102 end

104 %%%%%load case
    U=2.4;AL=7.5;%the total load;
106


108 UDLu=min(UDLu0);

110 DisMatrix=zeros(100,100);
    UAL0=zeros(100,1);
112
```

```
for j=1:100,
 UAL0(j)=j*UDLu/100;
n=zeros(1,100);%%%%%%%%%%factor to account for tension stiffening;
z=zeros(1,100);
r=zeros(1,100);%%%%%%%%factor to account for integration;
Ie=zeros(1,100);%%%%%%%%effective moment of inertia;
k=zeros(1,100);%%curvature
dr=zeros(1,100);%%%micro rotation without constant
for i=1:100,
  %  Ma(i)=(UAL0)*((L/2)^2-abs(y1(i)-1500)^2);
   if y1(i)<500,
        Ma(i)=0.5*(UAL0(j)*L)*y1(i);
    else
        if y1(i)<1000,
            Ma(i)=0.5*(UAL0(j)*L)*y1(i)-(UAL0(j)*L)/5*(y1(i)-500);
        else
            if y1(i)<1500,
                Ma(i)=0.5*(UAL0(j)*L)*y1(i)-(UAL0(j)*L)/5*(y1(i)-1000)-(UAL0(j)*L)/5*(y1(i)-500);
            else
                if y1(i)<2000,
                    Ma(i)=0.5*(UAL0(j)*L)*y1(i)-(UAL0(j)*L)/5*(y1(i)-1500)-(UAL0(j)*L)/5*
                    (y1(i)-1000)-(UAL0(j)*L)/5*(y1(i)-500);
                else
                    if y1(i)<2500,
                        Ma(i)=0.5*(UAL0(j)*L)*y1(i)-(UAL0(j)*L)/5*(y1(i)-2000)-(UAL0(j)*L)/5*
                        (y1(i)-1500)-(UAL0(j)*L)/5*(y1(i)-1000)-(UAL0(j)*L)/5*(y1(i)-500);
                    else
                        Ma(i)=0.5*(UAL0(j)*L)*y1(i)-(UAL0(j)*L)/5*(y1(i)-2500)-(UAL0(j)*L)/5*
                        (y1(i)-2000)-(UAL0(j)*L)/5*(y1(i)-1500)-(UAL0(j)*L)/5*
                        (y1(i)-1000)-(UAL0(j)*L)/5*(y1(i)-500);
                    end
                end
            end
        end
  end

    if Ma(i)<Mcr(i)
        Ie(i)=Ig(i);
    else

    n(i)=1-Icr(i)/Ig(i);
    z(i)=1-(1-Mcr(i)/(Ma(i)))^0.5;
    r(i)=(1.6*z(i)^3-0.6*z(i)^4)/(Mcr(i)/Ma(i))^2+2.4*log(2-z(i));
    Ie(i)=Icr(i)/(1-r(i)*n(i)*(Mcr(i)/(Ma(i)))^2); %%%%
    if Ie(i)>Ig(i),
        Ie(i)=Ig(i);
```

```
    end
    end
    k(i)=Ma(i)/Ec/Ie(i);
    if i<2,
    dr(i)=k(i)*dx;
    else
        dr(i)=dr(i-1)+k(i)*dx;
    end
end

Dr=zeros(1,100);%%%micro rotation with constant
C=-dr(50);
def=zeros(1,100);%%%deflection without constant
for i=1:100,

   Dr(i)=dr(i)+C;
    if i<2,
    def(i)=Dr(i)*dx;
    else
        def(i)=def(i-1)+Dr(i)*dx;
    end
    DisMatrix(j,i)=abs(def(i));
end


end

ard=zeros(100,1);%angle of reinforcement with deflection
ad=zeros(100,1); %angle caused by deflection

for i=1:100
ar=atan(2*(250-Ds)/1500^2*abs(y1(2)-1500));%angle of reinforcement at the edge
of the support
ad(i)=atan(DisMatrix(i,16)/16/dx);%%%%%% the angle caused
by deflection at the first loading jack
ard(i)=ar+ad(i);%%%%%%%%% angle of reinforcement =
initial angle + deflection angle
end

%%%%%%%%the actual stress of the longitudinal reinforcement and concrete
%%%%%%%%based on bending calculation at the calculated cross sections/ the
%%%%%%%%initial value of Vxy and ecn
ff=zeros(1,100);
ef=zeros(1,100);
fc=zeros(1,100);
ec=zeros(1,100);
```

```
sb=zeros(1,100);
ecn=zeros(1,100);
Mab=zeros(1,100);
Vxy=zeros(1,100);

for i=1:100
Mab(i)=0.5*(UAL0(i)*L)*y1(5);
ff(i)=Mab(i)/(d(5)-xc(5)/2)/Af(5);
ef(i)=ff(i)/Ef;
fc(i)=ff(i)*Af(5)/bfe(5)/xc(5)/b1;
ec(i)=ef(i)/(d(5)-xc(5))*xc(5);
ecn(i)=((d(5))/2-xc(5))*ec(i)/xc(5);%%%%%%strain of mid section
Vxy(i)=(UAL0(i)*3/2*1000)/(xc(5)*bfe(5)/3+bw(5)*(D(5)-25-xc(5)));
%%%%%%%parabola distribution of shear stress in the compression zone
%and stress block in the tension zone
end

%%%%%MCFT calculation

fcr=0.33*(fcu)^0.5;% the cracking strength
psy=0.00344;%%%%%%%%%%%%%%%%%%%%%%%%%% the vertical reinforcement ratio
psx=Af(2)/bw(2)/(d(2));%%%%%%%%%%%%%%%%%%%%%%%%%the reinforcement ratio
ecm=-0.002;
Esx=Ef;Es=108700;efvu=0.0065;%0.0051
fyx=efu*Esx;fyy=efvu*Es;
%%%%%%%%%%%%%%%%needs to be modified%
%%Esx=Ef;Es=108700;efvu=0.0139;
%fyx=efu*Esx;fyy=0.5*efvu*Es;
eyx=fyx/Esx;eyy=fyy/Es;fcm=-fcu;
smx=d(2);
smy=66;%%%%%%%%%%%%%%%%%%needs to be changed for every model
ecr=fcr/Ec;agg=10;

Fv=zeros(1,100);
Fc=zeros(1,100);
Fh=zeros(1,100);
Tv=zeros(1,100);
Th=zeros(1,100);
T=zeros(1,100);
Tfv=zeros(1,100);
ffv=zeros(1,100);
Fm4=zeros(1,100);
C3=zeros(1,100);

for i=1:100,
c3=10000;%%%%%%%%%%%%%%error for tensile force of shear resistance
```

```
252 while c3>15*i,
    e1=0.000001; %%%%%%%tensile principal strain
254
    c1=2;%%%%error of compressive stress
256 n=0;
    c2=1; %%%%%%%error of compressive strain
258
    while abs(c1)>0.1,
260 if e1>ecr,
        fc1=fcr/(1+(200*e1)^0.5);
262 else
        fc1=Ec*e1;
264 end
    A=-Es*psy*(e1-ecn(i));
266 B=-Vxy(i);
    C=Es*e1*psy+fc1;
268 a=((-B-(B^2-4*A*C)^0.5)/2/A);
    theta=atan(a);
270 rxy=2*(e1-ecn(i))*tan(theta);
    ey=e1-(e1-ecn(i))*tan(theta)^2;
272 e2=ecn(i)-(e1-ecn(i))*tan(theta)^2;
    if -e2+ecm>0,
274     c2=0;
        break
276 end
    fcx=fc1-Vxy(i)/tan(theta);
278 fcy=fc1-Vxy(i)*tan(theta);
    fc2=fc1-Vxy(i)*(tan(theta)+1/tan(theta));
280
    if 1/(0.8-0.34*e1/ecm)<1,
282     fc2max=(-fcu)*(1/(0.8-0.34*e1/ecm));
    else
284     fc2max=(-fcu);
    end
286
    fc2a=fc2max*(2*(e2/ecm)-(e2/ecm)^2);
288
    c1=fc2-fc2a;
290 if abs(c1)>0.1,
        e1=e1+0.0001;
292 end
    n=n+1;
294 end

296 %judge if the reinforcement yield or what
```

```
298
300 fsy=ey*Es;
302
    fsx=ecn(i)*Esx;
304
306 dfc1=fc1-psy*(fyy-fsy);
    s=1/(sin(theta)/smx+cos(theta)/smy);
308 w=e1*s;
    vcimax=(-(-fcu))^0.5/(0.31+24*w/(agg+16));
310 if dfc1<=0,
        vci=0;
312     fci=0;
    else
314     F=dfc1/tan(theta)-0.18*vcimax;
        if F<=0,
316         fci=0;
            vci=dfc1/tan(theta);
318     else
            D=0.82/vcimax;
320         E=1/tan(theta)-1.64;
            fci=(-E-(E^2-4*D*F)^0.5)/2/D;
322         vci=(fci+dfc1)/tan(theta);
        end
324 end

326 fsycr=fsy+(fc1+fci-vci*tan(theta))/psy;
    fsxcr=fsx+(fc1+fci+vci/tan(theta))/psx;
328
    %check failure mode
330 kc=1.64-1/tan(theta);
    if kc<0,
332     kc=0;
    end
334
    fm1=vcimax*(0.18+0.3*kc^2)*tan(theta)+psy*(fyy-fsy)-fc1;
336 fm2=(-fc2max+fc2)/(-fc2max);
    fm3=(fyx-fsxcr)/fyx;
338 fm4=(fyy-fsycr)/fyy;

340
    l=Ds/tan(theta);
342 theta0=atan(Ds/500);
```

```
Fv(i)=(xc(5)*bfe(5)/3+bw(5)*(d(5)-xc(5)))*Vxy(i);%l*psy*bw(2)*fsycr;

Fh(i)=Fv(i)*((sin(60/180*3.14)+cos(60/180*3.14))*cos(60/180*3.14)+cos(90/180*3.14))/
((sin(60/180*3.14)+cos(60/180*3.14))*sin(60/180*3.14)+sin(90/180*3.14));
%Fv(i)*(1.6*cos(60/180*3.14)+cos(90/180*3.14))/(1.6*sin(60/180*3.14)+sin(90/180*3.14));%
%%%%%%%%%%%%%%%%%%%%%%%%set the reinforcement parameters
T(i)=(UAL0(i)*3/2*1000-Fv(i)*(500-100-l/2)/500-Fh(i)*l*tan(theta-ad(i))/2/500)*
cot(theta0-ad(i))/(cot(theta0-ad(i))*tan(ard(i))*450/500+1)/cos(ard(i));%
Tv(i)=T(i)*sin(ard(i));
c3=abs(UAL0(i)*3/2*1000-Fv(i)-Tv(i));%-efc(i)*Ef*Af(2)*tan(ard(i))
Vxy(i)=(UAL0(i)*3/2*1000-Tv(i))/(xc(5)*bfe(5)/3+bw(5)*(d(5)-xc(5)));%-efc(i)*Ef*Af(2)*tan(ard(i))
Th(i)=T(i)*cos(ard(i));


C3(i)=c3;
end
ffv(i)=fsycr;
Fm4(i)=fm4;
nr=i;
if fsycr>=fyy,
%%%%%%%%%%%%%%%%%%%%%%%%%%%%%%%%needs to be changed based on
%the property of shear links
    fsycr=0;
    break
end


end

for i=nr:100,

    Fv(i)=0*Fv(nr);
Fh(i)=Fv(i)*(1.6*cos(60/180*3.14)+cos(90/180*3.14))/(1.6*sin(60/180*3.14)+sin(90/180*3.14));%Fv(i)*
(1.9*cos(60/180*3.14)+cos(90/180*3.14))/(1.9*sin(60/180*3.14)+sin(90/180*3.14));
%%%%%%%%%%%%%%%%%%%%%%%%set the reinforcement parameters
T(i)=(UAL0(i)*3/2*1000-Fv(i)*(500-100-l/2)/500-Fh(i)*l*tan(theta-ad(i))/2/500)*
cot(theta0-ad(i))/(cot(theta0-ad(i))*tan(ard(i))*450/500+1)/cos(ard(i));%
Tv(i)=T(i)*sin(ard(i));  %+efc(i)*Ef*Af(2)*tan(ard(i))
c3=abs(UAL0(i)*3/2*1000-Fv(i)-Tv(i)-Fc(i));%-efc(i)*Ef*Af(2)*tan(ard(i))
C3(i)=c3;
ffv(i)=ffv(nr)*0;
Fm4(i)=fm4;
end
```

# Appendix C

# Test data of fabric formed T beams

Not all the test data has been presented in Chapter 6. This section presents all the remaining data acquired from the T beam tests. All the data is plotted against the total applied load in the following figures.

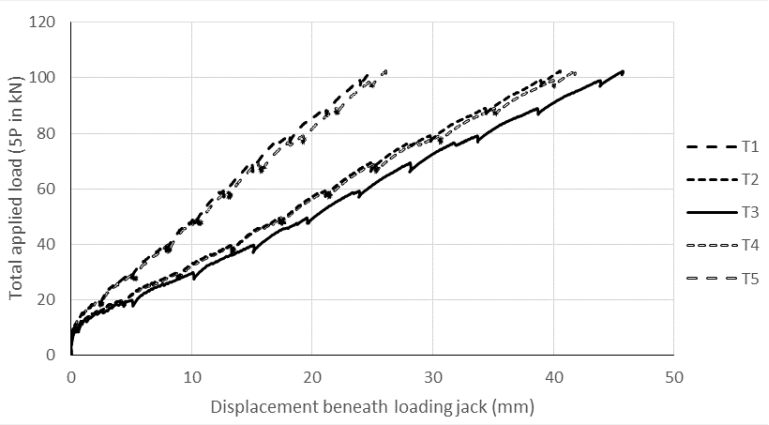


Figure C-1: Load-displacement curves of T1

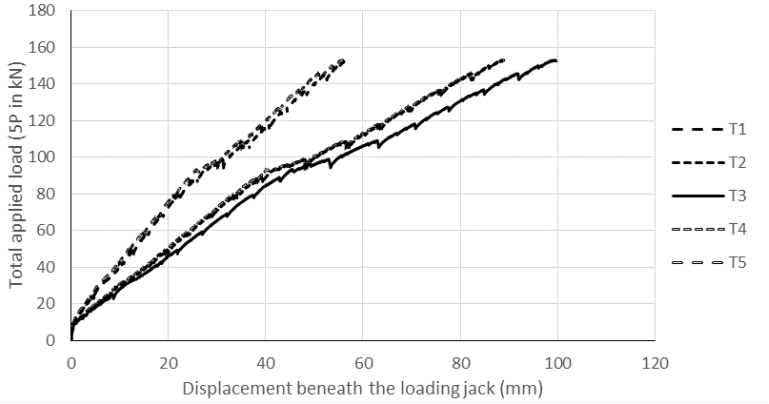


Figure C-2: Load-displacement curves of T2-1

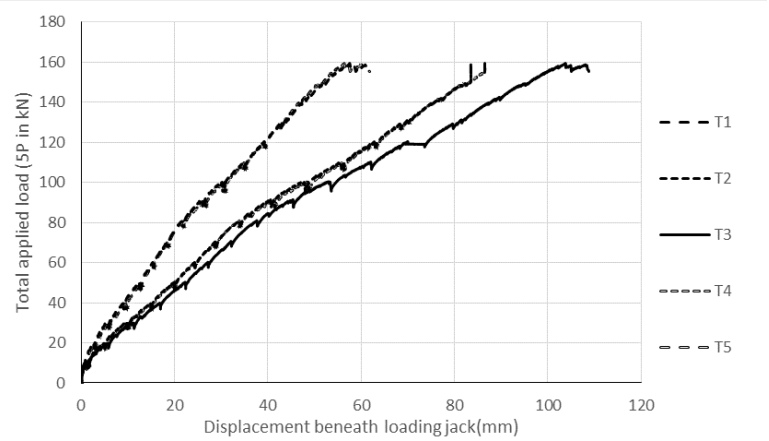


Figure C-3: Load-displacement curves of T2-2

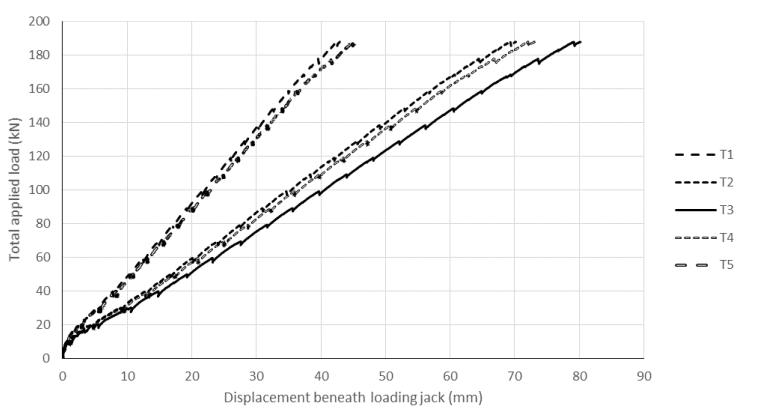


Figure C-4: Load-displacement curves of T2-1R

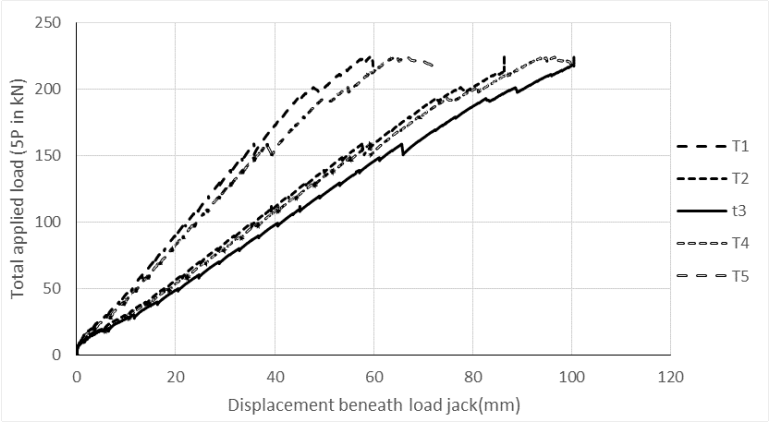


Figure C-5: Load-displacement curves of T2-2R

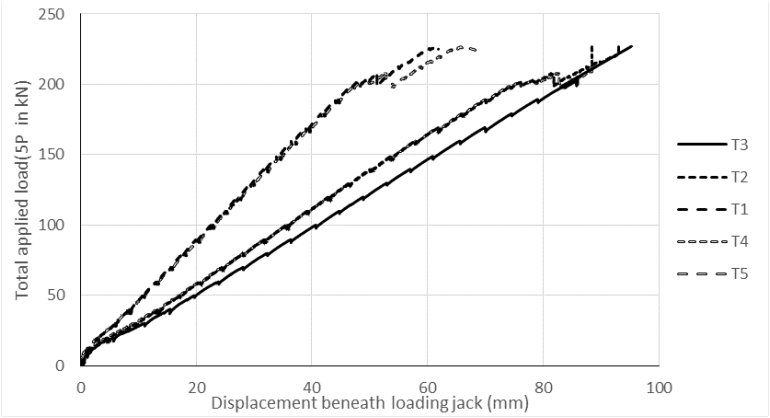


Figure C-6: Load-displacement curves of T3-1

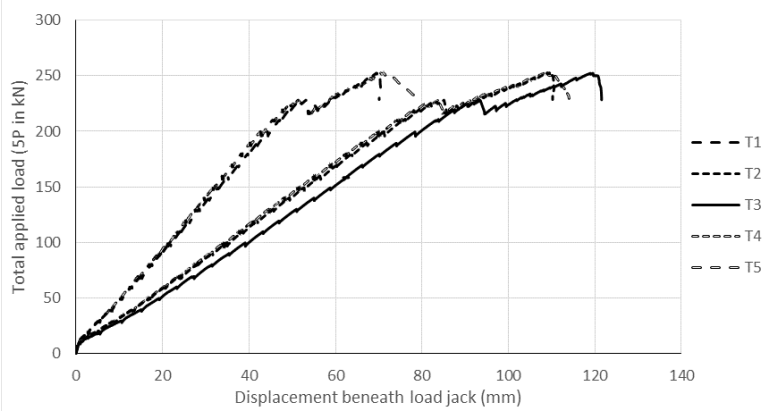


Figure C-7: Load-displacement curves of T3-2

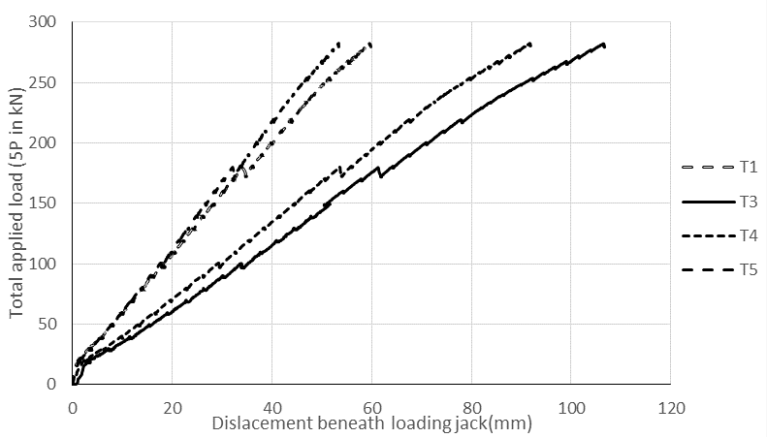


Figure C-8: Load-displacement curves of T4-1

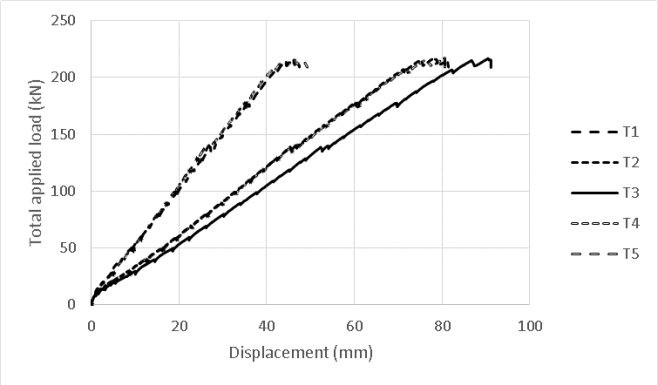


Figure C-9: Load-displacement curves of T4-2

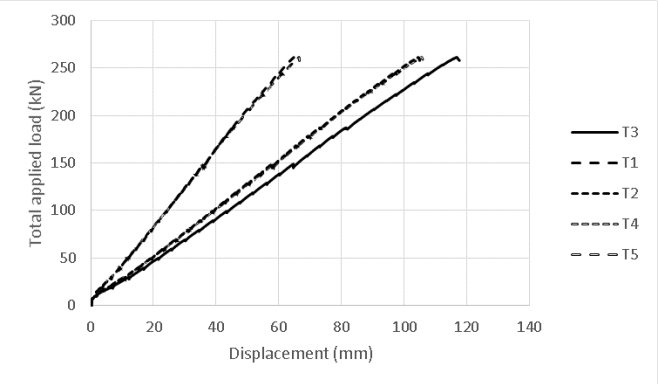


Figure C-10: Load-displacement curves of T5

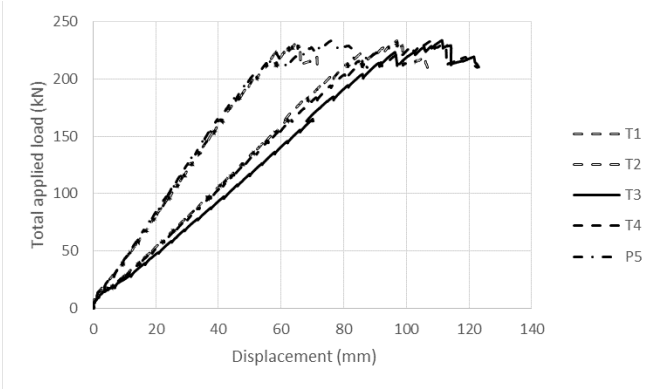


Figure C-11: Load-displacement curves of T6

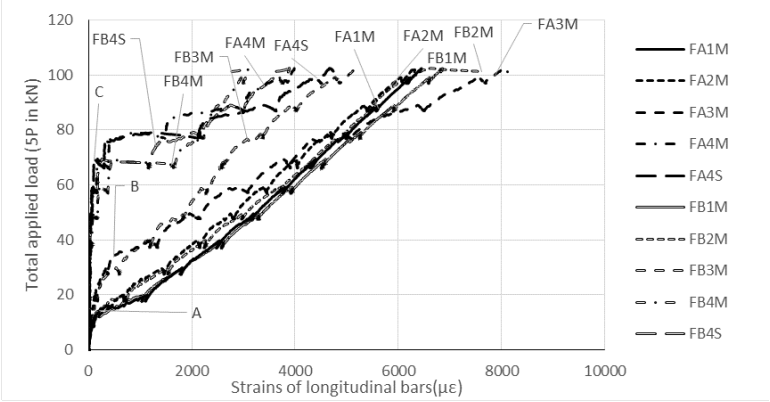


Figure C-12: Load-strain curves of longitudinal bars in T1

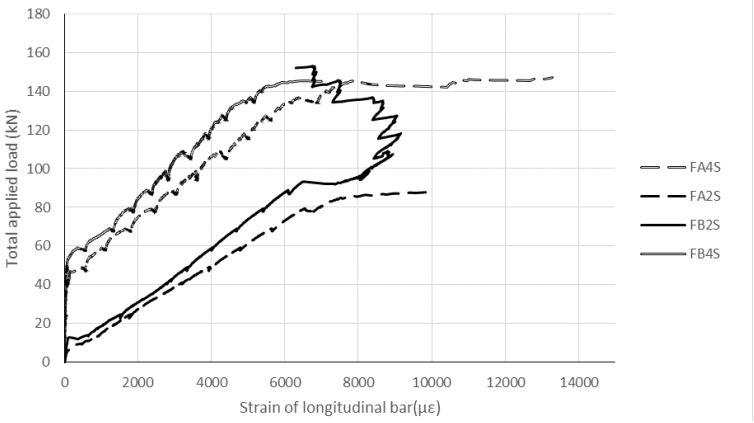


Figure C-13: Load-strain curves of longitudinal bars in T2-1

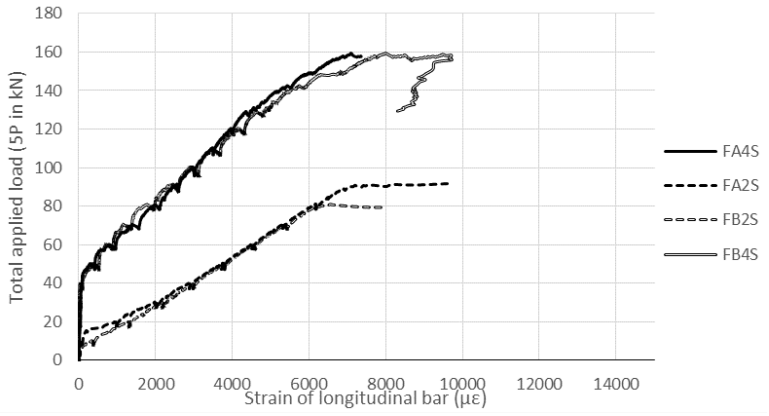


Figure C-14: Load-strain curves of longitudinal bars in T2-2

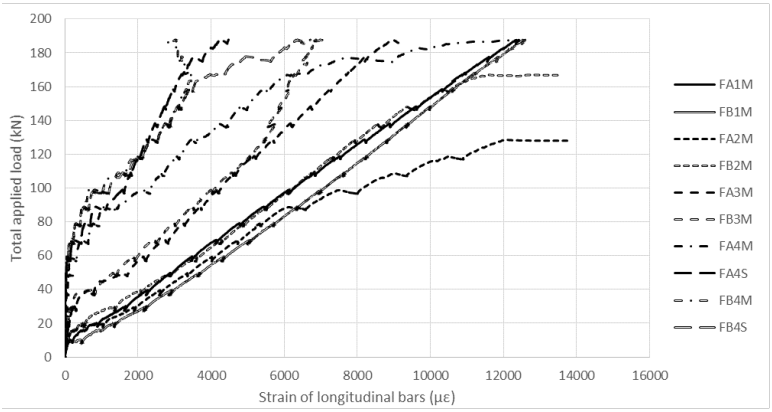


Figure C-15: Load-strain curves of longitudinal bars in T2-1R

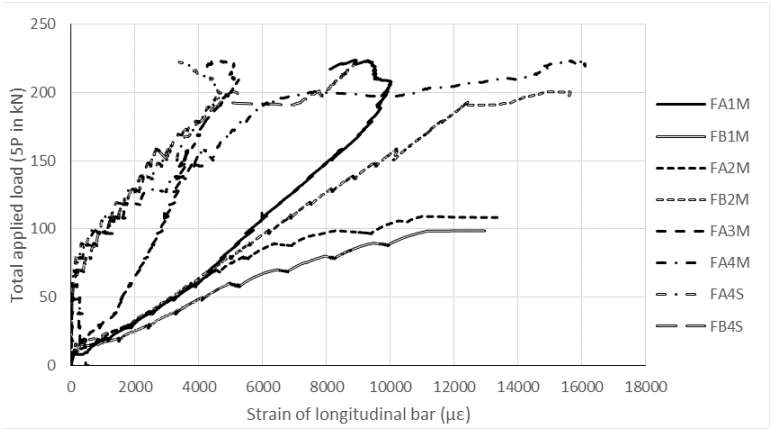


Figure C-16: Load-strain curves of longitudinal bars in T2-2R

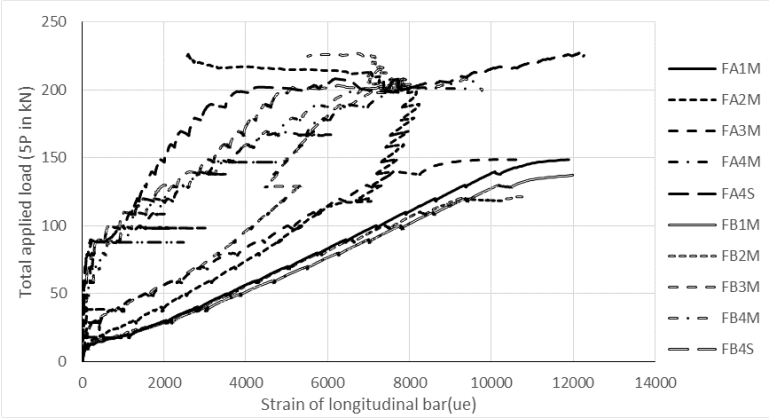


Figure C-17: Load-strain curves of longitudinal bars in T3-1

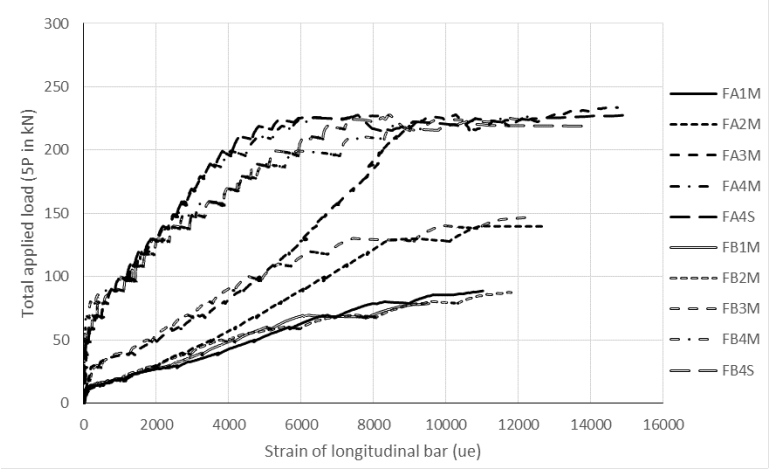


Figure C-18: Load-strain curves of longitudinal bars in T3-2

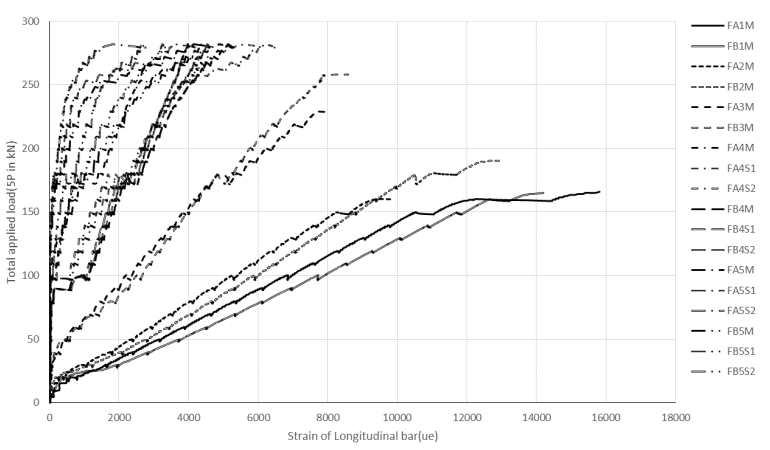


Figure C-19: Load-strain curves of longitudinal bars in T4-1

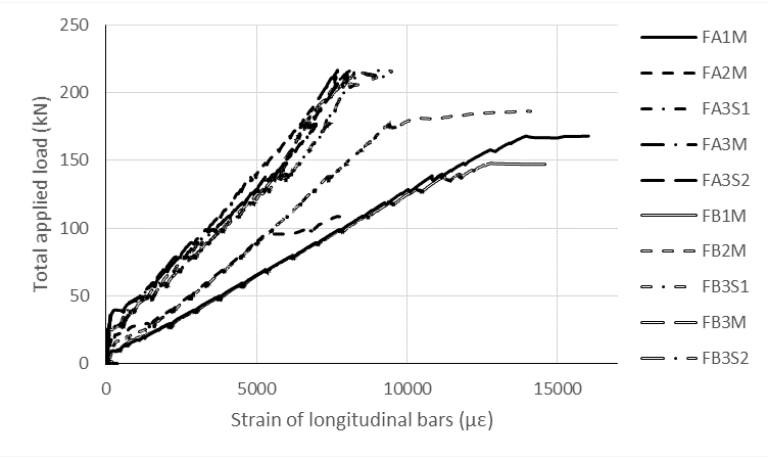


Figure C-20: Load-strain curves of longitudinal bars in T4-2 (except for the supports)

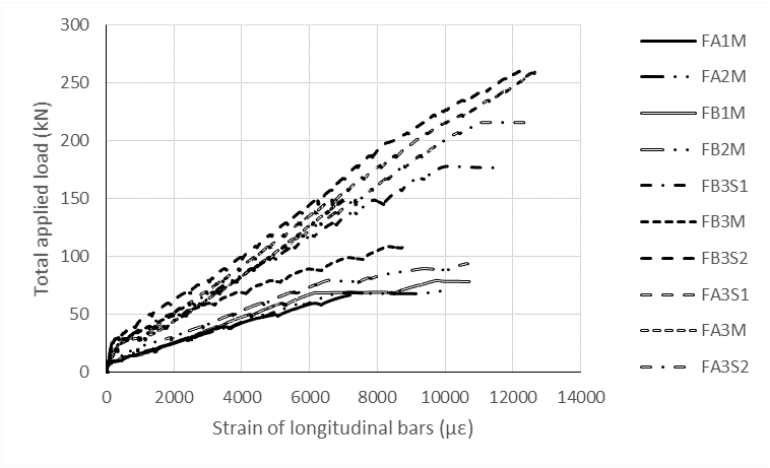


Figure C-21: Load-strain curves of longitudinal bars in T5 (except for the supports)

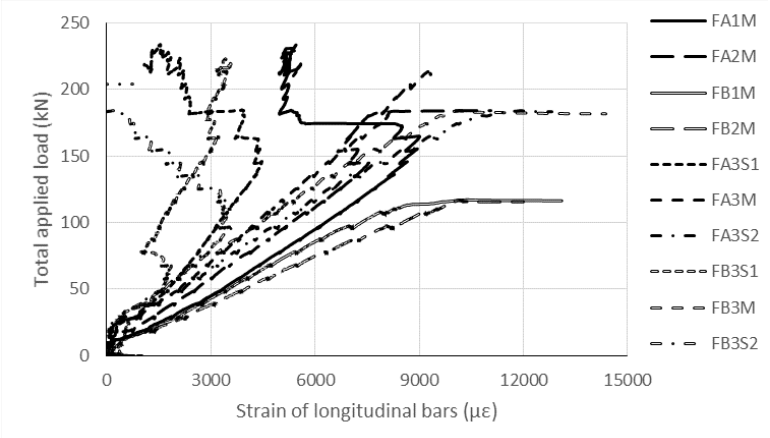


Figure C-22: Load-strain curves of longitudinal bars in T6 (except for the supports)

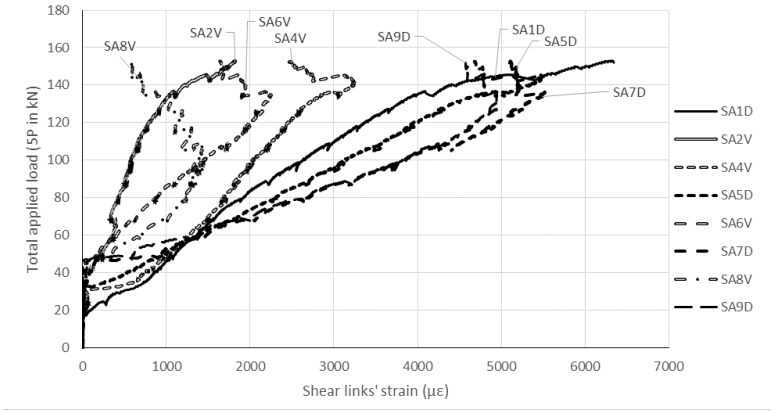


Figure C-23: Load-strain curves of shear links of side A in T2-1

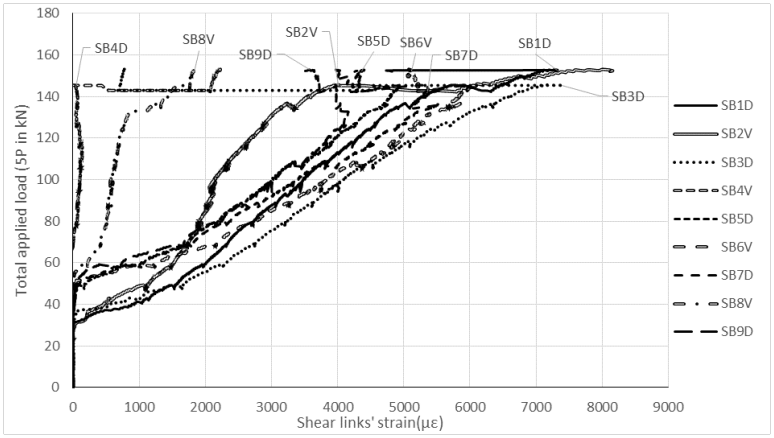


Figure C-24: Load-strain curves of shear links of side B in T2-1

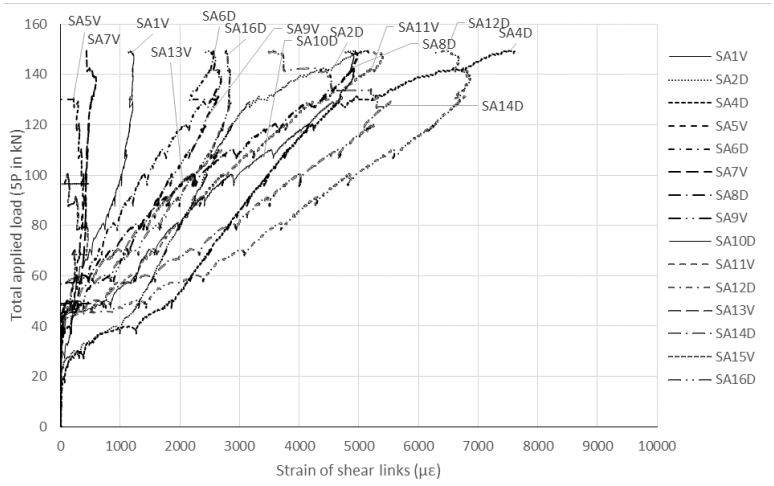


Figure C-25: Load-strain curves of shear links of side A in T2-2

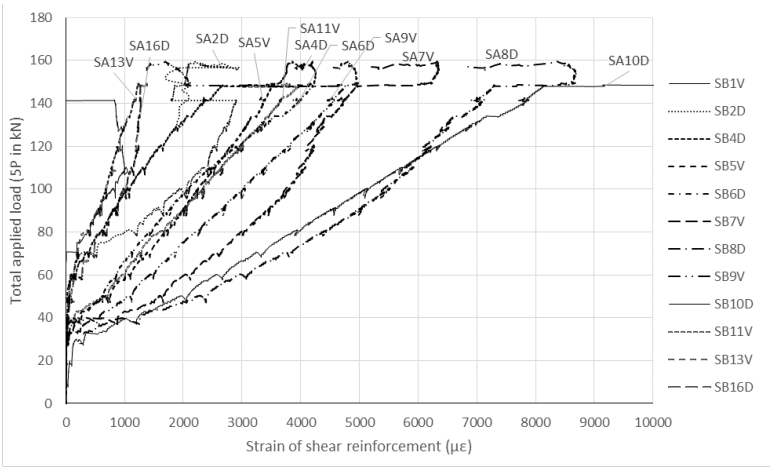


Figure C-26: Load-strain curves of shear links of side B in T2-2

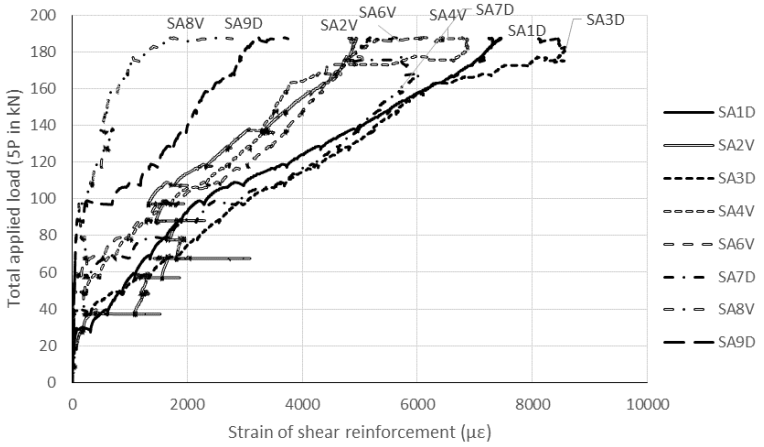


Figure C-27: Load-strain curves of shear links of side A in T2-1R

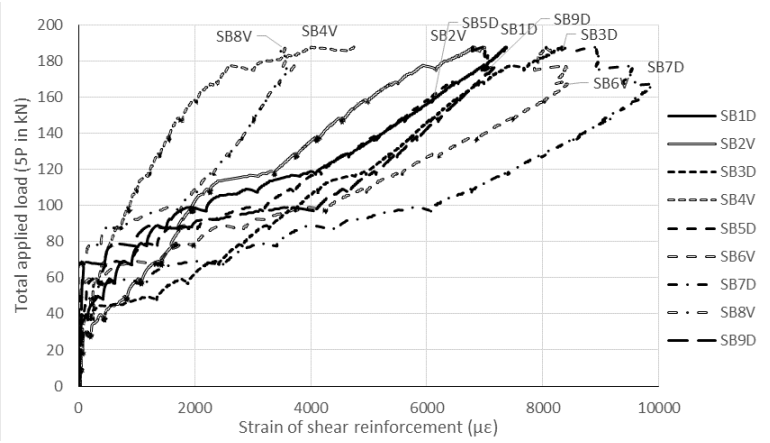


Figure C-28: Load-strain curves of shear links of side B in T2-1R

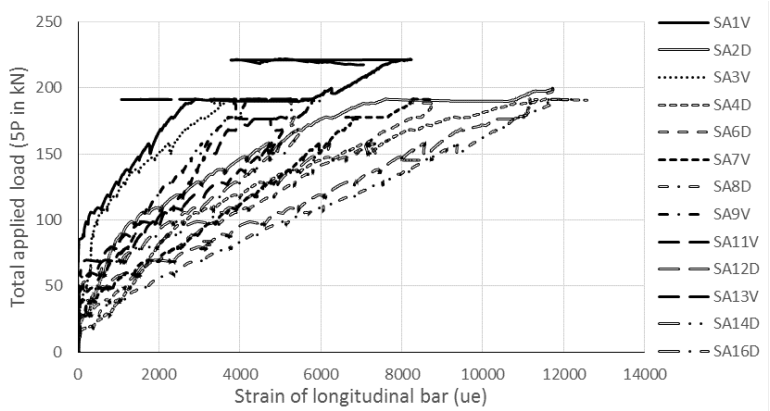


Figure C-29: Load-strain curves of shear links of side A in T2-2R

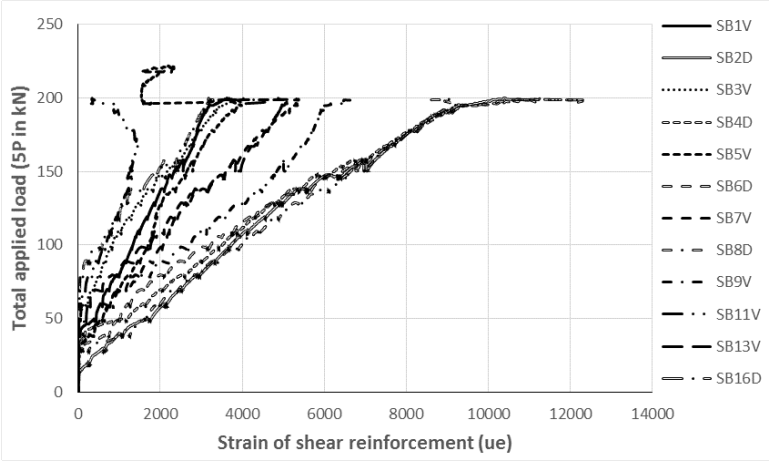


Figure C-30: Load-strain curves of shear links of side B in T2-2R

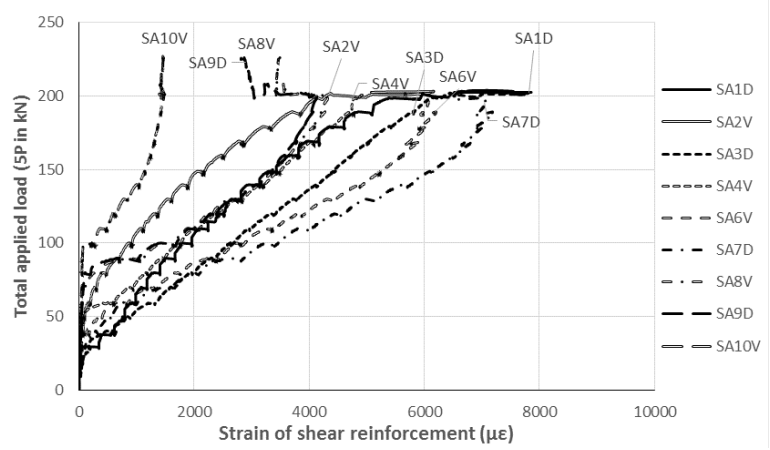


Figure C-31: Load-strain curves of shear links of side A in T3-1

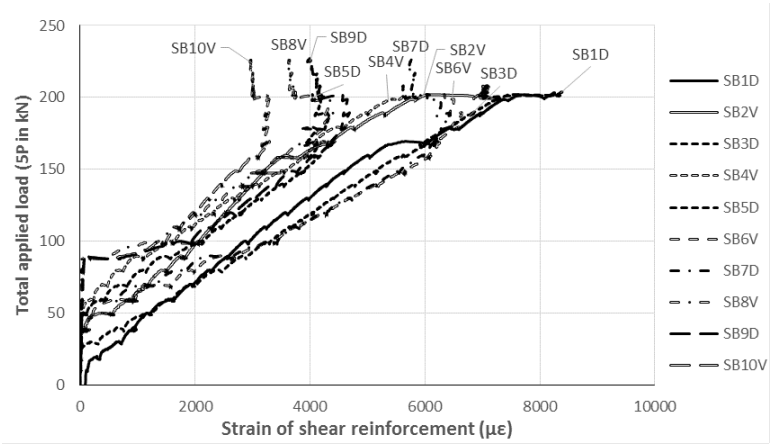


Figure C-32: Load-strain curves of shear links of side B in T3-1

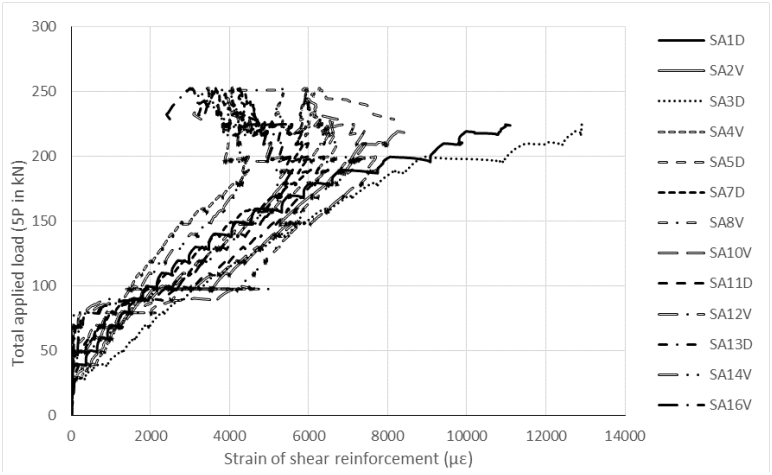


Figure C-33: Load-strain curves of shear links of side A in T3-2

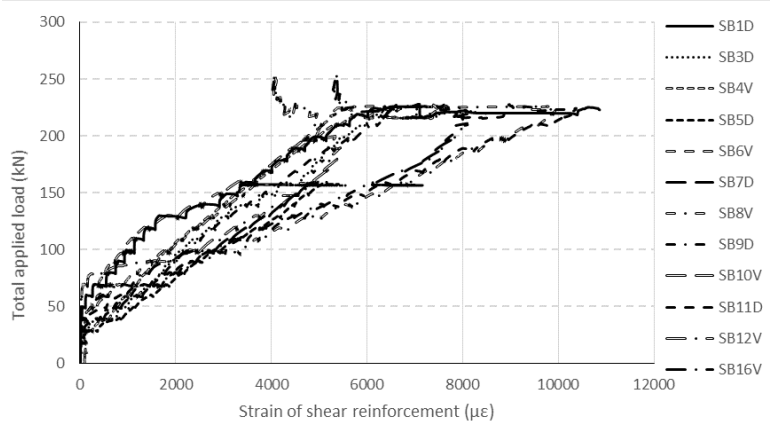


Figure C-34: Load-strain curves of shear links of side B in T3-2

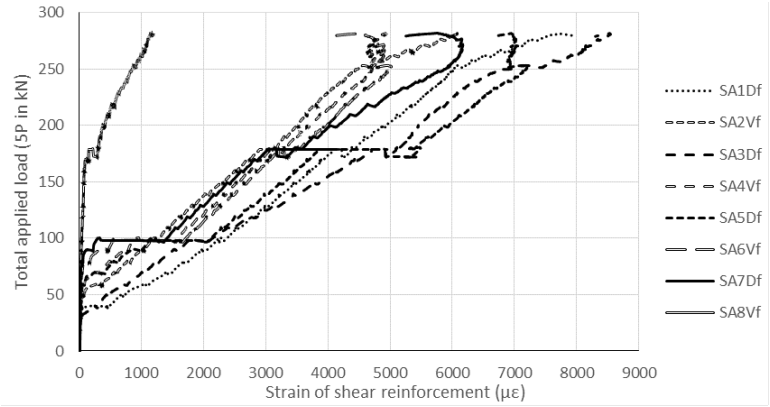


Figure C-35: Load-strain curves of shear links of side A1 in T4-1

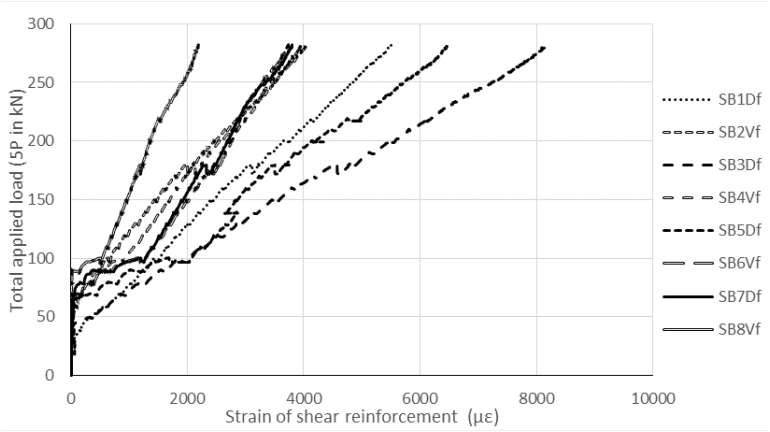


Figure C-36: Load-strain curves of shear links of side B1 in T4-1

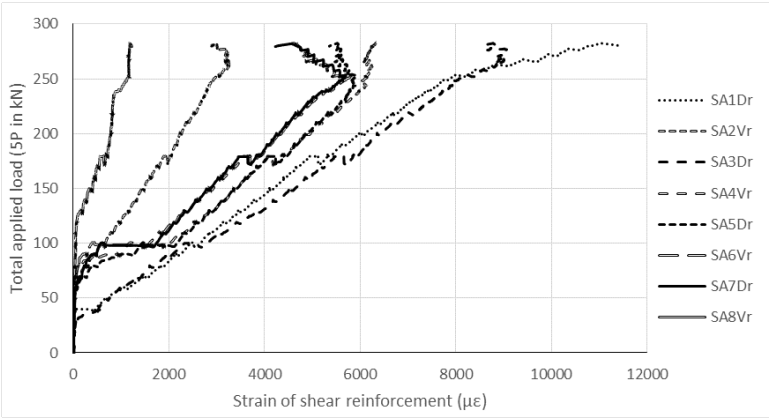


Figure C-37: Load-strain curves of shear links of side A2 in T4-1

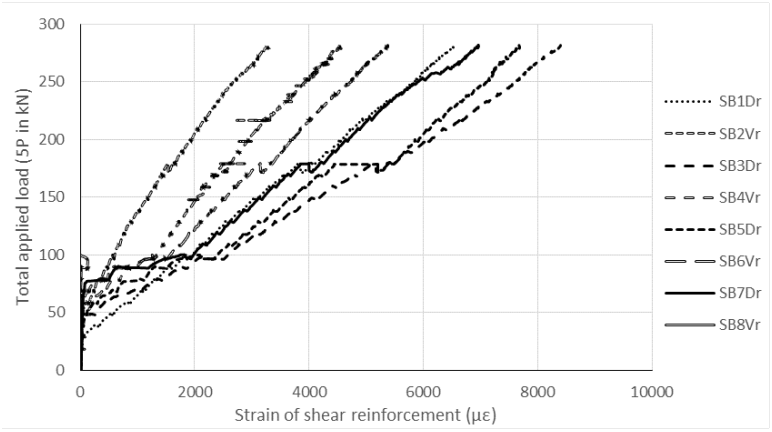


Figure C-38: Load-strain curves of shear links of side B2 in T4-1

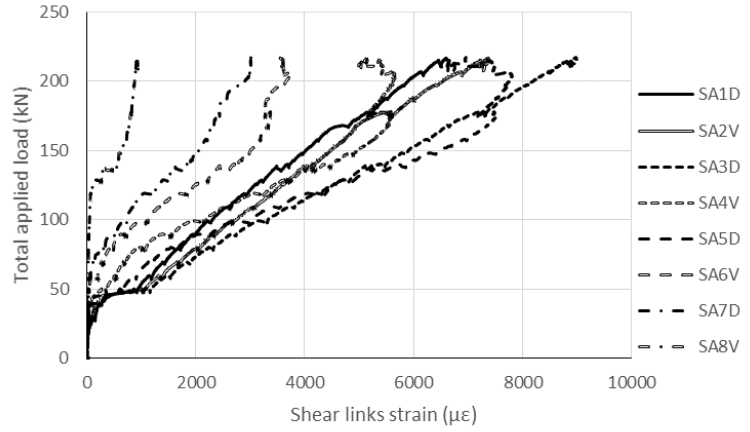


Figure C-39: Load-strain curves of shear links of side A in T4-2

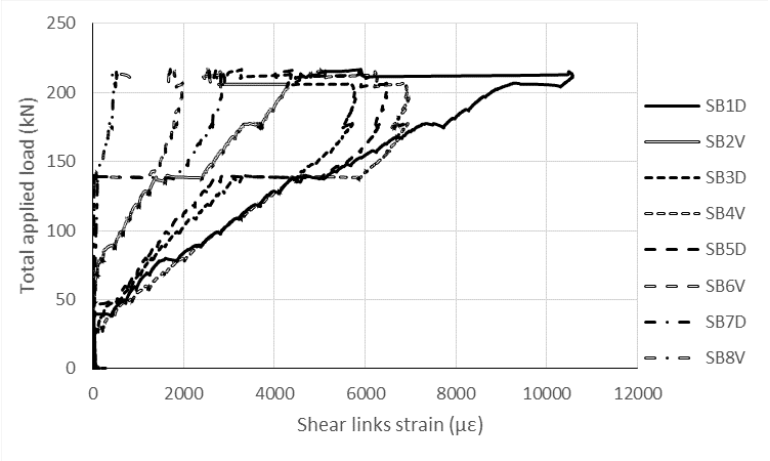


Figure C-40: Load-strain curves of shear links of side B in T4-2

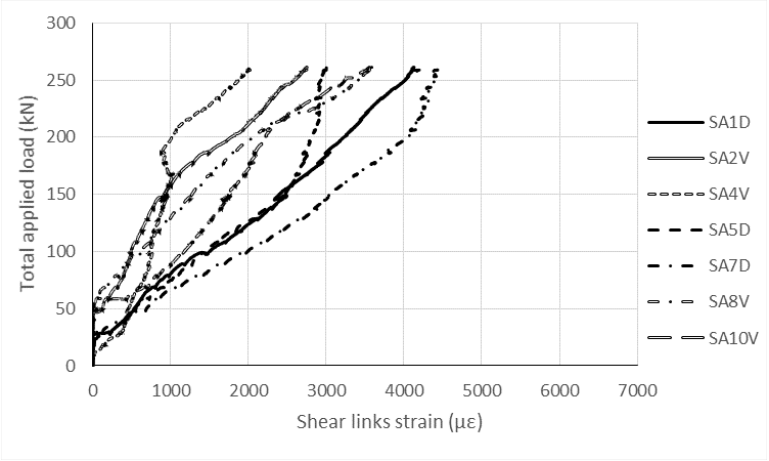


Figure C-41: Load-strain curves of shear links of side A in T5

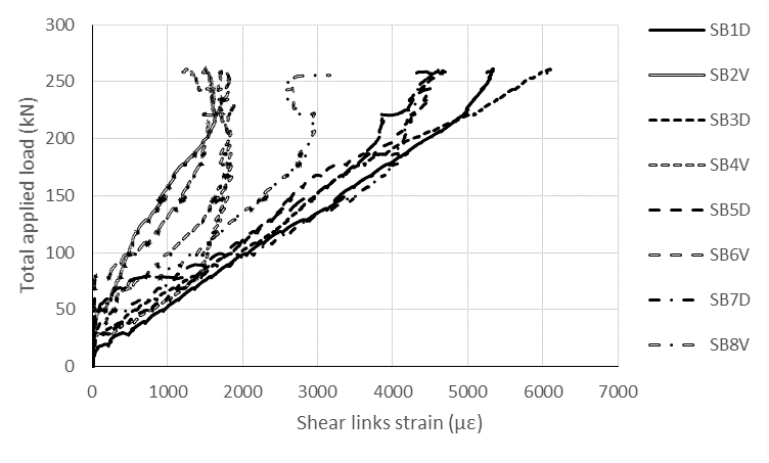


Figure C-42: Load-strain curves of shear links of side B in T5

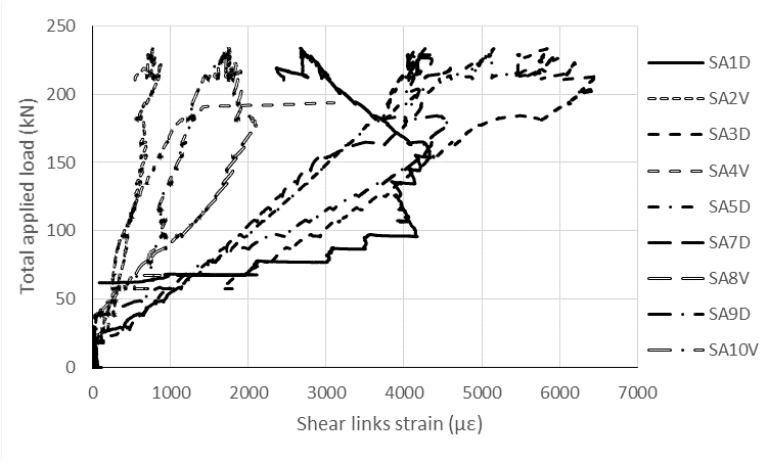


Figure C-43: Load-strain curves of shear links of side A in T6

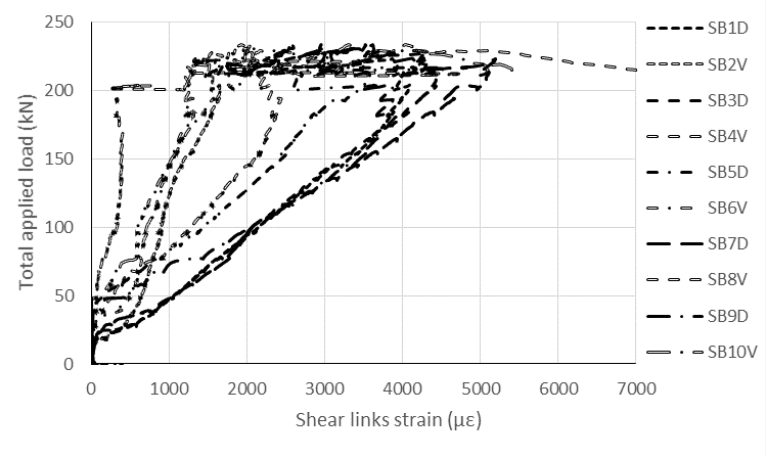


Figure C-44: Load-strain curves of shear links of side B in T6

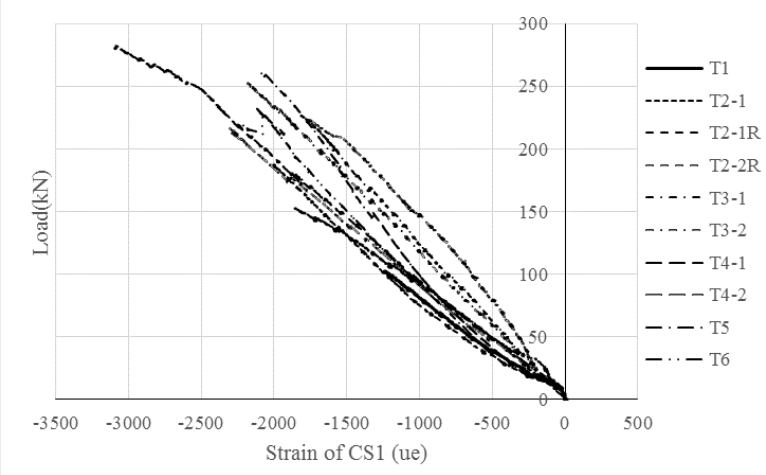


Figure C-45: Load-strain curves of concrete (CS1)

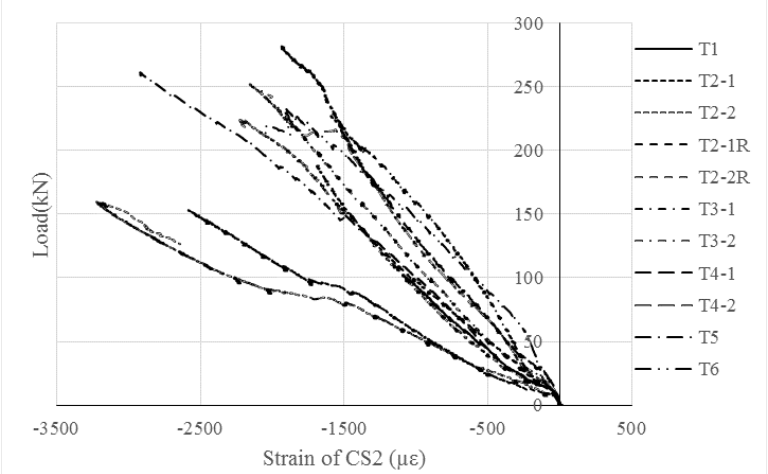


Figure C-46: Load-strain curves of concrete (CS2)

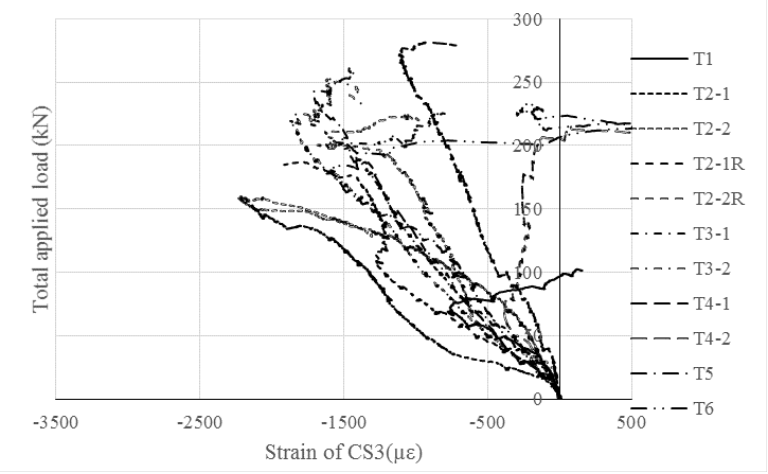


Figure C-47: Load-strain curves of concrete (CS3)

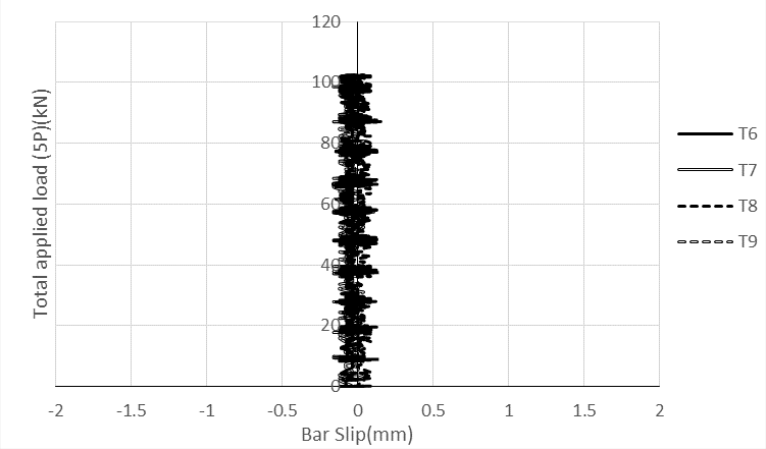


Figure C-48: Bar end slip of T1

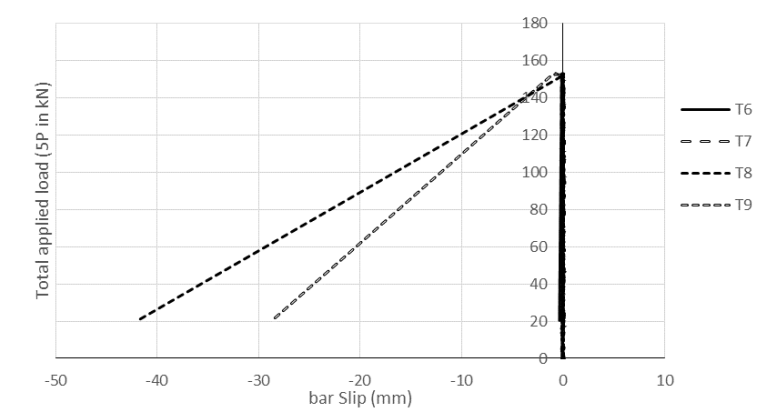


Figure C-49: Bar end slip of T2-1

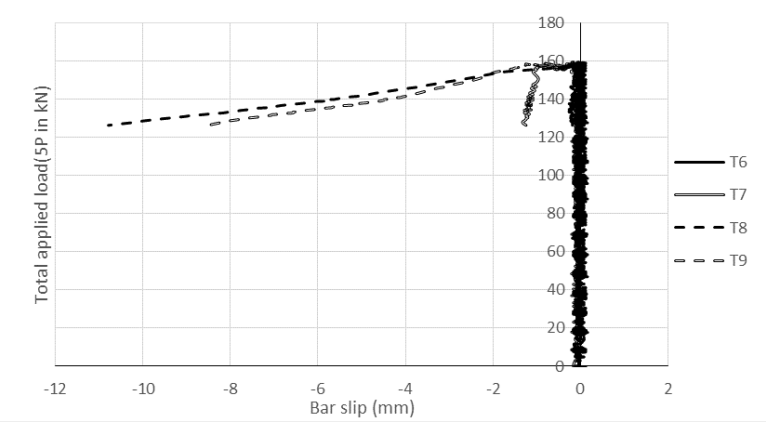


Figure C-50: Bar end slip of T2-2

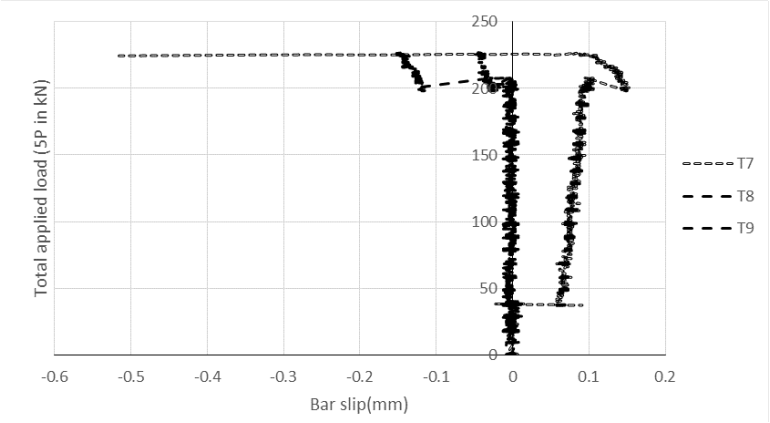


Figure C-51: Bar end slip of T3-1

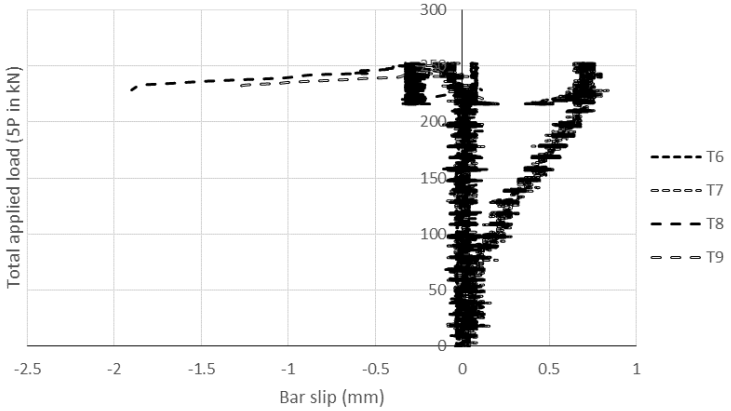


Figure C-52: Bar end slip of T3-2

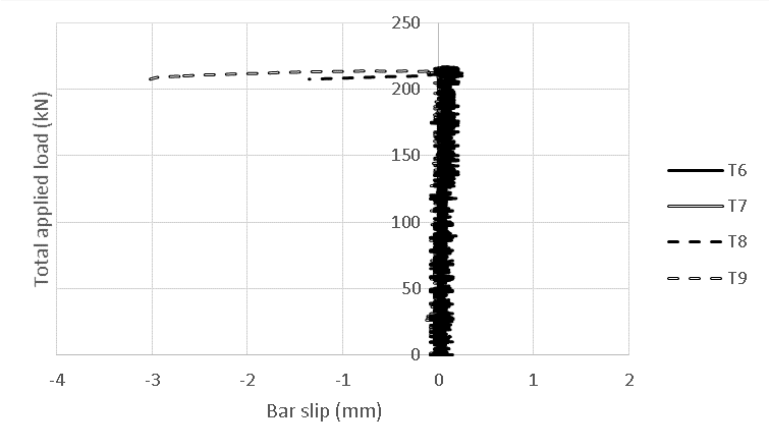


Figure C-53: Bar end slip of T4-2

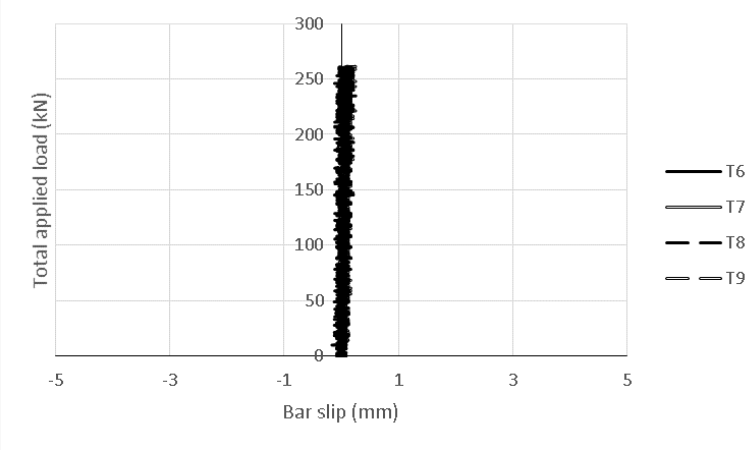


Figure C-54: Bar end slip of T5

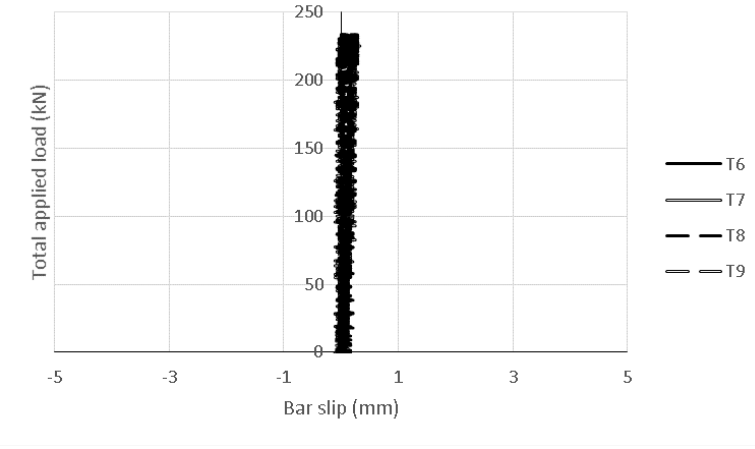


Figure C-55: Bar end slip of T6